Terahertz Scattering-Type Scanning Near-Field Optical Microscopy for Measurement of Plasmonic Effects

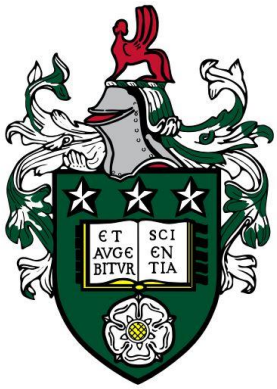

Daniel James Mohun

Pollard Institute

School of Electronic and Electrical Engineering

The University of Leeds

Submitted in accordance with the requirements for the degree of

Doctor of Philosophy

November 2024

Intellectual Property and Publication Statements

I confirm that the work submitted is my own, except where work which has formed part of jointly authored publications has been included. My contribution and the other authors to this work has been explicitly indicated below. I confirm that appropriate credit has been given within the thesis where reference has been made to the work of others.

The results discussed in Chapter 3 formed the basis for a journal publication in the Scientific Reports journal:

D. Mohun, N. Sulollari, M. Salih, L. Li, J.E. Cunningham, E.H. Linfield, A.G. Davies, and P. Dean, "Terahertz microscopy using laser feedback interferometry based on a generalised phase-stepping algorithm," Scientific Reports, 14(1), 2024

Paul Dean and Daniel Mohun conceived of the experiment, performed the measurements and interpreted the data. Nikollao Sulollari supported the experimental measurements and performed F.E.M. simulations, under the supervision of John E. Cunningham. Mohammed Salih processed the Q.C.L. devices. Lianhe Li grew the M.B.E wafers under the supervision of Edmund H. Linfield and A. Giles Davies. Paul Dean and Daniel Mohun wrote the paper with contributions from all authors.

Acknowledgements

Firstly, I would like to thank my supervisor Dr Paul Dean for providing me with the opportunity to work on this project and also for his invaluable support and guidance throughout.

Secondly, I would like to thank Dr Mohammed Salih and Dr Lianhe Li for fabricating and processing the QCLs, Dr Mark Rosamond for fabricating the samples using electron-beam lithography, my secondary supervisors Dr Joshua Freeman and Professor John E. Cunningham and the heads of department Professor Edmund H. Linfield and Professor A. Giles Davies.

Special thanks go to my colleague and friend Dr Nikollao Sulollari for training me on the THz-s-SNOM system and his enormous contribution to this project.

Lastly, I would like to thank my parents Helen and Stephen for their unwavering support and encouragement throughout.

Abstract

Recent advances in the development of scattering-type scanning near-field optical microscopy (s-SNOM) using terahertz (THz) frequency quantum cascade lasers (QCLs) have opened up new opportunities for THz measurements on the micro- and nano-scale. In this thesis the further development of THz-s-SNOM using QCLs is reported, as well as its application to the investigation of plasmonic effects in a range of systems.

It is shown how the frequency tuning of a QCL can be measured with high resolution using the self-mixing effect, but also exploited for coherent measurement of the scattered field in s-SNOM. The THz-s-SNOM is characterised with an optimisation of the spatial resolution achieving a value of 29 nm corresponding to $\lambda/3000$. Using THz-s-SNOM, a novel coherent stepped-frequency system is then reported, in which a generalised phase-stepped algorithm is employed to measure magnitude and phase data with as little as 4 sampling points per imaging pixel. This approach is used to successfully image the out-of-plane electric field supported by a THz micro-resonator.

A theoretical and experimental investigation of the excitation of surface plasmon polaritons (SSPs) in topological insulators (TI) is then presented. Experimental measurements are presented for unpatterned and patterned thin-film Bi_2Se_3 samples. A Bi_2Se_3 thin-film sample incorporating a metallic top gate is also investigated and it is demonstrated that the s-SNOM approach can successfully probe the TI surface beneath the top-gate. By expressing the resulting imaging data in the complex plane, it is seen that SPPs can be successfully launched and measured on the TI surface using this technique.

Furthermore, an improved metamaterial waveguide structure supporting spoof surface plasmon polaritons (SSPP) has been theoretically and experimentally investigated, wherein the out-of-plane electric field associated with SSPPs has been imaged using THz-s-SNOM showing a waveguide-to-waveguide SSPP energy transfer.

Contents

List of Figures

1.12 – The SP electric field normal to the surface $|E_z|$ decays with distance away from the surface δ_d and distance into the surface δ_m. Adapted from [11].

2.1 – Experimental set-up for LIV characterisation of the QCL. Adapted from [10].

2.2 – (a) QCL IV curves for a range of operating temperatures. (b) QCL LI curves for a range of operating temperatures. Both measured using the apparatus of Figure 2.1 and with the QCL in CW mode.

2.3 – Peak optical power for various QCL operating temperatures. (Blue) Experimental data taken from Figure 2.2b. (Red) Expected trend according to Equation 2.1.

2.4 – J_{th} values for various QCL operating temperatures. (Blue) Experimental data, calculated from the threshold current vales of Figure 5a. (Red) Expected trend according to Equation 2.2.

2.5 – Experimental set-up for FTIR characterisation of the QCL. Adapted from [10].

2.6 – QCL (L1612) spectra for different driving currents measured via FTIR.

2.7 – Three mirror model of laser feedback interferometry. Where M_1, M_2 and M_3 are mirrors, n_{in} is the internal cavity refractive index, n_{ext} is the external cavity refractive index, R is the reflectivity of M_3 and θ_R is the angle of M_3 with respect to the emission beam. Adapted from [12].

2.8 – The various waveforms involved in swept-frequency laser feedback interferometry. (a) The modulation current supplied by a signal generator. (b) The modulated current used to drive the laser. (c) The laser terminal voltage. (d) Interferometric fringes resolved by removal of the modulation waveform.

2.9 – Experimental set-up for self-mixing measurements using a QCL.

2.10 – Modulated self-mixing signal measured using the apparatus of Figure 2.9.

2.11 – Example of self-mixing signal embedded in the data of Figure 2.10. Revealed when removing the averaged background signal.

2.12 – SM fringes measured for the initial mirror position $\delta L = 0$ μm (blue) and a $\delta L = (-)$ 4 μm movement of the mirror parallel to the THz beam (orange).

2.13 – Change in frequency δf for each set of interferometric fringes (blue) calculated using the above analysis, alongside best fit of relation $\delta I = \delta f K$ (red).

2.14 – Interferometric fringes generated via mechanical beam path extension (blue) with Lang-Kobayashi fit (red). For this set the values of $C = 0.36$, $\alpha = -1.91$ and $\beta = 0.25$ mV were determined.

2.15 – The fringes of Figure 2.14 (blue) with a Lang-Kobayashi fit using initial fitting parameters of $\alpha = -1.85$ and $k = 0.168$ (red). Here $I = 650$ mA.

2.16 – Self-mixing parameters extracted from V_{SM} fringes using the L-K model, measured over a range of QCL driving currents. (a) Feedback parameter C, (b) linewidth enhancement factor α, (c) fringe amplitude β.

2.17 – THz-s-SNOM system schematic in which the QCL output is focused onto the tip of the AFM probe, oscillating at frequency Ω, and a portion of the scattered radiation is reinjected into the QCL cavity. The QCL is driven by a laser driver and the QCL terminal voltage is amplified by the low-noise preamplifier (LNP) before being demodulated by the lock-in amplifier (LIA) at harmonics of Ω. The half-wave plate (HWP) is used to adjust the polarisation of the THz beam. Adapted from [10].

2.18 – Diagram of oscillating s-SNOM probe tip where A is the peak-to-peak oscillating amplitude of the tip and h is $\frac{A}{2}$. For approach curve measurements, the tip begins at a predetermined height above the surface and is brought into close contact with it along the z-direction until $z = 0$ nm. Exaggerated scale.

2.19 – Approach curves for various demodulations of the tip tapping frequency $\Omega \sim 80$ KHz. Tip tapping amplitude $A = 400$ nm and tip size ~ 20 nm.

2.20 – Approach curves for various demodulations of the tip tapping frequency $\Omega \sim 80$ KHz. Tip tapping amplitude $A = 400$ nm and $h = 200$ nm and tip size ~ 500 μm.

2.21 – Fourier components of a tip-sample scattering cross-section with minimum tip-sample distance for larger (5a) and small (0.5a) tip oscillation amplitude, where the distance Z measured with respect to the tip radius a. Adapted from [13].

2.22 – Approach curves for various tip tapping amplitudes, demodulated at the $n = 2$ harmonic of the tip tapping frequency $\Omega \sim 80$ KHz, using a small tip ~ 20 nm.

2.23 – Approach curves for various tip tapping amplitudes, demodulated at the $n = 2$ harmonic of the tip tapping frequency $\Omega \sim 80$ KHz, using a large tip ~ 500 μm.

2.24 – THz-s-SNOM image of a gold/silicon boundary. (a) THz image. (b) AFM image.

2.25 – Edge imaging using a s-SNOM showing various tip positions (a)-(d) with respect to a dielectric edge (x_{tip}). (e) line profile of s-SNOM signal demodulated at the 2nd harmonic (A_2). (a) signal arising from a coupling solely with the substrate. (b) enhanced signal arising from a coupling between the tip apex and the substrate and the tip shaft and the edge. (c) signal reduction as the tip is displaced from the substrate resulting in a lower effective polarizability. (d) Coupling between the tip and the edge material surface. Adapted from [14].

2.26 – THz-s-SNOM image average in the y-direction showing surface features as a result of tip-edge interaction.

2.27 – Edge response function applied to the THz-s-SNOM image of Figure 2.24 averaged in the Y-direction. Blue – measured data, red – ERF fit, dotted black – positons of the 20% (black) and 80% (pink) criteria points from which a resolution of 50 nm was determined.

2.28 – THz-s-SNOM spatial resolution with tapping amplitude using a small tip (~ 20 nm) apex diameter.

2.29 – THz-s-SNOM spatial resolution with tapping amplitude using a large tip (~ 1 μm) apex diameter.

3.1 – A set of THz self-mixing interferometric fringes generated via a swept-frequency measurement with a current sweep of 200mA. This measurement was performed using the THz-s-SNOM system in conjunction with the hardware and control system described in this Chapter. Additionally show is a bounded area corresponding to a single fringe with example I_{start} and I_{end} values. The lock-in reference signal for this measurement was demodulated at 3Ω.

3.2 – A flow chart depicting the process by which the THz-s-SNOM system captures a 1D stepped-frequency image. This diagram specifically pertains to the operation of the LabVIEW virtual instrument that is used to control the measurement apparatus.

3.3 – LabVIEW virtual instrument block diagram for control of the data acquisition system.

3.4 – Number of unrecorded pixels vs microscope integration time for an image captured with a THz-s-SNOM using the data acquisition system. The image in question was a 10x10 pixel scan of a 15x2um gold-on-silicon structure. The lock-in reference signal for these measurements was demodulated at 3Ω.

3.5 – Single frequency THz-s-SNOM image of a Au/Si boundary captured using the data acquisition system described above. The colour bar represents the magnitude of the V_{SM} (mV). This image was captured with a microscope integration time of 300ms and the V_{SM} signal was demodulated at the third harmonic of the tapping frequency.

3.6 – ERF according to Equation 2.25 (red) fitted to a plot of the normalised V_{SM} signal of Figure 3.5 averaged in the y-direction (blue). The width of the curve is highlighted (black dashed) on which is the 20% (black) and 80% (pink) width markers.

3.7 – s-SNOM resolution for various values of T_2. Each data point has been extracted from the ERF edge response function analysis, an example of which can be seen in Figure 3.6.

3.8 – (a) Percentage error in the extracted amplitude and (b) absolute error in the extracted phase of LFI fringes, extracted using the GDRA in the limit $N \to \infty$, shown as a function of feedback parameter C and linewidth enhancement factor of the laser α.

3.9 – Synthesised LFI signal with $C = 0.5$, $\alpha = 0.5$, amplitude $\beta = 1$ and phase $\phi = 0$ (black dashed line) along with the SM voltages $V_{SM,i}$ sampled in three exemplar sets of $N = 4$ equally spaced phase points $\phi_{L,0} = \phi_i$ (with $i = 0 \to 3$) with $\phi_{i=0} = 2\pi m + 0$ (blue circles), $2\pi m + \pi/6$ (red circles) and $2\pi m + \pi/3$ (green circles). Also shown (coloured solid lines) are the corresponding functions $V_{SM,m} = \beta_m \cos(\phi_{L,0} - \phi_m)$ plotted using the values of β_m and ϕ_m determined from the GDRA applied to each set of ϕ_i.

3.10 – (a) Variation of the amplitude error as a function of the phase response of the target, ϕ, for exemplar cases in which $N = 4$ (top panel) and $N = 8$ (bottom panel). The corresponding maximum amplitude errors are $e_{A,max} = 6.6\%$ and 3.38%, respectively, as shown by the horizontal dashed lines. (b) Variation of the phase error for the same N as (a). The corresponding maximum phase errors are $e_{\phi,max} =$ 1.7° and 0.011°, respectively, as shown by the horizontal dashed lines.

3.11 – (a) Variation of the maximum amplitude error with the number of measurement points N, for feedback parameters $C = 0.01$ (black circles), $C = 0.1$ (blue circles), $C = 0.3$ (red circles) and $C = 1$ (green circles). (b) Variation of the maximum phase error for the same values of C. The solid lines are intended only to aid visualisation.

3.12 – (a) Variation of the maximum amplitude error with the number of measurement points N for $\alpha = 0$ (red circles), $\alpha = \pm 1$ (blue circles), $\alpha = \pm 2$ (black circles). (b) Variation of the maximum phase error for the same values of α. All results are shown for the exemplar case when $C = 0.3$. The solid lines are intended only to aid visualisation.

3.13 – Experimental set-up up for far-field frequency stepping LFI measurements.

3.14 –Self-mixing voltage measured as a function of laser driving current, showing one exemplar interferometric fringe obtained by far-field LFI (blue circles). Also shown is a fit to the L–K model (Equation 2.21), in which $\beta = 2.91$ mV and $\phi = -2.8°$.

3.15 – (a) Magnitude β_m and (b) phase ϕ_m values determined by applying the GPSA to the data in Figure 3.14, for N in the range 3–20. For each value of N there exists multiple possible subsets of phase sampling points corresponding to differing positions of the N points along the fringe, each of which yield a different pair β_m and ϕ_m values. Also shown (dotted lines) are the 'true' values of magnitude and phase as determined from the fit shown in Figure 3.14.

3.16 – (a) Maximum magnitude error $e_{A,max} = \max\left\{\left|\left(\frac{\beta_m - \beta}{\beta}\right)\right|\right\}$ calculated from the magnitude values β_m determined from the GPSA (shown in Figure 3.15) and expressed as a percentage error relative to the magnitude β determined from the fit shown in Figure 3.14; (b) maximum phase error $e_{\phi,max} = \max\{|\phi_m - \phi|\}$ calculated from the phase values ϕ_m determined from the GPSA (shown in Figure 3.15) and the phase ϕ determined from the fit shown in Figure 3.14.

3.17 – x- and y-component of the signal acquired by the lock-in for near-field frequency sweep using the stepped frequency measurement system.

3.18 – Self-mixing voltage obtained from demodulation of the laser voltage at the $n = 3$ harmonic of the tip tapping frequency, measured as a function of laser driving current (blue) fitted to which is the L-K model according to Equation 2.21 (red).

3.19 – (a) Maximum magnitude error $e_{A,max}$ and (b) maximum phase error $e_{\phi,max}$ determined from the magnitude and phase values obtained from the GPSA when applied to the data shown in Figure 3.18, expressed relative to those determined from the fit shown in Figure 3.18.

3.20 – Finite element simulations showing the spatial variation of the (a) magnitude β_z (a.u.), (b) phase ϕ_z (rads/π) and (c) real part $\mathrm{Re}(\beta_z e^{-i\phi_z})$ (a.u.) of the out-of-plane field in the x–y plane 20 nm above the DA, when illuminated under oblique incidence at a frequency 3.45 THz. Adapted from [15].

3.21 Terahertz image of the dipole antenna structure obtained by THz-s-SNOM, in which the antenna is obliquely illuminated with p-polarised radiation at a frequency 3.45 THz.

The colour scale represents the self-mixing voltage derived from the n =2 harmonic of the laser voltage, measured at a single laser driving current. The signal comprises of components capturing both the near-field dipole interaction between tip and sample surface, as well as the spatial distribution of the out-of-plane field supported by the sample under resonant excitation.

3.22 – Examples of single pixel V_{SM} data acquired for $N = 15$ data points acquired using the stepped frequency system (red) fitted to which is the GPSA (blue). (a) $\beta_m = 0.57$ mV and $\phi_m = -0.51$ rad. (b) $\beta_m = 1.2$ mV and $\phi_m = 0.43$ rad. (c) $\beta_m = 1$ mV and $\phi_m = 0.51$ rad. (d) $\beta_m = 1.1$ mV and $\phi_m = 0.39$ rad.

3.23 – Magnitude β_z, phase ϕ_z and real part $\mathrm{Re}(\beta_z e^{-i\phi_z})$ of the out-of-plane field component associated with the plasmonic dipole mode excited in the DA under resonant excitation by THz radiation. Blue circles show measured values, obtained by THz-s-SNOM and applying the GPSA with (a) N =15 and (b) N =4 measurements per pixel, plotted as a function of position along the principal axis of the antenna. Also shown (red lines) are the corresponding values derived from FEM simulations shown in Figure 3.20.

3.24 – Two-dimensional images showing the (a) real part $\mathrm{Re}(\beta_z e^{-i\phi_z})$ (a.u.) and (b) phase ϕ_z (rads/π) of the out-of-plane field component supported by the DA, obtained by THz-s-SNOM and applying the GPSA with $N = 4$ measurements per pixel. The first and last pixels of each row and column correspond to the substrate region of the sample. Both images have been generated by concatenating 1D scans taken at different y-positions on the sample.

4.1 – Energy-momentum diagram of a typical topological insulator showing the Fermi-energy level E_f and the momentum of spin up (blue arrow) and spin down (green arrow) electrons. Adapted from [16].

4.2 – (a) Diagram of s-SNOM scanning location on a graphene nano-ribbon (GNR) with incident radiation (red). (b) Imaging data of a ribbon with fields of the left and right sides of the ribbon, including s-SNOM tip location. Adapted from [17].

4.3 – Energy-momentum diagrams for Bi_2Se_2 modelled using a generalised gradient approximation (GGA) without (a) and with (b) spin orbit coupling (SOC). It can be seen that the presence of SOC provides a band gap of ~ 1 eV at the Γ K-point. For simplicity, E_f has been assumed to be 0 eV. Adapted from [18].

4.4 – Hexagonal Bi_2Se_3 atomic structure showing the Se_1-Be-Se_2-Be-Se_1 quintuple layer (red box). Adapted from [19].

4.5 – Dispersion relation of gold (blue) with free space wave vector (dashed red), according to Equation 4.1.

4.6 - Plasmon propagation length in gold according to Equation 4.2.

4.7 – Plasmon wavelength in gold according to Equation 4.3.

4.8 – Normalised plasmon propagation length in gold according to Equation 4.4.

4.9 – Contribution terms of the permittivity of Bi_2Se_3 according to Equation 6, using the values from Table 1 in [20].

4.10 – Real (red) and imaginary (blue) parts of the permittivity of Bi_2Se_3 according to Equation 4.6.

4.11 – Sapphire dispersion relation according to Equation 4.7.

4.12 – (a) Dispersion relation for Bi_2Se_2 according to Equation 8. (b) Plasmon propagation length in Bi_2Se_3 according to Equation 2. (c) Plasmon wavelength in Bi_2Se_3 according to Equation 3. (d) Normalised plasmon propagation length in Bi_2Se_3 according to Equation 4.4.

4.13 – Real part of the in-plane permittivity (blue) and out-of-plane permittivity (orange), according to Equations 4.9 and 4.10 as well as the real (yellow) and imaginary (purple) parts of the total permittivity.

4.14 – The dispersion relation (a), plasmon propagation length (b), plasmon wavelength (c) and normalised plasmon wavelength (d) of Bi_2Se_3 from Figure 4.12, determined using model 1 (Equation 4.6), with the equivalent plots determined using model 2 (Equations 4.9 and 4.10). The values plotted in (b) and (d) are the absolute values to maintain similar y-axis scaling to Figure 4.12.

4.15 - The dispersion relation (a), plasmon propagation length (b), plasmon wavelength (c) and normalised plasmon wavelength (d) of Bi_2Se_3 for a range of ω_D calculated from Equation 4.11, using a range of $n_{bulk} = 1 - 6 \times 10^{18}$ cm^{-3}.

4.16 – The dispersion relation (a), plasmon propagation length (b), plasmon wavelength (c) and normalised plasmon wavelength (d) of Bi_2Se_3 for thicknesses of 20 nm (blue), 40 nm (orange), 60 nm (yellow) and 80 nm (purple), according to Equation 4.8.

4.17 - The dispersion relation (a), plasmon propagation length (b), plasmon wavelength (c) and normalised plasmon wavelength (d) of Bi_2Se_3 for a range of k_F calculated from Equation 4.13, using a range of $n_{surface} = 1 - 6 \times 10^{13}$ cm^{-2}.

4.30 - (a) 3Ω THz and (b) topology images from a 20 μm x 20 μm THz-s-SNOM measurement of sample MBE210312, measured in the scanning location depicted in Figure 4.28.

4.31 – (a,d) Scanning area schematic (not to scale), (b,e) 3Ω THz and (c,f) topology images from two 85 μm x 85 μm THz-s-SNOM measurement of sample MBE210312 in different positions on the sample.

4.32 – (a) 3Ω THz and (b) topology images from a 90 μm x 90 μm THz-s-SNOM measurement of plain sapphire wafer.

4.33 - (a,d) Scanning area schematic (not to scale), (b,e) 3Ω THz images and (c,f) 1Ω THz images of two 90 μm x 90 μm THz-s-SNOM measurement of sample MBE210312 in different orientations of the same scanning area. Figures (e) and (f) have been rotated 90^0 to demonstrate the angle at which the scan was performed.

4.34 – (a) Scanning area schematic, (b) AFM image, (c) 3Ω THz image and (d) averaged THz image in the y-direction, of 30 μm wide ribbon on sample MBE20220536.

4.35 – (a) Scanning area schematic, (b) AFM image, (c) 3Ω THz image and (d) averaged THz image in the y-direction, of 4.25 μm wide ribbon on sample MBE20220536. The incident beam was p-polarised denoted by the beam direction k_0 and field direction E_0.

4.36 – (a) Scanning area schematic, (b) AFM image, (c) 3Ω THz image and (d) averaged THz image in the y-direction, of 4.25 μm wide ribbon on sample MBE20220536. The incident beam was s-polarised denoted by the beam direction k_0 and field direction E_0.

4.37 – Scanning area schematic of gated Hall bar Bi_2Se_3 sample. Omitted are the Au wires which connect to the Au contacts (yellow) and bottom gate (blue) to provide a bias across the TI.

4.38 – (a) 3Ω THz and (b) topology of the gated Hall bar sample, measured in the scanning area shown in Figure 4.37.

4.39 – (a) Horizontally averaged values from Figure 4.38a and (b) horizontally averaged values from Figure 4.38b.

4.40 – Single interferometric fringe generated by current step between 540 – 582 mA, performed in a similar manner to that shown in Chapter 3.

4.41 – Magnitude (a) and phase (b) extracted using the GPSA of Chapter 3 from a 1D coherent measurement scan of the gated Hall bar TI sample with $V_g = 0$ V.

bar for the area x = 0 – 104 μm (b) and x = 104 – 208 μm (c), fitted to which is Equation 5.2.

5.9 – Schematic of the DC structure showing the three regions of interest. The structure is designed so that SSPPs are launched at the beginning of WG1 and couple to WG2 within the interaction region. Adapted from [10].

5.10 – (a) Dispersion relation for even (solid) and odd (dashed) SSPP modes on DC structures with varying g values. (a, inset) Part of the dispersion relations of (a) cropped to the k_x values of interest. Real part of the out-of-plane field E_z of the SSPP even (b) and odd (c) modes obtained via FEM simulations of a DC structure with g = 0.5 μm. Adapted from [10].

5.11 – Magnitude (upper) and real part of the out-of-plane electric field (lower) on the surface of the DC structures obtained via wave port simulations. (a) g = 0.5 μm, (b) g = 0.7 μm, (c) g = 1 μm, (d) g = 1.5 μm and (e) g = 5 μm. Adapted from [10].

5.12 – Ring termination designs schematics. (a) d = 0 μm, (b) d = 1.5 μm, (c) d = 2.5 μm, (d) d = 3.5 μm, (e) d = 4.5 μm and (f) d = 5.5 μm.

5.13 – Magnitude of out-of-plane electric field for PSP waveguide with ring terminations acquired via free-space excitation simulations. (a) d = 0 μm, (b) d = 1.5 μm, (c) d = 2.5 μm, (d) d = 3.5 μm, (e) d = 4.5 μm and (f) d = 5.5 μm.

5.14 – Comparison of the performance of the ring termination designs.

5.15 – Tapered termination design schematics. (a) h = 7.5 μm, b = 8 μm, (b) h = 15 μm, b = 8 μm, (c) h = 7.5 μm, b = 2 μm and (d) h = 15 μm, b = 2 μm.

5.16 – Magnitude of out-of-plane electric field for PSP waveguide with tapered terminations acquired via free-space excitation simulations. (a) h = 7.5 μm, b = 8 μm, (b) h = 15 μm, b = 8 μm, (c) h = 7.5 μm, b = 2 μm and (d) h = 15 μm, b = 2 μm.

5.17 – Comparison of the performance of the tapered termination designs.

5.18 – Extension termination design schematics. (a) L = 5 μm, (b) L = 10 μm, (c) L = 15 μm and (d) L = 20 μm.

5.19 – Magnitude of out-of-plane electric field for PSP waveguide with tapered terminations acquired via free-space excitation simulations. (a) L = 5 μm, (b) L = 10 μm, (c) L = 15 μm and (d) L = 20 μm.

5.20 – Comparison of the performance of the extension termination designs.

5.21 – Grating termination design schematics. (a) a = 0.5 μm parallel, (b) a = various parallel, (c) a = 0.5 μm perpendicular and (d) a = various parallel.

5.22 – Magnitude of out-of-plane electric field for PSP waveguide with grating terminations acquired via free-space excitation simulations. (a) a = 0.5 μm parallel, (b) a = various parallel, (c) a = 0.5 μm perpendicular and (d) a = various parallel.

5.23 – Comparison of the performance of the grating termination designs.

5.24 – Comparison of wave port simulations of 208 μm gold and nickel PSP waveguides. (a) Real part E_z of gold waveguide, (b) real part E_z of nickel waveguide, (c) Figure 5.4 and (d) (Blue) Averaged E_z values for each bar of nickel PSP waveguide extracted from (b). (Red) Equation 5.2 with fitting parameters of $E_0 = 1.768$ MV/m, $k_x = 0.13$ cm^{-1}, $\theta = 3.05$ rad and $L_p = 14$ μm.

5.25 – S_{21} Parameters of nickel PSP waveguide with length L = 208 μm.

5.26 – Performance of nickel versions of each termination design with results of corresponding gold designs (a) Figure 5.17, (b) Figure 5.20) and (c) Figure 5.23.

5.27 – Schematic diagram of DC structure with grating and 10 μm nickel extension on beginning of WG2. The grating has dimensions a = 20 μm and $g_{off} = 10$ μm. The IR of the DC is considered to begin at bar n = 4 of WG1. The gap between WG1 and WG2 is g = 0.5 μm.

5.28 – Real part of the out-of-plane electric field of WG1 (a) and WG2 (b) of the DC structure obtained via free-space excitation simulations. (c) Averaged field per bars (dots) of the waveguide of (a) fitted to using Equation 5.10 (line) with fitting parameters E = 0.8 mV, $k_{xe} = 3750$ cm^{-1}, $k_{xo} = 3300$ cm^{-1}, $\theta_e = 1.4$ rad, $\theta_o = 2$ rad, L = 80 μm. (d) Averaged field per bars (dots) of the waveguide of (b) fitted to using Equation 5.10 (line) with fitting parameters $E_e = 1$ mV, $E_o = 1$ mV, $k_{xe} = 3650$ cm^{-1}, $k_{xo} = 3200$ cm^{-1}, $\theta_e = 1.9$ rad, $\theta_o = 1.9$ rad, L = 80 μm.

5.29 – Microscope image of DC structure with nickel terminations.

5.30 – THz s-SNOM (a) and AFM (b) images (n = 2) of WG1 IR of the DC structure of Figure 5.29.

5.31 – Averaged data per bar (dots) of 5.40a fitted to using Equation 5.12 (solid line) and Equation 5.16 (dashed line) with fitting parameters E = 0.6 mV, $k_{xe} = 4100$ cm^{-1}, $k_{xo} = 3300$ cm^{-1}, $\theta_e = -0.26$ rad, $\theta_o = -0.19$ rad, L = 75 μm.

List of Tables

Chapter 1

Introduction

1.1 Terahertz

Terahertz (THz) frequency radiation is defined as the range of electromagnetic (EM) frequencies between approximately 0.3 – 30 x10^{12} Hz (or range of wavelengths between 10 μm – 1 mm) [24]. This range lies between microwaves and infra-red radiation on the EM spectrum (Figure 1.1), otherwise known as the "THz Gap" [1]. The significance of the "THz Gap" arises from a historic lack of reliable, high-power sources for generating these frequencies, as they exist in the range that was beyond the limitations of traditional optical and electronic techniques, as well as their generally complex/expensive nature and common requirement of cryogenic cooling.

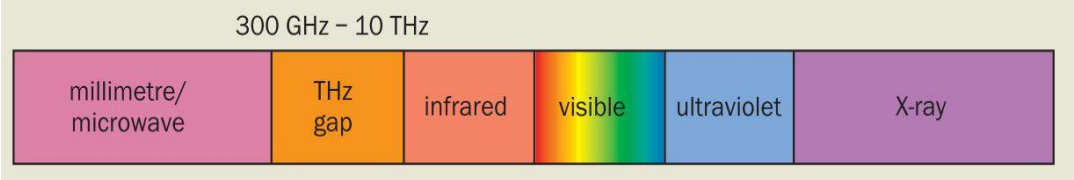

Figure 1.1 – Electromagnetic spectrum showing the region of THz frequencies. Adapted from [1].

Despite being first observed in the early 20th century [25], the THz range had been notoriously poorly explored. It was not until 1976 that the first application of THz (described at the time at "far infra-red") was recorded, by D. H. Baker *et al*. [26] in which a HCN laser, GaAs detector and LED camera were used to determine the transmittance and reflectance of various organic and inorganic materials, when subject to wavelengths between 337 – 1020 μm (0.3 – 0.9 THz). This inaugural demonstration of THz imaging was the first indication of its potential as a powerful investigative technique.

Despite this early interest, it would be over a decade later before the academic and industrial exploration of this spectral range progressed, thanks to the development of affordable, high-power THz sources (Section 1.2). Since then, the unique properties of THz radiation and its vast range of applications have been extensively studied [27]. Its non-ionising, non-destructive nature and high absorption by water makes it ideal for medical imaging, such as cancer screening [6], [28]. Additionally, these properties

provide an attractive alternative to x-rays for security applications such as contraband detection [29], [30]. As well as H_2O, many compounds display both rotational and vibrational absorption lines in the THz spectrum, making it suitable for chemical identification applications, such as astronomy [31] and spectroscopy [32]. Furthermore, many non-polar materials are transparent to THz, such as most polymers, which make them suitable for THz optical components, such as windows, filters, lenses and splitters and screening/inspection applications [33].

1.2 Terahertz sources

One of the earliest methods of THz generation was through the use of photoconductive antennae (PCA), wherein electron-hole pairs are excited via a high-power picosecond pump laser, producing transient currents that emit low-power broadband THz radiation [34]. For more narrowband emission, required by applications such as gas-spectroscopy [35], devices such as Schottky diode multipliers have been used, in which microwave frequencies are up-converted in the THz range [36]. Traditional gas lasers, such as CO_2 and methanol lasers, have been a reliable source of narrowband coherent THz but their large size and need for several kW power supplies renders them inconvenient. Other THz applications require only continuous-wave (CW) emission, such as imaging techniques that are less interested about frequency-domain and time-domain information [37]. For these systems, sources such as CW photomixers [38], [39] and Gunn emitters [40] have been developed. However, these sources typically suffer from low power and are limited to the lower end of the THz range.

More recently, a far more attractive THz source has been developed in the form of a small semiconductor device known as a quantum cascade laser (QCL). The QCL concept was first proposed in 1971 by Rudolf Kazarinov and Robert Suris [41] but was not put into practice until 1994 by Faist *et al* [42], who demonstrated a QCL operating at a wavelength of 4.26 μm (~ 70 THz) with a peak optical power of ~ 8.5 mW, and achieved lasing in pulsed mode at a device temperature of ~ 90 K.

The first use of a QCL in the THz range was seen in 2002 at the Cavendish Laboratory, Cambridge, by Köhler *et al* [43], which emitted at 4.4 THz with a peak optical power of ~ 2 mW and operated in pulsed mode at 50 K. Since, the optimisation of the QCL over the last two decades has enhanced its popularity and preference for THz generation, due

to its small size, low threshold current (commonly a few hundred mA), tunability [44], narrowband emission [45] and high output power (~W) [46].

1.3 QCL theory

A laser (*Light Amplification by Stimulated Emission of Radiation*) generates radiation via electron transitions from an upper to a lower energy level. When interacting with a photon with the correct energy, an electron occupying an upper level can transition and emit another photon with equal wavelength and phase as the incident photon, which is called stimulated emission. However, electrons occupying lower levels can absorb and be excited by these photons, resulting in no emission. To achieve lasing, the average number of electrons in the upper level must be greater than that in the lower, a condition referred to as a population inversion.

For simple interband semiconductor lasers, such as laser diodes, the conduction band E_c and valence band E_v of the material define the upper and lower energy levels. In these devices, the emitted photon energy is equal to the band gap E_G, which is determined solely by the semiconductor's composition (Figure 1.2a). An alternative design involves using quantum wells to generate a series of energy levels within E_c and E_v called subbands [47]. Since the energy levels associated with the subbands are dependent on the width of the quantum wells [48], the photon emission can be adjusted to energies other than E_G (Figure 1.2b). However, given that all electron transitions, regardless of the subbands between which they transition, are required to cross from E_c and E_v, the minimum photon energy possible to be emitted is E_G. The previously described "THz Gap" arises because there are no known semiconductor materials that possess a bandgap small enough to achieve THz frequency emission.

To circumvent this fact, a scheme was developed that relies on *intersubband* transitions, wherein photon emission is the result of electrons transitioning between subbands within the conduction band, permitting energies far smaller than E_G (Figure 1.2c).

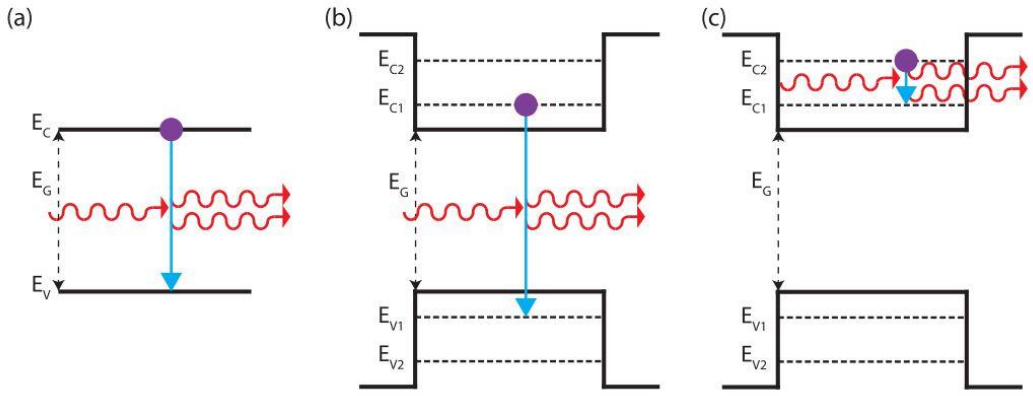

Figure 1.2 – Representation of photoemission mechanisms for three different laser designs. (a) Interband design where electron transition occurring between conduction band E_c and valence band E_v with photon energy equal to the band gap E_G. (b) Quantum well design where electron transition occurs between subbands in E_c and subbands in E_v, resulting in photon energies greater than E_G. (c) Intersubband design where electron transition occurs between subbands within E_C, resulting in photon energies less than E_G. Adapted from [2].

The QCL is a laser which utilises this technique. A QCL consists of semiconducting material (commonly GaAs/AlGaAs) engineered into stacked quantum wells, forming a series of identical repeating units. Each unit (Figure 1.3a) comprises an active region (the region in which the intersubband transitions take place) and injector/extractor regions (non-radiative regions). Both of these regions comprise multiple quantum wells, which allows for control of the emission wavelength and energy of injector/extractor states [49].

Careful engineering of quantum wells can permit the overlapping of neighbouring states to form bands of non-discrete energy levels called minibands. *Injector* minibands allow electrons to efficiently tunnel into the upper energy level of an active region, whereas *extractor* minibands allow for efficient tunnelling of electrons out of the lower energy level of an active region, when under an applied electric field. An organisation of these bands allows the extractor miniband of one active region to form the injector miniband of the next, permitting the cascading of electrons through the units of the device, hence the name. As seen below, some QCL designs employ the use of minibands within the active region, referred to as superlattice QCLs, whilst others comprise no minibands at all and instead rely on discrete electron states to form the upper and/or lower lasing level and longitudinal-optical (LO) phonon scattering for low level depopulation.

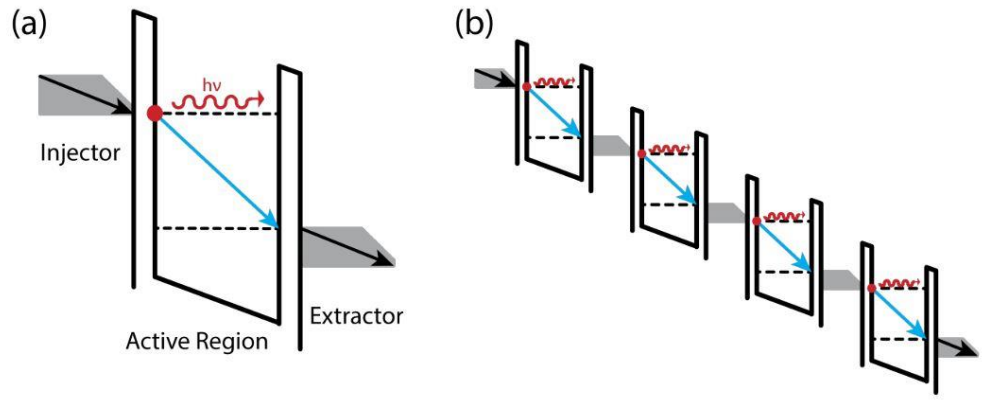

Figure 1.3 – Diagram of the QCL working principle. (a) Electrons tunnel through a potential barrier from an injector miniband into the upper level of the active region releasing a photon with energy hν, after which they tunnel out into an extractor miniband. (b) The process described in (a) for a series of stacked wells when under a bias, showing electrons cascading through the device. Adapted from [3].

Similar to any laser, to achieve lasing a population inversion must be reached within the active regions. In a QCL this is ensured by encouraging a depopulation of electrons from the lower lasing states. There are several QCL designs which can be used to bring about this process, a summary of which can be seen in Figure 1.4.

Chirped Superlattice (CSL) design:

A CSL utilises minibands to both improve the photon emission process and depopulate the lower energy level (Figure 1.4a). The active regions of a CSL QCL comprise an upper and lower miniband, the electron transition between which (the minigap) is radiative. Since electrons naturally relax to the lowest state of a miniband, electron transition occurs between the bottom of the upper miniband to the top of the lower, from where they then relax to the bottom of the lower miniband. This process both reduces the average transitioning distance between bands, which ensures a favouring of radiative intra-miniband transitions over non-radiative inter-miniband transitions, and encourages a depopulation the lower miniband. However, this design is at risk of thermal backfilling from injector states to the previous lower band, which occurs due to thermal excitation and/or absorption of longitudinal optical (LO) phonons [4] and consequentially limits the device maximum operating temperature.

Bound-to-continuum (BTC) design:

An improvement on the CSL, the BTC design uses a similar depopulation mechanism with the inclusion of a thin well placed adjacent to the injection barrier, forming a bound defect state within the minigap (Figure 1.4b). This enables a diagonal transition as the electron loses energy, resulting in a decrease of non-radiative scattering [4]. Additionally, the injection state's coupling with the upper state is stronger than that with the lower miniband, resulting in a more selective injection process. Consequentially, this design has an improved resistance to thermal backfilling, higher operating temperature and greater optical power [50], [51].

Resonant Phonon (RP) design:

The RP design (Figure 1.4c) removes the use of minibands and instead brings the lower lasing level close to the energy of the extractor states and engineers the gap between the extractor states and injector states to match the LO-phonon energy for GaAs ($\sim$ 36 meV). This ensures rapid depopulation from the lower lasing level to the extractor and sub-picosecond scattering from the extractor to the injector states.

Although the lack of minibands in the RP design does reduce the rate of radiative transitions compared to the BTC design, this is compensated for by its commonly shorter unit (or module) lengths L_{mod}, which result in an increase in the gain g, as $g \propto 1/L_{mod}$, since the number of units for a given device thickness is greater [52]. Furthermore, the high energy required to transport electrons from the injector state to the lower lasing level substantially reduces thermal backfilling and improves temperature performance [53]. However, the large energies associated with this design require a high bias in order to align the extractor/injector states, therefore QCLs that use this design commonly possess a greater threshold current density and electrical power required for operation.

Hybrid/Interlaced:

The hybrid (or interlaced) design (Figure 1.4d) combines the depopulation mechanics of the RP design with the diagonal transition concept of the BTC design [54], [55], ensuring a highly efficient device that benefits from the advantages of both approaches. The foremost of these is its low threshold current density, allowing the device to operate at higher temperatures and therefore perform better when operated in CW mode, which is desirable for applications such as self-mixing (Section 1.5). Because of this, the QCLs presented in the following sections (and remainder of this thesis) are based on the hybrid/interlaced design, the fabrication process for which can be found in [10].

To minimise THz radiation leakage from the active region into the device substrate, QCLs commonly employ waveguides fabricated on the outside of the active region. The two designs commonly used are the metal-metal (MM) waveguide and the semi-insulating surface plasmon (SI-SP) waveguide [56]. It is understood that the MM design tends perform better at higher temperatures but at the cost of poor beam quality. Hence, for the QCLs seen in Chapter 2 and after, they employ the SI-SP design.

Additionally, QCL emission is notoriously multi-frequency, which is undesirable for many applications such as THz imaging (Section 1.4). To ensure only single-frequency emission, some QCL designs incorporate optical gratings into their waveguides, which filter the emission into a single-frequency [57].

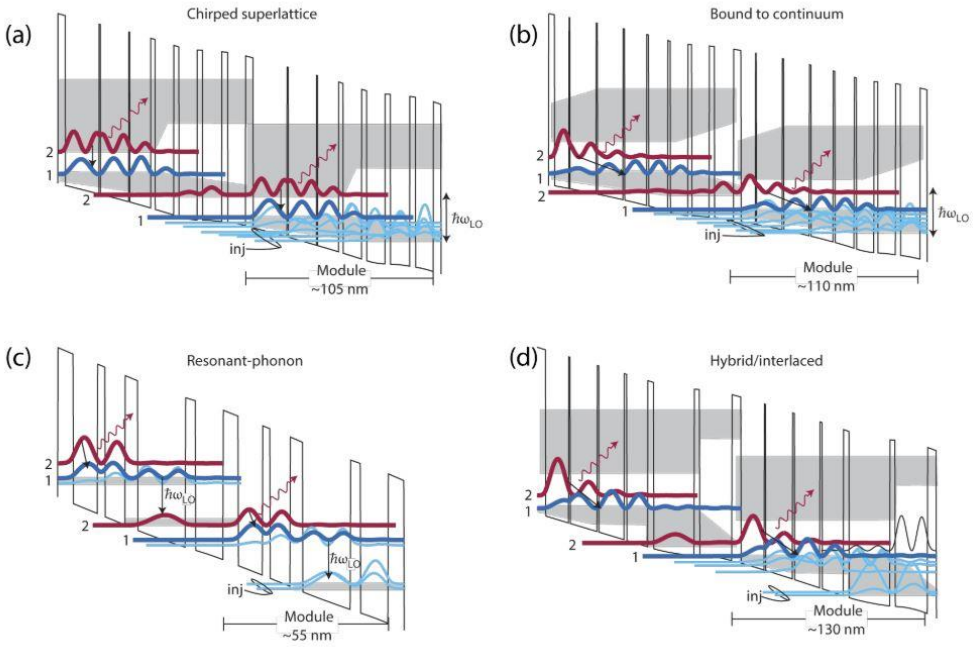

Figure 1.4 – Various THz-QCL active region designs. (a) Chirped Superlattice, (b) Bound-to-continuum (c) Resonant Phonon, and (d) Hybrid/Interlaced. (Red) Upper energy level wave function. (Blue) Lower energy level wave function. (Grey) Minibands. Adapted from [4].

1.4 Terahertz imaging using QCLs

As seen, imaging was the first practical demonstration of THz-based technology, which has now become its most widely-used application. Its unique transmittance and offer of sub-millimetre imaging resolution has given rise to the development of far-field and near-field imaging techniques.

An early example of these techniques used terahertz time domain spectroscopy (THz-TDS). Under this regime, the transmittance of THz pulses through a target substance is acquired by measuring the resulting radiation in the time-domain, from which information on the chemical composition of said target can be inferred. This technique has been known since the late-1980s [58] but the first practical images were not obtained until 1995 by Hu and Nuss [5], which was permitted by their optimisation of the technique. This optimisation included: a reduction in acquisition time of each THz waveform from minutes down to ~ 5 ms with a signal-to-noise ratio (SNR) of over 100:1, a down-conversion of the waveform into the kHz range, and real-time acquisition processing/display of the spectra data via the use of a digital signal processor. By raster scanning a sample, with the use of a two-axis motorised stage, a 2D THz image can be acquired, an example of which can be seen in Figure 1.5, where the water content of a leaf is compared immediately and 48 hours after being cut.

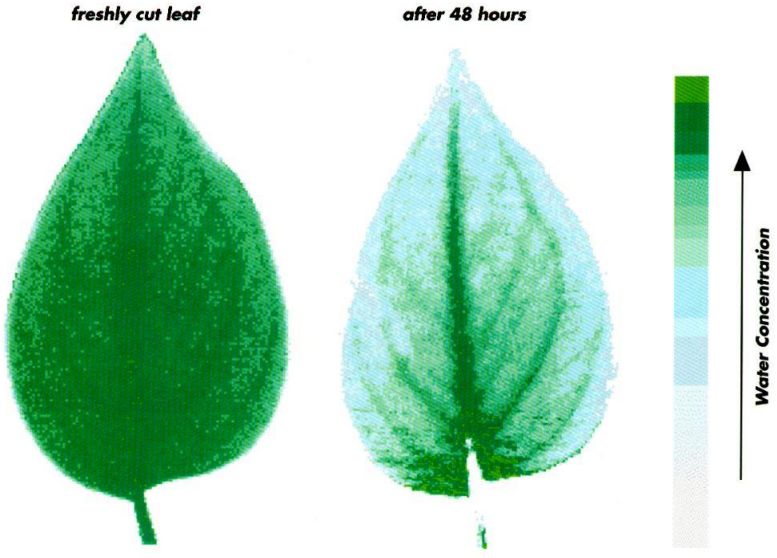

Figure 1.5 – Comparison between THz-TDS images of a freshly cut leaf (left) and the leaf 48 hours after cutting (right) showing the attenuation of THz due to water content. Adapted from [5].

The system described above employed a femtosecond pulsed Ti:sapphire laser-pumped PCA THz source, which was down-converted into the kHz range using a 15 cm/s delay line. However, using PCAs in this regime has several drawbacks, the most significant of which is the low output power (commonly ~ μW) of the optically pumped devices, which themselves requires very large and expensive laser systems. Furthermore, PCAs only emit broadband radiation which, as previously described, is inadequate for many applications.

To overcome these restrictions in the NIR range, devices such as heterostructure laser diodes have been employed. However, similar semiconductor-based sources, used in an attempt to solve these issues in the THz range, had posed a great challenge, due to the lack of materials with a sufficiently small bandgap for THz generation by intra-band electron transitions. It is these limitations that led to the development of the QCL, whose compact size and ability to generate high-power, spectrally pure, narrowband THz radiation makes it ideal for imaging applications [8].

For simplicity, early QCL imaging was concerned with incoherent THz detection, wherein only the amplitude of the measured THz signal is considered. The most rudimentary of these systems, such as that shown in Figure 1.6, involves a single-frequency THz-QCL, the output of which is focused onto a sample and the transmission is collected by an external THz detector. An image of the target is generated by raster-scanning the sample using a translation stage. These systems have been demonstrated for the imaging of biomaterials [6], electronic components [59] and a variety of chemical compounds [32]. For THz detection in these systems, a common instrument is the bolometer [60]–[62], which has been seen to achieve great sensitivity and a dynamic range of ~ 64 dB, but does require cryogenic-cooling. An alternative method, seen in [59], is the use of a pyroelectric sensor. However, it was considered that detector sensitivity and dynamic range could be improved with the use of a more powerful THz source, which would allow for the utilisation of a multi-element pyroelectric camera and remove the need for sample movement.

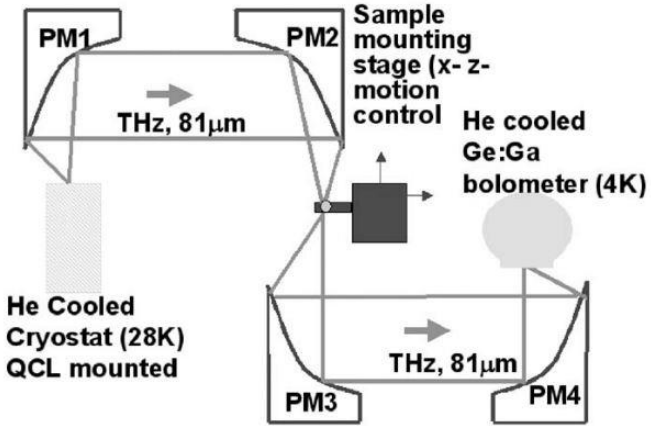

Figure 1.6 – Schematic diagram of THz imaging system employing a 3.7 THz QCL. Adapted from [6].

Despite offering greater imaging resolutions (~ 250 μm) [6], [61], [63], [64] compared with alternative imaging systems such as THz-TDS, due to the reduced diffraction limited beam resolution afforded by higher frequencies, THz-QCLs still fall short of the diffraction limit of ~ 64 μm at 3 THz [65]. This is primarily due to their irregular beam profiles, which is a result of a diffraction of the QCL output beam due to the sub-wavelength geometry of the metal-metal waveguide aperture [66]. To mitigate this, alternative techniques such as the semi-insulating waveguide has been used, providing superior beam quality and a reduction in beam divergence [43]. However, beam diffraction from both the substrate and waveguide ridge result in dual-emission lobes [67]–[69], as well as the emission profile comprising ring-like interference fringes [70], [71]. Modern QCLs may overcome these drawbacks by employing hollow dielectric waveguides to encourage a substantially Gaussian emission mode [65], [72]. An alternative technique is the spatial filtering of the QCL beam, which has been demonstrated in a 2.9 THz transmission-mode confocal microscope to achieve a spatial resolution of better than 70 μm [61].

Coherent imaging, in which both the amplitude *and phase* of the measured THz signal are considered, offers significant advantages over the systems described above. In a manner similar to THz-TDS, fully resolving the THz field acquired from measuring a sample allows for determination of the complex permittivity of the sample and therefore identification of the sample material [73]. Additionally, this regime offers the potential of high dynamic range/detection [7], [74] as well as applications such as depth-resolved imaging [75].

A caveat to these advantages is the complexity of the systems required to perform coherent imaging. A conventional method involves mixing the THz field with a reference signal in order to produce an intermediate frequency suitable for electronic detection. Furthermore, the line broadening and frequency drift of a QCL due to thermal and electronic noise, the magnitude of which is $\sim 1/f^2$, necessitates the use of frequency stabilisation [76], [77]. Methods for achieving this commonly involve an alternative laser source, such as that presented in (59), wherein a 2.41 THz $C0_2$ laser was used as a local oscillator to stabilise a QCL on a Schottky mixer with an offset frequency of 1.05 GHz. This system maintained a 20 – 30 KHz QCL linewidth over a scan period of 40 minutes. However, a phase drift of $\pm\, 7^0$ was observed, which was attributed to mechanical noise, resulting in a lengthening of the optical beam path.

An alternative method was demonstrated in [7], in which a 2.5 THz QCL, with an output of $\sim$ 2 mW at a temperature of 20 K, was stabilised using a 780 nm $\sim$ 100-femtosecond laser comb and employed two identical electro-optic detection units (EO1 and EO2) as shown in Figure 1.7a, the first to lock the QCL frequency to the laser comb and the second to detect the reflected QCL beam. The NIR laser, which operated at a repetition rate of $\sim$ 250 MHz, creates a series of beat-notes when mixed with the QCL output. The frequency of these notes is compared to an RF reference signal, the error of which is then used to control the QCL current through a phase-lock loop, which maintains the QCL frequency at $\sim 10^4$ harmonic of the NIR laser repetition rate. A portion of the laser comb is then used as a reference signal for coherent sampling of the reflected THz field using EO2. This system was used to image the amplitude (Figure 1.7b) and phase (Figure 1.7c) of the THz field reflected from a 10 cent Euro coin, from which the reflectivity and surface profile of the coin was extracted. The system achieved a spatial resolution of 160 μm and a long-period phase stability of $\leq 3^o$/h. In a similar manner to the previous technique, this stability is determined by the mechanical limitations of the apparatus.

It is evident from the examples highlighted here that, although a useful technique, QCL-based coherent imaging suffers from complex experimental setups required for frequency stabilisation and THz detection. These issues have since been addressed with the development of a far simpler and more compact optical arrangement based on the phenomenon of self-mixing in a THz QCL, an overview of which will be given in the following section.

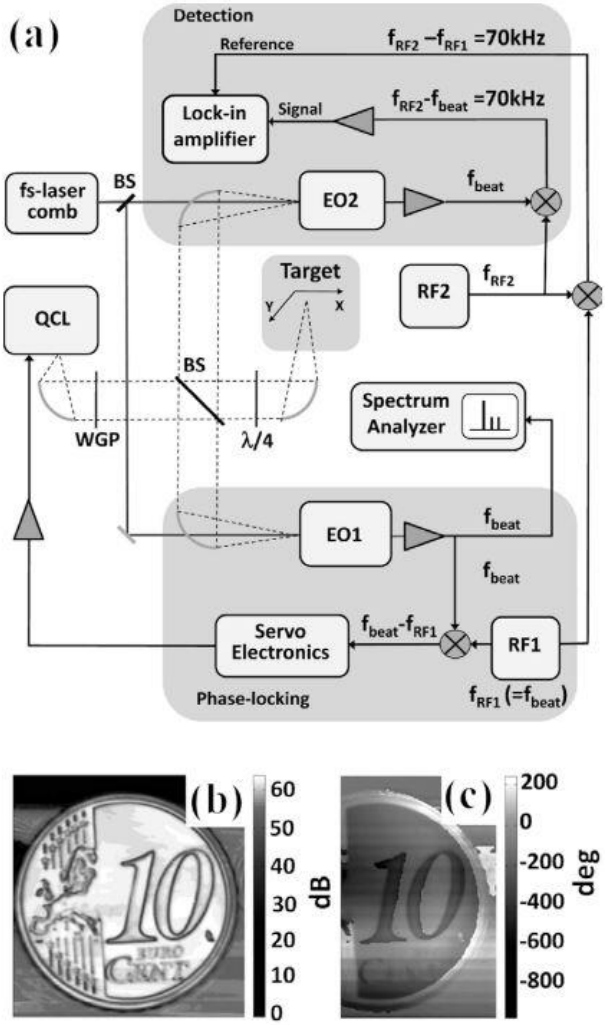

Figure 1.7 – (a) Experimental set-up for coherent THz imaging system using a frequency-locked 2.5 THz QCL. (b) THz power and (c) unwrapped THz phase images of a 10 cent euro coin. Individual images first published in [7]. *Figure adapted from* [8].

1.5 Self-mixing

The self-mixing (SM) effect is a well understood phenomenon in semiconductor lasers [78] but has only recently been fully utilised in THz frequency QCLs for sensing and imaging applications [79]. The SM effect is afforded by reinjection of part of the emitted radiation back into the laser cavity [64]. This 'mixing' of the initial and reinjected fields can be observed as a small change in optical power, lasing frequency and, more pertinently, device terminal voltage. Since the degree by which all of these values are affected depends on the amplitude and phase of the reinjected field, it can be seen that a QCL under optical feedback acts, itself, as an interferometric sensor, without need for external detection apparatus.

This scheme has many benefits over previous interferometric detection methods. The redundancy of an external detector makes for a simpler and less bulky optical set-up compare to those that employ THz bolometers, as well as far greater detector sensitivity compared to room temperature devices such as pyroelectric sensors, due to the inherent suppression of background radiation entering the laser cavity [80].

The standard theory of optical feedback in lasers, to be presented in Chapter 2, predicts a modulation to the self-mixing voltage V_{SM} according to Equation 1.1, a derivation of which can be found in [2].

$$V_{SM} \propto \varepsilon\sqrt{R_{ext}}\,\cos\left(\frac{4\pi L_{ext}\nu}{c}+\theta_R\right) \qquad 1.1$$

where ε is a constant accounting for losses, R_{ext} is the reflectivity of target, L_{ext} is the external cavity length, ν is the frequency of the radiation, c is the speed of light and θ_R is the phase change on reflection by the target. This phase arises from either the depth of the target surface or complex part of the material permittivity.

The dependence of V_{SM} on both L_{ext} and ν enable the generation of interferometric fringes by monitoring V_{SM} whilst varying either of these two parameters. As such, coherent imaging can be achieved via modulation of these two parameters. The latter of these parameters will be varied for the application of coherent THz near-field imaging presented in Chapter 3.

Given the aforementioned benefits and convenience of QCL THz sources, as well as the experimental simplicity of the SM sensing approach, it is not surprising that substantial research efforts have focused on combining these two technologies for THz imaging and sensing applications. Most notably, as described by Equation 1.1, the SM detection method is inherently sensitive to both amplitude and phase of the reinjected field, which enables a break-away from relying on traditional QCL-based imaging approaches , which have almost exclusively relied on incoherent thermal detectors [8]. Furthermore, coherent laser feedback interferometry (LFI) is significantly sensitive to changes in the optical phase in the external cavity. This changes can arise from changes in the cavity length, refractive index inside the cavity, on reflection from the target (as described above), or a combination of these effects. This sensitivity creates numerous opportunities for developing compact LFI systems for depth-resolved imaging [73], [81], displacement/vibration sensing [79], [82] and gas spectroscopy [83] at THz frequencies.

It should also be noted that Equation 1.1 has been expressed in terms of reflecting from a target with reflectance R_{ext}, such as that seen in Chapter 2. This scheme remains robust

for replacing this reflectance with a scattering source, such as the tip of an atomic force microscope, which is the case for THz scattering-type scanning near-field optical microscopy using a QCL (Section 2.4) on which this thesis is predominantly based.

1.6 THz-s-SNOM

For far-field THz imaging systems, where the target sampling is done from a distance d that is greater than the wavelength λ of light used to do so ($d \gg \lambda$), such as those seen in Sections 1.4 and 1.5, the imaging resolution is limited by the Abbe diffraction limit [84]. This defines the highest spatial resolution R for a free-space EM wave as,

$$R = 0.61\frac{\lambda}{NA} \tag{1.2}$$

where λ is the wavelength and NA is the numerical aperture of the system. Therefore, for far-field THz imaging systems, the maximum resolution is $\sim \lambda/2$ (or $\sim$ 50 μm for a system operating at 3 THz).

For THz imaging applications that benefit from sub-wavelength resolutions, such as biomedical imaging [85], [86], quantum dot detection [87], [88], semiconductor characterisation [89], [90], single molecule detection [91] and imaging of micro-scale resonators and metamaterials [10] to name a few, near-field techniques are required. In contrast to that described above, this regime involves the detection of the imaging information at a distance from the target that is less than the incident wavelength $d \ll \lambda$.

One method of achieving this criteria is aperture-type SNOM (a-SNOM), wherein a subwavelength-size detector or aperture is introduced into the near-field region of the sample [92]. However, the resolution afforded by this is not completely independent of the wavelength and therefore acts as a high-pass filter with a cut-off frequency f_c given by,

$$f_c = \frac{1.841c}{\pi d} \tag{1.3}$$

where c is the speed of light and d is the diameter of the aperture.

An aperture with diameter $d = 100$ µm would, therefore, have a cut-off frequency of $f_c = 1.76$ THz. Of course, one could overcome this limit by reducing the aperture size. However, this would drastically reduce the amount of signal available to detect. This becomes an issue when considering the position of the detector. Mair *et al* [93] demonstrated that the amplitude of a signal E_z transmitted through an aperture with diameter d exponentially decays with distance from the aperture z as,

$$E_x \propto e^{-z/td} \tag{1.4}$$

where t is a wavelength-independent factor with value $t \sim 0.65$ presuming the condition $z \ll \lambda$.

Therefore this regime is only viable by bringing the detector into close proximity of the sample, which is practically inconvenient. A wide range of detectors, compatible with both pulse and CW sources and covering almost all of the THz range, have been integrated into the a-SNOM technique to allow for improved sensitivity, spatial resolution and phase-sensitive detection [94]. These techniques enable THz imaging, such as that shown in Figure 1.8, with a moderate spatial resolution of ~ 2 – 30 µm, for applications such as mapping of fields in THz waveguides, plasmonic and dielectric resonators and THz metasurfaces [9], [95].

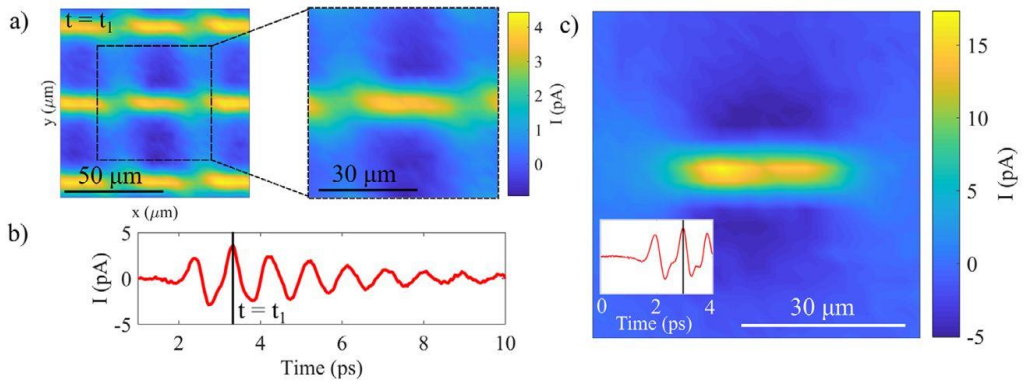

Figure 1.8 – (a) Interpolated near-field map of gold resonators array measured using the ASNOM technique. (b) Waveform showing time delay at which (a) was recorded, corresponding to maximum amplitudes. (c) Interpolated near-field map of single gold resonator at time corresponding to maximum of the waveform (inset). This system used an aperture size of 10 µm, integrated with a PCA detector. Adapted from [9].

A truly wavelength-independent near-field imaging technique is scattering-type scanning near-field microscopy (s-SNOM), sometimes referred to as apertureless (scattering-type) near-field scanning microscopy. This method utilises the AFM

principle, wherein a small probe (tip diameter ≤ 1 μm) is brought into close proximity with a surface that is mounted on a piezo-electric stage which can move with nanometer precision. The probe is mounted on a cantilever where it oscillates at close to its resonant frequency. By monitoring the vertical height of the probe, the topology of the surface can be measured [96].

The s-SNOM technique uses an external light source to illuminate the apex of the probe. Since the probe comprises a polarisable material (commonly W or Pt/Ir alloy), the incident radiation induces a dipole in the probe apex which, in turn, induces a localised mirrored dipole in the sample. The coupled dipole scatters radiation into the far-field, the efficiency of which is affected by the permittivity of the sample [13], [97]. By measuring the scattered field E_s, information about the local surface field and, in turn, the local dielectric constant, can be deduced. This method has been used with incident frequencies ranging from visible light to THz [98].

The resolution of this scheme is solely dependent on the probe apex diameter and probe-sample distance, both of which are substantially sub-wavelength.

The most common model for describing the probe-sample interaction is the point-dipole model [99]–[103], a visualisation of which can be seen in Figure 1.9. This model makes two assumptions:

1. Only the probe tip causes near-field interaction with the surface and is treated as a polarisable sphere with radius R, permittivity ε_t and polarizability α.
2. The incident EM field E_0 that illuminates the probe tip, has a polarisation in parallel with the direction on the tip and induces an almost infinitely small dipole at the centre of the tip.

According to the definitions given above, the dipole p induced in the tip by an incident EM field, without the presence of a sample, is given by,

$$p = \alpha E_0 \tag{1.5}$$

where the polarizability of the tip α is given by,

$$\alpha = 4\pi R^3 \frac{\varepsilon_t - 1}{\varepsilon_t + 2} \tag{1.6}$$

This tip dipole generates a mirrored dipole moment $p\beta_p$ in the surface with,

$$\beta_p = \frac{\varepsilon_s - 1}{\varepsilon_s + 1} \tag{1.7}$$

where ε_s is the complex permittivity of the sample.

This mirrored dipole couples with the tip dipole resulting in a field enhancement which increases the tip scattering efficiency [96].

Put another way, the near-field interaction between the tip and the sample affects the polarizability of the tip, which is now better described as the effective polarizability α_{eff} and is given by,

$$\alpha_{eff} = \frac{\alpha(1+\beta_p)}{1 - \frac{\alpha\beta_p}{16\pi(R+z)^3}} \tag{1.8}$$

where z is the tip-surface distance.

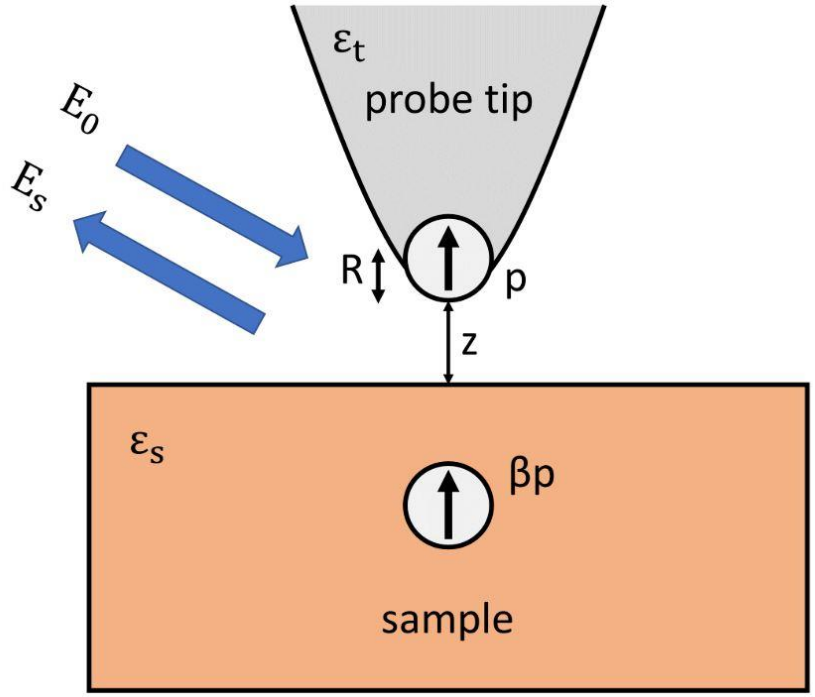

Figure 1.9 – Schematic diagram of the point-dipole model. Adapted from [10].

It can be seen from Equation 1.8 that as $z \to \infty$ the effective polarizability is approximated to the polarizability of the tip, i.e. $\alpha_{eff} \sim \alpha$. As the tip-surface distance reduces, $z \to 0$, the effective polarizability supersedes α, conveying a strong a near-field interaction between the tip and surface.

It is also known that the field scattered to the far-field is directly proportional to the tip polarizability $E_s \propto a_{eff}E_0$. Since the point-dipole model considers the induced dipole to be infinitely small, at large z, $E_s \rightarrow 0$ and alternatively at small z, the enhanced near-field interaction leads to a strong scattered field E_s. It is this dependence of the scattered field on the effective polarizability that allows information about the surface permittivity to be deduced from measurement of E_s.

Furthermore, the non-linear dependence of the near-field interaction with z allows for the near-field component of E_s to be distinguished from unwanted background far-field components, such as direct scattering from the probe shaft, through demodulation of E_s at higher harmonics of the probe oscillation frequency [13], [96], [101]. This background suppression technique will be investigated in Chapter 2.

A problem with the s-SNOM technique is the small E_s available for detection, despite the enhanced scattering efficiency when coupling the tip and surface. This arises from the relation $\alpha_{eff} \propto R^3$ as described by Equation 1.8. Since R is small ($R << \lambda_{E_0}$), this leads to a small effective polarizability and therefore small E_s. One study showed that only 0.4% of an incident 2 THz wave was scattered from an $R = 1$ μm probe tip to the far-field [104]. This demonstrates the requirement for high sensitivity detectors. Therefore, an ideal scheme for THz frequency s-SNOM (THz-s-SNOM) is by exploiting self-mixing in QCLs. Additionally, s-SNOM also requires fast detection in order to detect up to frequencies corresponding to higher harmonics of the tip tapping frequency, which is also afforded by the SM scheme.

The first demonstration of THz-s-SNOM using a SM QCL was in Dean *et al* [102], wherein a 2.53 THz QCL was incident at an angle of $\sim 50^0$ on a $R < 1$ μm Pt/Ir tip oscillating at a frequency of 90 Hz. This system achieved spatial resolutions of ~ 1 μm and ~ 7 μm, corresponding to $\sim \lambda/100$ and $\sim \lambda/14$ respectively, along orthogonal directions of an 80 x 60 μm image of a 115 nm thick gold on quartz sample.

Recently, the high sensitivity of LFI combined with the high out-put power and low phase-noise of THz frequency QCLs has been exploited to enable s-SNOM operating at frequencies beyond 2 THz. This advancement has created new possibilities for THz measurements at the micro- and nano-scale including the mapping of charge carriers in semiconductors and nanostructures [105]–[107], investigation of plasmon and phonon polaritons in emerging two-dimensional materials [23], [108], [109] and the microscopic investigation of metamatierals and micro- and nano-scale resonators [15], [110], [111]

1.7 Plasmonics

The term plasmon is defined as a collective oscillation of electrons on or within a free electron gas, for instance within a metal. Surface plasmon (SP) oscillations occur due to light-matter interactions on the interface between a conducting material and a dielectric, such as gold and air [11].

This interaction leads to two important classes of surface plasmon: *surface plasmon polaritons* (SPPs) which are EM modes with subwavelength confinement that propagate on the surface of a conducting materials; and *localised surface plasmons* (LSPs) which occur when the particles of the conduction medium are smaller than the incident wavelength and therefore accommodate SPs as localised standing waves[112]. Surface plasmonics offers a promising bridging between electronic and photonic technologies due to its ability to tightly confine light on the surface of a material on a sub-wavelength scale, thereby providing strong surface field enhancement. Its many potential applications include super-resolution imaging [113], high-density optical data storage [114] and bio-sensing [115].

To characterise the plasmonic response of a material, the frequency dependent permittivity $\varepsilon(\omega)$ is used, where ω is the frequency of the incident radiation [116]. This can be determined using the Drude model for metals, which is expressed as,

$$\varepsilon(\omega) = \varepsilon_\infty \left(1 - \frac{\omega_p^2}{\omega^2 + i\gamma\omega}\right) \tag{1.9}$$

where ε_∞ is a high frequency offset, γ is the average scattering rate of electrons and ω_p is the bulk plasma frequency according to,

$$\omega_p = \sqrt{\frac{ne^2}{m_e \varepsilon_0}} \tag{1.10}$$

where n is the electron density, e is the electron charge, m_e is the effective electron mass and ε_0 is the permittivity in a vacuum.

The electron-photon interaction at the surface of a conductor can be described by the dispersion relation, which described the frequency-dependent SP wave vector k_{SP}, obtained by solving Maxwell's equations for the SP mode [117],

$$k_{SP} = k_0 \sqrt{\frac{\varepsilon_d \varepsilon_m}{\varepsilon_d + \varepsilon_m}} \tag{1.11}$$

where, k_0 is the free-space wave vector which is described by $k_0 = \omega/c$ where c is the speed of light, ε_d is the permittivity of the dielectric medium and ε_m is the permittivity of the metal given by Equation 1.9.

Two conditions must be satisfied in order to support SPs: $\varepsilon_d \varepsilon_m < 0$ and $\varepsilon_d + \varepsilon_m < 0$. For these conditions to be satisfied, the real part of ε_m must be negative, which is satisfied for metals below the plasma frequency. The dispersion relation for a SP mode can be seen in Figure 1.10 and shows the momentum mismatch which must be overcome to achieve coupling between light and the SP mode.

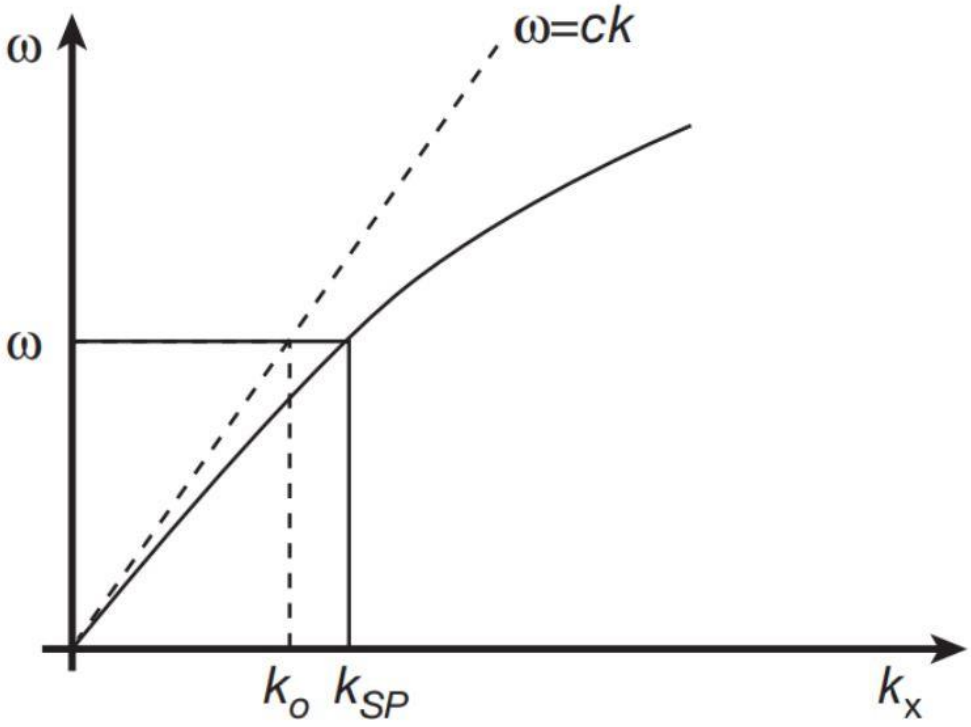

Figure 1.10 – Dispersion curve for a SP mode. The SP mode always has a greater momentum $\hbar k_{SP}$ than the free space wave $\hbar k_0$ for a given frequency ω, hence the momentum mismatch problem. Adapted from [11].

To overcome this momentum mismatch, several mechanisms have been employed, such as prism coupling [118], [119], scattering from topological defects [120], [121] and using gratings [122] which is a technique that can be seen in the structures of interest in Chapter 5. Alternatively, the momentum mismatch can also be solved by scattering the incident field from an s-SNOM probe. This method will be used in Chapters 4 and 5 to both launch and image SPs in a variety of materials.

Once coupling to the SPP mode has been achieved, the mode will propagate on the surface of the conducting material in a manner depicted in Figure 1.11, wherein the generation of surface charge carriers creates an electric field E normal to the surface and magnetic field H transversely parallel to the surface.

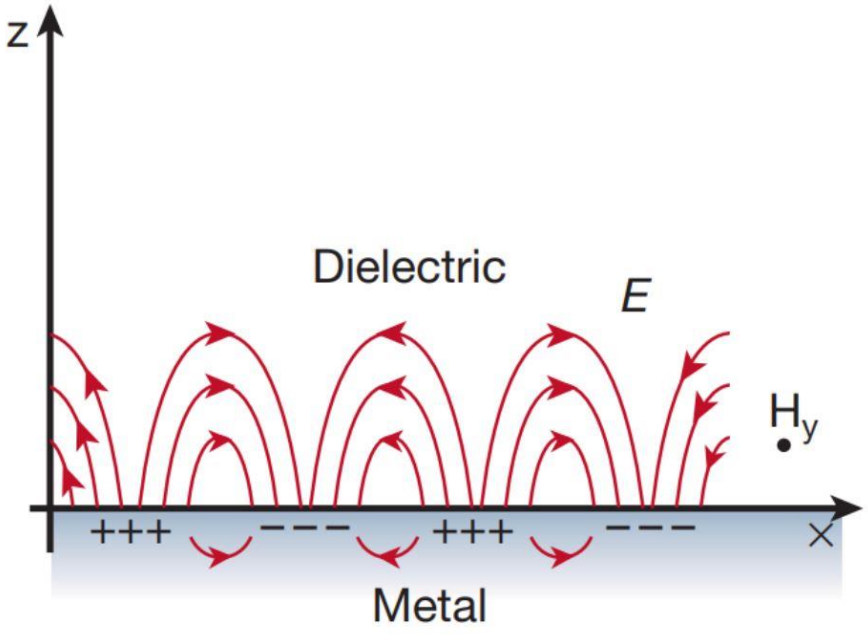

Figure 1.11 – SP propagating at the interface between a metal and a dielectric. The electric field E is perpendicular to the surface and the magnetic field H is transversely parallel. Adapted from [11].

The electric field decays exponentially with distance from the surface and is described as an evanescent field, which prevents power from radiating away from the surface. This decay of the electric field away from the surface δ_d is of the order of $\lambda/2$, whereas the decay of the field into the surface δ_m is determined by the material's skin depth. The relationship between these values and distance above/below the surface are visualised in Figure 1.12.

The SP mode will gradually attenuate due to absorption by the surface material. The rate of attenuation is determined by the imaginary part of the SP wave vector k''_{SP}. As such, the SP propagation length δ_{SP} can be obtain from Equation 1.12.

$$\delta_{SP} = \frac{1}{2k''_{SP}} = \frac{c}{\omega}\left(\frac{\varepsilon'_m + \varepsilon_d}{\varepsilon'_m \varepsilon_d}\right)^{\frac{3}{2}} \frac{\varepsilon'^2_m}{\varepsilon''_m} \qquad 1.12$$

where ε'_m and ε''_m are the real and imaginary parts of the dielectric function of ε_m.

It can be seen from Figure 1.10 and Equation 1.12 that k_{SP} increases with ω, whereas δ_{SP} deceases with ω. This leads to a compromise between confinement and propagation of the SP mode [123].

SPPs are typically exploited in the optical and UV range of frequencies which are near to the ω_p of metals such as gold. However, at lower frequencies, such as THz, these metals resemble perfect electric conductors, which results in extremely poor confinement of SPPs, such that the EM field propagates as a weekly confined Sommerfield-Zenneck surface wave. In Chapter 4 it will be seen how lower carrier density materials, such as topological insulators, support more tightly confined SPPs in the THz range. Furthermore, it will be seen in Chapter 5 how metals, such as gold, can be organised into structures that allow for THz confinement in the form of a spoof-surface plasmon polariton (SSPP).

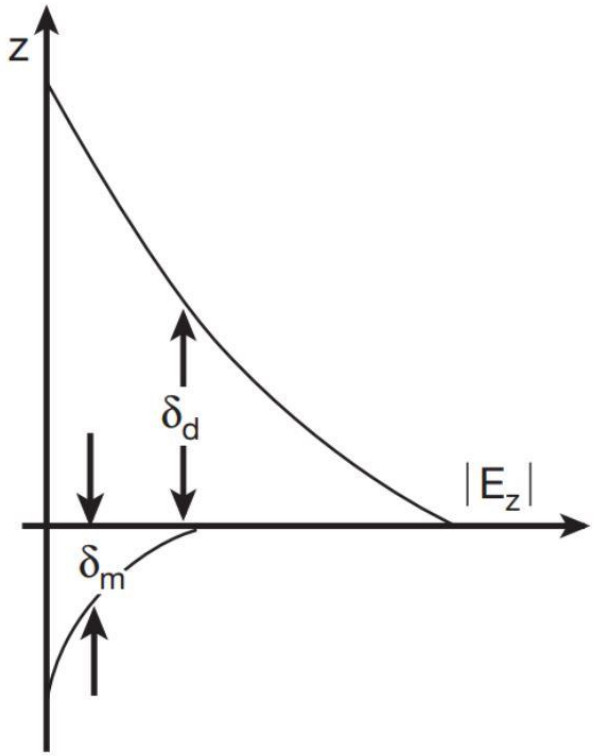

Figure 1.12 – The SP electric field normal to the surface $|E_z|$ decays with distance away from the surface δ_d and distance into the surface δ_m. Adapted from [11].

1.8 Thesis overview

Chapter 2 presents the experimental apparatus for characterisation of THz QCL devices, which are an essential component of the experimental work presented in the remainder of this thesis. This includes experimental measurements of voltage-current and power-current characteristics, from which the threshold current density as a function of operating temperature is determined, as well as measurements of the lasing spectra. Additionally, the frequency tuning coefficient of a QCL device is measured via two methods based on self-mixing detection. The self-mixing response of a QCL is further analysed, with particular focus on the behaviour of the feedback parameter, linewidth enhancement factor and signal amplitude as the driving current is varied. This investigation is particularly relevant to an experimental approach for coherent s-SNOM presented in Chapter 3.

Furthermore, Chapter 2 also presents the characterisation of a THz-s-SNOM system employing self-mixing in a QCL. This includes a demonstration of background signal reduction via demodulating at higher harmonics of the tapping frequency of the AFM probe tip, as well as an investigation of the dependence of signal size on demodulation harmonic and tip tapping amplitude, both of which have been investigated for both large and small tip sizes. Chapter 2 is concluded with an investigation of the THz-s-SNOM spatial resolution, which is realised via boundary measurements of a simple gold-on-silicon structure. The dependency of the resolution on tip size is evaluated, as well as a consideration of undesirable tip-edge coupling as a result of the tip profile, an example of which is experimentally demonstrated.

Chapter 3 presents an approach to coherent THz-s-SNOM based on self-mixing in a THz QCL. It is shown how the frequency tuning of a THz QCL via laser feedback interferometry, in conjunction with a sophisticated data acquisition and control program, can be exploited to capture coherent measurements data in the form of interferometric fringes realised in the self-mixing voltage V_{SM}. Using this technique, coherent near-field imaging with deep sub-wavelength resolution is demonstrated. Furthermore, a novel approach for extraction of the magnitude and phase from the acquired imaging data is demonstrated using a generalised phase-stepping algorithm (GPSA). The applicability of this analytical tool is investigated theoretically in both the far-field and near-field for a variety of lasing and sampling conditions, and is shown to be accurate for as little as $N = 4$ sampling points per imaging pixel, which drastically reduces the image acquisition time compared to previous coherent THz imaging

methods. Lastly, the use of this technique in THz-s-SNOM is demonstrated by imaging the out-of-plane field supported by a THz micro-resonator.

Chapter 4 explores the properties of topological insulators (TI) and their ability to support SPs in the THz range. This initially involves an overview of TI materials and the mechanics behind their unique properties. The plasmonic nature in the THz region of several novel patterned and unpatterned bismuth-based TI thin-film samples is predicted using a Drude-Lorentz model, the origin of which is also detailed. Using this model, the dispersion relation, plasmon propagation length and plasmon wavelength of a generic TI is determined, as well as those of the aforementioned samples, using material parameters acquired via THz-TDS.

Furthermore, the experimental samples are imaged using the THz-s-SNOM system described in Chapter 2, wherein 2D images acquired from unpatterned and ribbon-patterned thin-film samples demonstrate the challenges faced when launching and measuring SPs using this method. Lastly, the coherent THz-s-SNOM technique of Chapter 3 is used to investigate a Bi_2Se_3 thin-film sample incorporating a metallic top gate. It is demonstrated that the s-SNOM approach can successfully prope the TI surface beneath the top-gate. By expressing the resulting imaging data in the complex plane, it is seen that SPPs can be successfully launched and measured on the surface using this technique.

Chapter 5 presents an investigation into the design, improvement and near-field imaging of waveguides designed to support spoof surface plasmon polaritons (SSPPs) at THz frequencies. The work presented in this Chapter is a direct continuation of N. Sulollari 2022 [10] and opens with a summary of the relevant work therein. A series of additional SSPP waveguide end geometries, the goal of which is to impede unwanted coupling of incident radiation to the SSPP mode, are exhibited. All designs are subject to simulation using the software ANYSY HFSS in which the structures are excited using wave-ports and s-polarised free space excitation at 3.45 THz.

The prospect of using nickel as a waveguide termination design material instead of gold is also investigated. Based on these initial simulation results, the most effective geometry is chosen and incorporated in the design of an improved SSPP dual-waveguide structure designed to demonstrate coupling of SSPPs between spatially separated waveguides, which is then simulated in a similar manner. Finally, an experimental sample based on this new design is fabricated and measured using the THz-s-SNOM of Chapter 2.

Chapter 6 concludes the thesis with a short summary of the experimental chapters and suggestions for future work.

Chapter 2

THz-s-SNOM based on self-mixing in a QCL

2.1 Introduction

The work presented in the remainder of this thesis relies on three main components: the QCL, self-mixing detection, and the THz-s-SNOM system. The following Chapter will present and discuss the underlying theory of each of these components, and investigate their key aspects experimentally. Section 2.2 will describe the measurement approach/apparatus for measuring the LIV relationship and emission spectra of a QCL before presenting and discussing said characterisation of an exemplar QCL.

Section 2.3 will explore the frequency tuning of QCLs and will utilise self-mixing detection in a QCL to measure the tuning coefficient of an exemplar QCL. An overview of the self-mixing theory will be presented based on the Lang-Kobayashi model of a laser under optical feedback. A description of the experimental apparatus used to measure the tuning coefficient will be given and an analysis of the resulting data will show how the tuning coefficient can be realised via two methods. Additionally, Section 2.4 will include a detailed investigation of the self-mixing response in a QCL as a result of a change in driving current.

Section 2.5 presents a description and characterisation of the THz-s-SNOM system that will be used in the remainder of this thesis. This will include a guide to aligning the system, a demonstration of the techniques used to reduce background signal, and an optimisation of the system resolution and how it varies with tip size/surface features.

2.2 QCL Characterisation

Before using a QCL in a specific application, it is necessary to fully characterise it in order to determine its suitability. This section explains the characterisation procedure. Exemplar characterisation data is presented for a QCL that is later used to explore/characterise self-mixing detection signals in Section 2.3.This included the light-current voltage (LIV) characteristics, from which parameters such as the laser threshold current density J_{th}, maximum operating temperature T_{max} and peak operating power P_{max} were determined. As well the lasing spectra are obtained through Fourier-transform infra-red spectroscopy (FTIR). These characteristics are of particular importance when considering the frequency tuning of a QCL with current (Section 2.2) and use of a QCL in systems such as the microscope of Section 2.5.

2.2.1 Experimental set-up

A diagram of the experimental set-up used to measure the LIV characteristics of a QCL can be seen in Figure 2.1. The QCL was mounted on the cold-finger of a continuous flow Helium-cooled cryostat (Janis ST-100), which was mounted on three adjustable stages for ease of alignment. Prior to operation, the cryostat was vacuum pumped to a pressure of $\sim 1 \times 10^{-6}$ mbar and cooled to a temperature of 20 ± 0.01 K which was maintained by a (Lake Shore 335) temperature controller. The laser was characterised in continuous wave (CW) mode, provided by an Arroyo current driver, since it was only to be used experimentally in this operating mode.

The output beam of the laser was collimated and focused, by two identical parabolic mirrors (each with $f \sim 101.6$mm), which was detected by a cryogenically cooled Ge thermistor bolometer. To measure the absolute power of the QCL, the raw LIV data is obtained using the bolometer which is then calibrated using an absolute power meter.

A mechanical chopper was first used to align the system by modulating the beam at ~160 Hz. Throughout the experiment, the voltage signal from the detector was recovered via a DSP lock-in amplifier (LIA) using the frequency of the mechanical chopper f_{mod} as its reference. Both the QCL voltage and driving current are both read using an oscilloscope. Both the oscilloscope and LIA were connected to a PC and the LIV data was measured using a LabVIEW virtual instrument (VI).

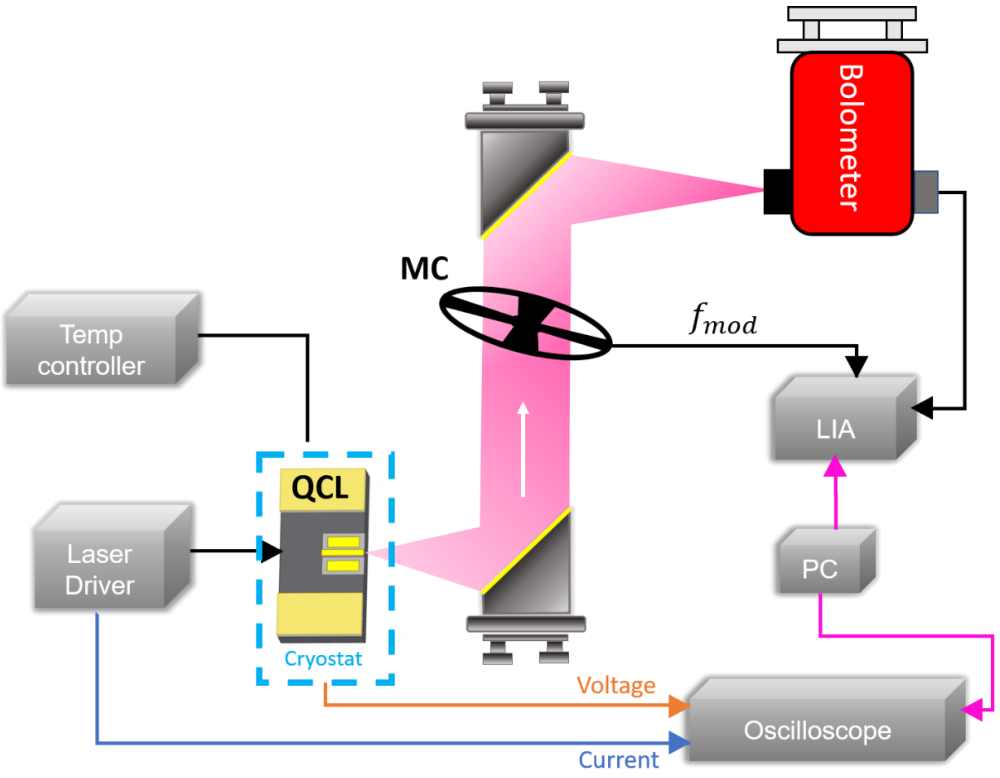

Figure 2.1 – Experimental set-up for LIV characterisation of the QCL. Adapted from [10].

2.2.2 LIV data

Figure 2.2 displays the current-voltage relationship and the power-current relationship of an exemplar QCL, measured using the apparatus of Figure 3. In this case, the device in question consisted of a 14 µm thick GaAs/AlGaAs 9-well active region [55] based on the hybrid design described in Chapter 1 Section 1.3, which was processed into a semi-insulating surface-plasmon ridge waveguide with dimensions of 1.8 mm x 150 µm. To achieve lasing on a single longitudinal mode, a 166 µm long finite-site photonic lattice was patterned through the top contact layer using focused ion beam milling [124].

Each set of measurements was taken over a range of operating temperatures from 20 – 50 K. Due to the geometry of its quantum wells, the voltage across the device determines the alignment of the injector and upper lasing level, and ultimately the device power output. For low voltages, electron transport through the active region is inhibited by misalignment of the extractor and injector states. As voltage increases, the states begin to align allowing electron tunnelling between wells, leading to population of the upper lasing levels and generating the emission of photons. Lasing occurs when the optical gain exceeds the losses of the device. The QCL driving current at which lasing is achieved, represented on Figure 2.2b as where the device output power becomes non-zero, is described as the threshold current. Optimum alignment of the lasing states provides the

peak optical power P_{max}. Further increasing of the voltage results in a secondary misalignment of the lasing states, at which the tunnelling efficiency reduces and consequentially lowers the power output.

Figures 2.3 and 2.4 show how P_{max} and J_{th} are affected by temperature. Peak power reduction occurs due to thermal backfilling and thermally-activated LO phonon emission, according to Equation 2.1 [10].

$$P = P_0 - P_1 \exp\left(\frac{T}{T_0}\right) \tag{2.1}$$

where T is the QCL operating temperature and P_0, P_1 and T_0 are fitting parameters. The maximum operating temperature for this laser is defined as the temperature at which the output power P drops to zero, which is $T_{max} \sim 50$ K.

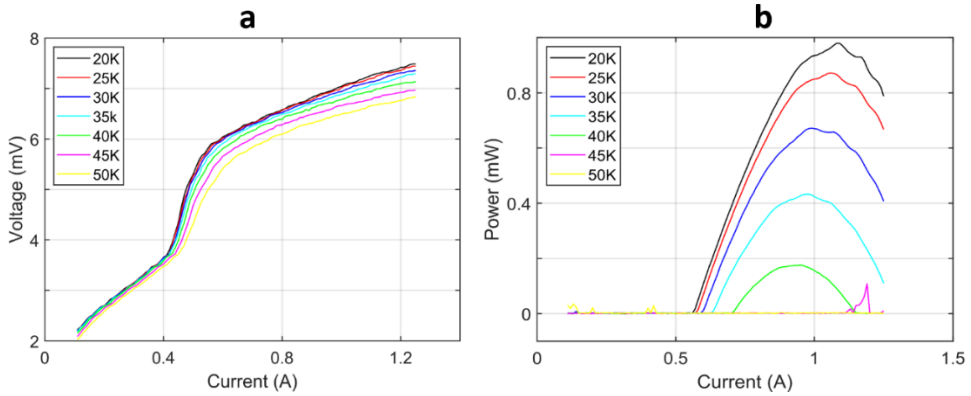

Figure 2.2 – (a) QCL IV curves for a range of operating temperatures. (b) QCL LI curves for a range of operating temperatures. Both measured using the apparatus of Figure 2.1 and with the QCL in CW mode.

Figure 2.3 shows the peak optical power of the QCL for different operating temperatures taken from Figure 2.2b. Also shown is a fit to Equation 2.1 from which the parameters values $P_0 = 1.6$ mW, $P_1 = 0.23$ mW and $T_o = 22.2$ K are determined.

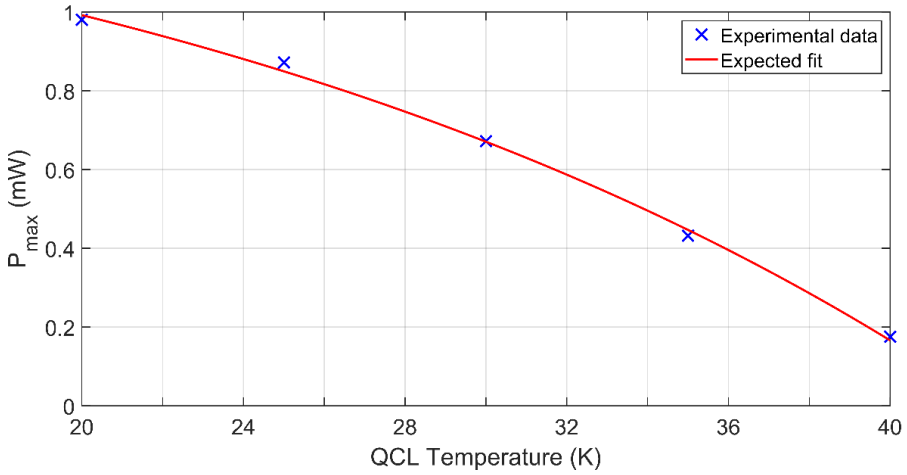

Figure 2.3 – Peak optical power for various QCL operating temperatures. (Blue) Experimental data taken from Figure 2.2b. (Red) Expected trend according to Equation 2.1.

Furthermore, a similar mechanism explains the increase in the threshold current density J_{th} with temperature, displayed in Figure 2.4. Here thermal backfilling means a larger current is required to achieve the optical gain needed to overcome the losses. This behaviour is also described by a Boltzmann fit in the form of Equation 2.2. In this equation the threshold is quoted as a threshold current *density*, as relating it to the device's dimensions allows for easy comparison between QCLs. For this device, J_{th} has been calculated using a QCL cross-sectional area of $A = 2.7\text{x}10^{-3}$ cm^2.

$$J_{th} = J_0 + J_1 \exp\left(\frac{T}{T_0}\right) \tag{2.2}$$

Figure 2.4 shows the fit to Equation 2.2, for which the fitting parameters are, $J_0 = 212.1$ A/cm^2, $J_1 = 1.07\text{x}10^{-3}$ A/cm^2, $T_0 = 3.71$ K.

From these evaluations, it can be seen that for a typical operating temperature of a QCL in CW mode (20K), a peak power of 0.98mW and threshold current density of $J_{th} \sim 210$ A/cm^2 was determined.

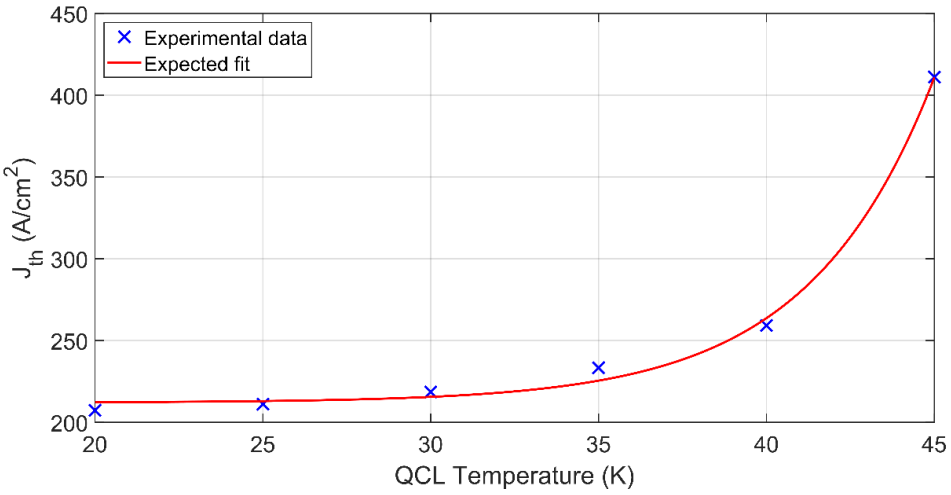

Figure 2.4 – J_{th} values for various QCL operating temperatures. (Blue) Experimental data, calculated from the threshold current vales of Figure 5a. (Red) Expected trend according to Equation 2.2.

2.2.3 Spectral data

Figure 2.5 shows the FTIR experimental set-up used to measure the frequency spectra of the QCL. This comprised similar components to Figure 2.2 and was based on a Michelson Interferometer with resolution 7.5 GHz. Briefly, a Fourier-transform infra-red (FTIR) spectrometer measures the spectrum of an incident radiation beam by splitting it into two different beams using a flexible split mirror and adjusting the phase difference between the two beams using a moveable mirror. The beams are recombined and the interference pattern is captured using an in-built detector. A Fourier-transform of the data reveals the emitted power as a function of emission frequency.

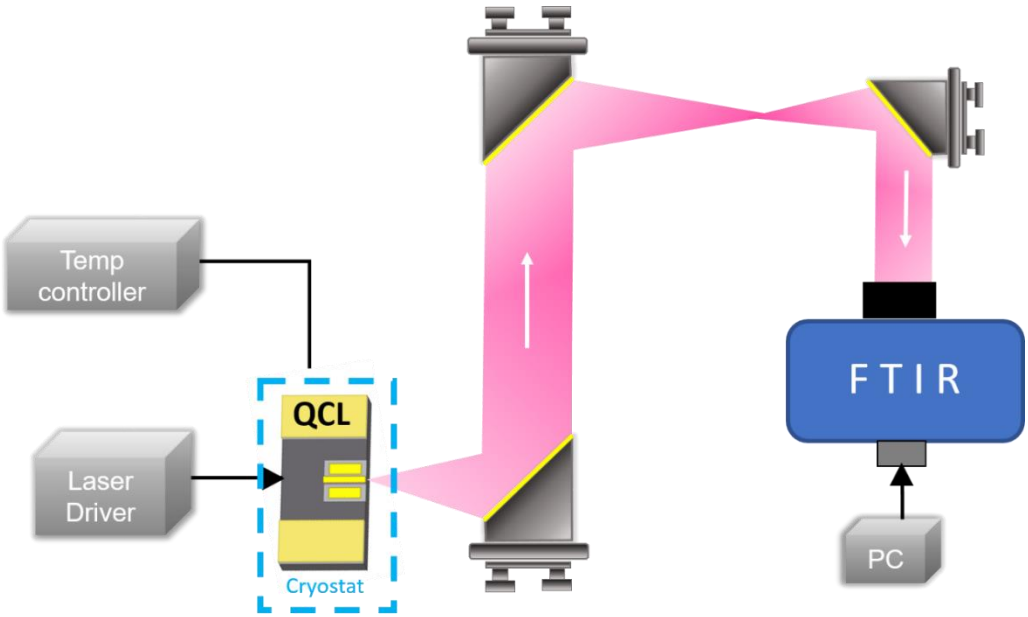

Figure 2.5 – Experimental set-up for FTIR characterisation of the QCL. Adapted from [10].

To perform the spectra measurements of Figure 2.6, the QCL was mounted in the apparatus of Figure 2.5 and measured using FTIR over a range of driving currents. The QCL was operated in CW mode and maintained at a temperature of 20 ± 0.01 K through the experiment using a (Lake Shore 335) temperature controller.

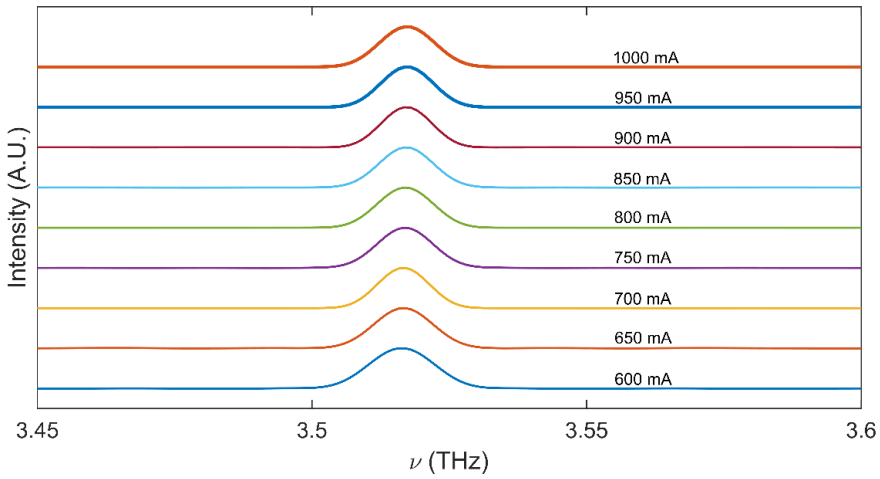

Figure 2.6 – QCL (L1612) spectra for different driving currents measured via FTIR.

From Figure 2.6 it can be seen that this device lases at a single mode of 3.52 THz. The single modality of the QCL is ensured by the addition of top layer photonic lattice employing a metallic grating that generates a narrow band-pass filter at the Bragg frequency of the lattice, due to the contrast between the refractive index of the etched and metallised areas of the waveguide [125]. It is expected that the frequency ν will tune with current but the resolution of the FTIR (7.5 GHz) does not allow this to be measured from Figure 2.6. Instead, it will be shown in Section 2.2 how self-mixing can be used to measure QCL frequency tuning with a high resolution.

2.3 Frequency tuning of QCLs

For QCL imaging applications in which both the amplitude and phase of the signal require resolving, one approach is to utilise the tuning of QCLs by sweeping the output frequency and measuring the change in the QCL voltage due to the self-mixing (SM) effect. This can be performed for both near-field and far-field techniques and has been observed in [73], [82], [126], [127].

There are several mechanisms that can be used to tune the output frequency of a QCL, such as modulation of its operating temperature [128], tuning due to rear facet illumination [129] and driving current modulation [130], [131]. Notably, tuning through temperature is afforded by the dependence of the QCL's refractive index on temperature and responds with a tuning coefficient governed by $K = \delta\nu/\delta T$. This temperature change is commonly brought about by varying the QCL heat-sink temperature, but can also occur by varying the QCL driving current through Joule heating. The speed at which the QCL can be thermally tuned is thus limited by the thermal time constant of the semiconductor material, which is usually of the order of 100 μs [132].

QCL tuning via modulation of the driving current is faster and widely used in spectroscopic techniques such as trace gas detection [133]. This technique is afforded by shifting the peak frequency of the intersubband gain within a QCL, by subjecting it to a change in the applied voltage, causing a change in the refractive index of the laser cavity, which in turn tunes the frequency continuously [134]. This method is therefore limited in speed only by the electrical time-constant of the QCL's modulation response [135] and has been demonstrated for tuning over a range of 4 GHz [136] and 19 GHz [137].

The tuning coefficient of a QCL is defined as the change in lasing output frequency as a result of a change in the driving current (or temperature depending on the method) [138]. The thermal tuning coefficient of QCLs typically varies from ~ 34 MHz/K to ~ 100 MHz/K. However, fast temperature tuning from a change in current is limited to ~ 5 MHz/mA. Alternatively, for some QCL designs, current tuning has been demonstrated at ~ 8 MHz/mA [139], which is degree similar value as the tuning coefficients determined in Section 2.3.3.

In the following Sections, a new approach for measuring frequency tuning with a high resolution based on SM is shown. Two implementations of interferometric fringe generation via SM are demonstrated, from which the tuning coefficient of the QCL characterised in Section 2.2 is determined. The two methods involve applying a frequency sweep through a modulation of the QCL driving current and mechanically extending the external cavity length.

2.3.1 Underlying theory of swept-frequency self-mixing

The response of a QCL under the SM scheme can be expressed using the steady-state solution of the model proposed by Lang-Kobayashi [140]. Alternatively, the same result can be obtained from the three mirror model [141], which is visualised in in Figure 2.7.

Here a laser cavity of length L_{in} is subject to optical feedback from an external mirror which forms an external cavity of length L_{ext}. Equation 2.3 is arrived at under the condition that the change in the compound cavity phase accumulation is zero at the cavity resonant frequency and is referred to as the excess phase equation. Equation 2.4 defines the change in the threshold carrier density N due to optical feedback [12].

$$2\pi\tau_{ext}(v_0 - v) + C\ sin(2\pi v\tau_{ext} - \arctan(\alpha)) = 0 \quad 2.3$$

$$N - N_0 = -\beta\cos(2\pi v\tau_{ext}) \quad 2.4$$

Here the subscript 0 denotes laser parameters in the absence of optical feedback, v is the lasing frequency, α is the linewidth enhancement factor and β is the coupling rate of optical feedback. τ_{ext} is the round-trip delay, defined as $\tau_{ext} = 2L_{ext}/c$, where L_{ext} is the external cavity length and c is the speed of light. C is a dimensionless parameter which encapsulates factors such as the target reflectivity R_{ext}, laser facet reflectivity R_{in} and is defined by,

$$C = \varepsilon\frac{\tau_{ext}}{\tau_{in}}\sqrt{1+\alpha^2}\sqrt{\frac{R_{ext}}{R_{in}}}(1 - R_{in}) \quad 2.5$$

where ε is a constant that accounts for various optical losses and τ_L is the laser cavity round trip time, defined as $\tau_{in} = 2L_{in}/c$, where L_{in} is the internal cavity length.

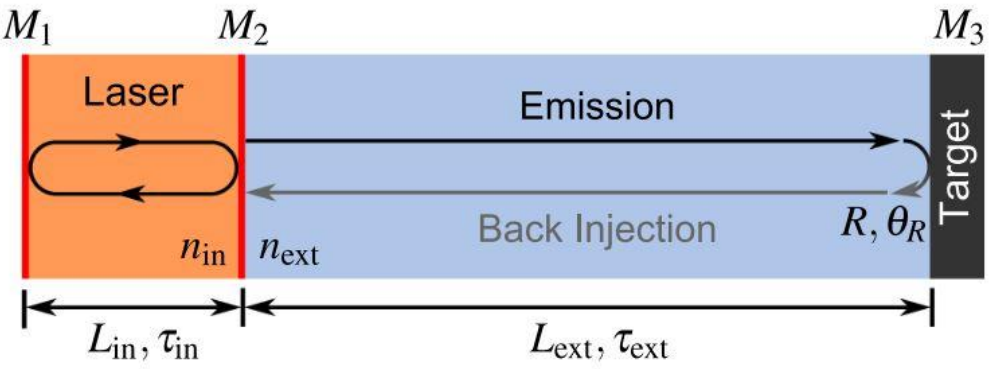

Figure 2.7 – Three mirror model of laser feedback interferometry. Where M_1, M_2 and M_3 are mirrors, n_{in} is the internal cavity refractive index, n_{ext} is the external cavity refractive index, R is the reflectivity of M_3 and θ_R is the angle of M_3 with respect to the emission beam. Adapted from [12].

The perturbation to carrier density described by Equation 2.4 causes a proportionate change to the emitted power and laser terminal voltage. This gives rise to the expression for the terminal voltage of a QCL under optical feedback described by Equation 1.4.

To acquire interferometric fringes, from which the tuning coefficient of the QCL can be determined, the QCL terminal voltage can be modulated via a change to the round trip phase of the external cavity. This can be generated by a modulation to the driving current, which in turn produces a change to the QCL frequency and therefore causes the desired phase change. The time-dependent interferometric phase of the SM signal under frequency modulation of the laser is given by,

$$\phi(t) = \frac{4\pi L_{ext}}{c}\gamma t + \frac{4\pi L_{ext}}{c}\nu_0 = 2\pi f_c t + \phi \qquad 2.6$$

where ϕ is the initial phase of the SM fringe at $t = 0$, c is the speed of light, L_{ext} is the external cavity length γ is the modulation rate of the system which incorporates the laser tuning coefficient K and f_c is the carrier frequency of the fringes given by $f_c = 2\gamma L_{ext}/c$ [2].

To modulate the current, a saw-tooth waveform can be applied to the QCL current driving (Figure 2.8a) which produces a modulated current (Figure 2.8b). The QCL terminal voltage can then be measured (Figure 2.8c) from which can be extracted the interferometric fringes by removal of the QCL voltage recorded without any feedback (Figure 2.8d).

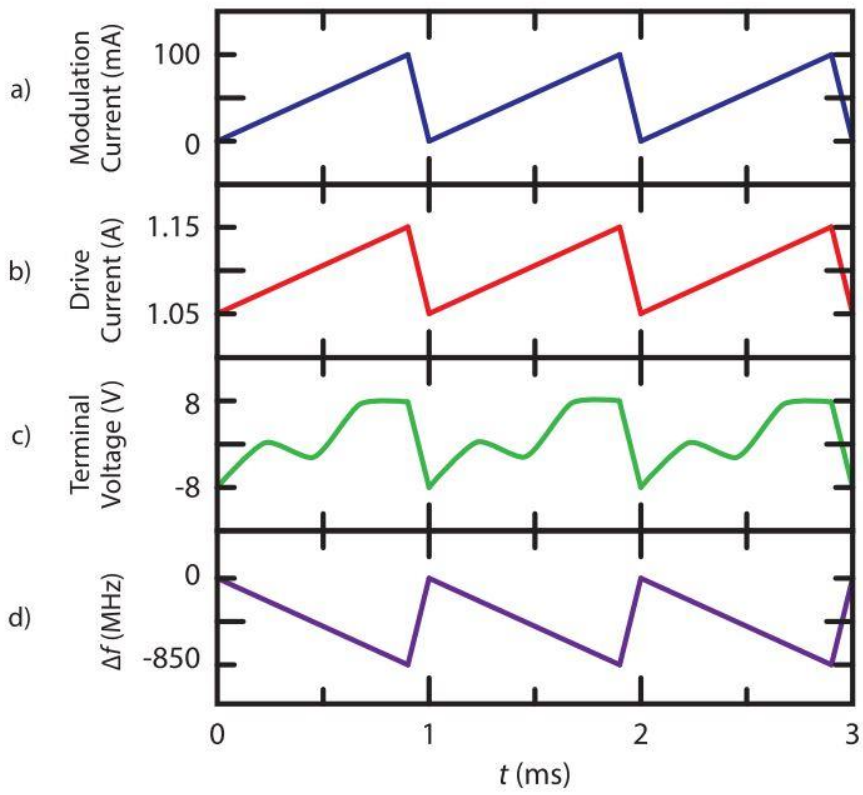

Figure 2.8 – The various waveforms involved in swept-frequency laser feedback interferometry. (a) The modulation current supplied by a signal generator. (b) The modulated current used to drive the laser. (c) The laser terminal voltage. (d) Interferometric fringes resolved by removal of the modulation waveform.

2.3.2 System set-up

The tuning coefficient of the QCL described in Section 2.2 was determined using two methods: a) comparing the positions of consecutive fringes acquired through swept frequency laser feedback interferometry, and also b) measuring the phase between sets of interferometric fringes due to a change in the external beam path length.

The experimentation associated with each of these methods was performed using the system seen in Figure 2.9. This comprises the QCL, mounted in a continuous flow helium cryostat, in a similar fashion to that seen in Section 2.2, the output of which is focused onto a reflective target mounted on a motorised translation stage moveable in the z-direction. The alignment is adjusted so that a portion of the reflected radiation travels back along the beam path and is reinjected into the laser cavity. The QCL is driven by an Arroyo current driver which is influenced by a signal generator to allow electronic modulation of the QCL output.

The QCL voltage was measured by a DAQ board and visually displayed via a LabVIEW virtual instrument. A modulation of the driving current using a 2 V peak-to-peak (resulting in a 400 mA increase from 600mA – 1000) saw-tooth wave with a frequency of 1 KHz and offset of ~ 0.3 V was used and monitored on the oscilloscope. For alignment purposes, the SM signal was first modulated with a mechanical chopper and acquired by a LIA.

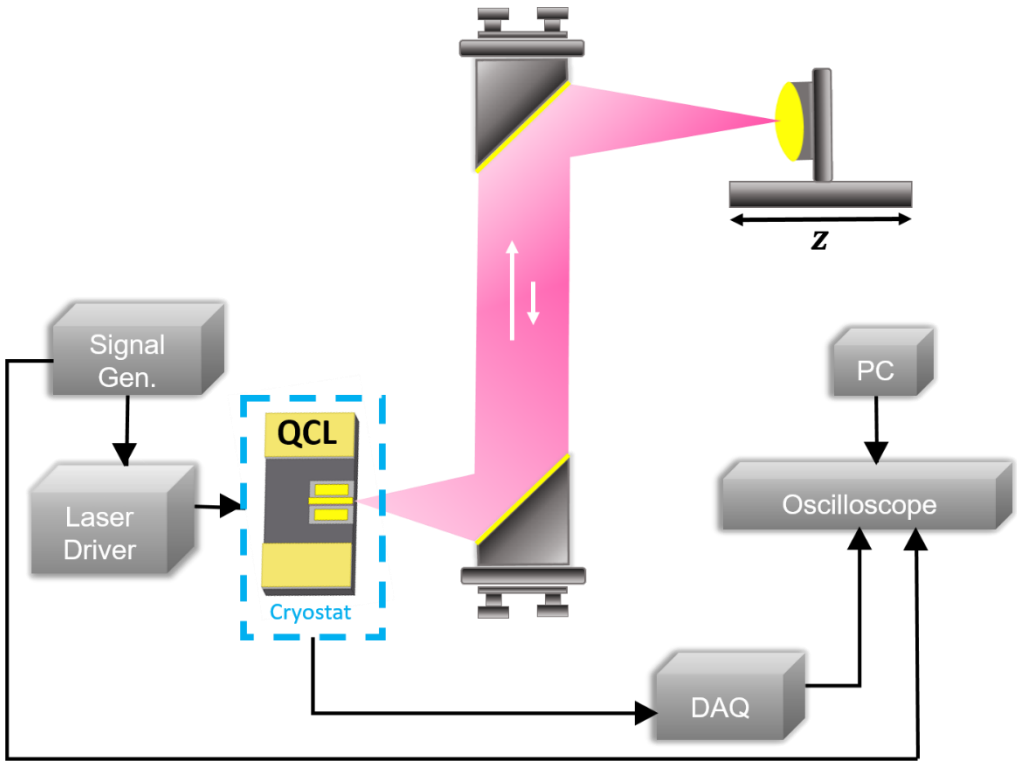

Figure 2.9 – Experimental set-up for self-mixing measurements using a QCL.

2.3.3 LFI measurements

To perform the self-mixing measurements, several recordings of the QCL terminal voltage were acquired by the DAQ board whilst subject to the current modulation described above. This was subsequently performed for various external beam path lengths, which were varied over a range of 40 μm with a step size of 4 μm. The initial starting path length was $L_{ext} = 30$ cm.

Compared to the modulation waveform, the self-mixing signal acquired from these measurements is very weak (≈ 3 mV) and therefore requires an extraction process to be observed. To do this, a non-reflective material was inserted into the optical path to negate the self-mixing signal. This blocked signal was measured 1000 times and

averaged to obtain an accurate reading of the background modulation waveform. The optical path was then unblocked and the swept frequency also averaged over 1000 measurements. The blocked signal was then subtracted from the averaged unblocked signal to reveal the self-mixing fringes, an example of which can be seen in Figure 2.10.

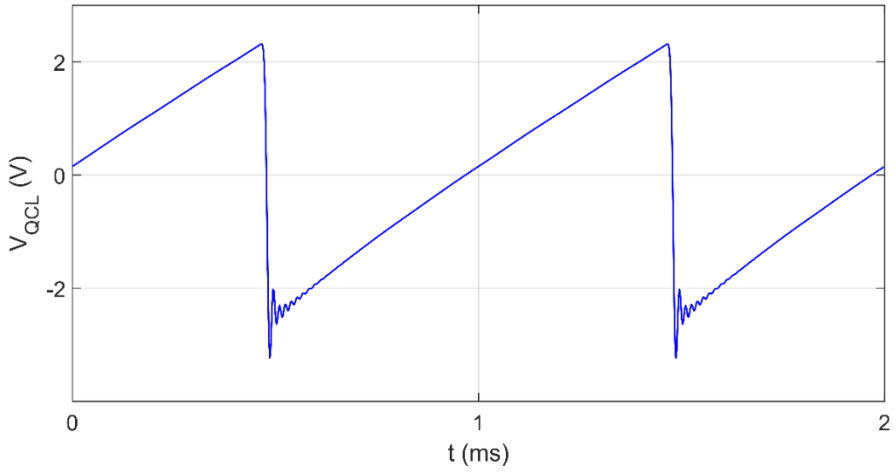

Figure 2.10 – Modulated self-mixing signal measured using the apparatus of Figure 2.9.

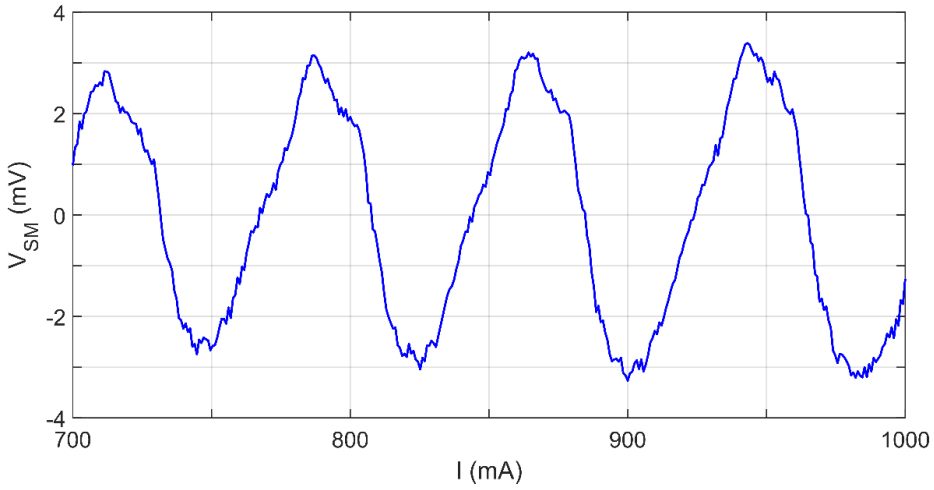

Figure 2.11 – Example of self-mixing signal embedded in the data of Figure 2.10. Revealed when removing the averaged background signal.

The interferometric fringes, such as those of Figure 2.11, can be used to characterise the frequency tuning of this QCL with a change in driving current. To evaluate this response, the following can be used. It can be seen from Figure 2.11 that the shape of the fringes is substantially sinusoidal which therefore suggests that the QCL is under a weak OF

(optical feedback) regime (C<<1). It is therefore reasonable to state, from Equation 2.3, that

$$\nu_0 \cong \nu \tag{2.7}$$

Therefore, Equation 1.4 from Chapter 1 becomes,

$$V_{SM} \propto \cos\left(\frac{4\pi\, \nu_0 L_{ext}}{c}\right) \tag{2.8}$$

where, L_{ext} is the external cavity length and c is the speed of light.

Since the fringes are assumed to be sinusoidal, at the peak of any fringe m the following must be satisfied,

$$\frac{4\pi\nu_m L_{ext}}{c} = 2\pi m \tag{2.9}$$

where m is an integer and ν_m is the laser frequency at the peak of the m_{th} fringe. By analogy, for the next consecutive fringe, this condition can be expressed as,

$$\frac{4\pi\nu_{m+1} L_{ext}}{c} = 2\pi(m+1) \tag{2.10}$$

Therefore, using equation 2.9 and 2.10,

$$(\nu_{m+1} - \nu_m) = \frac{c}{2L_{ext}} \tag{2.11}$$

Given the current tuning coefficient as,

$$K = \frac{(\nu_{m+1} - \nu_m)}{(I_{m+1} - I_m)} \tag{2.12}$$

it follows that,

$$K = \frac{c}{2L_{ext}\,(I_{m+1} - I_m)} \tag{2.13}$$

Where I_m is the current corresponding to the peak of the m_{th} fringe. Calculating K for each consecutive pair of fringes in Figure 2.11 and averaging these values gives a tuning coefficient of $\pm$ 4.09 MHz/mA.

Alternatively, and as stated above, the tuning coefficient can also be determined by measuring the shift in fringe position due to a change in the external optical path length. This was obtained by repeating the SM measurement for each position of the reflective mirror target, which was moved via the motorised stage, over a range of 40 µm with (-) 4 µm steps. Figure 2.12 shows two sets of fringes that were measured during this experiment, with different positions $L = L_{ext} + \delta L$ of the mirror, and demonstrates how a change in the optical path length can cause a shift in the fringe position.

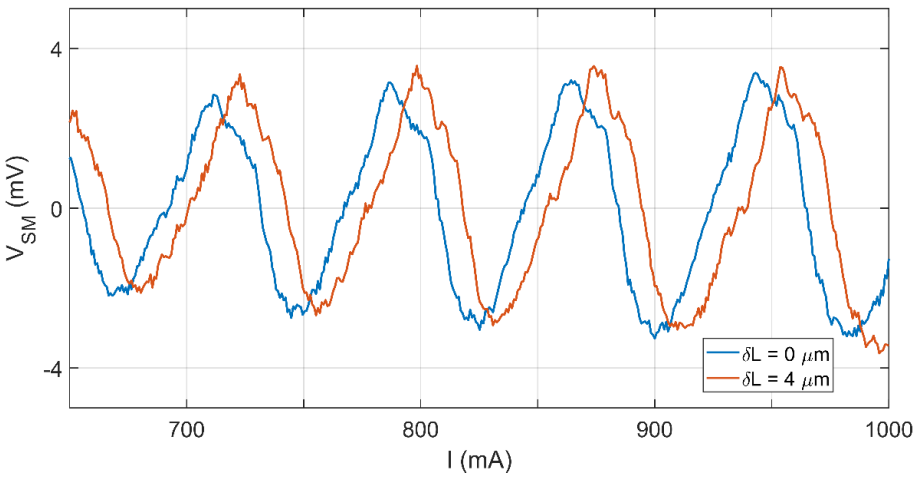

Figure 2.12 – SM fringes measured for the initial mirror position $\delta L = 0$ µm (blue) and a $\delta L = (-)$ 4 µm movement of the mirror parallel to the THz beam (orange).

As show in Figure 13, the fringe sets comprise four distinct peaks. To determine the change in current values at which the peaks of each fringe occur, the position of the corresponding peaks for each set were compared to that of the fringe set measured for $\delta L = 0\ \mu m$, and averaged to give the mean fringe shift for that set. For example, the

average change in current value between peaks of $\delta L = -4$ μm and $\delta L = 0$ μm was calculated to be $\delta I_{\Delta L=4} = 10.77$ mA. In order to calculate the change in frequency corresponding to this change in current, the following analysis is applied

From Equation 2.9 it can be seen that, for a change in both output frequency $\delta\nu$ and cavity length δL, the following is true,

$$\frac{4\pi(\nu_0 + \delta\nu)(L_{ext} + \delta L)}{c} = 2\pi m \tag{2.14}$$

it follows that,

$$\frac{4\pi\nu_0 L_{ext}}{c} + \frac{4\pi\delta\nu L_{ext}}{c} + \frac{4\pi\nu_0\delta L}{c} + \frac{4\pi\delta\nu\delta L}{c} = 2\pi m \tag{2.15}$$

However, given that, at the peak of the m_{th} fringe,

$$\frac{4\pi\nu_0 L_{ext}}{c} = 2\pi m \tag{2.16}$$

and,

$$\frac{4\pi\delta\nu\delta L}{c} \ll \frac{4\pi\nu_0 L_{ext}}{c}, \frac{4\pi\delta\nu L_{ext}}{c}, \frac{4\pi\nu_0\delta L}{c} \tag{2.17}$$

Equation 2.15 can be simplified to,

$$\frac{4\pi\delta\nu L_{ext}}{c} + \frac{4\pi\nu_0\delta L}{c} = 0 \tag{2.18}$$

from which we can obtain,

$$\frac{\delta\nu}{\nu_0} = -\frac{\delta L}{L_{ext}} \tag{2.19}$$

By calculating this change in frequency $\delta\nu$ for each path length extension δL, and plotting it against each corresponding value of δI, Figure 2.13 can be obtained, fitted to which is Equation 2.20.

$$\delta\nu = K\delta I \tag{2.20}$$

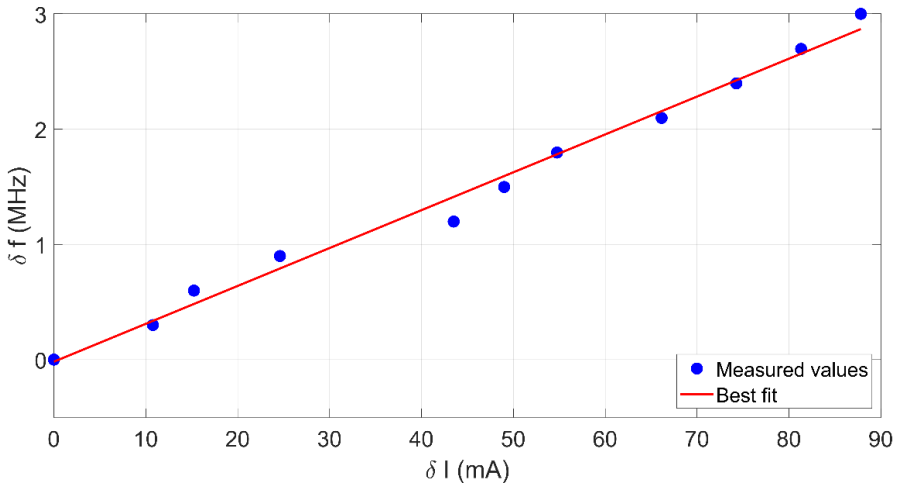

Figure 2.13 – Change in frequency δf for each set of interferometric fringes (blue) calculated using the above analysis, alongside best fit of relation $\delta I = \delta f K$ (red).

From the fit of Figure 2.13, as seen in red, a value of K = 3.29 MHz/mA was obtained. This value agrees reasonably well with the value of $\pm$ 4.09 MHz/mA determined by the previous method. The discrepancy between the tuning coefficients yielded by these two methods can be attributed, at least partly, to the ambiguity in the position of each fringe peak, since the fringes are not perfectly sinusoidal or well defined. Additionally, the approximation made in Equation 2.17 will add error. Furthermore, it is also assumed that the value of K remains constant across the current range, which may not be accurate.

In summary, the characterisation of a QCL has been undertaken as seen here and in Section 2.2. The QCL current-voltage and current-power response have been explored, which has yielded values for the maximum power and threshold current density and. A spectral analysis of the device has demonstrated a single mode of 3.52 THz, at an operating temperature of 20 K. Additionally, the self-mixing effect in a QCL has been demonstrate using this device, from which the tuning coefficient has been determined.

These results provide necessary information about this QCL, which are necessary for implementation of it into systems, such as the THz frequency scattering-type scanning near-field optical microscopy (THz-s-SNOM) characterised in Section 2.5, for coherent imaging applications. The following Section will further investigate self-mixing in a QCL, which will include how parameters, such as optical feedback strength C and linewidth enhancement factor α [142] vary with current.

2.4 Characterisation of the self-mixing response as a function of driving current

As seen in Section 2.3, the SM effect has been used to determine the tuning coefficient of a QCL. In this section, further investigation into the SM effect in a QCL itself will be undertaken. This analysis will explore the specific properties of a SM response that are expressed in Equations 2.3 – 2.5, such as the feedback parameter C, linewidth enhancement factor α and fringe amplitude β, for a range of QCL driving currents. These behaviour of these parameters is important to understand for applications such as that demonstrated in Chapter 3, where the frequency tuning of a QCL under optical feedback is used in a coherent imaging system.

2.4.1 System set-up

To investigate the effect of driving current on the SM response in a QCL, a series of interferometric fringes were generated via mechanical optical path extension, for a range of QCL driving current, using the QCL previously characterised. This was performed using an optical set-up schematically identical to that used in the tuning coefficient measurements of Section 2.3 (Figure 2.9), but omitting electrical modulation of the QCL driving current.

To generate a series of interferometric fringes, the QCL self-mixing voltage V_{SM} was recorded for each 0.5 μm increment of a 0.2 mm mechanical extension of the initial $L_{ext} = 300$ mm optical beam path. The mechanical chopper frequency was ~ 100 Hz, which was used as the LIA reference frequency, which had a time constant of $\tau = 100$ ms.

An example of the fringes generated can be seen in Figure 2.14, fitted to which is the Lang-Kobayashi (L-K) model for a laser under weak feedback, Equation 2.21. For this experiment, the laser driving current was kept constant at 650 mA.

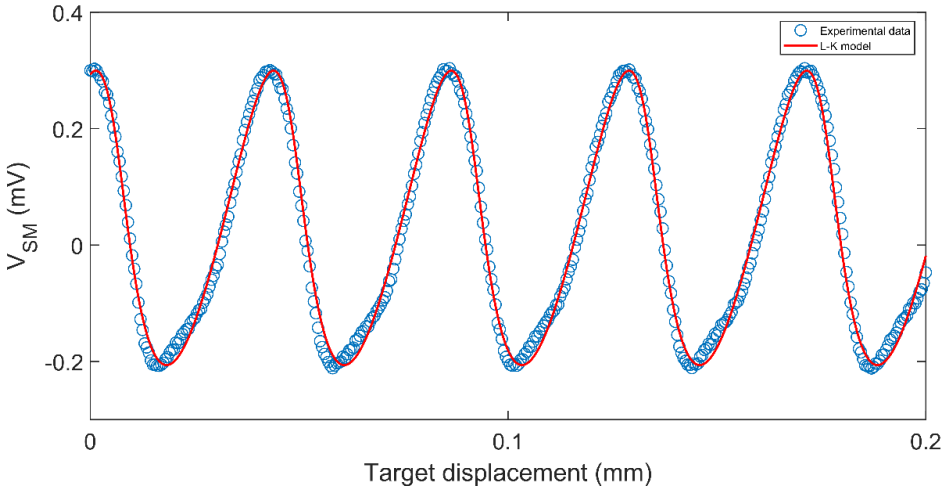

Figure 2.14 – Interferometric fringes generated via mechanical beam path extension (blue) with Lang-Kobayashi fit (red). For this set the values of $C = 0.36$, α = -1.91 and $\beta = 0.25$ mV were determined.

2.4.2 Analysis

To model the SM voltage signal, the equation introduced in Chapter 1 and reiterated in Equation 2.21, is fitted to each set of fringes to allow for extraction of each of the parameters stated above.

$$V_{SM} = \beta \cos\left(\frac{4\pi L_{ext}\nu}{c} + \theta_R\right) \qquad 2.21$$

where β is the amplitude of the SM fringes.

The QCL frequency under optical feedback ν is given from the solution to Equation 2.3. The method by which the values of C and α are fitted to the set of fringes uses the model given in [143]. The model first requires a preliminary guess for each of the fringe parameters, the most influential of which are the feedback parameter C and linewidth enhancement factor α, which are related through the following expression [12], as described previously by Equation 2.5,

$$C = k\sqrt{1+\alpha^2} \tag{2.22}$$

where the feedback coefficient k is defined as,

$$k = \varepsilon\frac{\tau_{ext}}{\tau_L}\sqrt{\frac{R_{ext}}{R_L}}(1-R_L) \tag{2.23}$$

in which R_{ext} is the reflectivity of the external target, R_L is the reflectivity of the emitting laser facet, ε is the portion of the reflected radiation that couples coherently with the laser and accounts for optical losses, τ_{ext} is the round-trip delay in the external cavity which is defined by $\tau_{ext} = 2L_{ext}/c$ (in which L_{ext} is the external cavity length and c is the speed of light) and τ_L is the round trip time for the laser cavity.

The linewidth enhancement factor α is a value that relates the change in phase of the laser output to a change in its optical gain and was first defined in [144] as ,

$$\Delta\varphi = \frac{\alpha}{2}\Delta g \tag{2.24}$$

where φ is the laser phase and g is the optical gain.

To initially determine a value of k with which to fit the C and α values for the various sets of fringes, the first three fringe sets, obtained using to driving currents of between 550 – 560 mA, were fitted to using a least-squared fit with k, C and α being free parameters. Once suitable values for all sets were established, the values of k were averaged and a value of $k = 0.168$ was determined. This value then was used as a constant to perform the fits for the subsequent data sets, wherein a least squares fit of the fringes was performed with α and β as free parameters. For each set of fringes, a value of C was determined from the α values using Equation 2.22.

To perform the least squares fit of each data set, initial guesses of the fitting parameter α, close to the true value, had to be given. To produce the fit seen in Figure 2.15, an initial value of α = -1.85 was chosen. Additionally, the amplitude β and DC offset V_0 were assumed to be $\beta = (V_{max} - V_{min})/2$ and $V_0 = (V_{min} + V_{max})/2$.

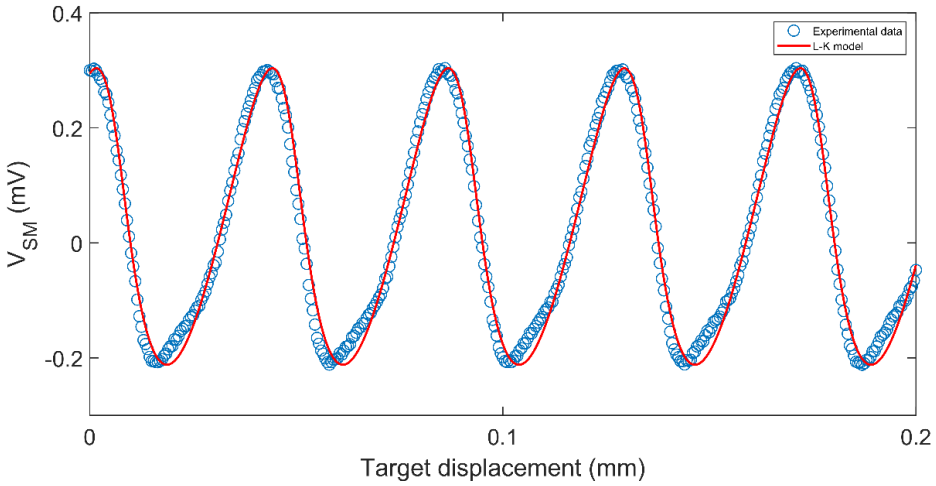

Figure 2.15 – The fringes of Figure 2.14 (blue) with a Lang-Kobayashi fit using initial fitting parameters of α = -1.85 and k = 0.168 (red). Here I = 650 mA.

Figure 2.16 shows the C, α and β values for a range of QCL driving currents between 575-1100 mA, determined using the method described above. Since k remains constant for these measurements and C is determined by using Equation 2.22, C is completely dependent on α and generally displays values indicative of weak feedback except for small driving currents ($<$ 600 mA). The values of α obtained agree well with previous studies using THz QCLs [79], [145], [146]. Furthermore, the trend observed between β and driving current agrees with previous studies [79]. Notably, the area in Figure 2.16c in which β remains substantially constant, provides an example of ideal QCL operation for applications such as swept-frequency interferometry.

This investigation has explored the nature of this QCL under the SM regime. The device could now be used in applications in which this regime is required, such as the s-SNOM system of Section 2.5.

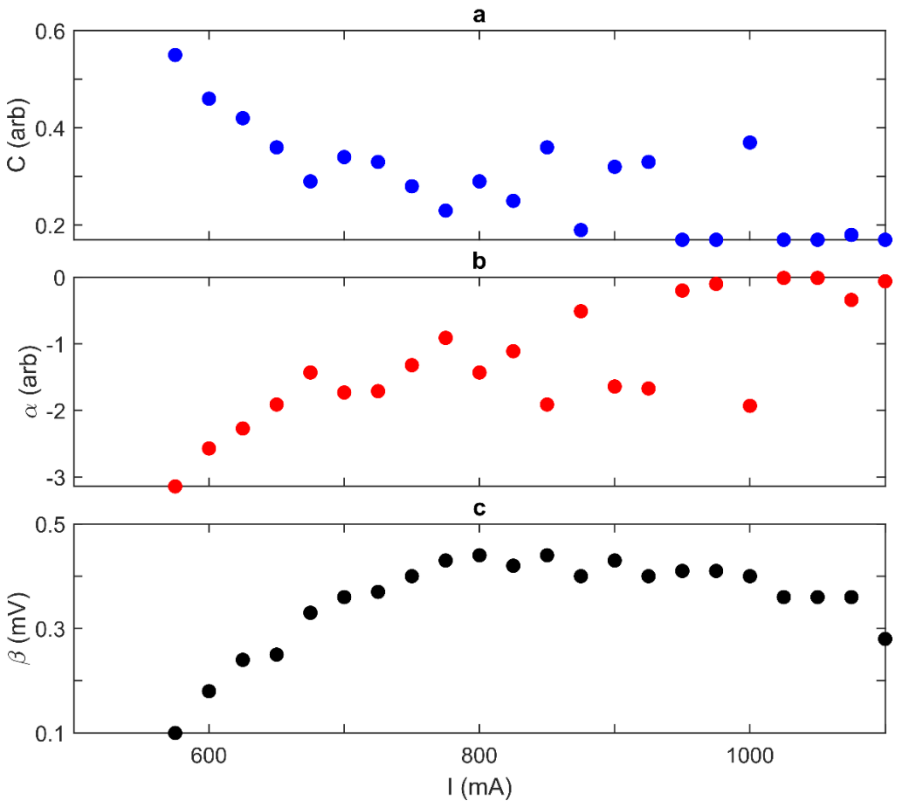

Figure 2.16 – Self-mixing parameters extracted from V_{SM} fringes using the L-K model, measured over a range of QCL driving currents. (a) Feedback parameter C, (b) linewidth enhancement factor α, (c) fringe amplitude β.

2.5 Characterisation of THz-s-SNOM

In later Chapters, THz-s-SNOM is used to investigate plasmonic effects in a range of materials. In this Section, the basic operation of THz-s-SNOM is presented and its key characteristics are investigated.

The THz-s-SNOM system presented here (Figure 2.17) and used in the remainder of this thesis is based on a commercial s-SNOM/AFM (neaSNOM, neaspec GmbH) and employs an external THz QCL emitting at $\nu \sim 3.45$ THz. The QCL (L1180) was fabricated by Dr P. Rubino and its LIV and spectra characteristics can be found in Section 2.4.3 of [10]. The QCL comprised a 14-µm-thick GaAs/AlGaAs nine-well hybrid active region, which was processed into a 1.8 mm × 150 mm SI-SP ridge waveguide. This heterostructure is nominally identical to that presented in Section 2.2, and as such similar operating characteristics are expected. During operation, the QCL was cooled using a continuous-

flow L-He cryostat to a temperature of 20 ± 0.01 K and maintained using a (Lake Shore 335) temperature controller. An Arroyo current source was used to drive the laser with a DC current of 420 mA during single-frequency use and between a range of 450-650 mA during swept-frequency operation, as seen in Chapter 3. During single-frequency imaging, the QCL voltage was 6.4 V and the emitted power was ~ 0.5 mW.

The QCL emission was focused to the tip of a vertically aligned Rocky Mountain Pt-Ir AFM tip at an angle of ~ 54^0 to the surface normal. The tip had length ~ 80 μm and apex diameter ~ 20 nm and was operated in tapping mode at a frequency of $\Omega = 80$ kHz. A portion of the radiation scattered by the probe was coupled back along the optical path and reinjected into the laser cavity, invoking the SM effect. The theory of SM in a QCL described in Section 2.3 and 2.4 are based on reflection from a reflective target. For this application of SM in a QCL, the theory still applies but the reflective target is replaced by a scattering source. This scheme, in turn, causes the reinjected signal to be far weaker, which requires the use of amplification of the V_{SM} signal by a factor of 5 x 10^3.

To identify the V_{SM} signal, the QCL terminal voltage was demodulated at harmonics of the tapping frequency Ω and amplified by a factor of 5×10^3 using an ac-coupled low-noise voltage amplifier. The ability to isolate the V_{SM} signal by using harmonics of the tip tapping frequency is explored in Section 2.5.2.

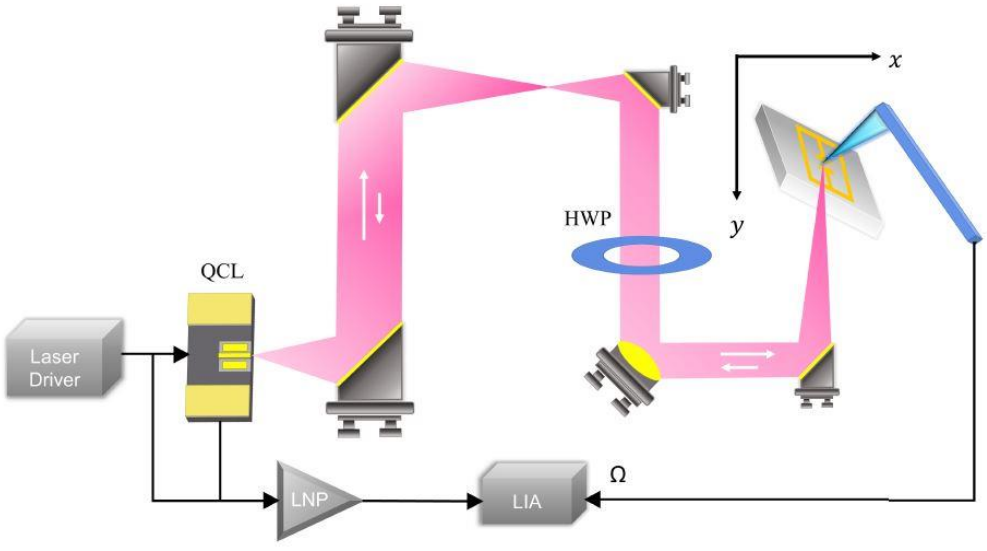

Figure 2.17 – THz-s-SNOM system schematic in which the QCL output is focused onto the tip of the AFM probe, oscillating at frequency Ω, and a portion of the scattered radiation is reinjected into the QCL cavity. The QCL is driven by a laser driver and the QCL terminal

voltage is amplified by the low-noise preamplifier (LNP) before being demodulated by the lock-in amplifier (LIA) at harmonics of Ω. The half-wave plate (HWP) is used to adjust the polarisation of the THz beam. Adapted from [10].

2.5.1 s-SNOM system alignment

This section will give a brief overview of the s-SNOM alignment process. The s-SNOM system described above focuses the THz beam to the area of the tip using an internal mirror controllable in x, y and z directions. Alignment of the THz beam is manually done by the user by moving the mirror and monitoring the amplitude and phase of the THz signal. This process not only involves alignment of the beam but also a series of checks and calibrations that are required before imaging can begin. These are as follows.

1. Replace the AFM probe tip if needed.
2. Perform a full frequency sweep of tip tuning spectrum.
3. Identify the tip resonance frequency Ω_0 and choose appropriate tip tapping frequency Ω (usually 80 % of the value of Ω_0).
4. Load the sample and position it substantially underneath the tip using the piezoelectric stage.
5. Bring the tip into contact with the sample surface.
6. Adjust the focussing mirror alignment until a suitable signal amplitude and stable phase has been achieved.

Once all steps have been completed, the system is ready to perform imaging. Examples of THz images using the s-SNOM system are presented later in this Chapter and in the remainder of this thesis.

2.5.2 Approach curves as a function of demodulation harmonic

One problem with the THz-s-SNOM method is the low signal to noise ratio (SNR) as a result of poor scattering efficiency of the probe tip at THz frequency. This arises from the fact that the QCL output wavelength is $\sim 10^4$ times smaller than the tip diameter. This renders the desired THz signal indistinguishable from unwanted background signal arising from reflections from the tip shaft and surrounding areas. To combat this, the tip is kept sinusoidally oscillating above the target surface (tapping mode) at a frequency, Ω (close to but not at the tip's natural resonant frequency) with which a lock-in amplifier (LIA) can extract the desired signal [147]. Additionally, demodulating the signal at high harmonics of Ω $(n \geq 2)$ can help distinguish the signal arising from the near-field

interaction between the probe tip and sample from the background signal arising from unwanted reflections or scattering from the shaft of the tip. To understand the effect of tip tapping amplitude and harmonic demodulation n on background noise suppression, the following characterisations were performed.

A series of measurements known as an 'approach curve' were performed to demonstrate how demodulating the SM signal at different harmonics of the tip tapping frequency and using different tapping amplitudes, affects signal purity. This procedure involves a monitoring of V_{SM} whilst the probe is brought in close contact with the surface, over a distance of several hundred nm in the z-direction, using a high-precision piezo stage, until reaching a predetermined height h, thus acquiring a description of the vertical dependence of the scattered near-field signal [101]. The value of h is usually chosen to be the closest distance to the sample surface in which the tip is allowed to operate at a specific tapping amplitude A. Since A is defined as the peak-to-peak oscillation distance of the tip, the minimum h value for a tip oscillating at amplitude A is therefore $\frac{A}{2}$ (Figure 2.18). The value z is defined as the distance between the position of the tip at the maximum of its oscillation amplitude in the –z-direction and the surface. Since the tip never actually 'touches' the surface, the $z = 0$ nm position present in Figures 2.19 and 2.20 are defined as the position at which the tapping amplitude A decreases by 2 % due to the presence of the surface.

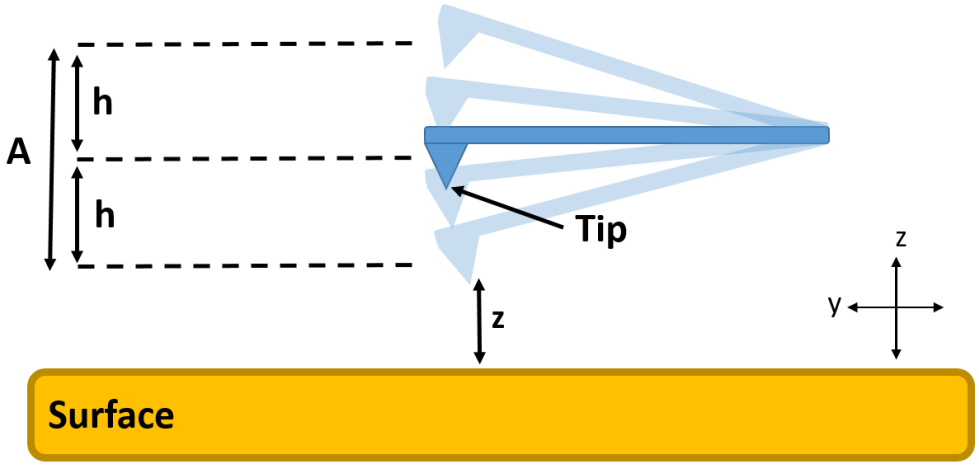

Figure 2.18 – Diagram of oscillating s-SNOM probe tip where A is the peak-to-peak oscillating amplitude of the tip and h is $\frac{A}{2}$. For approach curve measurements, the tip begins at a predetermined height above the surface and is brought into close contact with it along the z-direction until $z = 0$ nm. Exaggerated scale.

To determine the effect of signal demodulation, approach curves for $A = 400$ nm were measured for a range of harmonics of the demodulation frequency from $n = 1\Omega$ to $n = 5\Omega$ using a small tip with diameter $d \sim 20$ nm (Figure 2.19) and large tip with diameter $d \sim 1$ µm (Figure 2.20). The $n = 1\Omega$ data has been omitted from Figure 2.19 due to scaling.

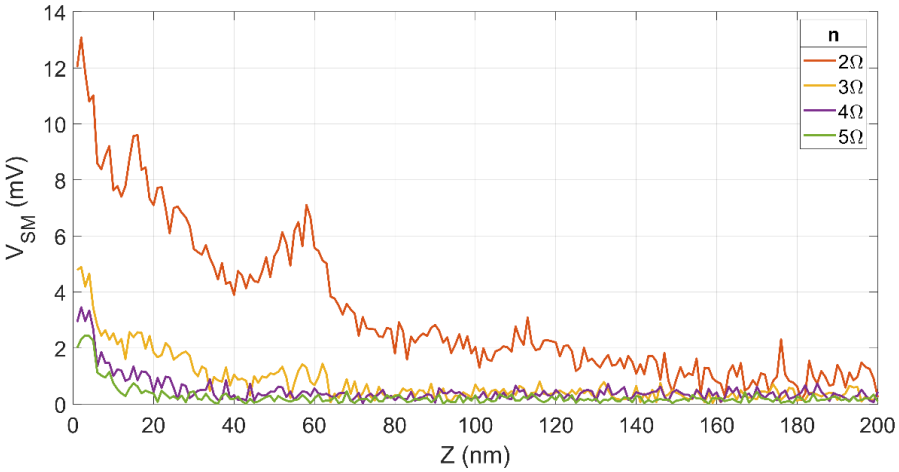

Figure 2.19 – Approach curves for various demodulations of the tip tapping frequency $\Omega \sim 80$ KHz. Tip tapping amplitude $A = 400$ nm and tip size ~ 20 nm.

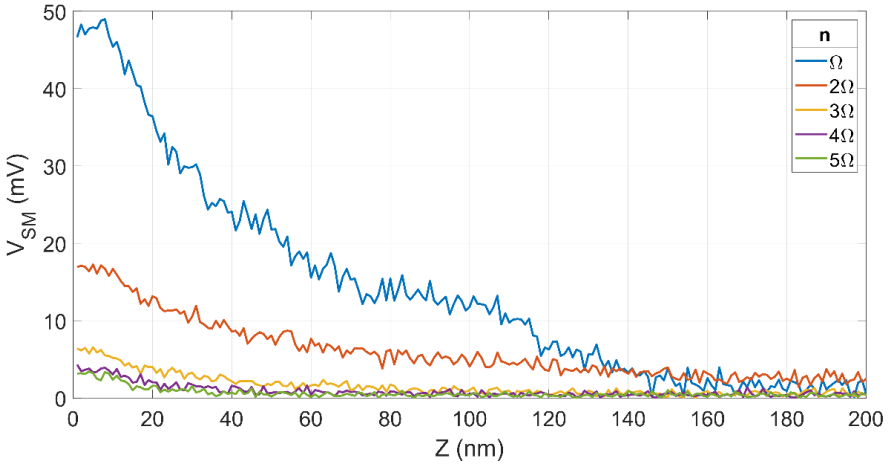

Figure 2.20 – Approach curves for various demodulations of the tip tapping frequency $\Omega \sim 80$ KHz. Tip tapping amplitude $A = 400$ nm and $h = 200$ nm and tip size ~ 500 µm.

It is demonstrated in both Figures 2.19 and 2.20 that the signal amplitude is heavily dependent on z. It can be seen for all cases that the signal amplitude decreases with increasing z, in agreement with the dipole model of the s-SNOM tip/sample interaction presented in Chapter 1 Section 1.6. Additionally, it can be seen that, for large z, the signal

amplitude plateaus. This is due to a constant background signal arising from radiation scattering directly from the probe tip edge and shaft.

It can also be seen from both Figures that at higher harmonics n at which the signal is demodulated, the signal amplitude decreases. This applied to both the near-field interaction and the background signal. In addition, the approach curves for higher n show a sharper drop off with increasing z. This arises from the $\frac{1}{r^3}$ dependence in the effective polarizability of the coupled tip-sample system [13]. This dependence has previously been theorised for small (0.5a) and large (5a) tip tapping amplitudes, where 'a' is the radius of the tip when modelled as a polarisable sphere (Figure 2.21).

Furthermore, it can be observed that for each value of n the approach curves using the large tip exhibit a consistently larger signal than those using the small tip. This is also in agreement with the point-dipole model, which predicts stronger scattering for larger tips. Another tip size-dependent observation is the sharper drop-off in signal amplitude of the approach curves for the smaller tip, which is in agreement with [147], which states that the signal amplitude drop-off occurs on a length scale that approximately corresponds to the tip radius.

2.5.3 Approach curves as a function of tapping amplitude

To mitigate the loss of signal amplitude when demodulating beyond the fundamental harmonic, larger tip tapping amplitudes are commonly used. Figures 2.22 and 2.23 depicts the approach curves obtained using the THz-s-SNOM system described above, for a range of tip tapping amplitudes, demodulated at the $n = 2$ harmonic of the tapping frequency ($\Omega \sim 80$ KHz) using a small and large tip respectively.

As seen in Figures 2.19 and 2.20, it is further demonstrated in Figures 2.22 and 2.23 that the signal amplitudes drops-off as z increases, in agreement with the dipole model, and plateaus beyond a certain value. Furthermore, it can also be observed from both Figures that a larger tapping amplitude results in a larger signal, and also the background signal, present in each measurement, persists for longer for larger tapping amplitudes. This effect is more prominent in Figure 2.23. Additionally, in concurrence with the point-dipole model and the results of Section 2.5.2, the larger scattering efficiency provided by the larger tip produces a greater signal amplitude.

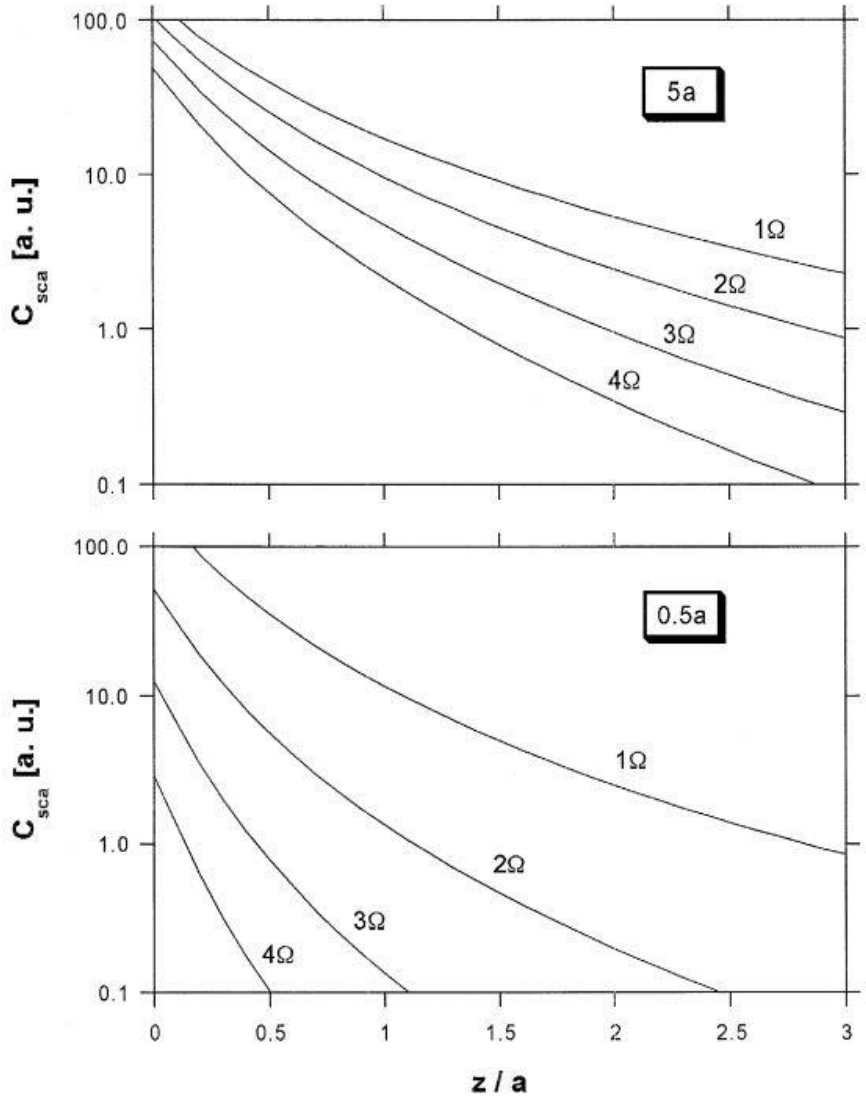

Figure 2.21 – Fourier components of a tip-sample scattering cross-section with minimum tip-sample distance for larger (5a) and small (0.5a) tip oscillation amplitude, where the distance Z measured with respect to the tip radius a. Adapted from [13].

From the results presented in this Section and in Section 2.5.1, it can be concluded that several factors are to be taken into consideration to optimise the s-SNOM imaging criteria. It can be seen that demodulating the V_{SM} signal at higher harmonics of the tip tapping frequency allows for better discrimination against background signals, but also reduces the overall signal amplitude. The signal amplitude can be preserved by using a larger tip tapping amplitude and/or larger tip size but both of these increase the amount of background signal. Furthermore, it is also known and will be demonstrated in Section 2.5.3, that optical contrast and image resolution both decreases for larger tip tapping amplitudes [147], as well as larger tip size.

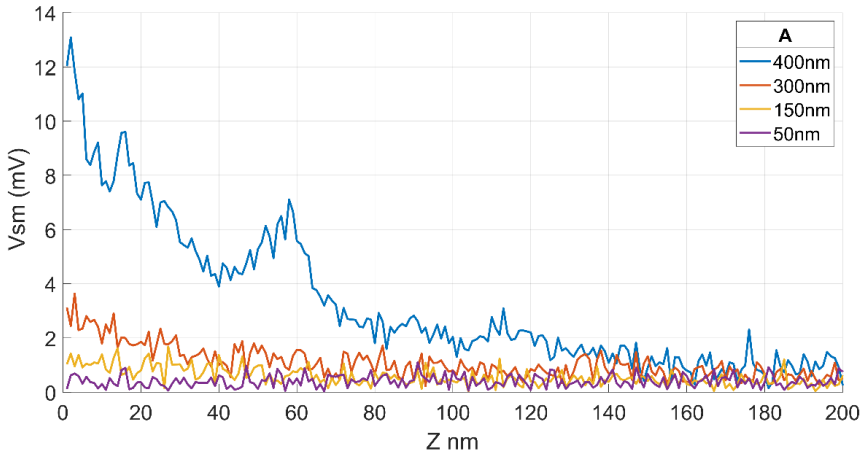

Figure 2.22 – Approach curves for various tip tapping amplitudes, demodulated at the $n = 2$ harmonic of the tip tapping frequency $\Omega \sim 80$ KHz, using a small tip ~ 20 nm.

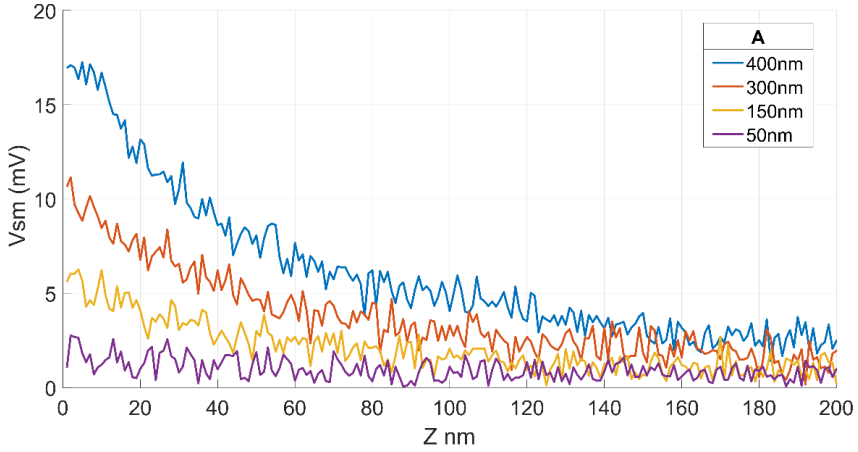

Figure 2.23 – Approach curves for various tip tapping amplitudes, demodulated at the $n = 2$ harmonic of the tip tapping frequency $\Omega \sim 80$ KHz, using a large tip ~ 500 μm.

These conclusions suggest that a compromise between tip size, tapping amplitude and the harmonic at which the signal is demodulated must be made in order to achieve an optimum s-SNOM imaging criterion.

2.5.4 s-SNOM resolution

To evaluate the spatial resolution of the THz-s-SNOM system, several two-dimensional single-frequency images were taken of a resolution target. The target consisted of a simple 50 nm thick gold pattern on a silicon substrate, manufactured via electron-beam lithography (EBL). The microscope resolution was determined from imaging one of the gold/silicon boundaries of the pattern.

To obtain a single-frequency THz image, the QCL output beam is focused onto the oscillating tip apex, which is brought into close confinement to the sample surface. There, the interaction between the tip and surface causes a near-field enhancement of the scattering cross-section that is influenced by the local permittivity of the sample, as described in Chapter 1 Section 1.6. By scanning the sample under the probe over a 2D area of a sample and measuring this near-field enhancement, through lock-in detection of the QCL V_{SM} signal, one can obtain an image in which the signal contrast relates to the sample material composition.

An example of a THz-s-SNOM image taken of a gold/silicon boundary can be seen in Figure 2.24a, from which the resolution analysis of Figure 2.25 was derived. This image was measured using a the same QCL used earlier in Section 2.5, which was operated in CW mode and cooled to a temperature of 20 ± 0.01 K using a L-He continuous flow cryostat, which was maintained by a (Lake Shore 335) temperature controller. The p-polarised output of the QCL was obliquely incident on the 20 nm probe tip apex at an angle of $\sim 54^0$. The probe was operated in tapping mode at a frequency of $\Omega \sim 80$ KHz and peak-to-peak amplitude of 94 nm. The QCL V_{SM} signal was amplified by a factor of $A = 5\text{x}10^3$ by a pre-amp before being demodulated at 3Ω. Figure 2.24 shows a 5 x 1 µm THz and AFM image comprising 120 x 30 pixels captured with the s-SNOM with an integration time of 150 ms per pixel.

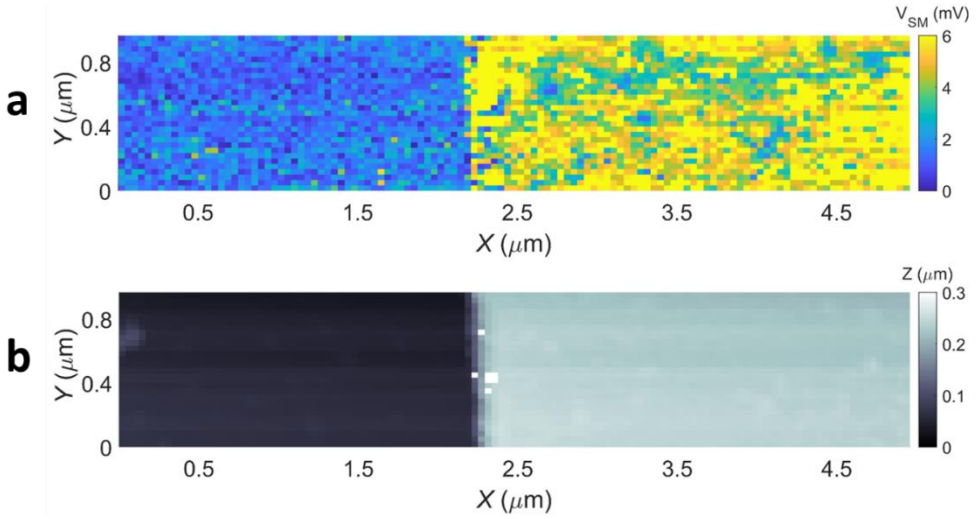

Figure 2.24 – THz-s-SNOM image of a gold/silicon boundary. (a) THz image. (b) AFM image.

As stated previously the most commonly used model to describe the tip/sample interaction is the point-dipole model [99], [148]. This model allows for an accurate

description of the tip/sample interaction but is poor at reproducing features that can appear at the edges of material boundaries, such as those used in the resolution measurements presented here [149]. To better understand the near-field response at a material boundary, the tip geometry must be taken into consideration. Figure 2.25 illustrates the optical interaction between an illuminated s-SNOM tip and metal/dielectric edge for different tip positions. It can be seen that, as well as the expected, strong near-field response between the tip apex and the surface, position (b) results in coupling of the tip shaft with the sample edge and position (c) results in a displacement of the tip from the surface, leading to a reduction in coupling strength. This behaviour gives rise to the anomalous features in the optical response of the boundary, as seen in Figure 2.25. There are also other effects that can spuriously affect the s-SNOM signal near material boundaries. For example, the thickness of the material at its boundary can vary due to imperfections in the sample fabrication process, which could lead to these boundary features. Additionally, a reduction in V_{SM} signal amplitude at the boundary of a sample can be caused by a screening of the tip's near fields by the metal sample, as have been demonstrated in [150].

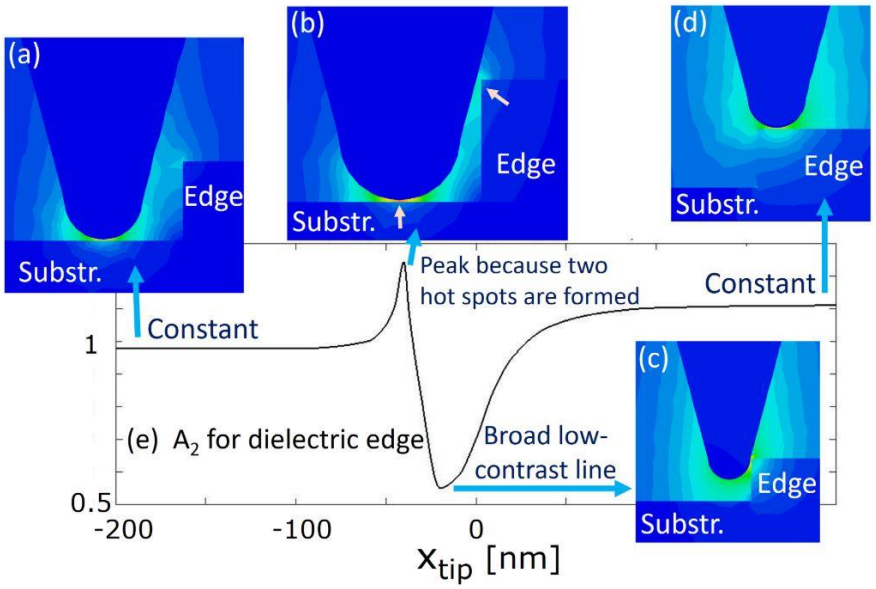

Figure 2.25 – Edge imaging using a s-SNOM showing various tip positions (a)-(d) with respect to a dielectric edge (x_{tip}). (e) line profile of s-SNOM signal demodulated at the 2nd harmonic (A_2). (a) signal arising from a coupling solely with the substrate. (b) enhanced signal arising from a coupling between the tip apex and the substrate and the tip shaft and the edge. (c) signal reduction as the tip is displaced from the substrate resulting in a lower effective polarizability. (d) Coupling between the tip and the edge material surface. Adapted from [14].

An example of these edge features can be seen in Figure 2.26, which shows the V_{SM} signal averaged in the y-direction for a 5 x 1 μm THz-s-SNOM image of a Au/Si boundary. In this case, the image comprised 120 x 30 pixels and was demodulated at the $n = 3$ harmonic of the tip tapping frequency, and the amplitude of which was 154 nm.

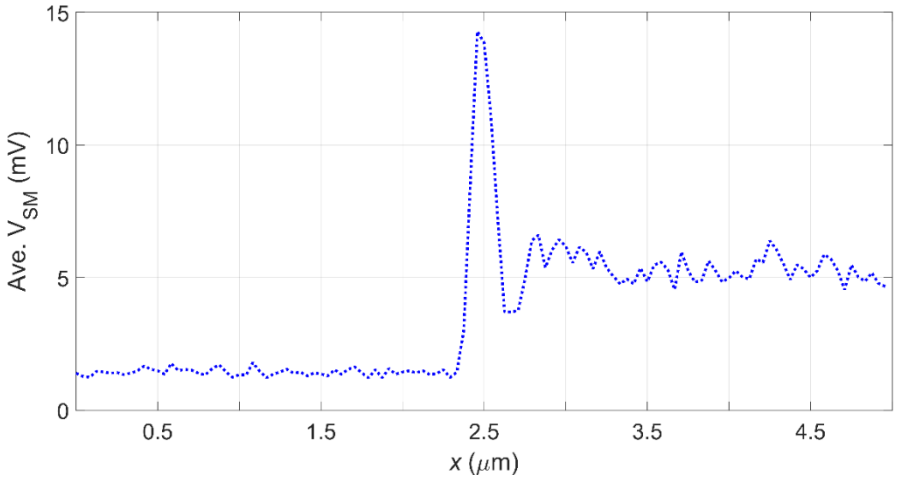

Figure 2.26 – THz-s-SNOM image average in the y-direction showing surface features as a result of tip-edge interaction.

The effects described here depend strongly on the tip geometry, material thickness/ topography and sharpness/shape of the edge regions, which can be affected by the fabrication process. Therefore, to some extent, these features can be mitigated by careful selection of the sample area, as well as choice of tip. These effects have been taken into consideration for the following resolution analysis.

To determine the imaging resolution achieved in the image shown in Figure 2.24, the V_{SM} signal was averaged in the y-direction and an edge response function (ERF) described by Equation 2.25 was fitted.

$$f(x) = \frac{I_0}{2}\left(A + er\left(2\sqrt{\log 2}\right)\right)\frac{(x - x_0)}{w} \qquad 2.25$$

where I_o, A, x_0 and w are fitting parameters associated with various dimensions of the curve, and $er(x)$ is an error function described by,

$$er(x) = \frac{2}{\sqrt{\pi}}\int_0^x e^{-t^2}dt \qquad 2.26$$

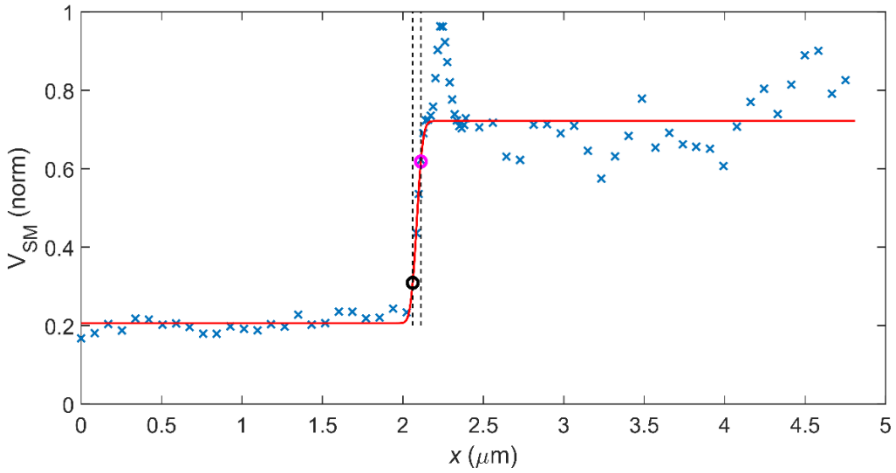

Figure 2.27 – Edge response function applied to the THz-s-SNOM image of Figure 2.24 averaged in the Y-direction. Blue – measured data, red – ERF fit, dotted black – positons of the 20% (black) and 80% (pink) criteria points from which a resolution of 50 nm was determined.

The criteria by which the resolution of the image is calculated is defined by the distance between the 20 % and 80 % height values of the fitted curve, as depicted in Figure 2.27. Using this criteria, a resolution of ~ 50 nm was determined.

It was explained in Section 2.5.2 that signal amplitude but also the background signal both increase for larger tip tapping amplitudes. To investigate the effect of tip tapping amplitude on imaging resolution, the analysis above was repeated for a range of tapping amplitudes between 25 – 125 nm. Figure 2.28 displays the resolutions obtained through ERF analysis of THz images of the same Au/Si boundary acquired using this range of tapping amplitudes. From Figure 2.28, it can be seen that the s-SNOM resolution is heavily dependent on tip tapping amplitude, which agrees with observations reported in the literature [147], [151]. This dependence is explained in [151] by imagining a non-vertically oscillating tip measuring the near-field, non-demodulated signal from a gold disk on a silicon surface, from a fixed height. Were the tip to increase its height above the surface, the spatial resolution would worsen and, thus, the FWHM of the disk would increase. Demodulation of the scattered signal from an oscillating tip can be thought of as a weighted average of images of the disk taken at different heights. Smaller oscillation amplitudes correspond to averaging over lower tip positions and therefore smaller FWHMs.

Furthermore, it can be seen that by using a small enough amplitude ($A \sim 25$ nm), a resolution of 29 nm can be achieved. This corresponds to a sub-wavelength resolution of $\lambda/3000$, which is the highest reported to date for a THz-s-SNOM using a THz QCL.

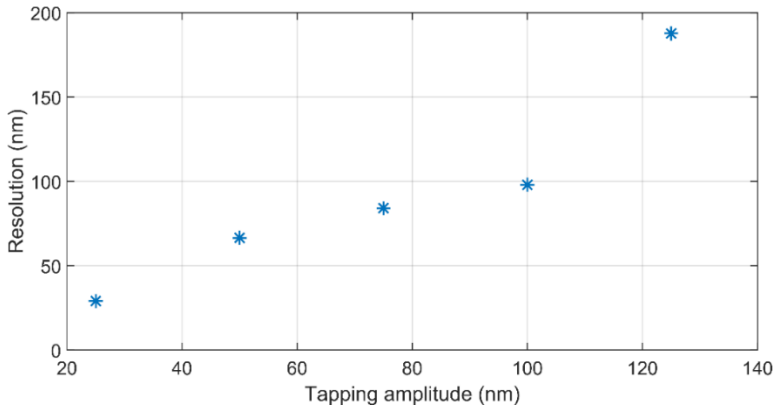

Figure 2.28 – THz-s-SNOM spatial resolution with tapping amplitude using a small tip (~ 20 nm) apex diameter.

As discussed in Section 2.5.3, it can be advantageous to use a large tip to perform s-SNOM measurements, as it can be used to increase the signal amplitude. It is also understood that imaging resolution is dependent on the size of the tip apex [152]. This was investigated by repeating the above analysis using a tip with a larger apex diameter. Figure 2.29 displays the spatial resolutions, calculated using the same ERF analysis as that shown in Figure 2.27, for images taken over a 50 – 150 nm range of tapping amplitudes using a 500 µm tip. Here the same trend as shown in Figure 2.28 is observed, although as expected the use of a larger tip yielded far larger spatial resolutions for each of the tapping amplitudes in the range previously used.

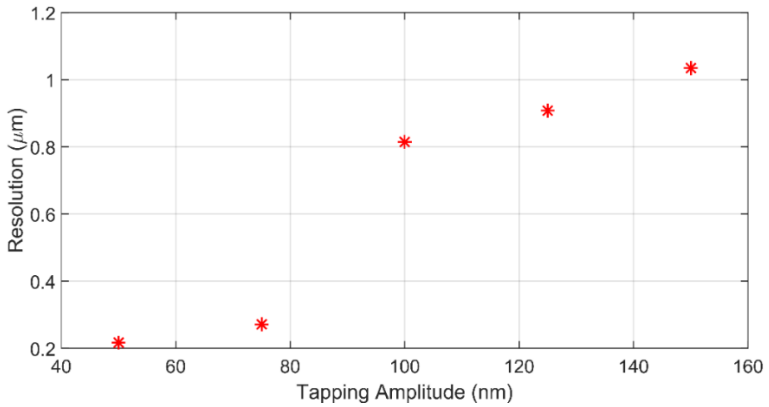

Figure 2.29 – THz-s-SNOM spatial resolution with tapping amplitude using a large tip (~ 1 µm) apex diameter.

2.6 Summary

This chapter has communicated an introduction into THz QCLs and has described the measurement approach/apparatus for measuring the LIV relationship and emission spectra of a QCL. Both the spectral behaviour and the LIV characteristics obtained from an exemplar QCL were presented (Section 2.2), from which parameters such as the laser threshold current density J_{th}, maximum operating temperature T_{max} and peak operating power P_{max} were determined.

The theory and experimental realisation of operating a QCL under optical feedback has also been presented (Section 2.3 and 2.4), including two implementations of interferometric fringe generation via SM. The two methods involve applying a frequency sweep through a modulation of the QCL driving current and mechanically extending the external cavity length. Therein a new approach for measuring frequency tuning with a high resolution based on SM was demonstrated, from which the tuning coefficient of the QCL characterised in Section 2.2 was determined (Section 2.3). These analyses yielded a tuning coefficient in the range of -3.29 – -4.09 MH/mA for the QCL operated in CW mode and at 20 ± 0.01 K.

Experimentally obtained interferometric fringes, generated via mechanical extension of the optical beam path, have been evaluated using the Lang-Kobayashi model, to extract SM parameters such as the feedback parameter C, linewidth enhancement factor α and interferometric fringe amplitude β. By performing this analysis for various driving currents of the QCL, the current-dependence of these parameters has been explored (Section 2.4). Knowledge of this behaviour is important for applications such as that demonstrated in Chapter 3, where the frequency tuning of a QCL under optical feedback is used in a coherent imaging system.

The characterisation of a THz frequency, scattering-type scanning near-field optical microscope has also been undertaken (Section 2.5). This has included a demonstration of background signal reduction through demodulating at harmonics of the tip tapping frequency beyond the fundamental, wherein approach curves using small and large diameter tips have further revealed the effects of both harmonic demodulation, tip tapping amplitude and tip size on the V_{SM} signal and background signal amplitude. Additionally, the spatial resolution of the microscope has been determined via boundary measurements of a simple gold-on-silicon structure, which have demonstrated that a resolution of 29 nm has been achieved. This value's dependency on tip-size has been

further evaluated, as well as a discussion of unwanted image features as a result of tip-edge coupling, an example of which has been experimentally captured.

Following these characterisations, this QCL THz-s-SNOM can now be used to investigate the optical properties of microstructures such as topological insulators (Chapter 4) and THz waveguides (Chapter 5).

Chapter 3

Coherent stepped-frequency THz-s-SNOM

3.1 Introduction

In this Chapter, a novel stepped-frequency system will be fully explored including descriptions of how coherent measurements can be performed using a THz-s-SNOM by exploiting the frequency tuning of a QCL, as seen in Section 2.3, enabling both the magnitude and phase of the scattered field to be resolved. Furthermore, the hardware to enable, and LabVIEW control VI to manage, the image acquisition is described. This system is in contrast to previous coherent measurement techniques, such as that presented in [15], as the primary improvement is that only a single scan of a sample is needed to obtain coherent imaging data. Section 3.2 presents a characterisation of the measurement system including an investigation into the optimal operation speed, the system resolution and methodology used to perform image data acquisition.

The use of this system is demonstrated, in conjunction with a generalised phase-stepping algorithm (GPSA), to coherently measure in the far-field (Section 3.4) and near-field, specifically the out-of-plane field supported by a dipole resonator structure in 1 and 2 dimensions using only a small number of sampling points, the published results of which can be seen in Section 3.5. A characterisation of the GPSA is also included in Section 3.3, with regards to the errors associated with the extraction of magnitude and phase information, from interferometric fringes generated via LFI, for a variety of measurement criteria and combinations thereof.

3.2 System/approach overview

To perform coherent THz measurements, a stepped frequency system employing a 3.45 THz QCL and the THz-s-SNOM system described in Chapter 2 was developed. To extract magnitude and phase information of the scattered THz signal, and thereby characterise the optical response of a target in the THz region, interferometric fringes are generated via laser feedback interferometry (LFI).

As described in Chapter 2 Section 2.3, the generation of interferometric fringes can be achieved by either mechanical extension of the beam path or modulation of the laser emission frequency. The method described here, which uses the latter, exploits the frequency tuning of a QCL with driving current to subject a target to a range (sweep) of emission frequencies afforded by a sequential stepping of the laser driving current, the resulting fringes of which can then be realised in the self-mixing voltage V_{SM}, as seen in Figure 3.1. It was seen in Chapter 2 Section 2.3 that a modulation to the laser frequency can be performed in a continuous manner with the use of a saw-tooth current modulation (*swept-frequency*). However, due to the need to demodulate V_{SM} at the tip tapping frequency Ω, the s-SNOM approach requires a sequential *stepping* of the lasing frequency instead.

Briefly, the coherent imaging system comprises a THz-s-SNOM based on a commercial s-SNOM/AFM platform (neaSNOM, neaspec GmbH) employing a 3.45 THz QCL driven by an Arroyo current driver, a low-noise preamplifier, a Zurich Instruments HF2LI 50 MHz lock-in amplifier and a LabVIEW control VI. To ensure a low value of the feedback parameter C (described further in Section 3.2.1), and therefore encourage the generation of sinusoidal fringes (necessary for applying a fitting model), a non-reflective attenuating material is placed in the laser beam path at the cost of the V_{SM} signal magnitude. For the THz-s-SNOM measurements described further in this chapter, the QCL was cooled using a continuous-flow L-He cryostat that was maintained at a heat sink temperature of 20 ± 0.01 K. The average emission power was ~ 1 mW, and illuminated a vertically aligned Rocky Mountain Pt-Ir s-SNOM tip with a minimum diameter of ~ 20 nm and length of ~ 80 μm, at an angle of ~ 54^0 relative to the surface normal. The incident radiation was p-polarised, so that there was an in-plane and out-of-plane component of the incident field parallel to the tip shaft.

As was the case in Chapter 2, the self-mixing signal is derived from the QCL terminal voltage. Since the scattered field from the tip is very small in s-SNOM, it is necessary to

amplify V_{SM} using a pre-amplifier. Typically, the gain used here and throughout is ~ 5 x 10^3.

To lock to the V_{SM} signal, the AFM tip of the s-SNOM is modulated at a frequency $\Omega \sim 60 – 80$ KHz, harmonics of which are used as the reference frequency for the lock-in. Whereas, previously described in Chapter 2 Section 2.5, the lock-in used to extract V_{SM} was internal to the neaspec system, in this Chapter it is necessary to use an external lock-in (mentioned above) to allow control over the recording and saving of the V_{SM} as the current is stepped.

As described in Section 2.5, whilst suppression of background signals improves at higher harmonics of Ω, the signal amplitude becomes weaker. It is therefore important to select an appropriate demodulation frequency that provides a good compromise between both of these effects, especially when the amplitude has been artificially reduced by the attenuating material. In these experiments, the V_{SM} values are commonly measured at a reference frequency of either 2Ω or 3Ω.

To perform a stepped-frequency measurement at a single position of a target (single pixel), the laser current driver is set to a predetermined starting value I_{start}. There is set delay time T_1 commonly ~ 10 ms, to allow for temperature stabilisation of the QCL. Following that there is a secondary delay T_2 which is usually set to be a multiple of the lock-in time constant T_{LI} and therefore determines the number of T_{LI} that are waited before each V_{SM} value acquisition, to allow for the lock-in signal to 'settle' on the correct value following each change in current. After these delays, a single value of the QCL terminal voltage is then acquired from the lock-in amplifier and stored in a 1D array. I_{start} is then increased by a predetermined increment δI, following which is the delays and further V_{SM} signal acquisition. This is repeated until the driving current reaches I_{end}, at which time the final V_{SM} value is recorded and the current driver is returned to I_{start}.

At the beginning of each experiment, to determine appropriate of I_{start} and I_{end}, a preliminary single-pixel set of stepped-frequency interferometric fringes is acquired over a current range of approximately 200mA (Figure 3.1). From this set, the current values corresponding to the consecutive peaks of a suitable fringe are chosen as I_{start} and I_{end}.

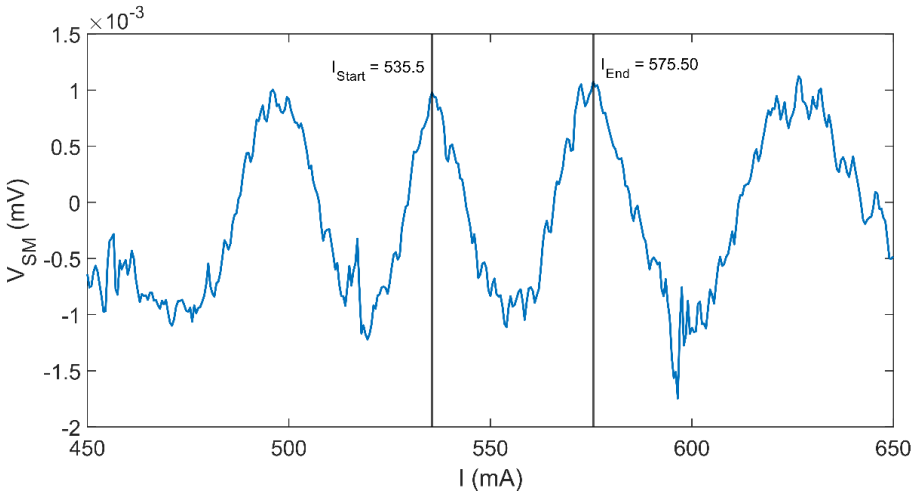

Figure 3.1 – A set of THz self-mixing interferometric fringes generated via a swept-frequency measurement with a current sweep of 200mA. This measurement was performed using the THz-s-SNOM system in conjunction with the hardware and control system described in this Chapter. Additionally show is a bounded area corresponding to a single fringe with example I_{start} and I_{end} values. The lock-in reference signal for this measurement was demodulated at 3Ω.

From these values, the current step δI can be determined from, $\delta I = \frac{I_{end} - I_{start}}{N}$ where N is the number of sampling points per pixel, the significance of which will be further investigated in Section 3.3.1

To perform a series of stepped-frequency measurements over a 1D line on a target, the coordinates of the first pixel to be measured are determined as well as the distance over which the measurement will be made. The acquisition of V_{SM} at each of the pixels is controlled by the LabVIEW VI which monitors the line and pixel clocks of the s-SNOM. These clocks measure the movement of the AFM tip along the x-axis (pixel clock) and y-axis (line clock) of the sample. Prior to initiating the movement of the s-SNOM tip to the first pixel, the LabVIEW VI is run to anticipate the triggering of the pixel clock at the said pixel, followed by acquisition of the N V_{SM} values. Figure 3.2 depicts the process by which the system performs a 1D measurement. To perform a 2D scan, this 1D process is repeated for every triggering of the line clock.

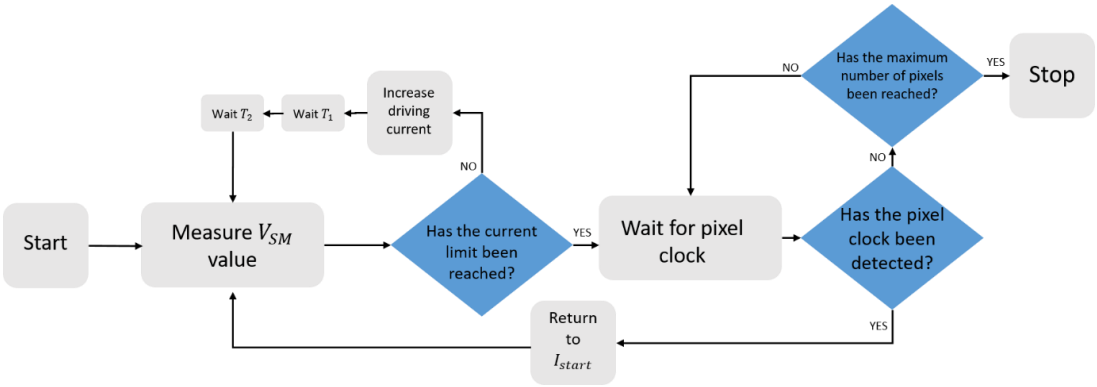

Figure 3.2 – A flow chart depicting the process by which the THz-s-SNOM system captures a 1D stepped-frequency image. This diagram specifically pertains to the operation of the LabVIEW virtual instrument that is used to control the measurement apparatus.

3.2.1 LabVIEW and hardware

The LabVIEW control VI comprises several sub VIs (Figure 3.3), each of which sequentially perform the tasks described in Figure 3.2. Among them includes: initialisation and addressing of the data acquisition system hardware; monitoring of the line and pixel clocks; triggering the synchronisation of stepping the QCL current controlled by an Arroyo current driver; V_{SM} data recording via a Zurich Instruments fast-detection lock-in amplifier; saving of V_{SM} values; and deactivation of the program.

3.2.2 Data acquisition program speed

To characterise the limitations of the acquisition rate of the data acquisition system, a simple 10 x 10 pixel single-frequency image of a simple gold-on-silicon structure was taken using THz-s-SNOM, whilst the LabVIEW data acquisition VI recorded one V_{SM} value per pixel. Following the measurement, the number of pixels that the program failed to acquire were counted.

For the system to capture all N of the V_{SM} values per pixel, the scanning time T_{scan}, defined as the time period over which the s-SNOM AFM tip remains on each pixel, must be greater than the total time that it takes the acquisition program to acquire each V_{SM} value, format the data and save it to a 1-dimensional array. If T_{scan} is too small, then the program will still be measuring the N V_{SM} data point when the next pixel clock occurs, and will therefore miss the next pixel clock value and subsequently the next pixel of data. In this sense, the results present in Figure 3.4 are characterising the fastest speed at which the programme can acquire data.

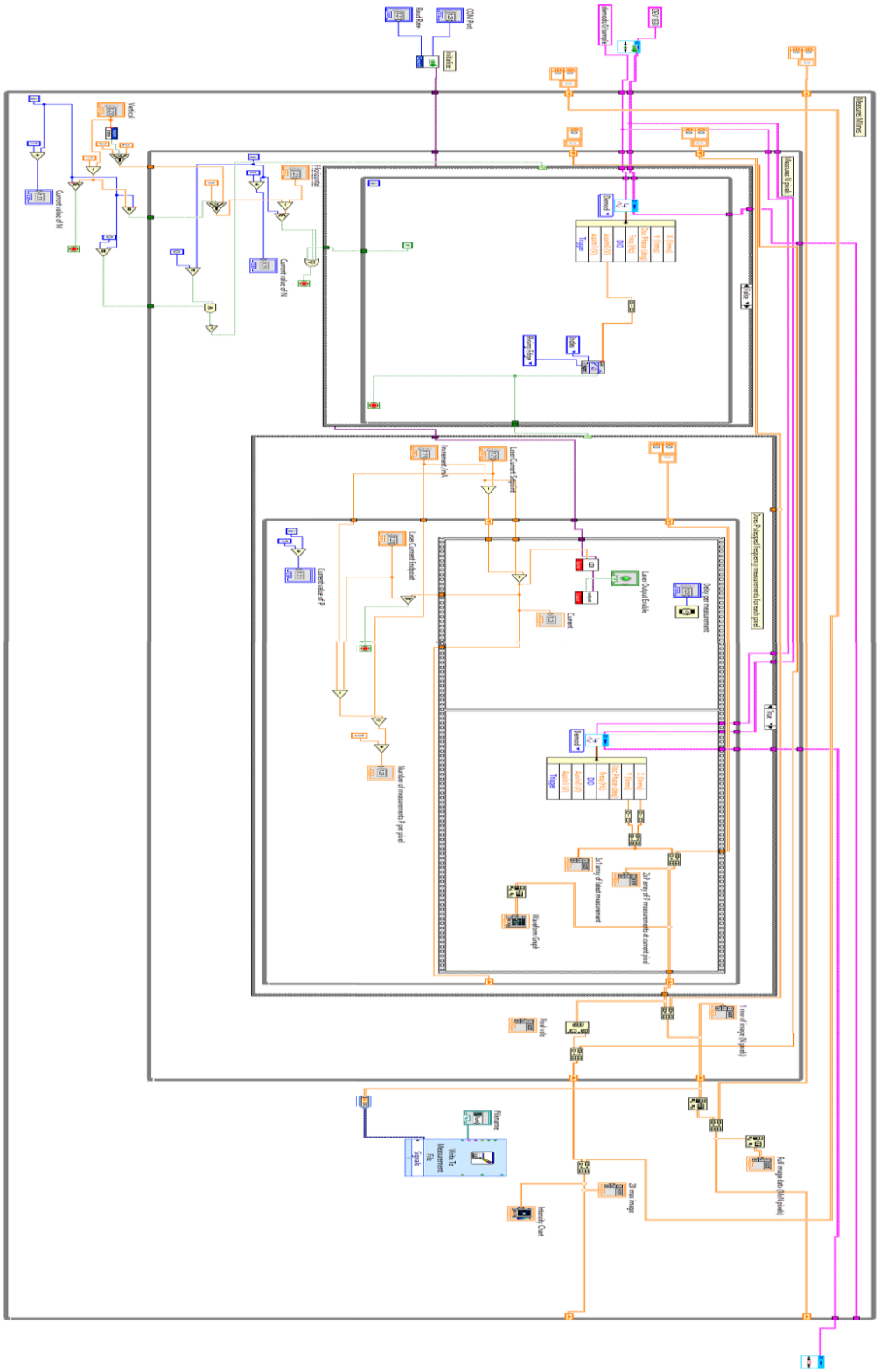

Figure 3.3 – LabVIEW virtual instrument block diagram for control of the data acquisition system.

This was repeated for a series of images using a range of scanning times $T_{scan} = 50 - 300$ ms. For each scan, the delay $T_2 = 2T_{LI}$, where T_{LI} was set to 50 ms. Figure 3.4 shows how the ability of the acquisition program to capture more of the image changes with the scanning time of the s-SNOM.

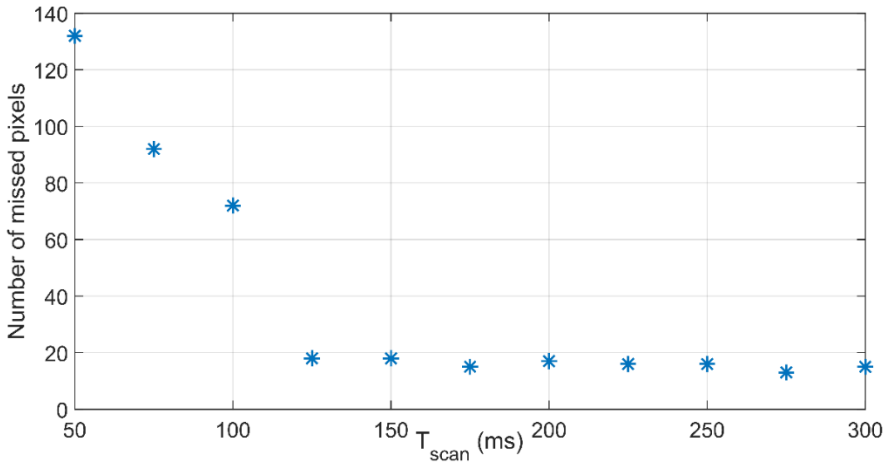

Figure 3.4 – Number of unrecorded pixels vs microscope integration time for an image captured with a THz-s-SNOM using the data acquisition system. The image in question was a 10x10 pixel scan of a 15x2um gold-on-silicon structure. The lock-in reference signal for these measurements was demodulated at 3Ω.

For a standard single-frequency image, the s-SNOM is operated in AFM mode. This type of scan causes the s-SNOM to only measure in one direction along the sample, and then return along the same path to the beginning of a row before measuring the next. However, the pixel clock remains counting during the return journey of the tip, and therefore still triggers the recording of V_{SM} values by the acquisition program. For a 10 x 10 pixel scan there are therefore 200 pixels available for the program to capture. The pixels recorded during the return journey of the tip would usually be omitted from images, however, they were included here for convenience.

It is evident by Figure 3.4 that the ability of the acquisition program to capture more of the image data initially improves with increasing scanning time, but plateaus at approximately 125 ms. This value can therefore be described as the fastest acquisition time at which the program can be run, under these sampling conditions, that maximises efficiency whilst not being unnecessarily slow. This is an important factor to consider when performing multi-frequency imaging, as described in Section 3.3.

It can be seen from Figure 3.4 that even when T_{scan} is large enough to give ample time for the acquisition program to capture the data of each pixel, it still fails to acquire ~ 20

pixels. This is due to an absence of the pixel clock for the last pixel of each row and, therefore, results in the last pixel of each row being omitted from the image. Were the program to be improved upon, this feature is something that could be considered.

3.2.3 Data acquisition program resolution

To further assess the timing variables of the data acquisition program, the relationship between the lock-in time constant T_{LI} and delay T_2 is investigated. To do this, the resolution of the imaging system was evaluated for a range of different values of T_2 according to $T_2 = nT_{LI}$, where $n = 0.5 - 3$ and T_{LI} was kept at a constant value of 100 ms. For these measurements, the s-SNOM scanning time was maintained a $T_{scan} = T_2$.

The resolution of the system was determined in a manner similar to that seen in Chapter 2 Section 2.5. A high resolution image of a Au/Si boundary was acquired by the s-SNOM, with dimensions 100 nm x 400 nm and a pixel size of 10 nm, whilst the acquisition program recorded one V_{SM} value per pixel. As explained in Chapter 2 Section 2.5, the resolution of a THz-s-SNOM image is dependent on the size of the AFM tip and the magnitude at which it is tapped during a scan. Therefore, to achieve a high resolution with this system, each measurement was performed using a small AFM tip with radius 20 nm, which was operated at a tapping amplitude of 200 nm. The collected data was processed into a 2D field-map, an example of which is shown in Figure 3.5. An edge response function, described by Equation 2.25, was then calculated as shown in Figure 3.6. As described previously, using this model the resolution is determined by the distance between the 20% and 80% height positions on the width of the boundary region. Figure 3.7 plots these values for images taken over a range of T_2 values. This analysis was performed for a series of images of the same Au/Si boundary, for each value of T_2.

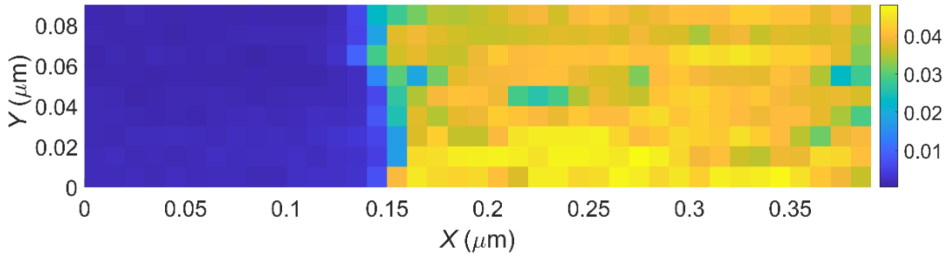

Figure 3.5 – Single frequency THz-s-SNOM image of a Au/Si boundary captured using the data acquisition system described above. The colour bar represents the magnitude of the V_{SM} (mV). This image was captured with a microscope integration time of 300ms and the V_{SM} signal was demodulated at the third harmonic of the tapping frequency.

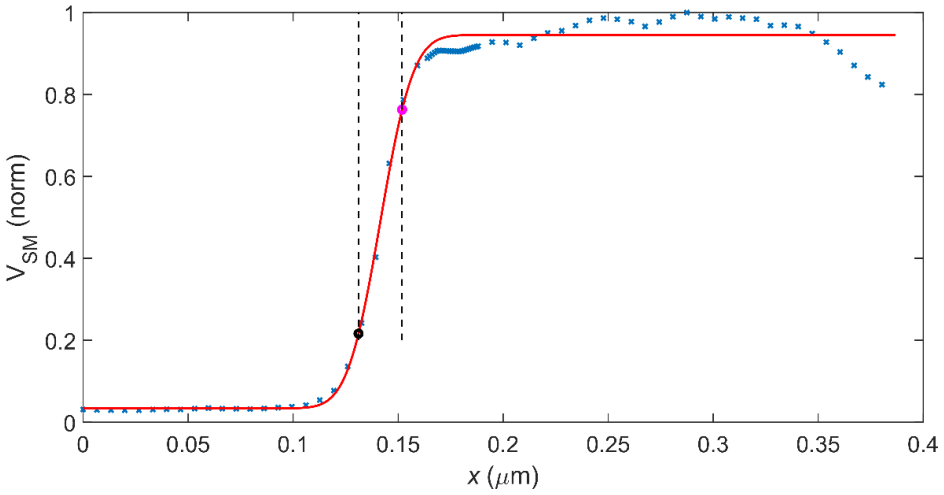

Figure 3.6 – ERF according to Equation 2.25 (red) fitted to a plot of the normalised V_{SM} signal of Figure 3.5 averaged in the y-direction (blue). The width of the curve is highlighted (black dashed) on which is the 20% (black) and 80% (pink) width markers.

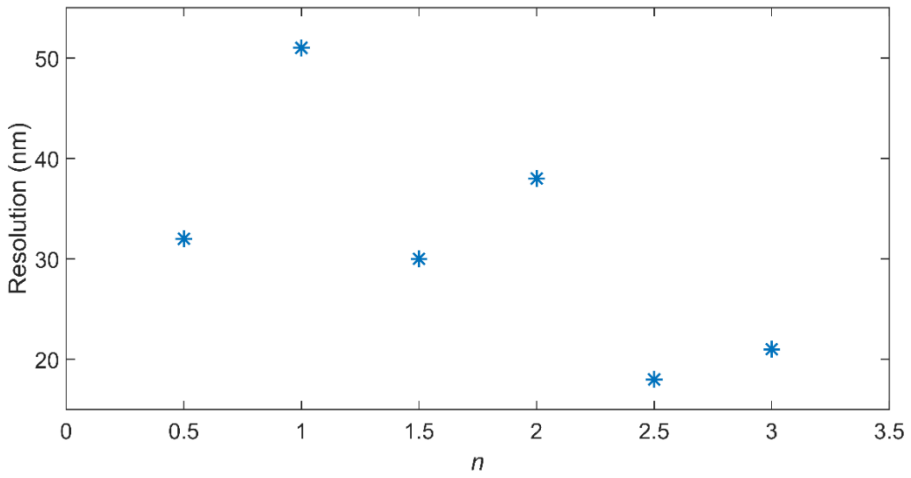

Figure 3.7 – s-SNOM resolution for various values of T_2. Each data point has been extracted from the ERF edge response function analysis, an example of which can be seen in Figure 3.6.

It can be seen that the resolution achieved by the acquisition program for an s-SNOM integration time of 50ms (n=1) is counter-intuitively high compare to that achieved for longer integration times. This result is believed to be an irregularity as the results of that seen in Figure 3.4 suggest that when operated at an integration time of 50 ms the acquisition program fails to capture most of the image. It is therefore assumed that the

results of the edge response function when applied to such a poor quality image are unreliable.

By omitting this anomaly, it can be seen that the resolution of the system improves as T_2 becomes larger with respect to T_{LI}. This is because, if T_2 is too short, then the lock-in does not have enough time to settle of a new V_{SM} value. In this case, the signal value at the current pixel will be affected by the signal value at the previous pixel, which manifests as a degradation of resolution.

From the analyses presented in Section 3.2.2 and 3.2.3, it can be concluded that a compromise is to be made between the values of T_{scan}, T_{LI} and T_2. T_{scan} must be adequately long, for a given value of T_2, to allow for the acquisition of the V_{SM} data from each pixel and T_2 must be sufficiently greater than T_{LI} to ensure that there is no 'blurring' of the data between pixels. However, these values must be small enough so to not result in an unnecessarily long total measurement time, which becomes an important factor to consider for greater N values taken over a large pixel area, as shown in Section 3.5.

To this end, the measurements presented in the remainder of this Chapter use values of $T_2 = 2T_{LI}$, where T_{LI} is usually set to be 200 ms and T_{scan} is adjusted depending on the N value.

3.3 Stepped-frequency imaging using a generalised phase-stepping algorithm

One limitation of LFI in both far- and near-field implementations stems from the need to acquire full interferometric signals for reliable extraction of amplitude and phase information from a target. This is most commonly achieved by mechanical extension of the optical beam path [75], [153], which results in slow data acquisition. Alternatively, interferometric fringes can be acquired by fast electronic modulation of the laser emission frequency [73], [126]. However, modulation rates may then be restricted by the available sampling and signal processing bandwidth [154]. These issues are compounded further by the challenge of detecting a typically small SM voltage perturbation superimposed on a large quiescent signal, which demands long integration times to achieve high signal-to-noise ratios. This is particularly applicable in THz-s-SNOM in which the scattering efficiently of the nanometric probe scales approximately as $\sim \lambda^{-4}$ and is therefore extremely low at THz frequencies. One means to address these

challenges that has been implemented for phase-shifting interferometry at visible and near-infrared wavelengths [155], enabling applications including digital holography [156], [157] and optical coherence tomography [158], [159], is through reduced optical sampling of the interferometric signals. However the adoption of this approach in LFI is non-trivial owing to the non-sinusoidal nature of the interferometric signals, which are dependent on the strength of optical feedback as well as operating parameters of the laser.

This section refers to work undertaken to produce an improved method of coherent sensing through the use of a generalised phase-stepping algorithm (GPSA) to extract magnitude and phase data from interferometric fringes acquired by laser feedback interferometry (LFI).

The following will include a characterisation of the GPSA using simulated data and its applicability under different levels of optical feedback, lasing parameters and sampling conditions. Additionally, the stepped-frequency interferometric fringe generation system, based on that discussed in Section 3.2, will be demonstrated in the far-field and near-field regime. Its use in conjunction with the GPSA will be shown to enable coherent imaging of the out-of-plane field supported by an individual micro-resonator at THz frequencies, in 1 and 2 dimensions. Furthermore, it will be demonstrated how fully coherent sensing can be reliably achieved with as little as 4 sampling points per imaging pixel, opening up opportunities for fast coherent sensing not only at THz frequencies but across the visible and infra-red spectrum.

3.3.1 Characterisation of the GPSA

In reiteration of Chapter 2 Section 2.3, a modification to the laser carrier population that is responsible for the V_{SM} signal in a QCL under optical feedback also induces a perturbation to the laser frequency ν. This effect is encapsulated through the transcendental excess phase equation (Equation 2.3), which relates the round-trip phase under feedback ϕ_L to the phase calculated for the unperturbed frequency of the solitary laser ν_0.

$$\phi_{L,0} = \frac{4\pi L_{\text{ext}} \nu_0}{c} \tag{3.1}$$

As a result the shape and form of the interferometric fringes described by Equation 2.21 are inherently dependent on the strength of optical feedback, quantified by the feedback parameter C, as well as the linewidth enhancement factor of the laser α. Nevertheless, in the limit of weak feedback ($C < 1$) the perturbed laser frequency is approximately equal

to that of the solitary laser, $\nu \approx \nu_0$, such that $\phi_L \approx \phi_{L,0}$. In this case the SM voltage signal closely follows a cosinusoidal dependence on $\phi_{L,0}$ as,

$$V_{\mathrm{SM}} \approx \beta \cos(\phi_{L,0} - \phi) \tag{3.2}$$

in which ϕ represents the phase response of the target. Crucially, under these conditions, the interferometric fringes encoded within the SM voltage can be reduced to a close approximation by a series of discrete voltage measurements $V_{\mathrm{SM},i}$, where $i = 0 \rightarrow (N - 1)$, taken at $N > 3$ arbitrary but known phase points $\phi_{L,s} = \phi_i$ equally spaced over a single interferometric fringe. Estimates of the true magnitude β and phase ϕ may then be extracted from the N voltage measurements by applying a generalised phase-stepping algorithm (GPSA) based on a least-squares regression. This algorithm has been adopted previously for phase-shifting interferometry at visible/infrared wavelengths [155].

The GPSA models the self-mixing voltage signal as a series of N discrete voltages $\mathrm{V}_{\mathrm{SM},i}$ measured at phase points ϕ_i, where $i = 0, 1 \ldots N - 1$, according to,

$$\mathrm{V}_{\mathrm{SM},i} = a_0 + \beta_m \cos(\phi_i - \phi) = a_0 + a_1 \cos\phi_i + a_2 \sin\phi_i \tag{3.3}$$

in which a_0 is a constant voltage offset, $a_1 = \beta_m \cos\phi_m$, and $a_2 = \beta_m \sin\phi_m$.

To solve for a_0, a_1 and a_2 according to the least-squares method we use the matrix equation

$$\boldsymbol{A}(\boldsymbol{\phi_i})\boldsymbol{a} = \boldsymbol{b}(\boldsymbol{\phi_i}) \tag{3.4}$$

where,

$$\boldsymbol{A}(\boldsymbol{\phi_i}) = \begin{bmatrix} N & \sum_{i=0}^{N-1} \cos\phi_i & \sum_{i=0}^{N-1} \sin\phi_i \\ \sum_{i=0}^{N-1} \cos\phi_i & \sum_{i=0}^{N-1} \cos^2\phi_i & \sum_{i=0}^{N-1} \cos\phi_i \sin\phi_i \\ \sum_{i=0}^{N-1} \sin\phi_i & \sum_{i=0}^{N-1} \cos\phi_i \sin\phi_i & \sum_{i=0}^{N-1} \sin^2\phi_i \end{bmatrix} \tag{3.5}$$

$$\boldsymbol{a} = \begin{pmatrix} a_0 \\ a_1 \\ a_2 \end{pmatrix} \tag{3.6}$$

and,

$$\boldsymbol{b}(\boldsymbol{\phi_i}) = \begin{bmatrix} \sum_{i=0}^{N-1} V_{SM,i} \\ \sum_{i=0}^{N-1} V_{SM,i} \cos\phi_i \\ \sum_{i=0}^{N-1} V_{SM,i} \sin\phi_i \end{bmatrix} \tag{3.7}$$

If $\boldsymbol{A}$ is not ill-conditioned, then we obtain,

$$\boldsymbol{a} = \boldsymbol{A^{-1}}(\boldsymbol{\phi_i})\boldsymbol{b}(\boldsymbol{\phi_i}) \tag{3.8}$$

The magnitude β_m and phase ϕ_m of the V_{SM} signal can then be obtained from the relations

$$\beta_m = \sqrt{a_1^2 + a_2^2} \tag{3.9}$$

and,

$$\phi_m = \tan^{-1}\frac{a_2}{a_1} \tag{3.10}$$

As will be shown, the accuracy of β_m and ϕ_m extracted through this approach depends not only on the chosen value of N but also the phase response of the target itself, as well as the feedback parameter C and linewidth enhancement factor α, both of which influence the shape of the interferometric fringes encoded in the laser voltage.

Figure 3.8a illustrates the percentage error in the fringe magnitude extracted using the GPSA, according to Equation 3.11, in the limit $N \to \infty$ when applied to a numerically synthesised SM voltage signal described by Equation 2.8, for varying combinations of C and α.

$$e_A = \left(\frac{\beta_m - \beta}{\beta}\right) \times 100 \tag{3.11}$$

Figure 3.8b similarly shows the absolute error in determination of the target phase,

$$e_\phi = \phi_m - \phi \tag{3.12}$$

To generate the data in Figures 3.8, a V_{SM} signal was synthesised for a particular combination of C and α with a magnitude and phase chosen to be $\beta = 1$ mV and $\phi = 0$ rad using Equation 1.4. This is done for a large N ($\sim 100{,}000$) phase points equally spaced over 1 fringe as $\phi_i = 2\pi \frac{i}{(N-1)}$. The matrices $A(\phi_i)$ and $b(\phi_i)$ are then calculated from Equations 3.5 and 3.7 respectively, following which, the vector a is determined from Equation 3.8. Using a, the values β_m and ϕ_m are calculated from Equations 3.9 and 3.10 respectively and finally the errors e_A and e_ϕ can be obtained from Equations 3.11 and 3.12. This process was repeated for combinations of C and α for ranges $C = 0$ – 1 and $\alpha =$ -2 – 2, as show in Figure 3.8.

In this limit of large N both e_A and e_ϕ depend solely on the parameters C and α; these error values represent the fundamental limits of the GPSA approach imposed by the deviation of V_{SM} from a purely cosinusoidal function. As expected, for extremely weak feedback ($C <$0.1), for which V_{SM} closely approximates a cosinusoidal dependence on $\phi_{L,0}$, the errors are small with $e_A < 0.4\%$ and $e_\phi < 0.08°$. Even with $C =$0.5, which is typical for many LFI systems employing THz QCLs, e_A remains below 10% and e_ϕ below 2° according to Figure 3.8, which may be considered acceptable for many applications. Indeed, the phase noise associated with frequency instability due to thermal drift of the laser source can often exceed this value[75], [126]. For stronger feedback with 0.5< $C <$1, however, the GPSA performs poorly with e_A exceeding 30% in cases although with e_ϕ still remaining below 9°.

A major benefit of this approach for determining magnitude and phase parameters in LFI is that, under weak levels of feedback, the GPSA remains robust even for small values of N. Outside the limit of large N, however, the magnitude and phase errors are also dependent on the phase response of the target ϕ. Equivalently this dependence can be viewed as originating from the choice of phase points ϕ_i (and hence the choice of $(\phi_{L,0} - \phi)$) at which the V_{SM} signal is sampled, which becomes more critical as the signal departs further from a cosinusoidal dependence on $\phi_{L,0}$. This effect is illustrated in Figure 3.9, which shows an exemplar synthesised V_{SM} signal along with three possible sets of ϕ_i, each with differing values of $\phi_{i=0}$, for the case $N = 4$. Also shown are the corresponding functions $V_{\mathrm{SM,m}} = \beta_m \cos(\phi_{L,0} - \phi_m)$ determined by applying the GPSA approach described above to each of these sets, revealing the variation in the extracted values of β_m and ϕ_m.

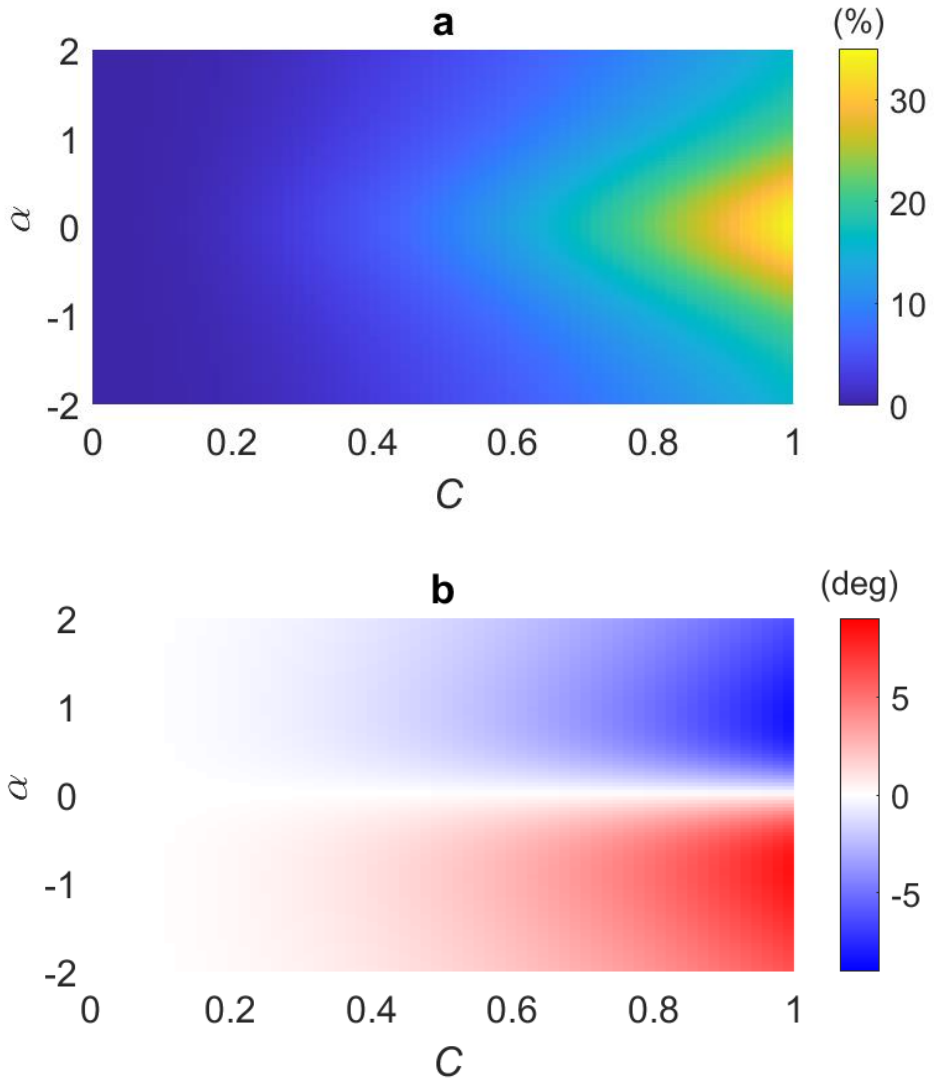

Figure 3.8 – (a) Percentage error in the extracted amplitude and (b) absolute error in the extracted phase of LFI fringes, extracted using the GDRA in the limit $N \to \infty$, shown as a function of feedback parameter C and linewidth enhancement factor of the laser α.

This variation in β_m and ϕ_m is further illustrated in Figures 3.10a and 3.10b, which show typical examples of how the error values e_A and e_ϕ vary with the phase response of the target ϕ, for the case in which ϕ_i is arbitrarily fixed with $\phi_{i=0} = 2\pi m$. Both β_m and ϕ_m (and hence e_A and e_ϕ) are seen to vary with a periodicity $2\pi/N$ and with a magnitude that decreases significantly with increasing N. The former of these observations is particularly relevant to the typical experimental situation in which the value of ϕ (and therefore $(\phi_{L,0} - \phi)$) is not known. To capture this effect quantitatively, the *maximum* magnitude error (Equation 3.13), and *maximum* phase error (Equation 3.14) that can be attained within the range $\phi = 0 \to 2\pi$ respectively, are defined as,

$$e_{A,\max} = \max\{|e_A|\} \quad 3.13$$

$$e_{\phi,\max} = \max\{|e_\phi|\} \quad 3.14$$

In the case for Figure 3.10, $e_{A,\max}$ is determined to be 6.6 % (shown by the dotted line) and $e_{\phi,\max}$ is determined to be 1.7^0 for $N = 4$. With a larger value of $N = 8$, these values decrease to $e_{A,\max}$ = 3.38 % and $e_{\phi,\max} = 0.011^0$.

Figure 3.11a shows how the value of $e_{A,\max}$ varies with the number of measurement points N, for different levels of feedback and assuming α =0. The variation of $e_{\phi,\max}$ is similarly shown in Figure 3.11b. As expected, in the limit of large N the values of $e_{A,\max}$ and $e_{\phi,\max}$ tend towards those reported in Figures 3.8a and 3.8b. Crucially, however, it can be seen that for extremely weak feedback ($C \leq 0.1$) small maximum error values are achieved for all values of N >3; in the case $C = 0.1$, $e_{A.\max}$ remains less than 1% and $e_{\phi,\max}$ below 1° even down to N =4. Moreover, $e_{\phi,\max}$ remains below 1° for all $C \leq 1$ with N =8.

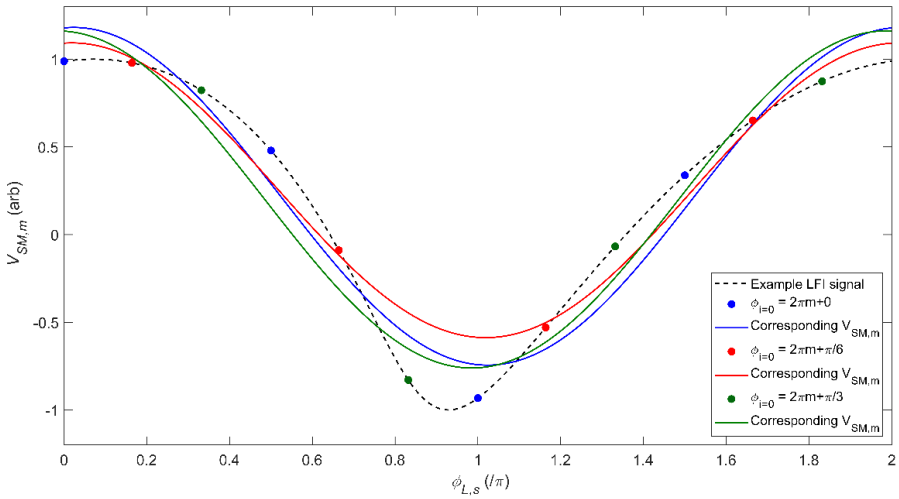

Figure 3.9 – Synthesised LFI signal with $C = 0.5$, $\alpha = 0.5$, amplitude β =1 and phase ϕ =0 (black dashed line) along with the SM voltages $V_{SM,i}$ sampled in three exemplar sets of $N = 4$ equally spaced phase points $\phi_{L,0} = \phi_i$ (with $i = 0 \rightarrow 3$) with $\phi_{i=0} = 2\pi m + 0$ (blue circles), $2\pi m + \pi/6$ (red circles) and $2\pi m + \pi/3$ (green circles). Also shown (coloured solid lines) are the corresponding functions $V_{SM,m} = \beta_m \cos(\phi_{L,0} - \phi_m)$ plotted using the values of β_m and ϕ_m determined from the GDRA applied to each set of ϕ_i.

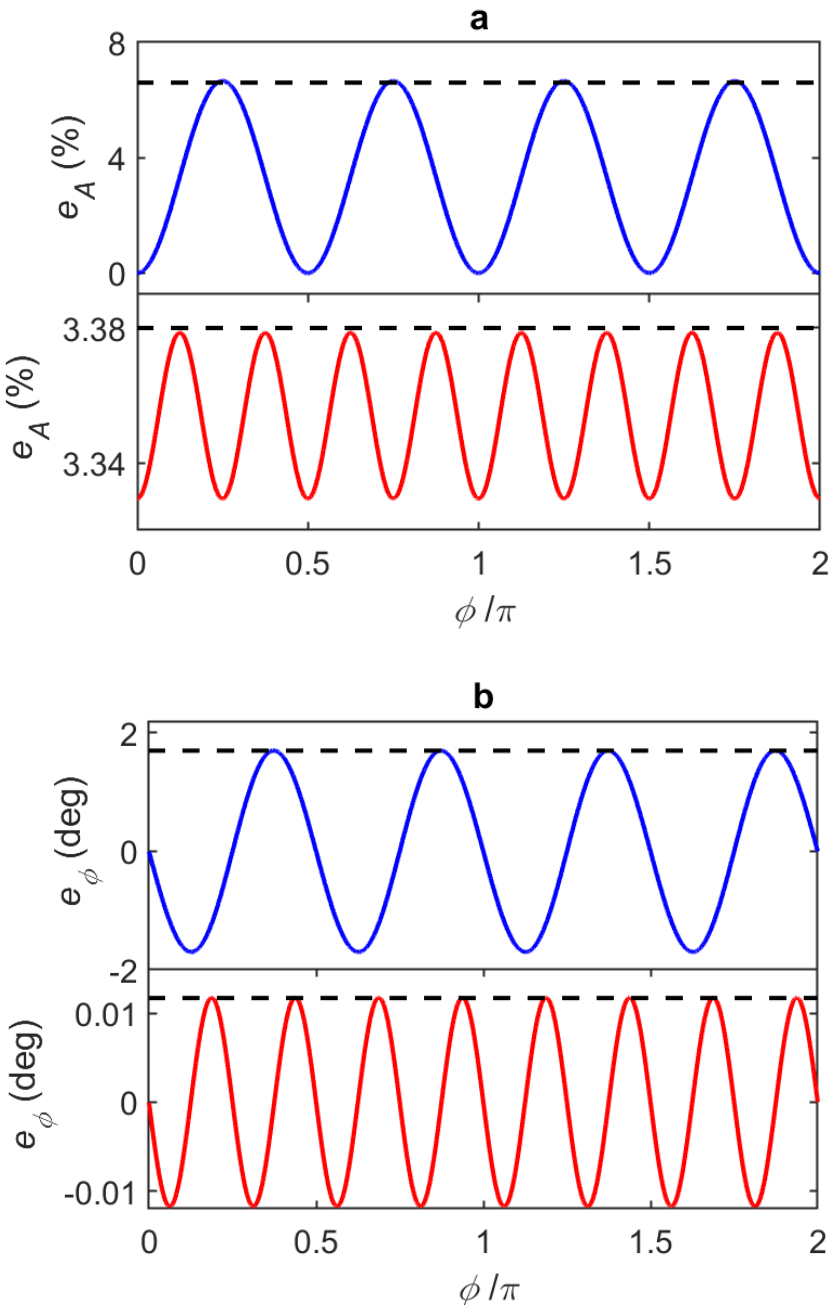

Figure 3.10 – (a) Variation of the amplitude error as a function of the phase response of the target, ϕ, for exemplar cases in which $N = 4$ (top panel) and $N = 8$ (bottom panel). The corresponding maximum amplitude errors are $e_{A,max} = 6.6\%$ and 3.38%, respectively, as shown by the horizontal dashed lines. (b) Variation of the phase error for the same N as (a). The corresponding maximum phase errors are $e_{\phi,max} = 1.7°$ and 0.011°, respectively, as shown by the horizontal dashed lines.

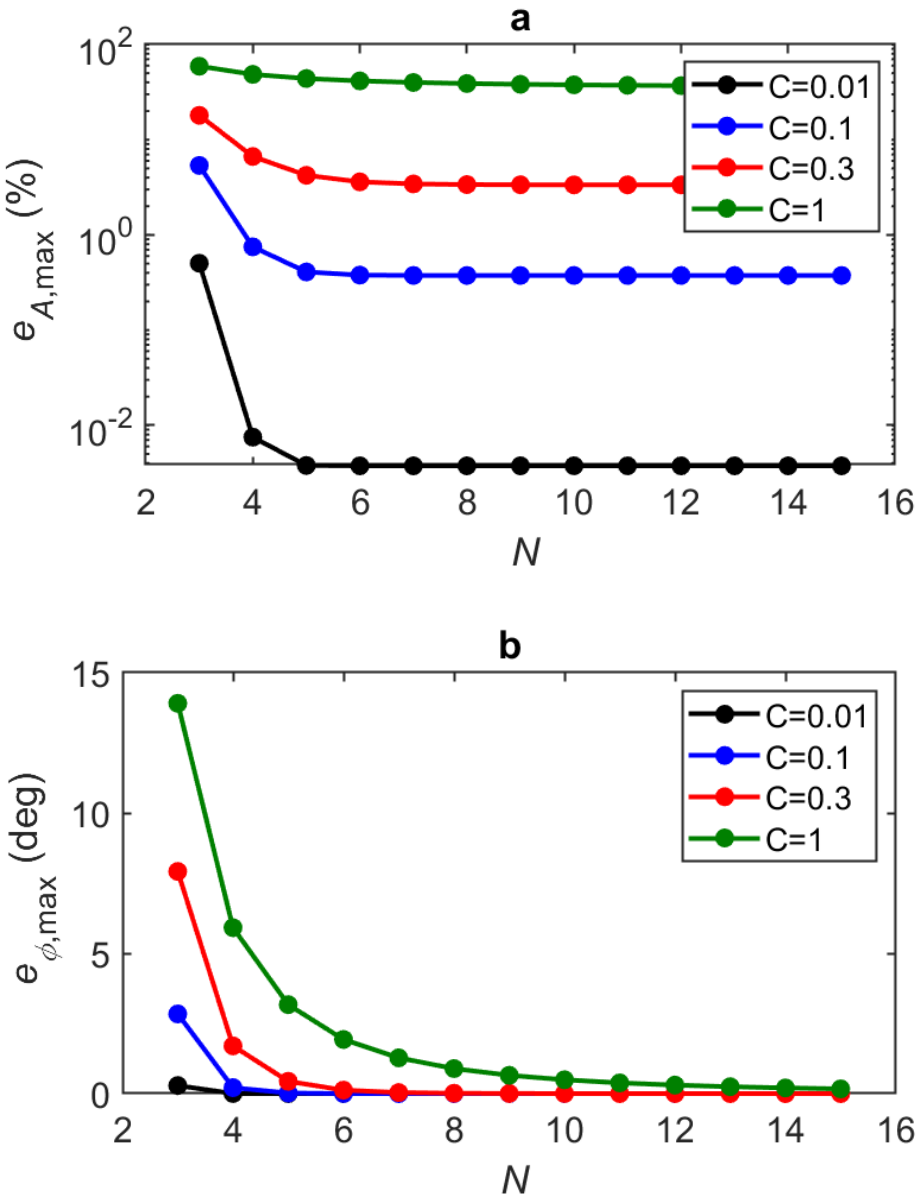

Figure 3.11 – (a) Variation of the maximum amplitude error with the number of measurement points N, for feedback parameters C =0.01 (black circles), C =0.1 (blue circles), C =0.3 (red circles) and C =1 (green circles). (b) Variation of the maximum phase error for the same values of C. The solid lines are intended only to aid visualisation.

Although small values of α in the range ~ −0.1 to ~ 0.5 are typical for THz QCLs based on a bound-to-continuum active region design [64], [145], significantly larger values have been reported [153], [160], [161] for active regions with phonon-assisted electron injection such as that employed in this work. Such values of α are known to impose notable asymmetry on the interferometric fringes observed in LFI, which in turn results in larger values of $e_{\phi,\max}$, particularly under stronger feedback. This behaviour is illustrated in Figure 3.12b for the exemplar case C =0.3. As can be seen, even with an

extreme value of $\alpha = \pm 2$, the maximum phase error remains within ~ 1° of that reported in Figure 3.11b for all feedback levels $C \leq 0.3$. At the same time the value of $e_{A,\max}$ is found to *decrease* as the magnitude of α increases, as shown in Figure 3.12a.

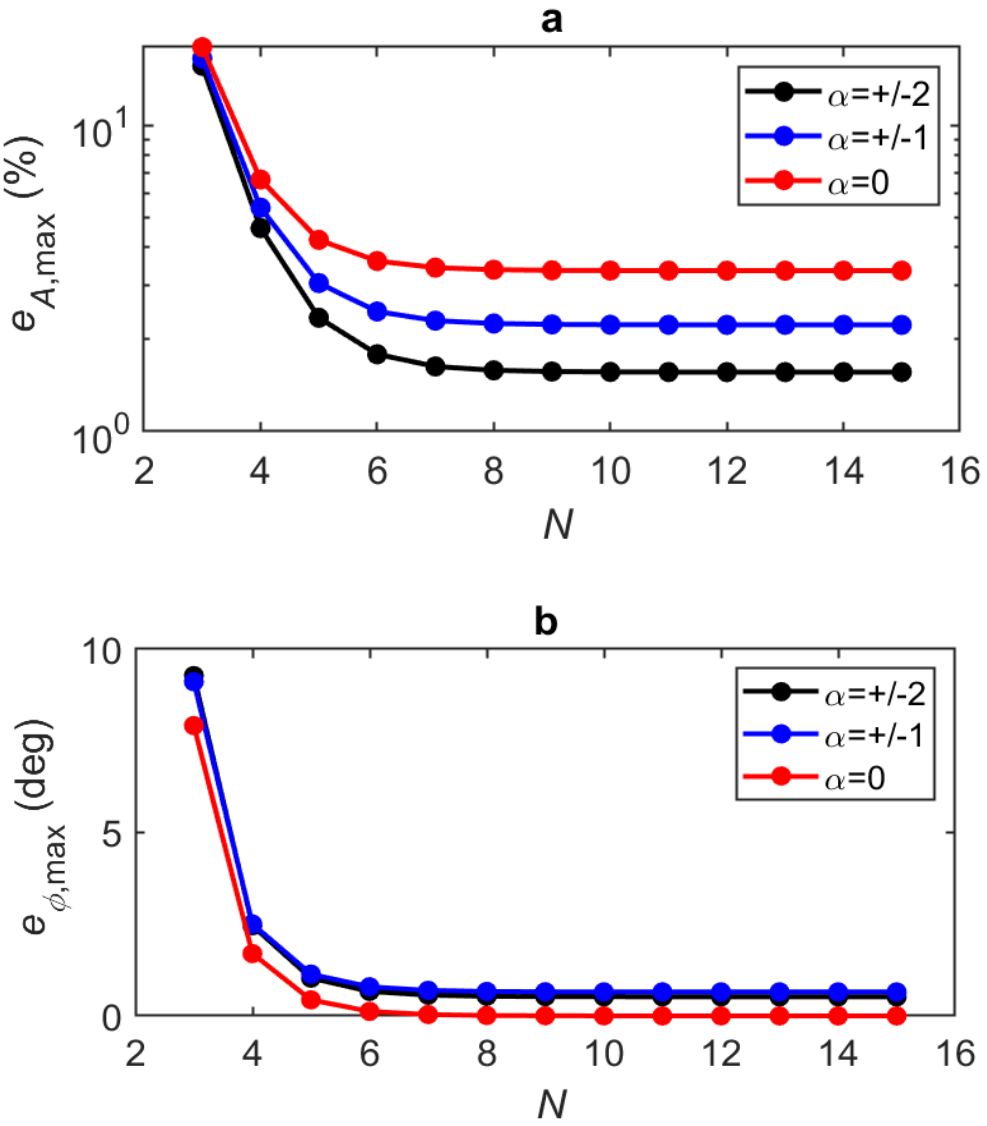

Figure 3.12 – (a) Variation of the maximum amplitude error with the number of measurement points N for α =0 (red circles), α = ±1 (blue circles), α = ±2 (black circles). (b) Variation of the maximum phase error for the same values of α. All results are shown for the exemplar case when C =0.3. The solid lines are intended only to aid visualisation.

Overall the results presented in Figures 3.8 – 3.12 confirm that the GPSA is well suited for reliably extracting both magnitude and phase parameters from typical V_{SM} signals acquired over a range of feedback levels and linewidth enhancement factors. Moreover, this approach remains robust even in the limit of small N. Notably this is particularly true in the case of extremely weak feedback, as may typically be encountered in THz-s-

SNOM where the scattering efficiency of the tip is extremely low. In such cases, where commonly $C \leq 0.1$ [153], [161], [162], the analysis presented predicts that magnitude and phase errors far smaller than 1% and 1°, respectively, may be attainable with $N = 4$ (see Figures 3.11 and 3.12).

3.4 Far-field LFI using a GPSA

The applicability of the use of the GPSA for determination of magnitude and phase parameters in LFI was investigated initially using a far-field optical feedback system (Figure 3.13) employing the QCL characterised in Chapter 2 Section 2.2. The 3.52 THz QCL device was based on a 10-µm-thick bound-to-continuum active region incorporating a phonon extraction/injection stage. The device was processed into a semi-insulating surface-plasmon ridge waveguide with dimensions 1.8 mm x 155 µm. A grating with periodicity Λ = 11.8 µm was defined in the 150-nm-thick Au layer on top of the ridge, consisting of $\sim$ 1.8-µm-wide regions with no metal and from which the 50-nm-thick n+ layer was removed to ensure that the surface plasma cannot be supported.

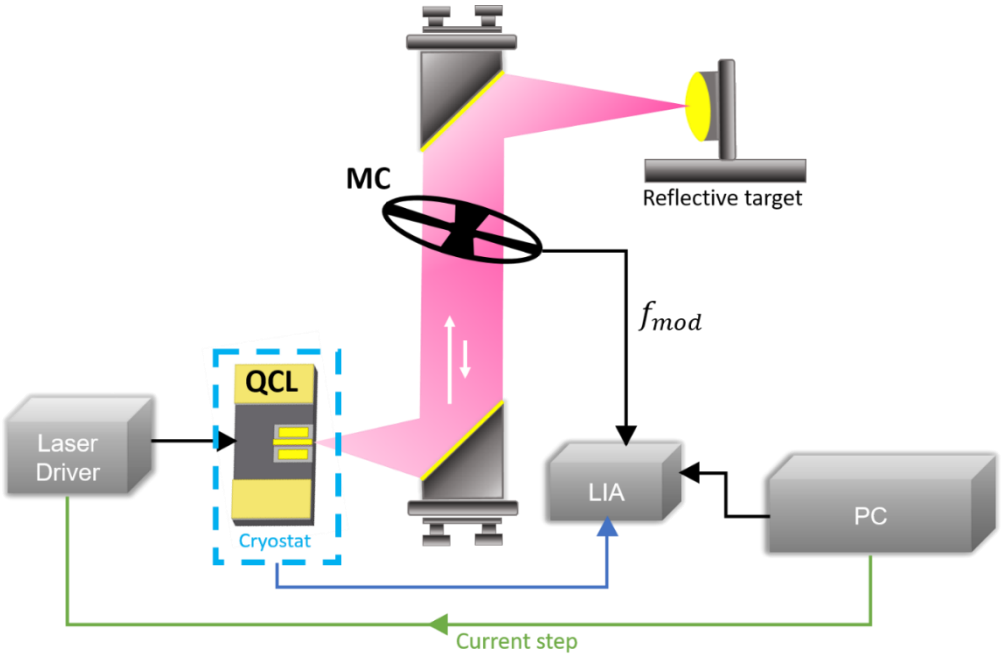

Figure 3.13 – Experimental set-up up for far-field frequency stepping LFI measurements.

The QCL was cooled in a continuous-flow helium cryostat and was maintained at a heat sink temperature of 20 K. Radiation from the QCL was collimated and focused using two

identical F/2 parabolic mirrors onto a plane mirrored target. The beam was reflected back along the same optical path and reinjected into the laser cavity, forming an external cavity of length $L_{ext} = 47$ cm.

Interferometric data was acquired via the laser terminal voltage using an all-electronic method of LFI that exploits the tunability of the QCL emission frequency with current [124]. In this approach, the QCL frequency is tuned by a sequential stepping of the QCL driving current over N equally spaced values in a manner similar to that described in Section 3.2.

Specifically, in the case of arbitrary N, the interferometric signal is obtained from a series of discrete voltage samples $V_{SM,i}$, where $i = 0 \rightarrow (N-1)$, taken at $N > 3$ phase points $\phi_{L,0} = \phi_i$ equally spaced over a single interferometric fringe. In our case this is achieved through control of the emission frequency of the solitary (unperturbed) QCL, which depends on the laser drive current I_i according to the relationship,

$$\nu_i = \nu_0 + \gamma(I_i - I_{start}) \tag{3.15}$$

where γ is the current tuning coefficient and ν_0 is the emission frequency of the solitary laser at a drive current I_{start}. It follows from Equations 2.4 and 3.15 that equally spaced phase points are generated for a series of driving currents given by,

$$I_i = \frac{i}{N}\frac{2\pi}{\gamma\tau_{\text{ext}}} + I_{start} \tag{3.16}$$

In Chapter 2 Section 2.3.1, continuous tuning of the laser frequency was presented in the swept-frequency approach, described by Equation 2.6. Here, Equations 3.15 and 3.16 are analogous to that approach but use discrete frequency tuning instead of continuous. In our experiment I_{start} is chosen such that $\nu_0 = \frac{m}{\tau_{ext}}$, where m is an integer, and V_{SM} thereby attains a maximum value for $i = 0$ when the phase response of the target $\phi = 0$.

To generate one interferometric fringe for the experimental arrangement described above, the QCL driving current was stepped within the range $I_{start} = 788$ mA to $I_{end} = 826$ mA. Throughout its operation over this range, the QCL maintained lasing on a single longitudinal mode which was tuned by ~ 319 MHz. At each driving current the QCL terminal voltage $V_{SM,i}$ was recorded via lock-in detection afforded by mechanically modulating the THz beam in the external cavity at a frequency $f_{mod} \sim 100$ Hz. The level

of optical feedback was controlled using attenuators placed in the beam in the external cavity.

Figure 3.14 shows an exemplar single fringe acquired with $N = 94$ measurement points, measured at current values defined by Equation 3.16. Also shown is a fit to the L–K model (Equation 2.21) from which the feedback parameter $C = 0.24$ and linewidth enhancement factor $\alpha = 1.9$ are determined. This fit also yields a magnitude $\beta = 2.91$ mV and phase $\phi = -2.8$, which are regarded as estimates of the true values to which the results of the GPSA analysis can be compared.

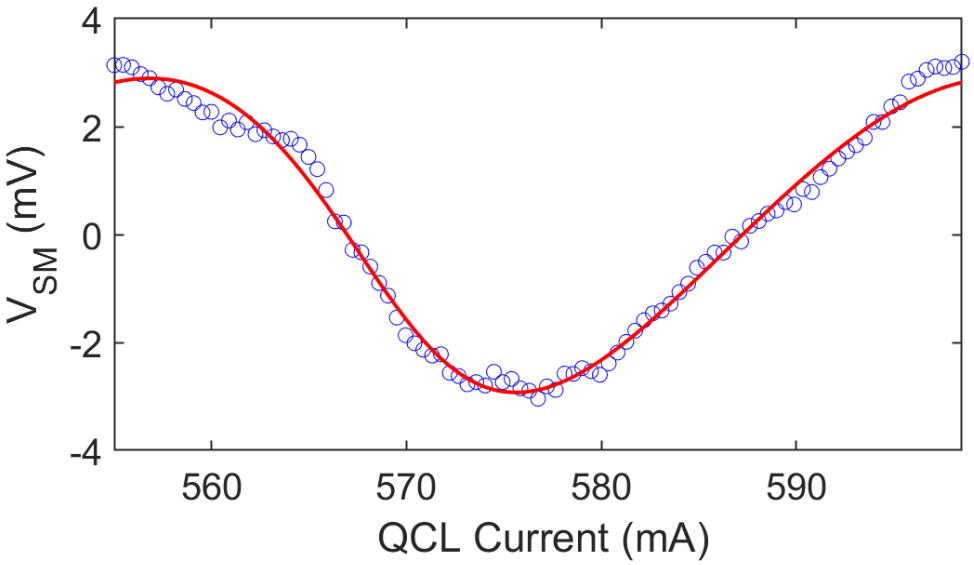

Figure 3.14 –Self-mixing voltage measured as a function of laser driving current, showing one exemplar interferometric fringe obtained by far-field LFI (blue circles). Also shown is a fit to the L–K model (Equation 2.21), in which $\beta = 2.91$ mV and $\phi = -2.8°$.

Using the data presented in Figure 3.14, multiple sets of discrete V_{SM} measurements, $V_{\mathrm{SM},i}$ with $i = 0 \rightarrow (N-1)$, each with progressively reducing value of N, can be extracted. Similarly to the situation depicted in Figure 3.9, within each set there furthermore exists multiple possible subsets of the N phase sampling points ϕ_i, each with differing values of $\phi_{i=0}$ i.e. with differing positions of the N points along the fringe. It should be noted these subsets are conceptionally equivalent to sets of measurements acquired with a fixed value $\phi_{i=0}$ but varying values of $(\phi_i - \phi)$ which may arise due to variation in the phase response of the target ϕ. These subsets thereby reproduce the typical experimental situation in which ϕ is not known in advance.

To reiterate the process by which the magnitude β_m and phase ϕ_m values were determined, the V_{SM} values were extracted from the data set at equally spaced phase points $\phi_i = 2\pi\frac{i}{(N-1)} + \phi_{i=0}$. The matrices $A(\phi_i)$ and $b(\phi_i)$ are then calculated from Equations 3.5 and 3.7 respectively, following which, the vector a is determined from Equation 3.8. Using a, the values β_m and ϕ_m are calculated from Equations 3.9 and 3.10. This was repeated for each value of $\phi_{i=0}$, the number of which will depend on the N used. This process was then completed for each value N in the range 3 to 20, to produce the results of Figure 3.15. Also highlighted are what are regarded as the 'true' values of the magnitude and phase, β and ϕ respectively, as determined from the fit to the L–K model shown in Figure 3.14.

As can be seen, and in agreement with the analysis presented in Figures 3.9 and 3.10, each subset of measurements $V_{\mathrm{SM},i}$ yield different values of magnitude β_m and phase ϕ_m, the range of which varies with N. Furthermore, as N increases this range converges on values close to the true values β and ϕ.

Also evident in Figure 3.15 and as elucidated by Figure 3.8, is that the values determined from the GPSA in the limit of large N deviate slightly from β and ϕ due to the non-cosinusoidal nature of the fringes. This behaviour is summarised in Figure 3.16 which display the maximum magnitude error and maximum phase error, respectively, for given values of N. Here $e_{A,\mathrm{max}}$ and $e_{\phi,\mathrm{max}}$ have been estimated from the range of values β_m and ϕ_m shown in Figure 3.15, and can be used as an indication of the accuracy of the GPSA when applied to the experimental LFI signals. For large N >15 these errors found experimentally converge on values of $e_{A,\mathrm{max}} \approx 5\%$ and $e_{\phi,\mathrm{max}} \approx 1.6°$, which are slightly larger than the values $e_{A,\mathrm{max}} = 1\ \%$ and $e_{\phi,\mathrm{max}} = -0.4°$ predicted for synthesised LFI signals with the same C and α (see Figure 3.8). This discrepancy can be explained due to the presence of voltage and frequency noise in the experimental LFI signals, which arise primarily from laser driver current noise and thermal instability of the QCL. Nevertheless, as can be seen, even with $N = 4$ the experimental errors remain low ($e_{A,\mathrm{max}} < 12\%$ and $e_{\phi,\mathrm{max}} < 5^0$), which may be considered suitable for many experimental situations. Ultimately the choice of N adopted experimentally will be a compromise between the required accuracy and data acquisition time.

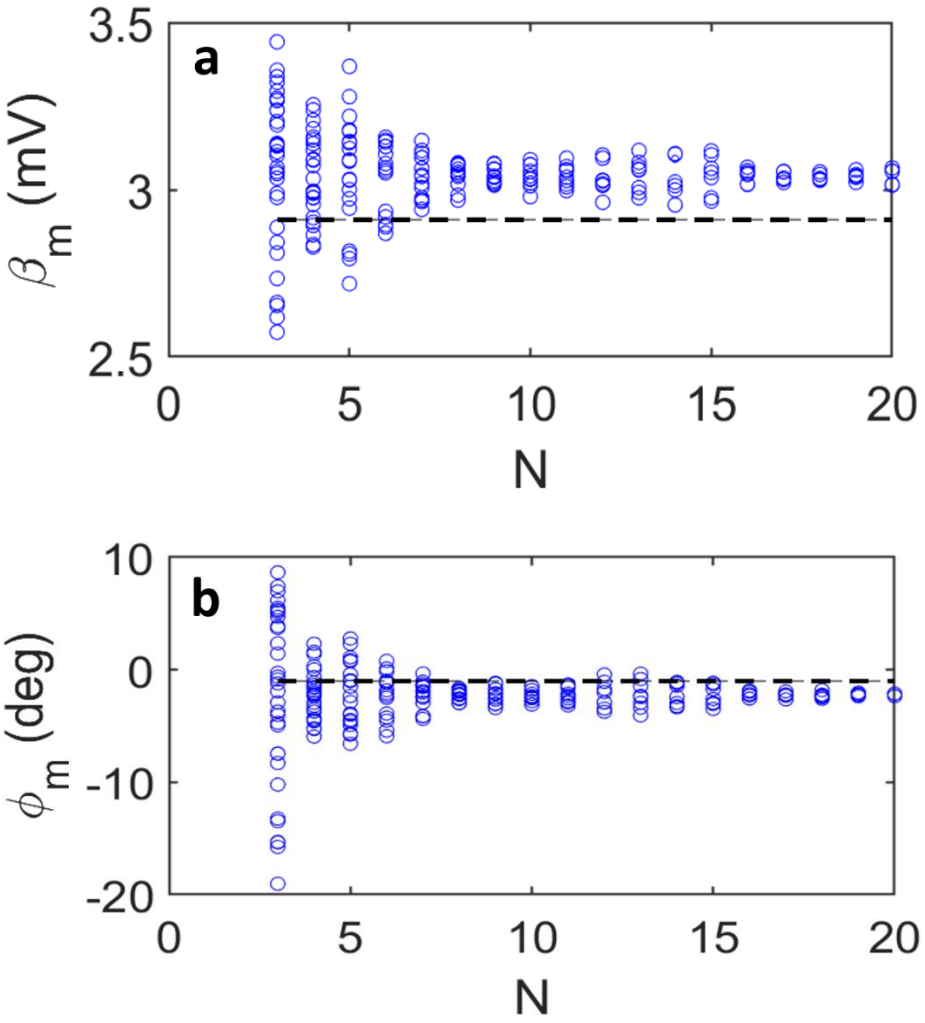

Figure 3.15 – (a) Magnitude β_m and (b) phase ϕ_m values determined by applying the GPSA to the data in Figure 3.14, for N in the range 3–20. For each value of N there exists multiple possible subsets of phase sampling points corresponding to differing positions of the N points along the fringe, each of which yield a different pair β_m and ϕ_m values. Also shown (dotted lines) are the 'true' values of magnitude and phase as determined from the fit shown in Figure 3.14.

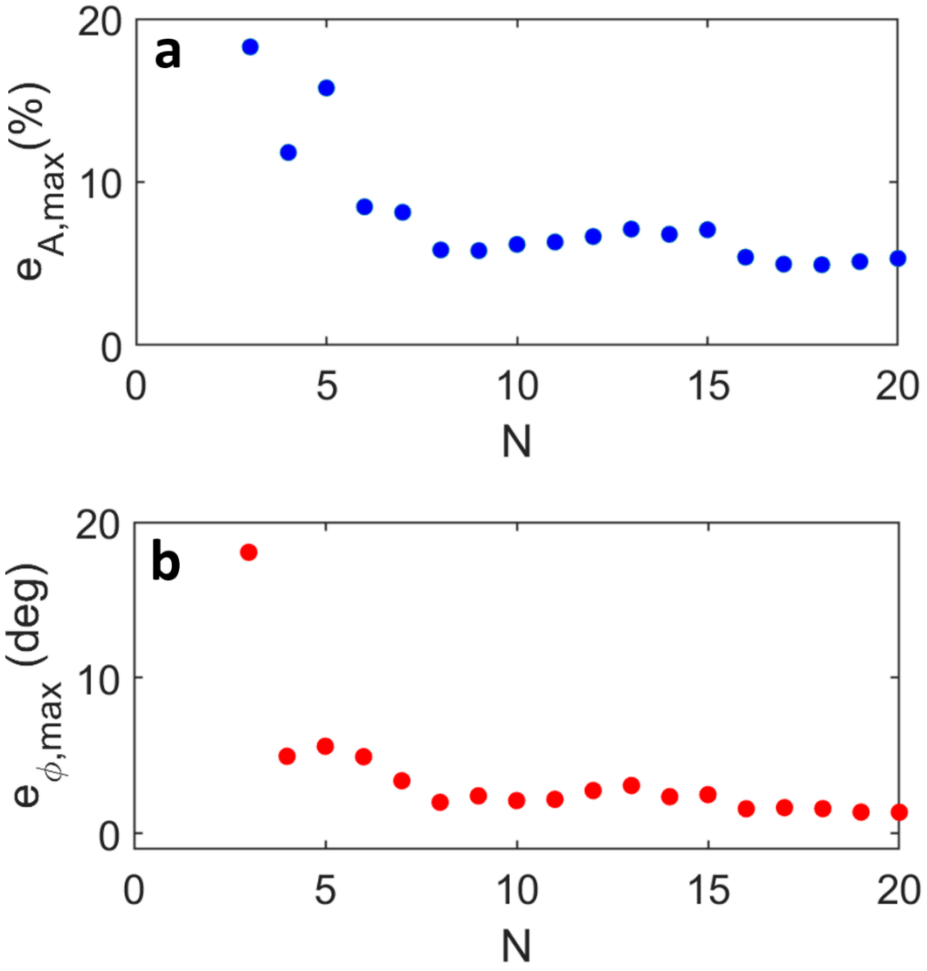

Figure 3.16 – (a) Maximum magnitude error $e_{A,max} = max\left\{\left|\left(\frac{\beta_m - \beta}{\beta}\right)\right|\right\}$ *calculated from the magnitude values* β_m *determined from the GPSA (shown in Figure 3.15) and expressed as a percentage error relative to the magnitude* β *determined from the fit shown in Figure 3.14; (b) maximum phase error* $e_{\phi,max} = max\{|\phi_m - \phi|\}$ *calculated from the phase values* ϕ_m *determined from the GPSA (shown in Figure 3.15) and the phase* ϕ *determined from the fit shown in Figure 3.14.*

3.5 Near-field LFI using a GPSA

3.5.1 Characterisation of the GPSA for s-SNOM

The 3.45 THz QCL device used for THz-s-SNOM consisted of a 14-μm-thick GaAs/AlGaAs 9-well active region based on LO-phonon-assisted interminiband transitions, which was processed into a semi-insulating surface-plasmon ridge waveguide with dimensions of 1.8 mm × 150 μm. To achieve lasing on a single longitudinal mode a 166-μm-long finite-site photonic lattice was patterned through the top contact layers using focused-ion beam milling [124]. The lattice period was 13.2 μm with a 70% mark-space ratio and a central 8-μm-wide phase defect.

The system used for coherent s-SNOM is as described in Chapter 2 Section 2.5. Briefly, p-polarised radiation from the QCL was focused to the vertically aligned tip of the s-SNOM system at an angle of $\sim 54^0$ relative to the surface normal and the length of the external cavity formed between the tip and the QCL facet was $L_0 = 60$ cm. The self-mixing signal, arising from the field scattered from the s-SNOM tip and reinjected to the laser cavity, was derived from the QCL terminal voltage which was demodulated at $n =$ 1–5 harmonics of the tip tapping frequency ($\Omega \sim 80$ kHz) after 5 x 10^3 amplification using an AC-coupled low-noise voltage amplifier.

In order to resolve both the magnitude β_m and phase ϕ_m of the field scattered from the s-SNOM probe an interferometric fringe can be generated at the chosen sampling position by stepping the laser driving current according to Equation 3.16, with $V_{SM,i}$ being recorded at each current. Prior to each stepped frequency measurement, a single set of interferometric fringes is generated by the imaging system to determine appropriate I_{start} and I_{end} values over which to perform the frequency step. This measurement is usually performed following successful alignment of the s-SNOM system and with the probe tip positioned on a sample that provides a relatively high V_{SM} amplitude. An example of this can be seen in Figure 3.17, wherein a 450 mA – 650 mA current step was performed with $\delta I = 0.5$ mA increments. The sample measured by the s-SNOM system to obtain the fringes displayed in Figure 3.17 was a simple gold-on-silicon structure.

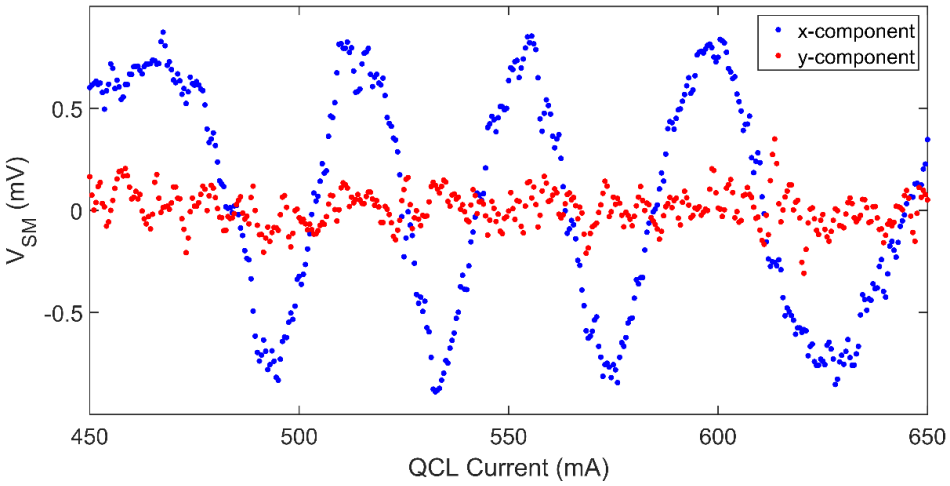

Figure 3.17 – x- and y-component of the signal acquired by the lock-in for near-field frequency sweep using the stepped frequency measurement system.

Before acquiring imaging data, it is important that the phase of the lock-in is nulled, in order for V_{SM} to be recovered from the x-component of the lock-in signal. It can be seen from Figure 3.17 that the y-component of the signal has been successfully nulled and the fringes can be resolved solely from the x-component data.

To characterise the GPSA for near-field data acquisition, an exemplar single-fringe acquired via the stepped frequency technique described above was captured using 87 measurement points and is displayed in Figure 3.18, for which $I_{start} = 555$ mA and $I_{end} = 600$ mA Also show is a fit to the L-K model (Equation 2.21) from which the parameters $C = 0.13$ and $\alpha = 0.95$, $\beta = 0.76$ mV and $\phi = 0.26$ rad.

Following the same procedure as described previously the data in Figure 3.18 can be used to estimate the maximum magnitude error and maximum phase error when applying the GPSA to these experimental s-SNOM signals. Figure 3.19 shows the results of this analysis for values of $3 \leq N \leq 20$. The errors associated with both of these quantities follow similar trends to those observed in the case of far-field LFI signals (Figure 3.16), with $e_{A,max}$ and $e_{\phi,max}$ converging on values <1% and <1^0, respectively, for large $N > 16$. However, despite the smaller value of C in the near-field case, larger errors are generally observed compared to those reported for the far-field case. This is primarily due to the significantly lower signal-to-noise ratio common to THz-s-SNOM measurements, which arises from the weak scattering efficiency of the tip as well as signal demodulation at higher harmonics of the tip modulation frequency. Nevertheless, even for small $N = 4$, moderate error values $e_{A,max} \sim 9\%$ and $e_{\phi,max} \sim 8°$ are attained,

which are sufficiently low to enable reliable magnitude and phase extraction of near-field LFI signals using the GPSA.

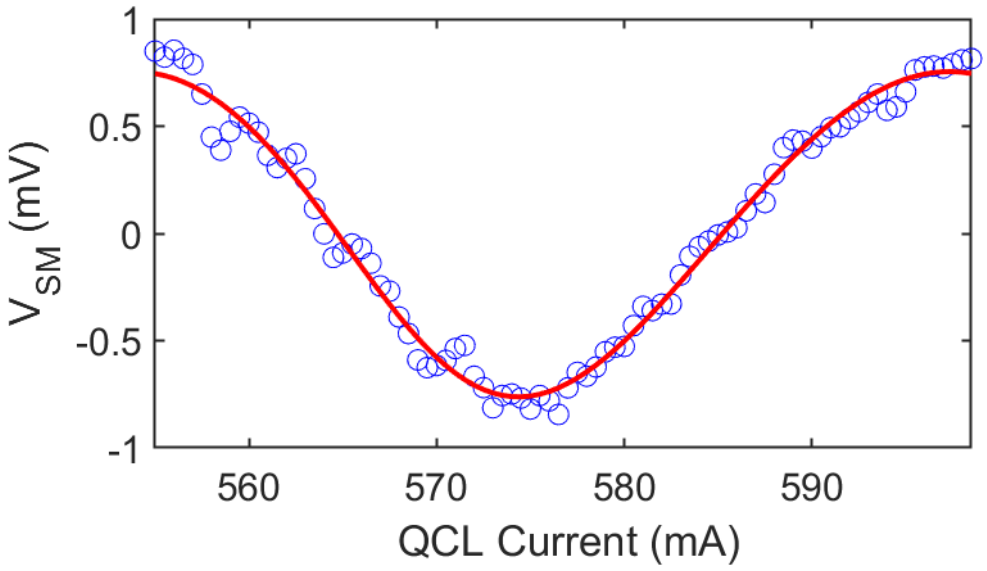

Figure 3.18 – Self-mixing voltage obtained from demodulation of the laser voltage at the $n = 3$ harmonic of the tip tapping frequency, measured as a function of laser driving current (blue) fitted to which is the L-K model according to Equation 2.21 (red).

3.5.2 Near-field imaging using the GPSA

To demonstrate coherent near-field imaging using LFI in conjunction with the GPSA, a target consisting of a simple dipole antenna (DA) resonant structure was chosen. The primary difference between this sample and the sample that was measured in the Chapter 2 Section 2.5, is that this structure has a resonance at the frequency of the QCL used. This allows the out-of-plane surface field to be mapped, which can be seen in the simulations results of Figure 3.20 and experimental image of Figure 3.21. This structure comprised a 15 μm × 2 μm gold-on-silicon antenna engineered to support a plasmonic resonance at the frequency 3.45 THz. Figure 3.20a shows a spatial map of the out-of-plane field E_z measured 20 nm above the sample surface, obtained from finite-element method (FEM) simulations of the DA structure when illuminated obliquely by a p-polarized excitation beam with an in-plane field component oriented along the long axis of the antenna. Also shown in Figures 3.21b and c are the corresponding magnitude and phase of the field. The field is strongly enhanced at both ends of the structure, with a π radian phase difference between the two ends, which is characteristic of a dipolar plasmonic mode being excited in the structure. These simulations were performed by Dr Nikollao Sulollari and have been adapted from [15].

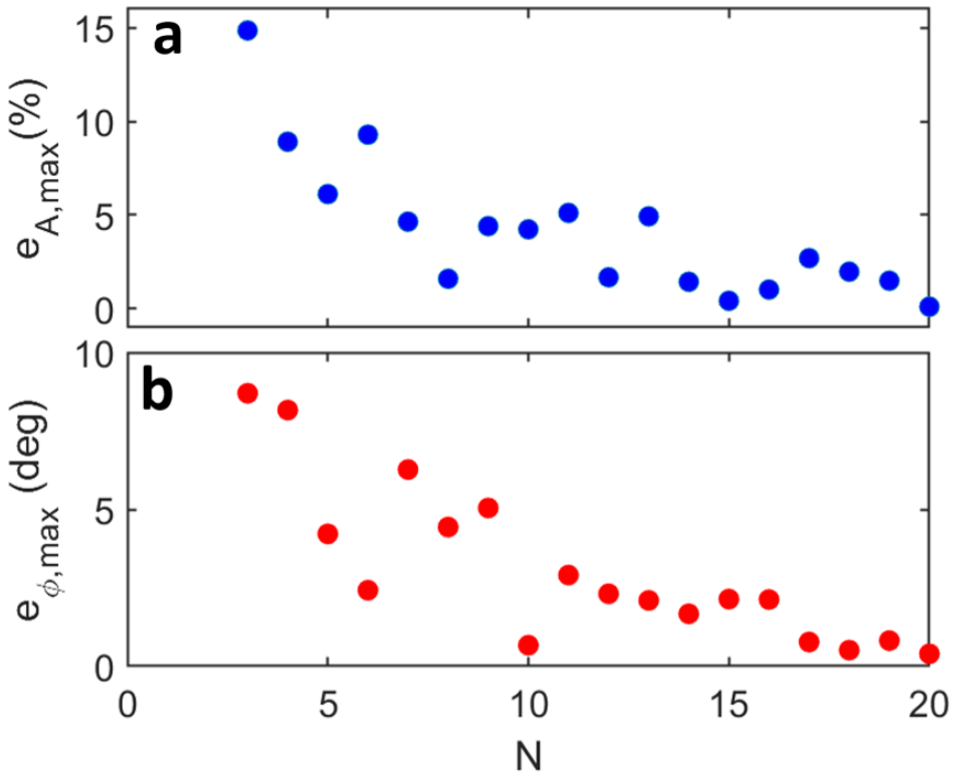

Figure 3.19 – (a) Maximum magnitude error $e_{A,max}$ and (b) maximum phase error $e_{\phi,max}$ determined from the magnitude and phase values obtained from the GPSA when applied to the data shown in Figure 3.18, expressed relative to those determined from the fit shown in Figure 3.18.

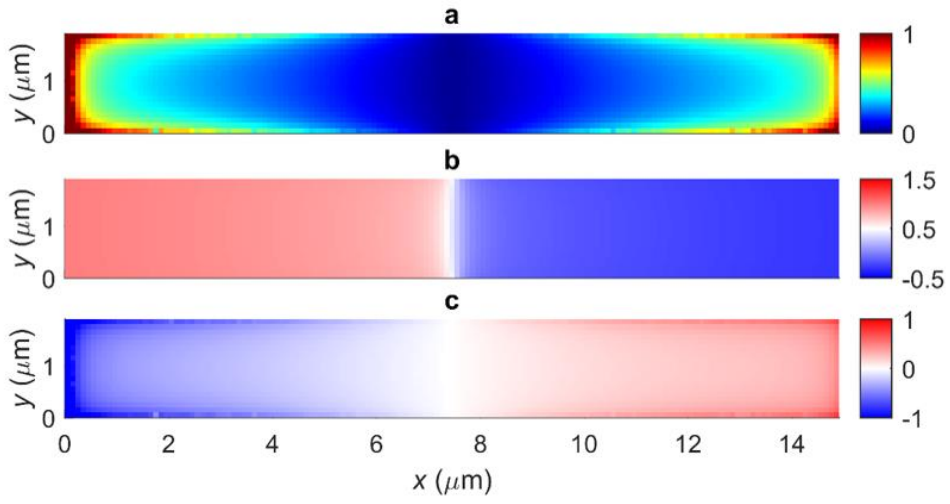

Figure 3.20 – Finite element simulations showing the spatial variation of the (a) magnitude β_z (a.u.), (b) phase ϕ_z (rads/π) and (c) real part $Re(\beta_z e^{-i\phi_z})$ (a.u.) of the out-of-plane field in the x–y plane 20 nm above the DA, when illuminated under oblique incidence at a frequency 3.45 THz. Adapted from [15].

The dipole antenna resonator structure was fabricated using standard electron-beam lithography on a high resistivity ($> 10000\ \Omega$cm) undoped silicon substrate with a thickness 525 ± 25 μm. The thickness of the Ti/Au resonator was ~ 2 nm/~ 100 nm, an array of which were patterned across a 2 x 2 mm^2 region of the substrate with a periodicity of 13 μm.

Initially, single-frequency THz-s-SNOM images of the DA were acquired with a step size of 200 nm, a tip tapping amplitude of ~ 75 nm and an integration time of 200 ms. An exemplar image can be seen in Figure 3.21 which shows the dipole resonance across the length of the DA, superimposed on which is a constant signal due to the dipole interaction between the tip and the surface. This is described by Equations 3.17 and 3.18 below, where it is explained how this constant can be subtracted from the image in order to better observe the signal corresponding to the out-of-plane field supported by the structure under resonance.

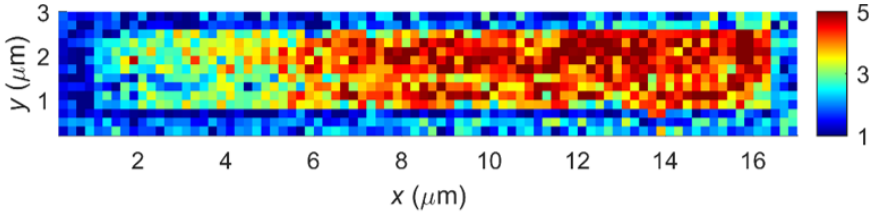

Figure 3.21 Terahertz image of the dipole antenna structure obtained by THz-s-SNOM, in which the antenna is obliquely illuminated with p-polarised radiation at a frequency 3.45 THz. The colour scale represents the self-mixing voltage derived from the $n = 2$ harmonic of the laser voltage, measured at a single laser driving current. The signal comprises of components capturing both the near-field dipole interaction between tip and sample surface, as well as the spatial distribution of the out-of-plane field supported by the sample under resonant excitation.

To demonstrate coherent near-field imaging, a set of interferometric fringes with chosen N were acquired at each pixel during a single raster-scan of the sample. By applying the GPSA to the interferometric data obtained at each pixel, one- or two-dimensional maps of both magnitude β_m and phase ϕ_m of the scattered field were thereby obtained.

One-dimensional coherent measurements of the DA were performed initially by scanning the structure parallel to its principal-axis, wherein at each pixel a set of $N = 15$ data points were acquired spanning one interferometric fringe. To perform these

measurements, the THz-s-SNOM and data acquisition system, characterised previously in this chapter, was used. Each 1D scan comprised the imaging of 40 pixels, with each measured over a current sweep of 45 mA. For $N = 15$, therefore, the required current increment was $\delta I = 3$ mA.

As previously established, the speed at which the s-SNOM can be efficiently run in conjunction with the data acquisition system equates to an acquisition time of > 125 ms per data point. It is also known that due to instrument limitations, the maximum scanning time allowed by the s-SNOM software is 10 s. Since the scanning time is defined as the period over which the microscope AFM tip remains on one pixel, and for this imaging technique the system is required to record 15 data points per pixel, the lock-in time constant T_{LI}, must be chosen to allow for accurate data acquisition without exceeding the maximum scanning time permitted by the microscope. Furthermore, the time over which a pixel measurement is performed is ultimately determined by the delay T_2 between each stepping of the QCL current, which is controlled by the LabVIEW program and chosen to be long enough to allow for stabilisation of the QCL emission frequency and reliable recording of the lock-in values. With that understood, a lock-in time constant of $T_{LI} = 200$ ms, stepping delay of $T_2 = 400$ ms and microscope scanning time of $T_{scan} = 8$ s was chosen. This enabled the system to coherently measure each pixel within the period of 6 s, with the remaining 2 s giving the AFM tip enough time to move to the subsequent pixel and return the driving current to I_{start}. This method culminated in a 20 um coherent 1D scan with resolution = 500 nm per pixel (Figure 3.23a) being performed in under 5.5 minutes.

Four examples of the V_{SM} imaging data acquired from single pixels within a 1D scan of 40 pixels across the length of the DA, acquired experimentally using the measurement parameters described above, are presented in Figure 3.22. The $N = 15$ data points for each pixel, corresponding to one fringe, are fitted to using the GPSA, from which the fringe magnitude β_m and phase ϕ_m have been acquired. For each pixel, the current was stepped in increments of $\delta I = 3$ mA between $I_{start} = 550$ mA and $I_{end} = 592$ mA.

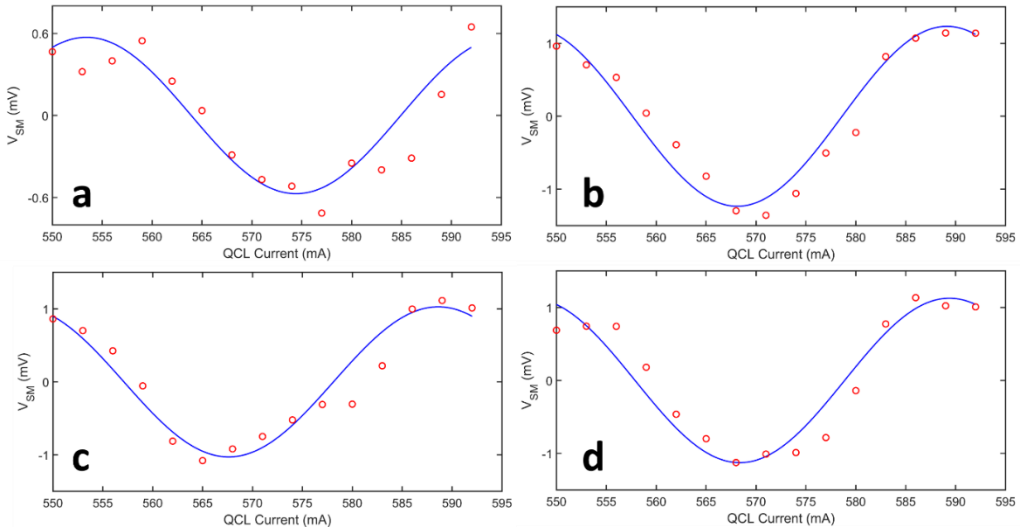

Figure 3.22 – Examples of single pixel V_{SM} data acquired for $N = 15$ data points acquired using the stepped frequency system (red) fitted to which is the GPSA (blue). (a) $\beta_m = 0.57$ mV and $\phi_m =$ -0.51 rad. (b) $\beta_m = 1.2$ mV and $\phi_m = 0.43$ rad. (c) $\beta_m = 1$ mV and $\phi_m = 0.51$ rad. (d) $\beta_m = 1.1$ mV and $\phi_m = 0.39$ rad.

It has been shown previously [15] that the self-mixing voltage signal in THz-s-SNOM comprises two signal components according to Equation 3.17. The first of these is principally excited by p-polarised components of the incident THz field and captures information about the local permittivity of the sample. In contrast the second component is insensitive to the bulk material properties but captures the spatial distribution of both the magnitude β_z and phase ϕ_z of the out-of-plane field E_z supported by the sample due to resonant excitation by in-plane components of the incident field. By exploiting its spatial symmetry the former of these can be removed from the total measured signal, thereby isolating the complex amplitude $\beta_z e^{-i\phi_z}$ associated with the out-of-plane field for each pixel.

The V_{SM} signal recorded at each position on the sample is given in complex notation by [15],

$$V_{SM} = \beta_m e^{i(\phi_L - \phi_m)} = \left[\beta_\varepsilon e^{-i\phi_\varepsilon} + \beta_z e^{-i\phi_z}\right] e^{i\phi_L} \qquad 3.17$$

from which it follows that

$$\beta_m e^{-i\phi_m} = \beta_\varepsilon e^{-i\phi_\varepsilon} + \beta_z e^{-i\phi_z} \qquad 3.18$$

Here β_ε and ϕ_ε are the magnitude and phase, respectively, of the signal contribution arising from the near-field dipole interaction between illuminated tip and sample surface. The parameters β_z and ϕ_z are directly related to the magnitude and phase of the out-of-plane field component, E_z, associated with resonant modes supported by the sample. The field distribution associated with the plasmonic dipole mode excited in the DA exhibits equal magnitude but opposite phase in opposite halves of the structure (i.e. $\beta_z e^{-i\phi_z}$ is spatially asymmetric) and will therefore spatially average to zero. As such the spatially constant term $\beta_\varepsilon e^{-i\phi_\varepsilon}$ can be readily estimated from the spatial average of the signal recorded across all gold regions of the sample. Using Equation 3.18 this value can then be subtracted from the measured signal $\beta_m e^{-i\phi_m}$ to isolate the magnitude β_z and phase ϕ_z for each pixel.

Figure 3.23a shows the magnitude, phase and real part of the complex amplitude $s_z e^{-i\varphi_z}$ obtained using the procedure described above. To generate this phase data, it was first necessary to apply a phase unwrapping process to the values of ϕ_m extracted from the GPSA along the x-direction. To experimentally confirm the limits of the GPSA, the 1st, 5th, 9th and 13th V_{SM} values of each pixel were also extracted to form a new $N = 4$ data set to which the GPSA was applied. The results from this equivalent scan with $N = 4$ are shown in Figure 3.23b.

Also plotted in these Figures are the corresponding values of the out-of-plane electric field component E_z associated with the plasmonic mode calculated from FEM simulations (Figure 3.20). In calculating the simulated phase it is necessary to also account for the phase retardation arising from the oblique illumination geometry, which causes the phase of the excitation field to vary as the spatially-structured sample is scanned within the beam. In our experimental geometry this phase retardation $\Delta\phi$ is described by

$$\Delta\phi = -\frac{2\pi}{\lambda} x \sin\theta \qquad 3.19$$

where x is the coordinate along the principal axis of the DA, θ is the incident angle of the THz beam and λ is its wavelength. The varying of this positional-dependent phase also contributes to the image contrast seen in Figure 3.21.

It can be seen that the experimental measurements show good agreement with theoretical expectations and furthermore there is little to no discrepancy between the

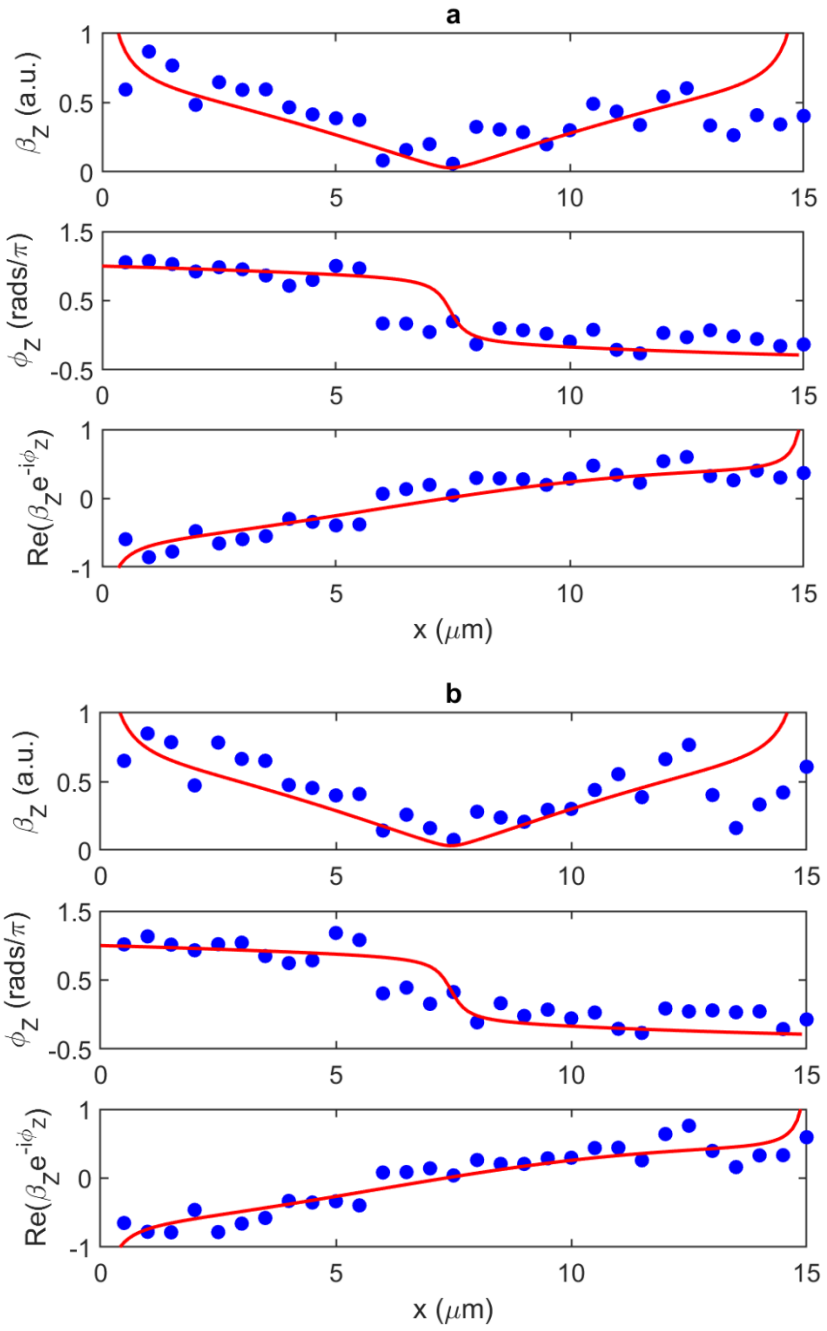

Figure 3.23 – Magnitude β_z, phase ϕ_z and real part $Re(\beta_z e^{-i\phi_z})$ of the out-of-plane field component associated with the plasmonic dipole mode excited in the DA under resonant excitation by THz radiation. Blue circles show measured values, obtained by THz-s-SNOM and applying the GPSA with (a) N =15 and (b) N =4 measurements per pixel, plotted as a function of position along the principal axis of the antenna. Also shown (red lines) are the corresponding values derived from FEM simulations shown in Figure 3.20.

N =15 and N = 4 scans. It can therefore be concluded that N = 4 phase measurement points is sufficient for this technique to capture magnitude and phase of the out-of-plane field.

By repeating this measurement procedure across several adjacent rows of pixels, a two-dimensional coherent image of the DA was also acquired as shown in Figure 3.24, for the case of $N = 4$. To perform these measurements a lock-in time constant of $T_{LI} = 200$ ms, stepping delay of $T_2 = 400$ ms and microscope scanning time of $T_{scan} = 8$ s was used. Each pixel was, therefore, measured within a 6 s period. Each 20 μm scan across the length of the DA comprised 40 pixels, therefore giving a pixel resolution of 500 nm. The current was stepped over a range $I_{start} = 550$ mA and $I_{end} = 592$ mA with increments of $\delta I = 10.5$ mA. The total imaging time for this coherent two-dimensional image was 33 minutes.

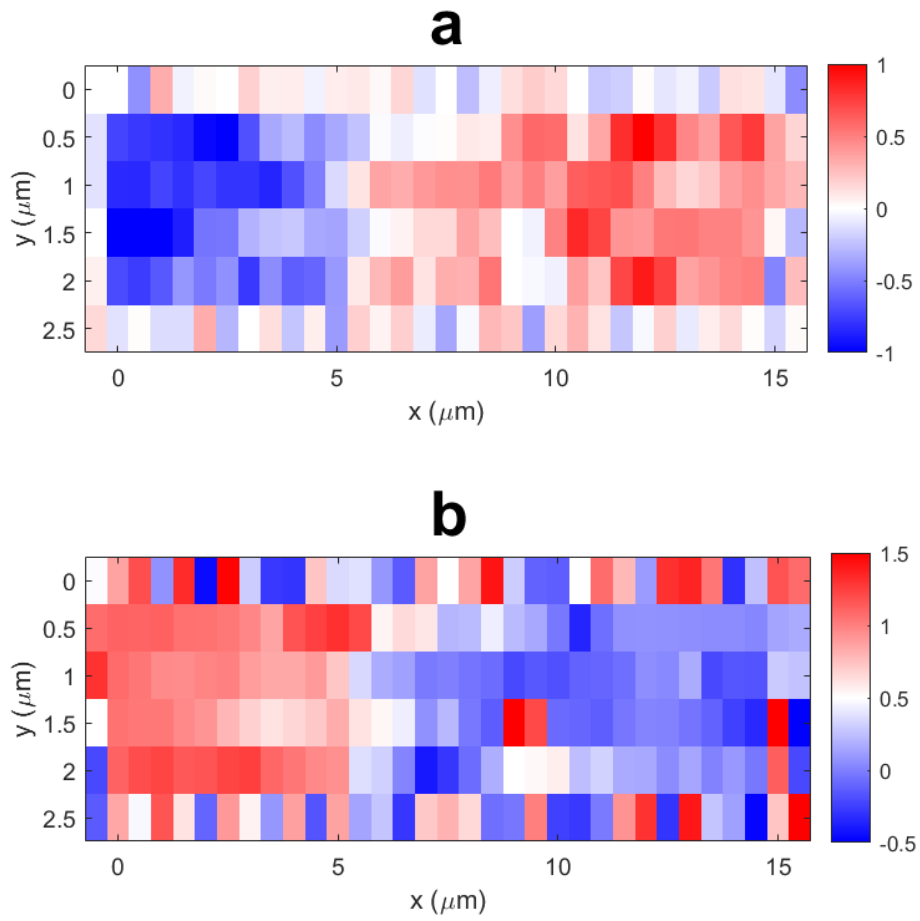

Figure 3.24 – Two-dimensional images showing the (a) real part $Re(\beta_z e^{-i\phi_z})$ (a.u.) and (b) phase ϕ_z (rads/π) of the out-of-plane field component supported by the DA, obtained by THz-s-SNOM and applying the GPSA with $N = 4$ measurements per pixel. The first and last pixels of each row and column correspond to the substrate region of the sample. Both images have been generated by concatenating 1D scans taken at different y-positions on the sample.

As can be seen, these images reveal a clear signal contrast between opposite ends of the DA, which is characteristic of the dipolar plasmonic resonance excited in the structure and in excellent agreement with the simulations shown in Figure 3.20.

3.6 Summary

In this chapter, it has been demonstrated how coherent THz imaging can be achieved by exploiting the frequency tuning of a THz QCL via laser feedback interferometry. The s-SNOM and laser control system used to perform these measurements has been fully divulged including specifics of the LabVIEW virtual instrument that: monitors the line and pixel clocks of the s-SNOM, triggers the data acquisition of a V_{SM} signal via a fast-detection lock-in amplifier and saves said data to an array for post processing. To characterise this scheme, the system data acquisition speed and resolution were investigated by performing several single-frequency measurements of simple gold structures, to determine the optimum microscope scanning time T_{scan}, lock-in time constant T_{LI} and data acquisition delay T_2in order to operate the stepped frequency system efficiently.

It has also been demonstrated how magnitude and phase information can be extracted from interferometric fringes, acquired by LFI, through the use of a generalised phase-stepping algorithm. The applicability of this approach has been investigated theoretically for different levels of optical feedback, different laser parameters, and for different sampling conditions. An analysis of this approach has revealed how its accuracy reduces for decreasing sampling points N, as well as increasing feedback strength due to the associated asymmetry induced in LFI signals. It has been determined that both magnitude and phase values can be measured with sufficient accuracy over a wide range of weak feedback levels and linewidth enhancement factors typical to common experimental situations, even down to $N = 4$.

This approach based on the GPSA has been validated experimentally, initially through the analysis of V_{SM} signals measured from a THz-frequency QCL in a far-field LFI geometry. It has thereby been demonstrated that for an exemplar value of feedback parameter $C = 0.24$, the magnitude and phase can be determined experimentally with an inaccuracy of only < 12% and < 5^0, respectively, with only $N = 4$ measurement points, but decreasing to < 5% and < 2^0 for larger N.

Using this technique, successful deeply sub-wavelength-resolution coherent imaging of the out-of-plane field supported by a THz micro-resonator under resonant excitation has been demonstrated. A comparison between images acquired using different N confirms that $N = 4$ measurements per pixel is sufficient to extract magnitude and phase information, with little impact on the image quality.

Chapter 4

Terahertz microscopy of topological insulators

4.1 Introduction

Topological insulators (TI) are a relatively new classification of materials that are characterised by Dirac-like edge states (in 2D) or surface states (in 3D) that arise due to a unique property of the bulk wave function [163]. These states occur due to spin-orbit interactions akin to the spin Hall effect [164] which leads to chiral surface spin currents, in which electrons with spin $S = \frac{1}{2}$ propagate on the edge (or surface) of a material in one direction and those with $S = -\frac{1}{2}$ propagate in the opposite direction [16]. These states are protected from backscattering into the valence band by time-reversal symmetry, in that the geometry of the band structure of the material, at the interface with a dielectric, is such that backscattering would require a ±1 change of spin, as can be visualised in Figure 4.1.

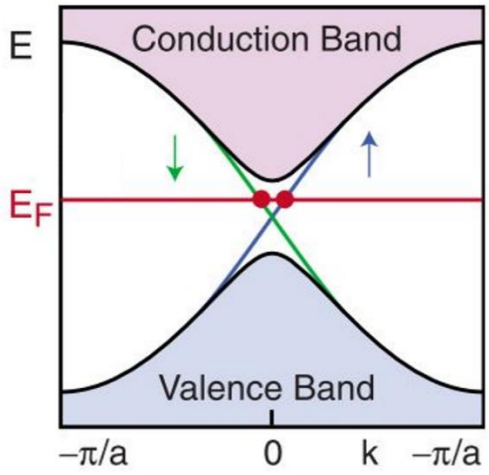

Figure 4.1 – Energy-momentum diagram of a typical topological insulator showing the Fermi-energy level E_f and the momentum of spin up (blue arrow) and spin down (green arrow) electrons. Adapted from [16].

A caveat of observing these surface states is that, usually, the Fermi-level E_f intersects the conduction/valence bands thus giving rise to a finite conductivity in the bulk, which subverts the topological nature of the material and must be rectified by a tuning of E_f [165]. This has commonly been achieved by doping [166]–[169], TI layering [170], [171] or with the inclusion of a gate [172]–[175], an example of which will be considered in Section 4.3 and onwards. Solving this issue results in a material that comprises a bulk possessing the qualities of a traditional insulator but an edge (or surface) that allows for charge carrier conduction similar to that of a metal.

As well as being of purely academic interest, it has been proposed that these materials have many applications, such as spintronics [176] and topological quantum information processing [16].

Due to these unique properties, it had been theorised that TIs could support collective oscillations on their surface, such as surface plasmon polaritons [20], [177] and phonon polaritons [178] that would provide great potential for light-matter confinement. The following review will demonstrate these phenomena in various TI materials.

4.1.1 Graphene

One of the first 2D materials predicted to exhibit TI-like properties is graphene [179] following the discovery of materials that display finite spin-Hall conductivity [180]. This property of graphene was, however, unobservable due to the small spin-orbit coupling of carbon. It was not until the engineering of doped graphene that quantum spin-Hall (QSH) states were experimentally confirmed [181], which was facilitated by the progress made in fabrication of thin-film graphene [182]. Since this confirmation, graphene has been the subject of many investigations into both collective optical and acoustic oscillations, most notably massless Dirac plasmons which are a product of Dirac states [109], [183]–[185].

In the THz range, graphene provides potential for the prospect for novel optical THz devices, such as sensors [186], diodes [187] and modulators [188], to name a few, due its high charge carrier mobility, low energy consumption and scalability [108], [189]. Additionally, the material can be gated, allowing the material to be used in applications wherein its plasmonic properties can be electronically tuned.

Naturally, the plasmonic nature of graphene has been extensively investigated in the THz and near-IR range [190]–[196]. Using the s-SNOM technique (as discussed previously), plasmonic resonances have been excited and launched in both unpatterned [197] and

patterned [17] graphene (Figure 4.2), the first examples of which can be seen in [198] and [199].

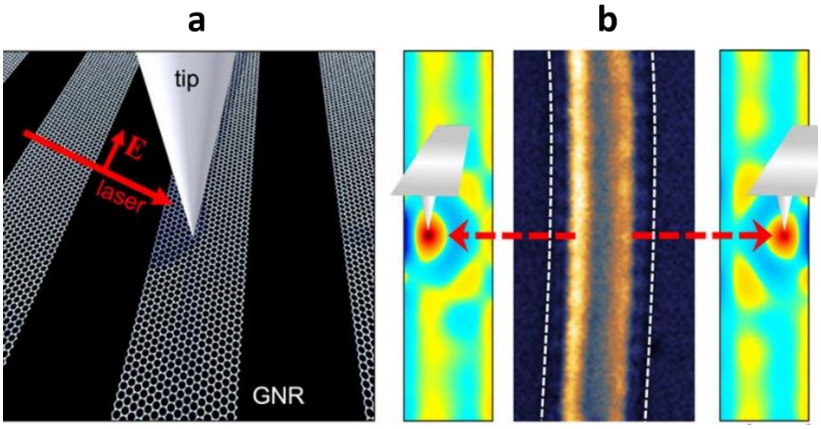

Figure 4.2 – (a) Diagram of s-SNOM scanning location on a graphene nano-ribbon (GNR) with incident radiation (red). (b) Imaging data of a ribbon with fields of the left and right sides of the ribbon, including s-SNOM tip location. Adapted from [17].

4.1.2 3D topological insulators

Since the discovery of three dimensional TIs, first realised in $Bi_{0.9}Sb_{0.1}$ alloy, using angle resolved photoemission spectroscopy (ARPES) [200], bismuth-based compounds have emerged as the primary subject of study of topological surface states [201].

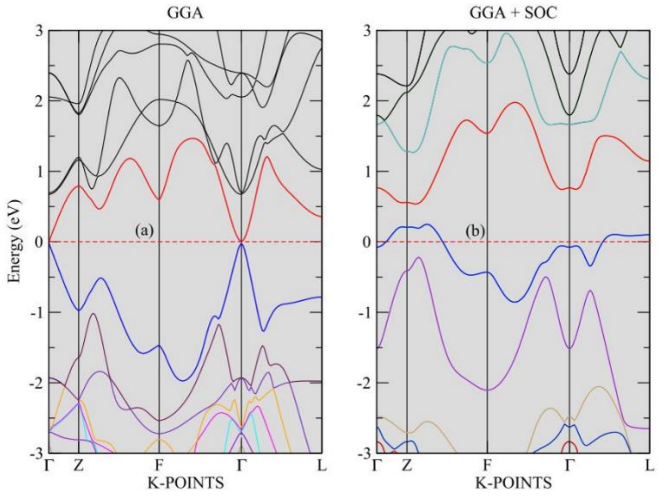

Figure 4.3 – Energy-momentum diagrams for Bi_2Se_2 modelled using a generalised gradient approximation (GGA) without (a) and with (b) spin orbit coupling (SOC). It can be seen that the presence of SOC provides a band gap of ~ 1 eV at the Γ K-point. For simplicity, E_f has been assumed to be 0 eV. Adapted from [18].

Bismuth (and to a lesser extent antimony) displays strong spin-orbit coupling, owing to the large size and charge of its nuclei [202], and therefore possesses a band structure which resembles a TI (Figure 4.3).

It was discovered that crystalline compounds such as Bi_2Se_3, Bi_2Te_3 and Sb_2Te_3 have surface states consistent with TIs. In particular, Bi_2Se_3 possesses a non-trivial band gap ($> \sim 0.3$ eV), making it an ideal subject for the study of 3D TIs [201]. Early X-ray diffraction analysis of Bi_2Se_3, and other bismuth based compounds [203], showed that it has a z-direction hexagonal layered structure, comprising quintuple layers of Bi and Se in a Se_1-Be-Se_2-Be-Se_1 order (Figure 4.4).

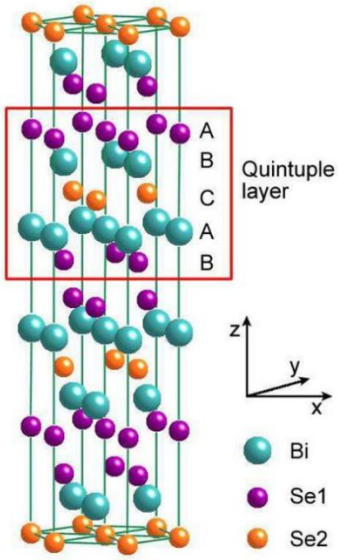

Figure 4.4 – Hexagonal Bi_2Se_3 atomic structure showing the Se_1-Be-Se_2-Be-Se_1 quintuple layer (red box). Adapted from [19].

Naturally, 3D TIs are predicted to have applications which may benefit from the exploitation of collective charge-carrier oscillations, such as that seen in graphene (Section 4.1.1). Though plasmonic effects are predicted to be visible at room temperature for these materials, their dispersion relation is such that they cannot be directly excited by EM radiation, when using common probe frequencies such as IR and THz, due to a momentum mismatch similar to that described in Chapter 5. To overcome this, a patterned resonant structure, such as a grating, is commonly used [204], a technique that was utilised in the same way to observe confined plasmons on ribbons of Bi_2Se_3 in the far-field for the first time in the THz range [205] and later in rings of Bi_2Se_3, which offer a greater plasmonic spectrum [177].

However, the far-field probing of plasmons has been open to interpretation and controversy, owing not least to the further complication of THz bulk phonon polaritons in Bi_2Se_3, which hinders the observation of plasmons [206], as well as Fano interference [207], which is caused by the far-field signal being a superposition of the field scattered from the surface and the incident field transmitted through the sample. In addition, far-field techniques do not permit direct mapping of the localised fields associated with SPs, and so, recently, near-field techniques, such as THz-s-SNOM of Chapters 2 and 3 have been employed to observe such [23], [208]–[210].

4.1.3 Chapter overview

In this chapter, an investigation of plasmonic effects in various TI samples will be undertaken. This will entail a theoretical description of a generic TI material according to past models, which are used to calculate the dispersion relation of SPs and key parameters such as their propagation length in the THz range. The models then allow for investigation into how these parameters are affected by the material properties.

Using these models, a similar theoretical analysis of several bulk, ribbon and electrically gated thin-film bismuth-based TI samples will be undertaken to predict their optical response in the THz range (Section 4.2), with material parameters determined via THz-TDS. Furthermore, these samples will be examined using THz-s-SNOM (Section 4.4-4.6), which will include both incoherent and coherent imaging, based on the system of Chapter 3.

4.2 Simulation of topological insulators

4.2.1 Plasmonic behaviour of a conventional material

To define the relationship between the frequency ω and wave vector k of SPs supported by the boundary between two materials, the dispersion relation is used. As will be seen in Chapter 3, for a conventional metal, the dispersion relation can be determined from the following, a derivation of which can be found in [211].

$$k = \frac{\omega}{c}\sqrt{\frac{\varepsilon_m \varepsilon_D}{\varepsilon_m + \varepsilon_D}} \tag{4.1}$$

where ε_m is the permittivity of the metal, ε_D is the permittivity of the dielectric surface and c is the speed of light.

The frequency dependent permittivity of a conventional metal can be determined using the Drude model, which will be shown for the case of TIs in Section 4.2.2. The dielectric medium is assumed to be air, therefore, $\varepsilon_D = 1$. Figure 4.5 shows the real $k'(\omega)$ part of the dispersion relation along with the free space wave vector k_0.

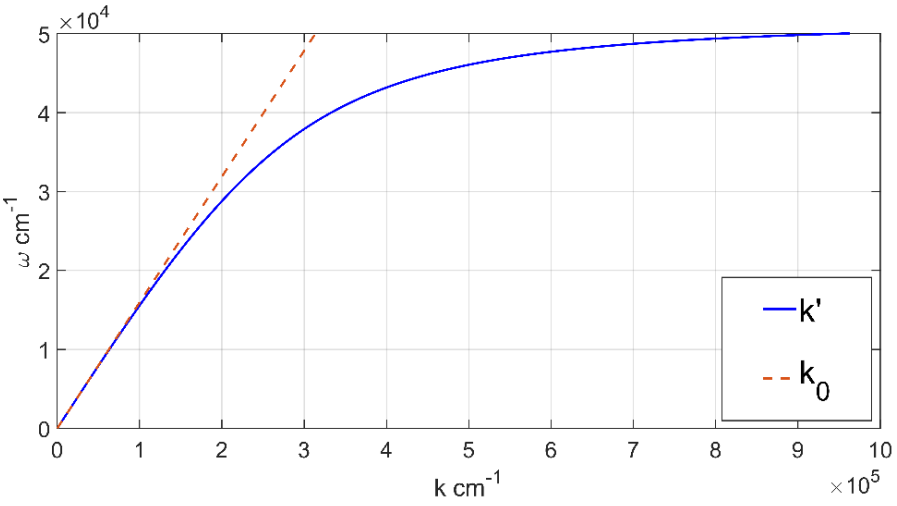

Figure 4.5 – Dispersion relation of gold (blue) with free space wave vector (dashed red), according to Equation 4.1.

It can be seen that at THz frequencies (~ 100 cm^{-1}), the wave vector closely matches that of the free space and therefore surface confinement is poor.

Furthermore, as the plasmon propagates on the surface of the material it will attenuate due to losses arising from absorption. This is captured within the imaginary part of the wavevector, $k''(\omega)$, allowing the surface plasmon propagation length L can be determined [211] as,

$$L = {}^{1}/_{2k''} \tag{4.2}$$

where L is defined as the distance after which the plasmon intensity drops to ${}^{1}/_{e}$ of its initial value and can be seen in Figure 4.6.

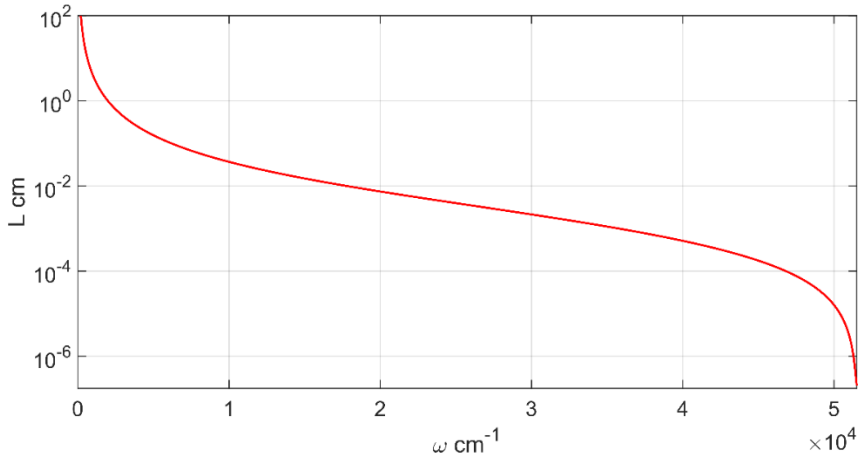

Figure 4.6 - Plasmon propagation length in gold according to Equation 4.2.

Additionally, the expected plasmon wavelength λ_{SP} can be determined from the real part of $k(\omega)$, given by Equation 4.3, as seen in Figure 4.7.

$$\lambda_{SP} = \frac{2\pi}{k'(\omega)} \tag{4.3}$$

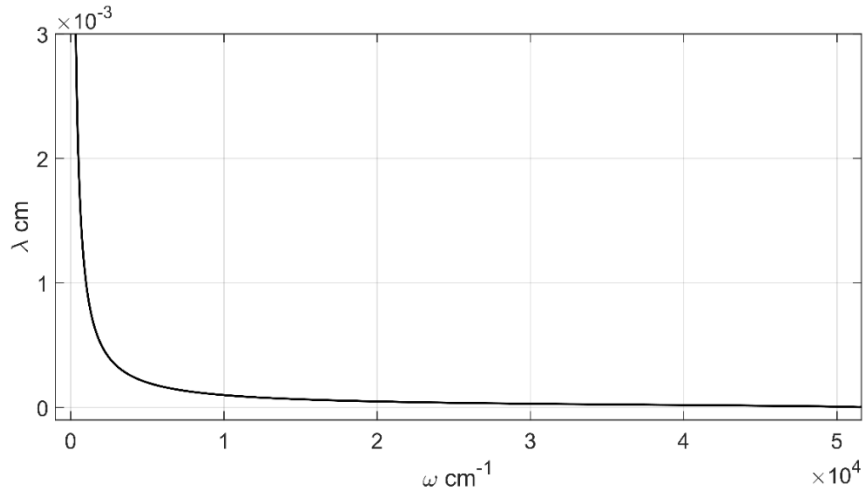

Figure 4.7 – Plasmon wavelength in gold according to Equation 4.3.

Therefore, the normalised plasmon propagation length L_{norm} (the number of wavelength cycles travelled before decaying) can be determined from,

$$L_{norm} = \frac{L}{\lambda_{SP}} \tag{4.4}$$

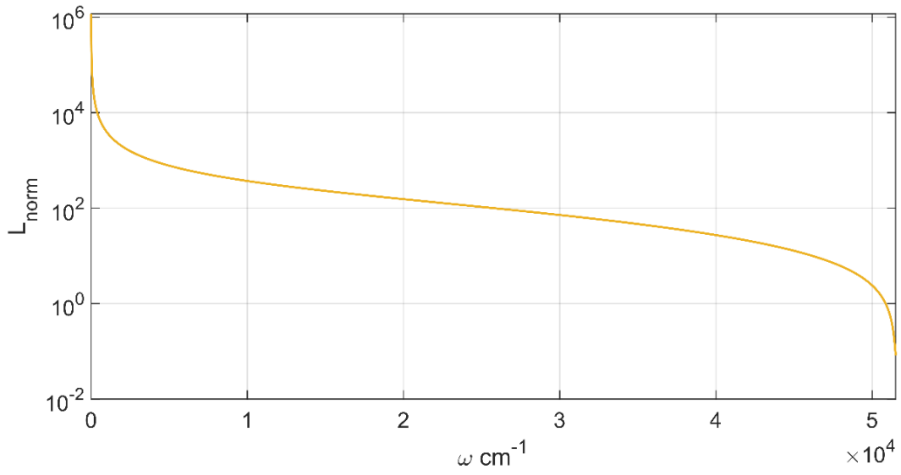

Figure 4.8 – Normalised plasmon propagation length in gold according to Equation 4.4.

To summarised, it can be seen from Figure 4.5 that in the THz range, $k_{SP} \cong k_0$ (i.e. $\lambda_{SP} \cong \lambda_0$ where λ_0 is the wavelength of the free-space beam). This indicates that the SP is very poorly confined on the surface of the metal. In effect, the field extends a long distance about the metal, with little to no penetration into its surface. This results in minimal absorption and so the propagation length distance is very large at these frequencies.

The parameters defined and presented in this Section will be used later to characterise the properties of SPs supported by TI samples.

4.2.2 Plasmonic behaviour of Bi_2Se_3

The dispersion relation $\omega(k)$ for collective modes of a massless Dirac plasma, such as that present in Bi_2Se_3 had previously been understood to take the form $\omega(k) \propto \sqrt{k}$ where ω is the incident frequency and k is the wave vector [184]. However, this was revised to include interaction contributions from both top and bottom surfaces of the TI and the bulk as well as taking film thickness into account, which leads to the relation of Equation 4.5 [212],

$$\omega = \sqrt{\frac{Ak}{\varepsilon_T + \varepsilon_B + dk\varepsilon_{TI}}} \tag{4.5}$$

where ε_T and ε_B are the dielectric functions of the medium at the top and bottom of the TI respectively, ε_{TI} is the dielectric function of the TI, d is the TI thickness and A is a constant that incorporates the Fermi velocity v_F and Fermi wave vector k_F.

However, this model did not satisfy experimental data but was further reconciled in [20] by expressing both ε_{TI} and ε_B in terms of ω. This was performed using the Drude-Lorentz model (Equation 4.6), which, as well as the Drude-plasma contribution, takes into account several Lorentz oscillator terms that account for phonon contributions to the permittivity,

$$\varepsilon_{TI} = \varepsilon_\infty - \frac{\omega_D^2}{\omega^2 + i\omega\gamma_D} + \sum_{j=1}^{j=3} \frac{\omega_{pj}^2}{\omega_{0j}^2 - \omega^2 - i\omega\gamma_j} \tag{4.6}$$

where ε_∞ is the dielectric function as $\omega \to \infty$, $\omega_D$is the Drude plasma frequency, γ_D is the Drude scattering frequency, ω_{0j}, ω_{pj} and γ_j are the central frequency, amplitude and scattering frequency of mode j respectively.

To determine these parameters for a thin film sample of Bi_2Se_3, values of $\omega_D = 908.66$ cm^{-1}, $\gamma_D = 7.43$ cm^{-1} and the parameters listed in Table 1 were used.

j	$\boldsymbol{\omega_0}$, cm^{-1}	$\boldsymbol{\omega_p}$, cm^{-1}	$\boldsymbol{\gamma}$, cm^{-1}
1	63.03	675.9	7.43
2	126.94	100	17.5
3	2029.5	11249	3920.5

Table 1 – Drude-Lorentz model (Equation 4.6) parameters extracted from mid-IR reflectance measurements of Bi_2Se_3 at room temperature. Taken from [20].

Figure 4.8 summarises the relative contributions from each term in the Drude-Lorentz model of the bulk dielectric function of Bi_2Se_3 according to Equation 4.6 It can be seen that ε is mostly influenced by the Drude term and first Lorentzian oscillator.

The total real ε' and imaginary ε'' parts of the permittivity according to this model are displayed in Figure 4.10, in which it can be seen that the permittivity is dominated by the phonon mode at $\omega \sim 63$ cm^{-1}.

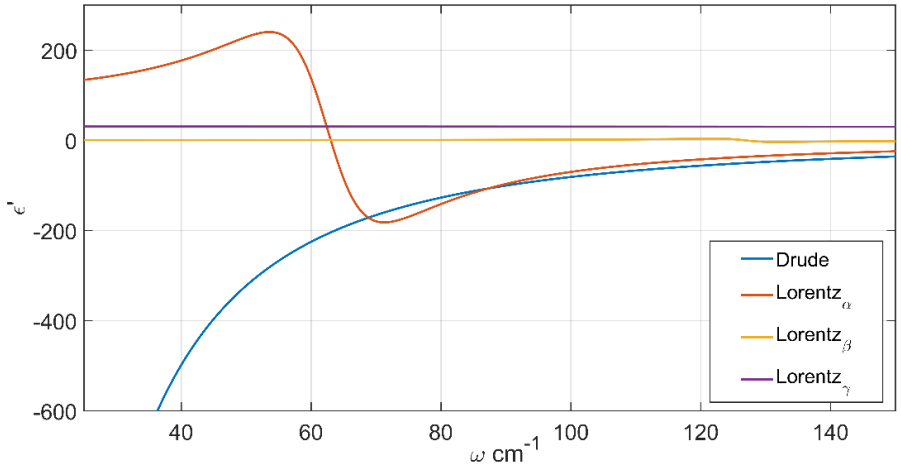

Figure 4.9 – Contribution terms of the permittivity of Bi_2Se_3 according to Equation 6, using the values from Table 1 in [20].

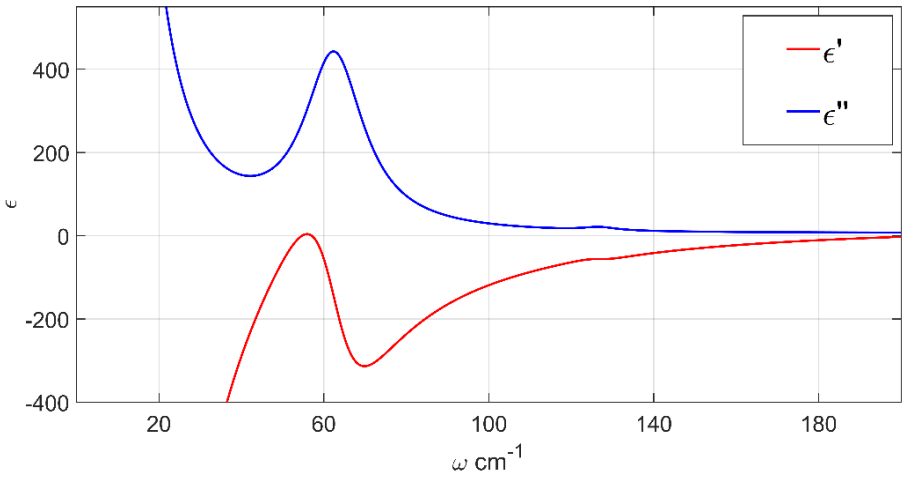

Figure 4.10 – Real (red) and imaginary (blue) parts of the permittivity of Bi_2Se_3 according to Equation 4.6.

As stated, to accurately express the dispersion relation of surface plasmons in TI samples, the dielectric function of the TI substrate ε_B must be considered. For bismuth-based TIs, sapphire (Al_20_3) is commonly used a growth substrate [213]–[215]. To determine $\varepsilon_B(\omega)$, the following expression was used.

$$\varepsilon_B = n_0^2 + (n_0^2 - 1)(\lambda\omega)^2 + i\gamma(n_0^2 - 1)(\lambda\omega) \tag{4.7}$$

Where, n_0 is the refractive index, λ is the incident wavelength and γ is a damping constant

Using experimentally determined values of $n_0 = 3.2$, $\lambda = 20.4$ x 10^4 cm^{-1} and $\gamma = 0.036$ [216], ε_B were obtained, the real and imaginary parts of which can be seen in Figure 4.11.

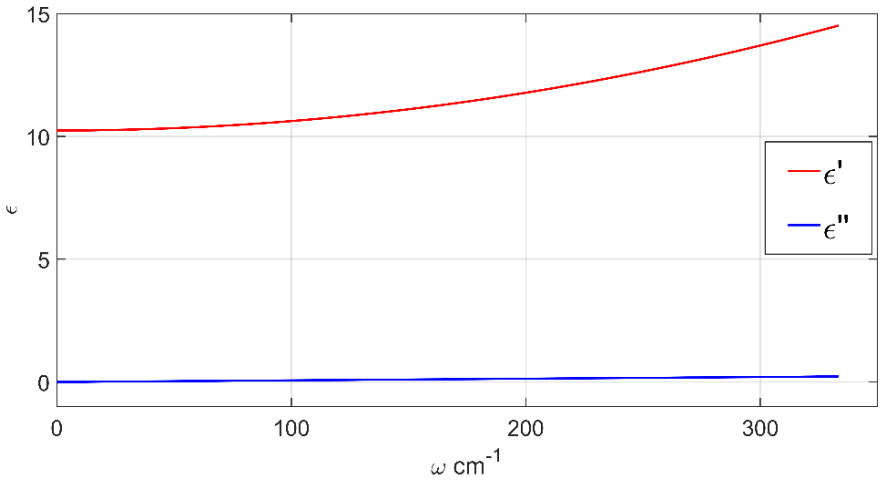

Figure 4.11 – Sapphire dispersion relation according to Equation 4.7.

By combining the above, an expression for the wave vector $k(\omega)$ of surface plasmons Bi_2Se_3 can now be determined. Inverting Equation 5 yields,

$$k(\omega) = \frac{A^{-1}\omega^2[\varepsilon_T + \varepsilon_B]}{1 - A^{-1}\omega^2 d\varepsilon_{TI}} \tag{4.8}$$

Where, $A^{-1} \equiv \frac{\varepsilon_0 h}{v_F k_F e^2}$

By substituting in the appropriate expressions for ε_{TI} (from Equation 4.6), ε_B (from Equation 4.7) and assuming $\varepsilon_T = 1$ since the top medium is assumed to be air, the wave vector $k(\omega) = k(\omega)' + ik(\omega)''$ can be obtained. The real part of $k(\omega)$ then yields the dispersion relation $\omega(k')$ and plasmon wavelength λ_{SP} according to Equation 4.3, the results of which are shown in Figures 4.12a and c. Also, the imaginary part of $k(\omega)$ yields the plasmon propagation length from Equation 4.2 , as shown in Figure 4.12b. For these calculations, the following values, from [20], have been used: $h = 6.63\text{x}10^{-34}$ Js, $v_F = 6\text{x}10^5$ ms^{-1}, $k_F = 1.52\text{x}10^9$ m^{-1}, $e = 1.6\text{x}10^{-19}$ C and $d = 27.4\text{x}10^{-9}$ m.

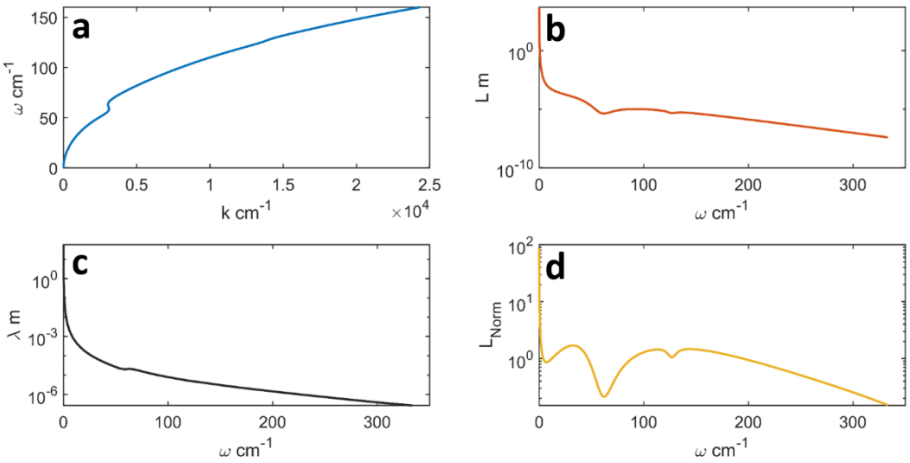

Figure 4.12 – (a) Dispersion relation for Bi_2Se_2 according to Equation 8. (b) Plasmon propagation length in Bi_2Se_3 according to Equation 2. (c) Plasmon wavelength in Bi_2Se_3 according to Equation 3. (d) Normalised plasmon propagation length in Bi_2Se_3 according to Equation 4.

The frequency with which the samples described in Section 4.3 will be probed is 3.45 THz ($\omega \sim 114$ cm^{-1}) at which a wave vector of $k \sim 1.1\text{x}10^4$ cm^{-1}, plasmon propagation length $L \sim 8.3$ µm, plasmon wavelength $\lambda \sim 5.8$ µm and therefore normalised propagation length of $L_{Norm} \sim 1.4$, would be expected according to Figure 4.12, assuming comparable material parameters. An exploration of how these values vary according to different material and sample parameters will be presented in Section 4.2.4.

4.2.3 Plasmonic behaviour of Bi_2Se_3 accounting for anisotropy

A recent alternative model of the bulk dielectric properties of Bi_2Se_3 can be found in [23]. Due to the large anisotropy of Bi_2Se_3 crystals, this model defines the permittivity differently for in-plane directions $\varepsilon_\perp$ and out-of-plane directions $\varepsilon_{//}$. Each of these components is described by two Lorentz oscillators α and β, while ε_∞ incorporates the electronic contribution in the frequency range ω.

These permittivity components take the form of the above Drude-Lorentz model (Equation 4.6) and are expressed as such,

$$\varepsilon_\perp = \varepsilon_{\perp_\infty} + \frac{\left(s_{\perp_\alpha}\right)^2}{\left(\omega_{\perp_\alpha}\right)^2 - \omega^2 - i\omega\gamma_{\perp_\alpha}} + \frac{\left(s_{\perp_\beta}\right)^2}{\left(\omega_{\perp_\beta}\right)^2 - \omega^2 - i\omega\gamma_{\perp_\beta}} \tag{4.9}$$

$$\varepsilon_{//} = \varepsilon_{//_\alpha} + \frac{\left(s_{//_\alpha}\right)^2}{\left(\omega_{//_\alpha}\right)^2 - \omega^2 - i\omega\gamma_{//_\alpha}} + \frac{\left(s_{//_\beta}\right)^2}{\left(\omega_{//_\beta}\right)^2 - \omega^2 - i\omega\gamma_{//_\beta}} \quad (4.10)$$

Where $s_{\perp_\alpha}$, $s_{\perp_\beta}$, $s_{//_\alpha}$ and $s_{//_\beta}$ are the amplitude of the α and β modes in the in-plane and out-of-plane directions respectively, $\omega_{\perp_\alpha}$, $\omega_{\perp_\beta}$, $\omega_{//_\alpha}$ and $\omega_{//_\beta}$ are the central frequencies of the α and β modes in the in-plane and out-of-plane directions respectively, $\gamma_{\perp_\alpha}$, $\gamma_{\perp_\beta}$, $\gamma_{//_\alpha}$ and $\gamma_{//_\beta}$ are the scattering frequencies of the α and β phonon modes in the in-plane and out-of-plane directions respectively and ω is the frequency range over which the sample is measured. It should be noted that in the original text, the equation from which Equations 4.9 and 4.10 have been adapted contains several typographical errors.

	$\boldsymbol{\varepsilon_\infty}$	$\boldsymbol{s_\alpha}$, cm^{-1}	$\boldsymbol{s_\beta}$, cm^{-1}	$\boldsymbol{\omega_\alpha}$, cm^{-1}	$\boldsymbol{\omega_\beta}$, cm^{-1}	$\boldsymbol{\gamma_\alpha}$, cm^{-1}	$\boldsymbol{\gamma_\beta}$, cm^{-1}
$\perp$	29	704	55	64	125	3.5	3.5
//	17.4	283	156	135	156	3.5	3.5

Table 2 – Anisotropic Drude-Lorentz model (Equations 4.9 and 4.10) parameters. Taken from the supplementary material of [23].

Using the values of Table 2, the real and imaginary parts of the total dielectric function can be determined from Equations 4.9 and 4.10. Figure 4.13 displays the real parts of $\varepsilon_\perp$ and $\varepsilon_{//}$ as well as the real and imaginary part of the total permittivity ε_{Total}, defined as $\varepsilon_{Total} = \sqrt{\varepsilon_\perp \times \varepsilon_{//}}$.

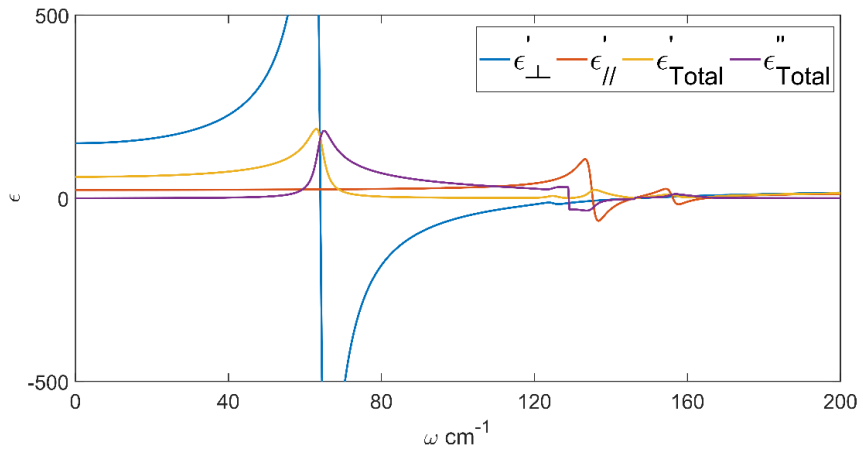

Figure 4.13 – Real part of the in-plane permittivity (blue) and out-of-plane permittivity (orange), according to Equations 4.9 and 4.10 as well as the real (yellow) and imaginary (purple) parts of the total permittivity.

Combining these terms in the expression of Equation 4.8, the plasmonic nature of Bi_2Se_3 can be determined according to this anisotropic model (2). A comparison to the results of the previous isotropic model (1) can be seen in Figure 4.14.

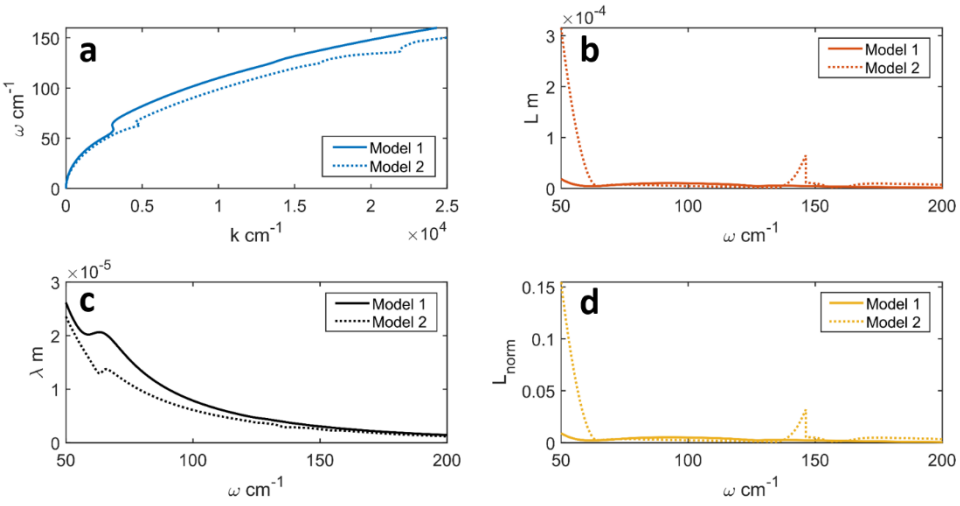

Figure 4.14 – The dispersion relation (a), plasmon propagation length (b), plasmon wavelength (c) and normalised plasmon wavelength (d) of Bi_2Se_3 from Figure 4.12, determined using model 1 (Equation 4.6), with the equivalent plots determined using model 2 (Equations 4.9 and 4.10). The values plotted in (b) and (d) are the absolute values to maintain similar y-axis scaling to Figure 4.12.

Overall it can be seen from Figure 4.14 that there is little discrepancy between the results yielded from both models. Therefore, for simplicity, the following sections will adopt model 1 in calculation of permittivities.

4.2.4 Varying ω_D

This Section and the following Sections 4.2.5 and 4.2.6 will explore the effect of changing certain material properties on the plasmonic characteristics of Bi_2Se_3, determined by the model described in Section 4.2.2.

Perhaps the most significant of these properties, in regards to the confinement of SPPs, is the Drude frequency ω_D appearing in Equation 4.6. It is notable that ω_D represents the contribution from free electrons in the *bulk* material, and is heavily dependent on the bulk charge carrier density n_{bulk}. In [20] it is argued that it is important to fully consider the bulk Drude term for the following reasons: 1) Bi_2Se_3 has a relatively narrow band gap; 2) the Fermi level lies in the bulk conduction band, and 3) intrinsic bulk defects increase the free carrier concentration. Here we calculate the Drude frequency according to the relation [217],

$$\omega_D = \sqrt{\frac{4\pi n_{bulk} e^2}{m_{eff}}} \tag{4.11}$$

where e and m_{eff} are the charge and effective mass of the conducting electrons, which for Bi_2Se_3 is $m_{eff} = 0.15m_e$ according to [23].

The bulk carrier density of TIs is determined predominantly by the doping materials but can be affected post-fabrication by applying an external voltage across the device via an integrated gate structure. Typical values of n_{bulk} for thin-film samples of Bi_2Se_3 are in the range from 1 – 6 x 10^{18} cm^{-3} [23], [172]. Adjusting this value shows how the ω_D contribution term is affected. By determining the values of ε_{TI} for this range of Drude frequencies, using Equations 4.6, and calculating the corresponding range of wave vectors from Equation 4.8, the dependence of the key plasmonic characteristics of Bi_2Se_3 on n_{bulk} can be seen. Figure 4.15 shows the SP dispersion relation, plasmon propagation length, plasmon wavelength and normalised propagation length for n_{bulk} values in the range 1 – 6 x 10^{18} cm^{-3}.

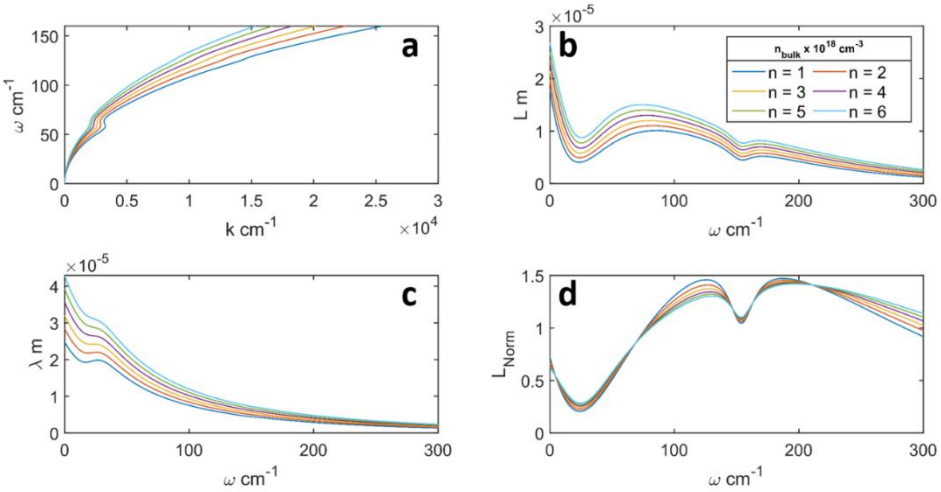

Figure 4.15 - The dispersion relation (a), plasmon propagation length (b), plasmon wavelength (c) and normalised plasmon wavelength (d) of Bi_2Se_3 for a range of ω_D calculated from Equation 4.11, using a range of $n_{bulk} = 1 - 6 \times 10^{18}$ cm^{-3}.

To summaries these results, it can be seen from Figure 4.15a and b that as n_{bulk} increases, the dispersion relation tends to lower values of k and the plasmon propagation length increases (and therefore so does the normalised propagation length). This is expected, as increasing n_{bulk} causes the material to behave more like a conventional metal, and therefore these results should more resemble those of Section 4.2.1. From Figure 4.15c it can be seen that the plasmon wavelength changes little within

the range of interest ($\omega \sim 100$ cm^{-1}), but overall the change in the dispersion relation suggests poorer confinement at higher values of n_{bulk}. This highlights the need for small n_{bulk} in experimental samples.

4.2.5 Varying d

As seen from Equation 4.8, the wave vector is dependent on the TI film thickness d. This dependence was explained in Stauber *et al* [212]. For sample thicknesses larger than six quintuple layers ($d > 6$ nm) the surface wave functions on the top and bottom of the sample couple only electrostatically and so for thick samples and large wave vectors $dk \gg 1$, this coupling can be neglected. However, for thin samples $dk < 1$, significant coupling can occur leading to the emergence of optical and acoustic modes and modification of the dispersion . For TIs this was first discussed in [183] and [218]. The model presented by Equations 4.5 and 4.6 attempts to account for these effects, and so it was used to evaluate the dispersion relation within the thin sample regime, from which the plasmon properties were obtained. These properties were evaluated in the range 20 nm $\leq d \leq$ 80 nm (Figure 4.16).

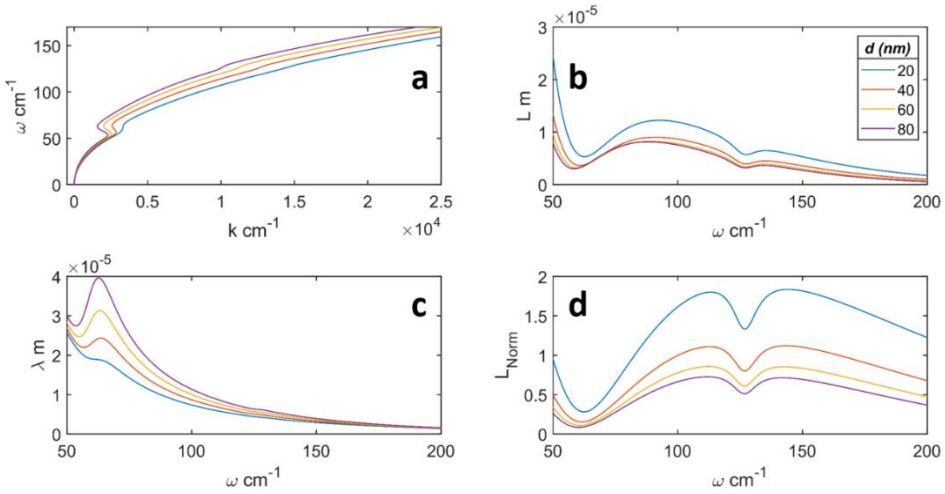

Figure 4.16 – The dispersion relation (a), plasmon propagation length (b), plasmon wavelength (c) and normalised plasmon wavelength (d) of Bi_2Se_3 for thicknesses of 20 nm (blue), 40 nm (orange), 60 nm (yellow) and 80 nm (purple), according to Equation 4.8.

The results present in Figure 4.16a and b indicate that stronger confinement is achieved for thinner samples, as the dispersion relation move towards larger values of k (i.e. away from the free-space dispersion) and λ reduces. In addition, Figure 4.16b shows that L becomes larger for smaller values of d

However, there are several factors that are not considered by the model used to determine these results, such as the presence of parasitic conduction channels formed between the top and bottom layers of the TI for small d which may disturb the surface modes [219]. Furthermore, the material quality will vary with d which may produce unpredictability in the material properties.

In general, whilst this model can give some insight on how the SP confinement in a TI is affected by the film thickness d, it is made somewhat unreliable by additional factors. The optimum value of d is therefore a compromise between these factors, which are outside of the scope of this thesis.

4.2.6 Varying E_f

The extensive study of Bi_2Se_3 can be attributed to the simplicity of its surface states as they consist of a single Dirac cone, as depicted in Figure 4.1 [220]. However, electron accumulation due to selenium deficiency causes the Fermi-energy E_f to drift away from the Dirac point into the conduction band. This can cause a significant bulk carrier density in the material, which can lead to a difficulty in detecting surface states [221]. One solution is doping the material to allow a tuning of E_f, such as that seen using Ag doping in [222]. Consequentially, E_f is an important factor to consider when fabricating and characterising TIs. Furthermore, E_f is known to have a significant effect on the dispersion of SPs, as can be seen from Equation 4.8 in which the Fermi wave vector k_F is related to E_f through the relation,

$$E_f = \frac{\hbar^2 k_F^2}{2m_e} \tag{4.12}$$

In turn, k_F is dependent on the surface charge carrier concentration $n_{surface}$ according to,

$$k_F = \sqrt{2\pi n_{surface}} \tag{4.13}$$

To observe the effects of varying k_F (or equivalently E_f), $k(\omega)$ was determined for values of k_F calculated for a range of surface carrier concentrations between $1 \leq n_{surface} \leq 6$ x 10^{13} cm^{-2}. According to Equations 4.12 and 4.13 this relates to a range of Fermi

energies ~ 0.2 eV ≤ E_f ≤ ~ 1.4 eV. The plasmonic characteristics calculated over this range are shown in Figure 4.16.

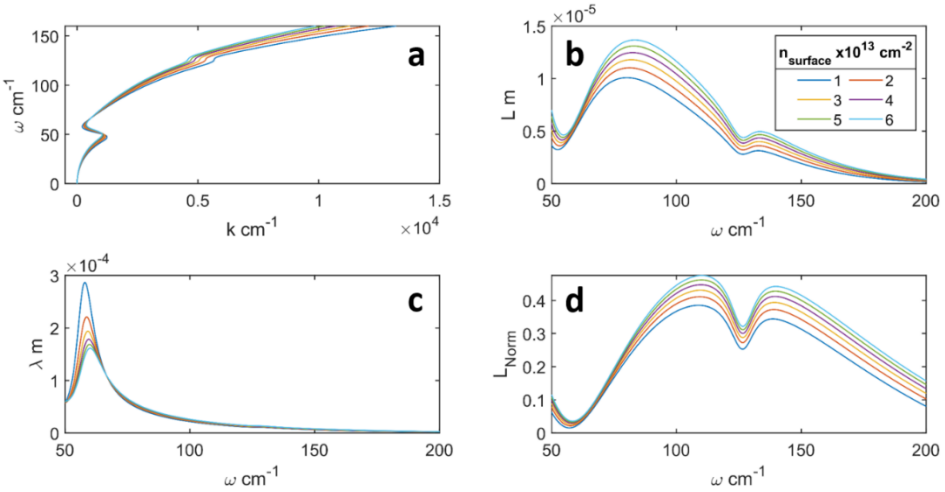

Figure 4.17 - The dispersion relation (a), plasmon propagation length (b), plasmon wavelength (c) and normalised plasmon wavelength (d) of Bi_2Se_3 for a range of k_F calculated from Equation 4.13, using a range of $n_{surface}$ = 1 – 6 x10¹³ cm⁻².

It can be concluded from the results presented in Figure 4.17 that SP confinement is good in the region of interest (ω ~ 100 cm^{-1}). L expectedly increases with $n_{surface}$ suggesting better confinement at lower surface carrier densities. Additionally, at ω ~ 100 cm^{-1} λ slightly increase with increasing $n_{surface}$ further suggesting better confinement at smaller $n_{surface}$ values. .

Furthermore, from Figure 4.17a it can be seen that at frequencies above and below the phonon mode of Bi_2Se_3 (~ 63 cm^{-1}) the plasmon wavelength increases with increasing $n_{surface}$. However, at frequencies at and around the phonon mode, the opposite of this trend is true. This highlights that a hybridisation between phonon polaritons and surface plasmon polaritons can occur. Modelling this effect correctly requires more sophisticate theoretical models, such as that developed by Wu *et al* [206].

These results concisely detail the plasmonic nature of a generic 3-dimensional TI for a variety of material parameters. Now, these models can be applied to custom grown TI samples with material parameters determined by THz-TDS analysis.

4.3 Experimental TI sample parameters

This section will detail newly fabricated MBE-grown TI films, the material parameters of which have been experimentally determined via THz-TDS (Section 4.3.2). The samples examined were three unpatterned TI films, two consisting of Bi_2Se_3, the other consisting of a ternary alloy of $Bi_2(Te_{0.67}Se_{0.33})_3$; a film of Bi_2Se_3 that has been patterned in a ribbon structure and a TI film incorporating a top gate, comprising a Bi_2Se_3 Hall bar with a $Ni_{0.8}Cr_{0.2}$ top gate layer. The fabrication of each of these samples, as well as the THz-TDS measurements performed of them was performed by Dr Craig Knox.

Bi_2Se_3 was chosen as the primary TI material to measure because of its nontrivial direct energy band gap of 0.3 eV [223] which is high compared to other TIs such as Bi_2Te_3 [224]. Furthermore, high Te-content alloys such as $Bi_2(Te_{0.67}Se_{0.33})_3$, possess a Fermi level that crosses only the topological surface state Dirac cone and, therefore, is expected to behave as an ideal 2D electron gas [225].

4.3.1 Fabrication

All samples were prepared via molecular-beam epitaxy (MBE) under a base pressure of $\sim 1x10^{-10}$ Torr. They were grown on 0.65 mm thick sapphire at a temperature of 230-240 ^{0}C, before cooling at a rate of 3 ^{0}C/min to ensure a good TI material surface. The TIs were grown via co-deposition of evaporated bismuth and selenium for the binary samples and bismuth, selenium and tellurium for the ternary sample. The bismuth and selenium were evaporated from dual-filament Knudsen calls whereas the tellurium was evaporated from a valve cracker source. All samples were grown in a chalcogenide-rich atmosphere to ensure sample quality and control of growth [21]. The resulting unpatterned samples comprised two Bi_2Se_3 films of 20 nm and 30.6 nm thickness (respectively) and one 34.4 nm thick alloy of $Bi_2(Te_{0.67}Se_{0.33})_3$.

To create the ribbon-patterned sample (wafer MBE20220536), a plain 27.4 nm thick film of Bi_2Se_3 was fabricated, using the above mentioned process, patterned using photolithography (using the photolithography mask shown in Figure 4.18) and etched using ceric ammonium nitrate solution. The sample comprised ribbons with a variety of pitches $2W$, where the width of each ribbon is W, between 8.5 μm to 40 μm.

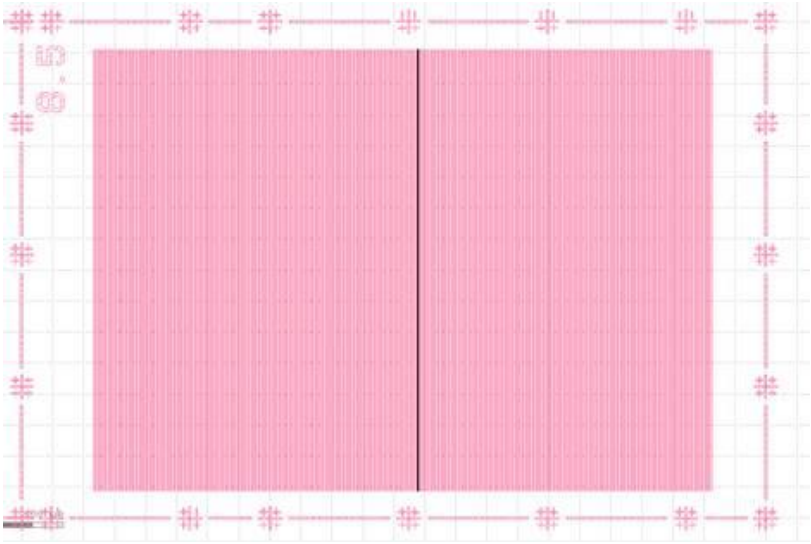

Figure 4.18 – Photolithography mask used to fabricate ribbon sample (wafer MBE20220536).

The gated Bi_2Se_3 sample (Figure 4.19) was patterned into 1 mm^2 Hall bars via chemical wet etching. 50 nm thick Cr/Au ohmic bottom contacts were deposited to the substrate via thermal evaporation, after which was sputtered a 1 nm Al layer, which was left to oxidise for 2 hours, and then a 25 nm sapphire layer was deposited via atomic layer deposition. The 5 nm $Ni_{0.8}Cr_{0.2}$ gate was then deposited via thermal evaporation, to which the 50 nm thick Cr/Au top contacts were deposited. This resulted in an 18 nm-thick layer of Bi_2Se_3 sandwiched between two dielectric layer, as seen in the inset of Figure 4.19.

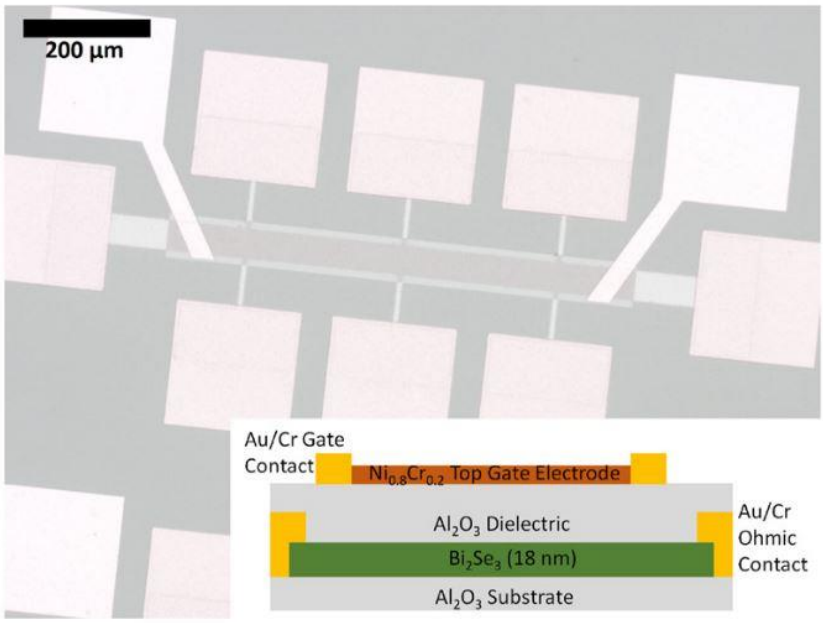

Figure 4.19 – Gated Hall-bar Bi_2Se_3 sample (wafer MBE20220530) microscope image with cross-sectional diagram (inset). Adapted from [21].

4.3.2 Simulations of samples

In order to predict the plasmonic characteristics of these experimental samples, in a similar manner to that shown in Section 4.2, the necessary material parameters for each sample must be determined. This was accomplished via THz-TDS measurements of each sample.

As mentioned in Chapter 1, THz-TDS is a powerful tool that allows for the material characterisation of a sample by measuring the transmittance of ps THz pulses through the sample in the time domain, thereby probing the response of the material to a broad range of THz frequencies. From the resulting time-domain THz field, the material properties, such as the frequency dependent real $\varepsilon'(\omega)$ and imaginary $\varepsilon''(\omega)$ parts of the dielectric function, can be determined. The permittivity can then be fitted to an appropriate model (for example Equation 4.6), to estimate key material parameters required for predicting the expected dispersion relation of surface plasmons supported by the sample.

The following figures will display $\varepsilon'(\omega)$ and $\varepsilon''(\omega)$ of the aforementioned TI films, as determined from THz-TDS measurements. Also shown are fits of the experimental data according to Equation 4.6. Furthermore, based on these fits for each sample, the calculated dispersion relation and key properties of surface plasmons (as described in Section 4.2) will be presented. The $\varepsilon'(\omega)$ and $\varepsilon''(\omega)$ values were obtained using the system described in [226]. The THz-TDS measurements were performed at 4.2 K with a spectral range of 0.5 – 4.5 THz, emitted from two LT-GaAS-on quartz PCAs. A constant bias was applied between the top gate and TI. The transmittance of the sample was acquired from the complex result of the Fourier transform, which was used to determine the optical conductivity of the sample according to Equation 1 in [21], from which the permittivity was obtained.

Figures 4.20 and 4.21 show the permittivity and plasmonic characteristics of a Bi_2Se_3 film, respectively. The film (wafer MBE210312) has thickness $d = 30.6$ nm and total carrier concentration $n = 2.79\text{x}10^{13}$ cm^{-2}. It was assumed that the surface carrier concentration would be $n_{surface} = 0.2n$ corresponding to a Fermi wave vector of $k_F = 6$ x 10^8 m^{-1}. The total carrier concentration of the films were determined via electrical transport measurements [21] by Dr Craig Knox.

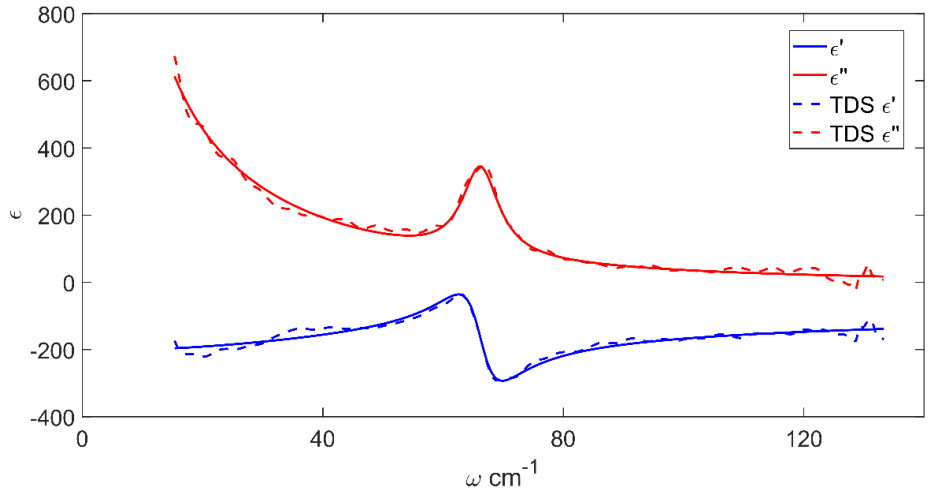

Figure 4.20 – Real (blue) and imaginary (red) part of the permittivity of sample MBE210312, according to Equation 4.6, using material parameters obtained from fitting the real (blue dashed) and imaginary (red dashed) parts of the permittivity acquired via THz-TDS.

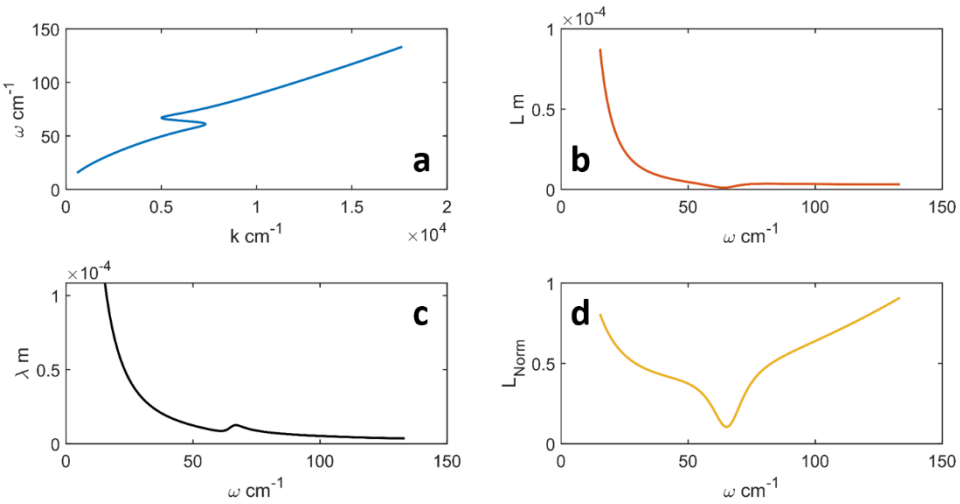

Figure 4.21 – The dispersion relation (a), plasmon propagation length (b), plasmon wavelength (c) and normalised plasmon wavelength (d) of sample MBE210312, according to Equation 4.8, using the permittivities of Figure 4.20.

From Figure 4.21 it can be predicted that, for an excitation frequency of 3.45 THz (~ 114 cm^{-1}), this sample would support SPPs with a wave vector of $k \sim 1.45 \times 10^4$ cm^{-1}, plasmon propagation length $L \sim 3.23$ µm, plasmon wavelength $\lambda \sim 4.34$ µm and therefore normalised propagation length of $L_{Norm} \sim 0.75$. THz-s-SNOM measurements of this sample will be presented in Section 4.4.

Figures 4.22 and 4.23 show the permittivity and plasmonic characteristics of a film of the ternary alloy $Bi_2(Te_{0.33}Se_{0.67})_3$ sample, respectively. The film (wafer number: MBE210318) has thickness $d = 34.41$ nm and surface carrier concentration $n_{surface} = 1.25 \times 10^{13}$ cm^{-2} corresponding to a Fermi wave vector of $k_F = 8.87 \times 10^8$ m^{-1}.

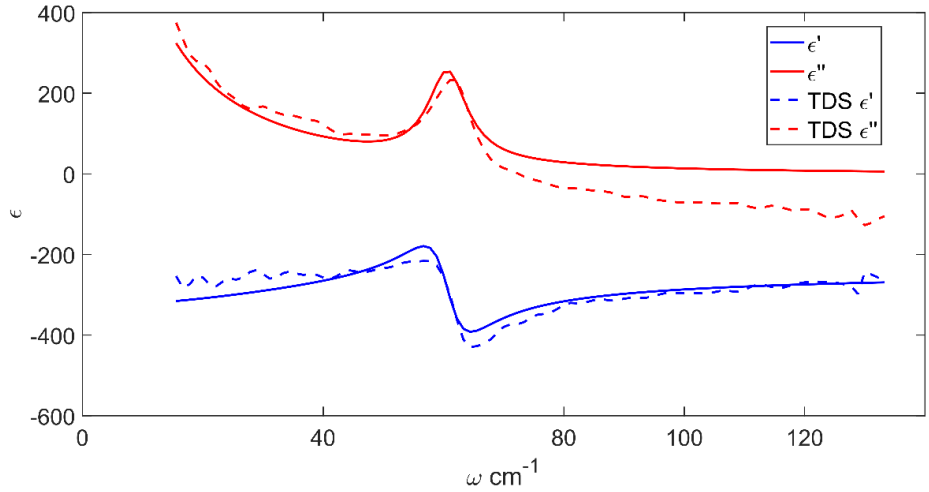

Figure 4.22 – Real (blue) and imaginary (red) part of the permittivity of sample MBE210318, according to Equation 4.6, using material parameters obtained from fitting the real (blue dashed) and imaginary (red dashed) parts of the permittivity acquired via THz-TDS.

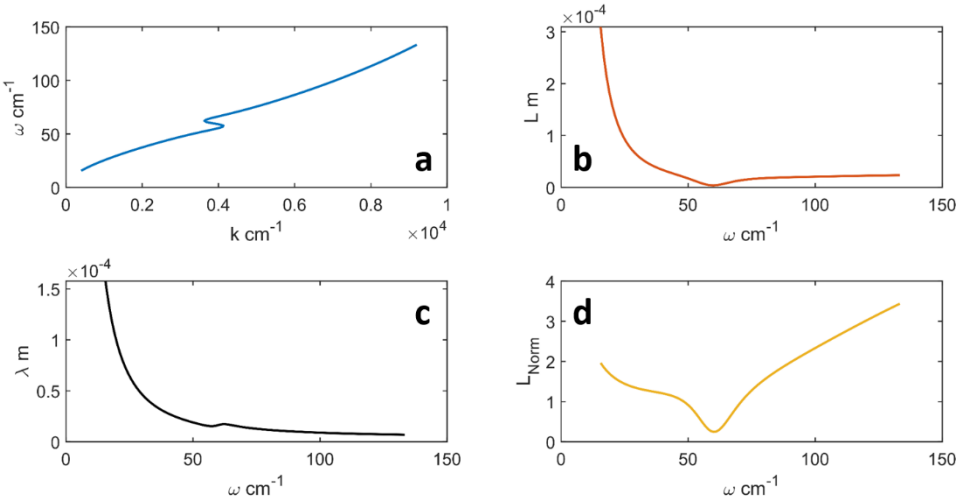

Figure 4.23 – The dispersion relation (a), plasmon propagation length (b), plasmon wavelength (c) and normalised plasmon wavelength (d) of sample MBE210318, according to Equation 4.8, using the permittivities of Figure 4.22.

From 4.23, it can be predicted that illuminating this sample with a frequency of 3.45 THz (~ 114 cm^{-1}) would yield a SPP with a wave vector of $k \sim 0.81 \times 10^4$ cm^{-1}, plasmon

propagation length $L \sim 22$ µm, plasmon wavelength $\lambda \sim$ 7.8 µm and therefore normalised propagation length of $L_{Norm} \sim 2.8$. THz-s-SNOM measurements of this sample will be presented in Section 4.4.

Figures 4.24 and 4.25 show the permittivity and plasmonic characteristics of a bulk Bi_2Se_3 sample from which the ribbon sample was fabricated. The sample (wafer MBE20220536) has thickness $d = 27.4$ nm and surface carrier concentration $n_{surface} =$ 0.53 x 10^{13} cm^{-2} corresponding to a Fermi wave vector of $k_F = 5.76$ x 10^8 m^{-1}.

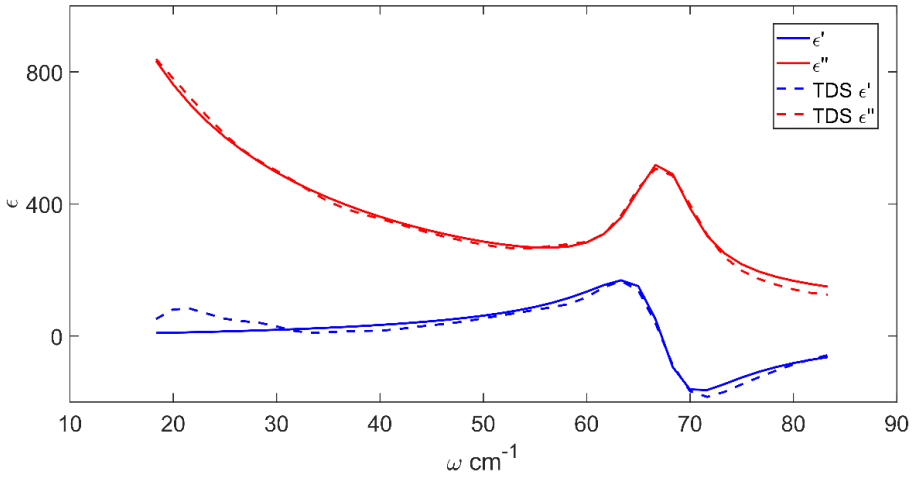

Figure 4.24 – Real (blue) and imaginary (red) part of the permittivity of sample MBE20220536, according to Equation 4.6, using material parameters obtained from fitting the real (blue dashed) and imaginary (red dashed) parts of the permittivity acquired via THz-TDS.

From 4.25, it can be predicted that illuminating this sample with a frequency of 3.45 THz (~ 114 cm^{-1}) would yield SPP with a wave vector of $k \sim 2.46$ x 10^4 cm^{-1}, plasmon propagation length $L \sim 0.3$ µm, plasmon wavelength $\lambda \sim$ 2.55 µm and therefore normalised propagation length of $L_{Norm} \sim 0.1$. THz-s-SNOM measurements of this sample will be presented in Section 4.4.

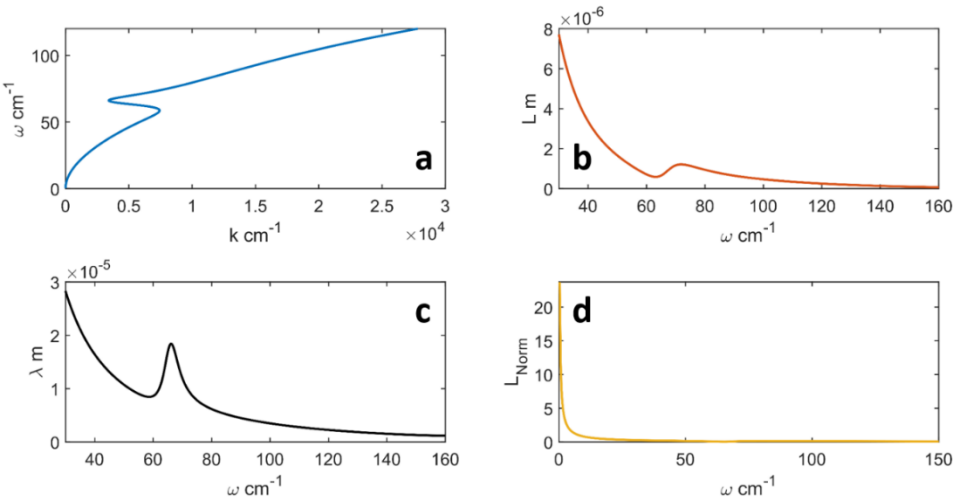

Figure 4.25 – The dispersion relation (a), plasmon propagation length (b), plasmon wavelength (c) and normalised plasmon wavelength (d) of sample (wafer MBE20220536) according to Equation 4.8, using the permittivities of Figure 4.24.

Figures 4.26 and 4.27 show the permittivity and plasmonic characteristics of a Bi_2Se_3 sample from which the gated TI film sample, seen in Figure 4.19, was fabricated. The sample (wafer MBE20220530) has thickness $d = 18$ nm and surface carrier concentration $n_{surface} = 0.7$ x 10^{13} cm^{-2} corresponding to a Fermi wave vector of $k_F =$ 6.6 x 10^8 m^{-1}.

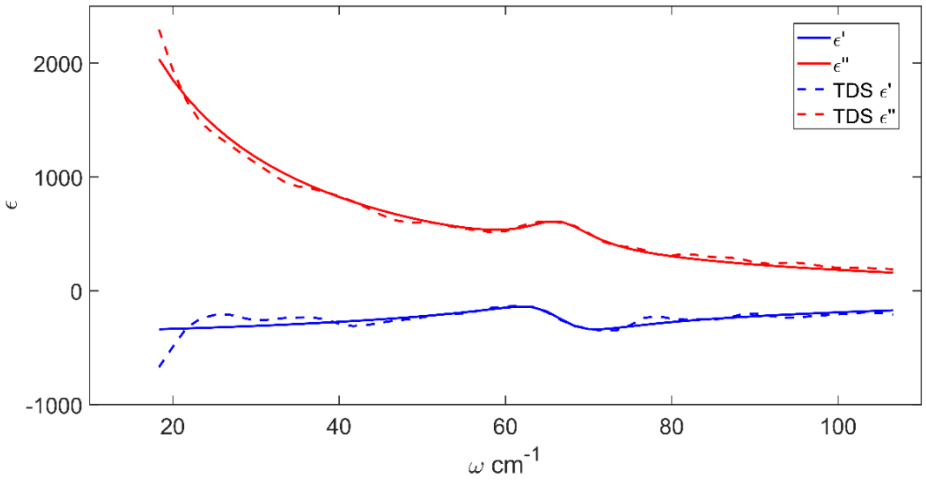

Figure 4.26 – Real (blue) and imaginary (red) part of the permittivity of sample MBE20220530, according to Equation 4.6, using material parameters obtained from fitting the real (blue dashed) and imaginary (red dashed) parts of the permittivity acquired via THz-TDS.

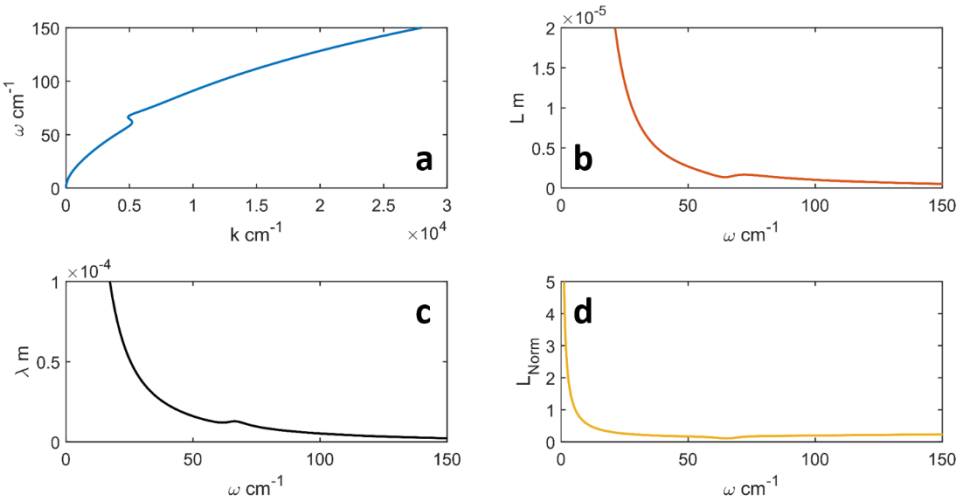

Figure 4.27 – The dispersion relation (a), plasmon propagation length (b), plasmon wavelength (c) and normalised plasmon wavelength (d) of gated Hall bar sample (wafer MBE20220530) according to Equation 4.8, using the permittivities of Figure 4.26.

From 4.25, it can be predicted that illuminating this sample with a frequency of 3.45 THz (~ 114 cm^{-1}) would yield SPP with a wave vector of $k \sim 1.56 \times 10^4$ cm^{-1}, plasmon propagation length $L \sim 0.83$ μm, plasmon wavelength $\lambda \sim 4$ μm and therefore normalised propagation length of $L_{Norm} \sim 0.2$. THz-s-SNOM measurements of this sample will be presented in Section 4.4.

From the simulations presented in Section 4.3.2, it can be seen that these samples generally possess material qualities that would support surface plasmons. The SP wavelengths and propagation lengths predicted above are all of the expected scale (≥ 1 μm) and show a normalised propagation length that should allow plasmons to be visible over a range of at least $\sim 3L_{Norm}$. These samples can now be investigated using the THz-s-SNOM technique of Chapter 2.

4.4 THz-s-SNOM of unpatterned TI films

To investigate the optical response of the TI film samples detailed in Sections 4.3.1 and 4.3.2, the THz-s-SNOM system of Chapters 2, 3 and 5 was used. As seen previously, the THz-s-SNOM technique is an ideal method with which to observe SPPs in TI materials, not least for its high resolution (See Chapter 2 Section 2.5.4) but the strong confinement,

afforded by the sharp probe tip, is sufficient to bridge the photon-surface plasmon momentum-mismatch and launch SPPs [227]. Furthermore, to purely excite SP modes, low-energy photons must be used to prevent contributions from the bulk of the material [228], [229], which is characteristic of this technique.

Initially, large areas (100 μm x 100 μm) of the Bi_2Se_3 film were measured substantially near the edges of the wafer, so that edge reflection of SPPs may be visible. These areas were also measured with scanning directions both parallel and perpendicular to the sample edge to help identify any signal variations caused by thermal drift of the laser temperature that could interfere with plasmonic imaging; these variations would principally appear parallel with the scanning direction, whereas SPP fringes were predicted to be orientated predominately parallel with the surface edge. An example of this phenomenon can be seen in similar measurements of the ternary alloy sample of $Bi_2(Te_{0.67}Se_{0.33})_3$. All subsequent images were measured using a frequency of $\nu = 3.45$ THz. Each of the scanning areas were located substantially near to the edge of the sample (within $\sim L$) in an attempt to observe the reflection of SPPs from the sample edge.

Figure 4.28 illustrates the scanning area from which the images of Figures 4.29 and 4.30 were measured. For both images, a tip tapping amplitude of $A \sim 200$ nm and s-SNOM scanning time per pixel $T_{scan} = 50$ ms was used. Figure 4.29 comprised a 100 μm x 100 μm image with a pixel resolution of 1 μm in both the x- and y-directions. Each THz image was demodulated at the $n = 3$ harmonic of the tip tapping frequency which was $\Omega \sim 80$ KHz.

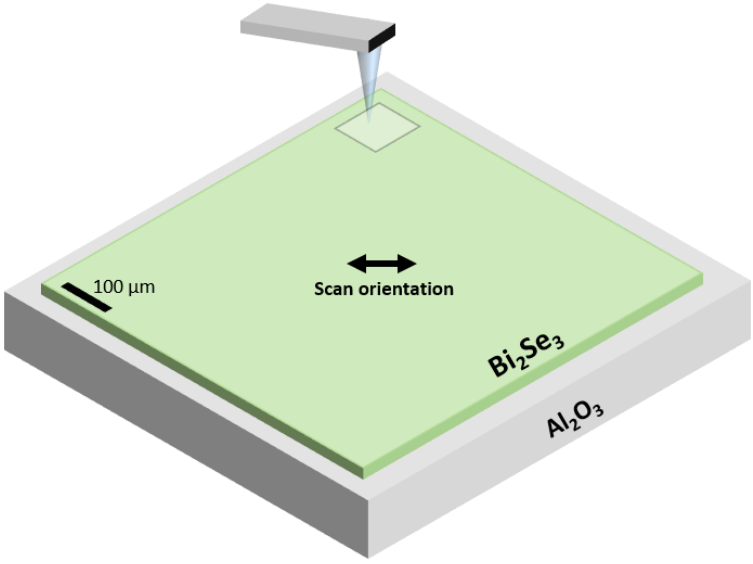

Figure 4.28 – Schematic of the scanning area of sample MBE210312. Not to scale.

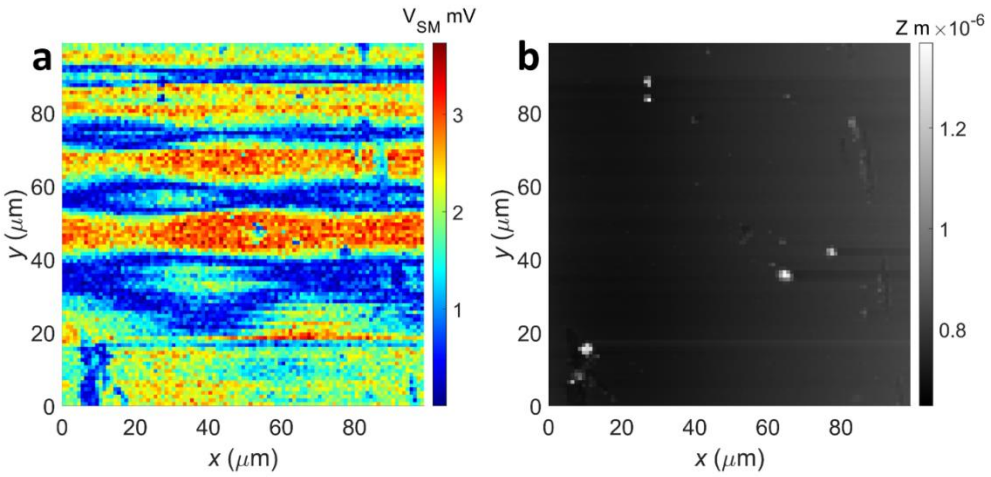

Figure 4.29 – (a) 3Ω THz and (b) topology images from a 100 μm x 100 μm THz-s-SNOM measurement of sample MBE210312, measured in the scanning location depicted in Figure 4.28.

The periodicity of the horizontal bands of large signal, displayed on Figure 4.29a, are characteristic of fringes caused by the interference between SPPs launched from the tip and SPPs reflected from the top edge of the sample. Subsequently, this area was imaged using a higher resolution with adjusted microscope parameters. Below shows a 20 μm x 20 μm measurement of an area within the scanning location seen in Figure 4.28, from which the images of Figure 4.30 were captured. Figure 4.30 has a pixel resolution of 200 nm in both the x- and y-directions.

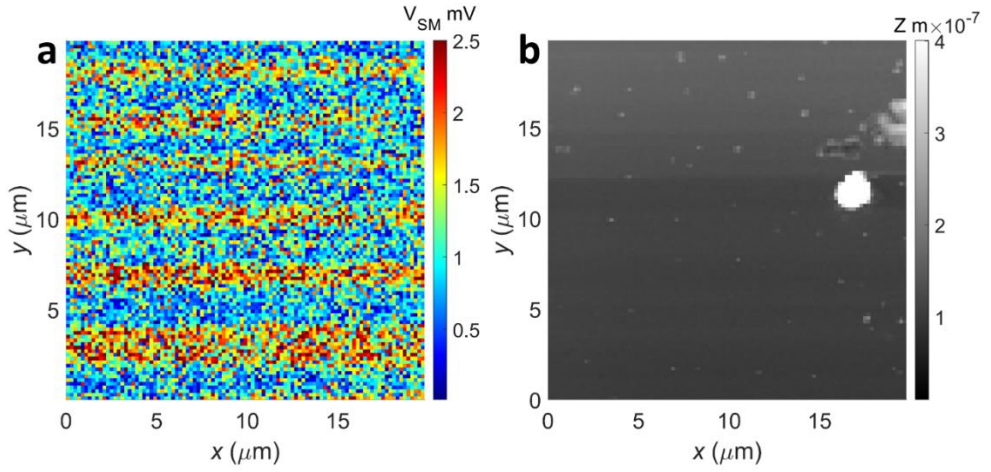

Figure 4.30 - (a) 3Ω THz and (b) topology images from a 20 μm x 20 μm THz-s-SNOM measurement of sample MBE210312, measured in the scanning location depicted in Figure 4.28.

Whilst the fringes of Figure 4.30a still look periodic, it can be seen that they vary in width and periodicity, which is uncharacteristic of SPP fringes, as well as not being of the correct wavelength predicted by Figure 4.21. Furthermore, they appear to change width according to the dimensions of the scan. This suggests that they are a features of the scan itself, such as a periodic thermal drift of the laser, rather than a feature of the TI. Thermal drift (slight variations of the QCL temperature during the scan) affects both the laser power and frequency. This manifests as a variation in the V_{SM} measured here. Further examples of this effect will be shown in Figure 4.33.

In addition to Figures 4.29 and 4.30, the same wafer MBE210312 was also measured in several other locations, examples of which can be seen in Figure 4.31. These comprised an imaging area of 85 µm x 85 µm, with a pixel resolution of 1 µm in both the x- and y-directions. A tip tapping amplitude and T_{scan} time similar to Figures 4.27 and 4.28 was used.

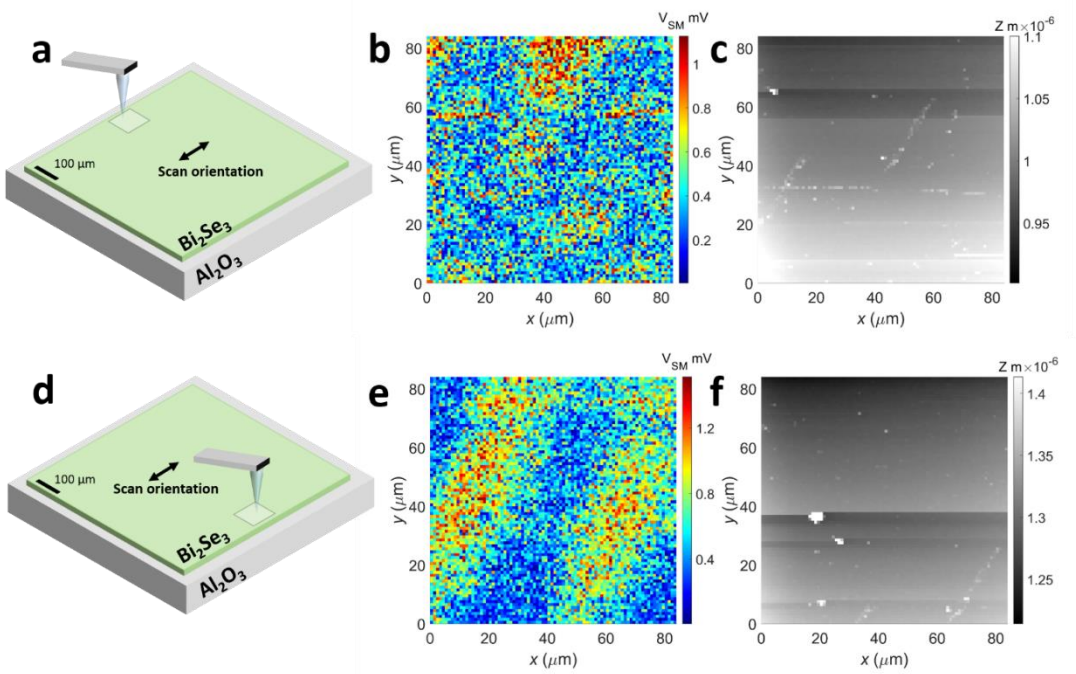

Figure 4.31 – (a,d) Scanning area schematic (not to scale), (b,e) 3Ω THz and (c,f) topology images from two 85 µm x 85 µm THz-s-SNOM measurement of sample MBE210312 in different positions on the sample.

The signal variations present in these images are the incorrect periodicity to be SPPs and are not parallel to the sample edge. It is possible that these patterns were rather the result of a signal contribution arising from a property of the substrate. To investigate this, a plain sapphire substrate wafer was imaged using a similar measurement criteria as that stated above Figure 4.31.

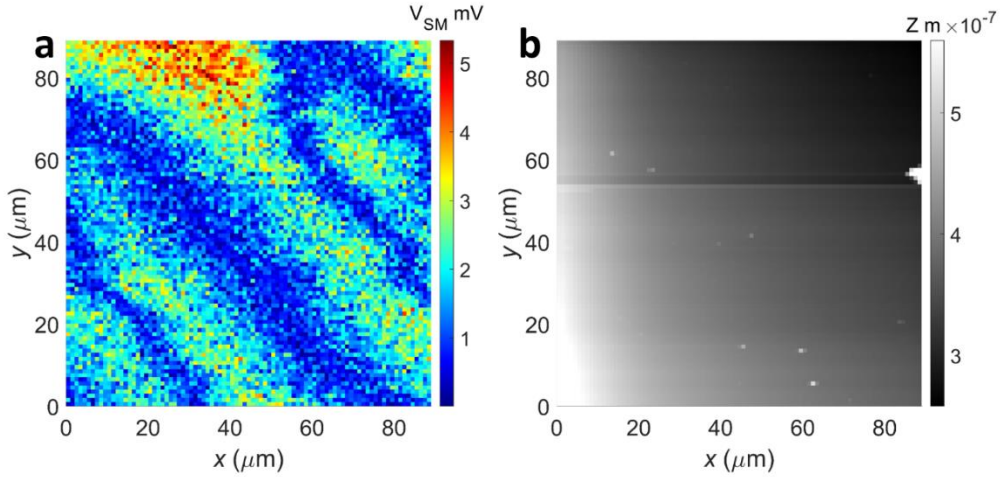

Figure 4.32 – (a) 3Ω THz and (b) topology images from a 90 μm x 90 μm THz-s-SNOM measurement of plain sapphire wafer.

It can be seen from Figure 4.32a that the THz-s-SNOM images of the sapphire substrate resembled the images of Figure 4.31 and, therefore, may explain the results of Figure 4.31. One possible explanation is that these features are the result of an etalon effect, wherein the THz beam is reflecting from the bottom of the substrate and causing an interference with the incident beam. Further investigation would be required to fully characterise these results.

In addition to the previous measurements, a film of the ternary alloy comprising $Bi_2(Te_{0.67}Se_{0.33})_3$ (wafer MBE210318) was measured. Similarly, these results did not yield images of SPPs, however, the images captured clearly demonstrate the sensitivity of this measurement technique to temperature variations of the QCL. Figure 4.33 shows two THz-s-SNOM images of sample MBE210318, showing the same 90 μm x 90 μm imaging area but rotated 90^0. Included are the images captured from measuring at the $n = 3$ harmonic of Ω as well as $n = 1$ to demonstrate the effects of thermal drift. Each image was captured using a tip tapping amplitude of $A \sim 100$ nm and pixel scanning time of $T_{scan} = 30$ ms. The area of each scan was 20 μ x 20 μm and had a pixel resolution of 100 nm in both the x- and y-directions.

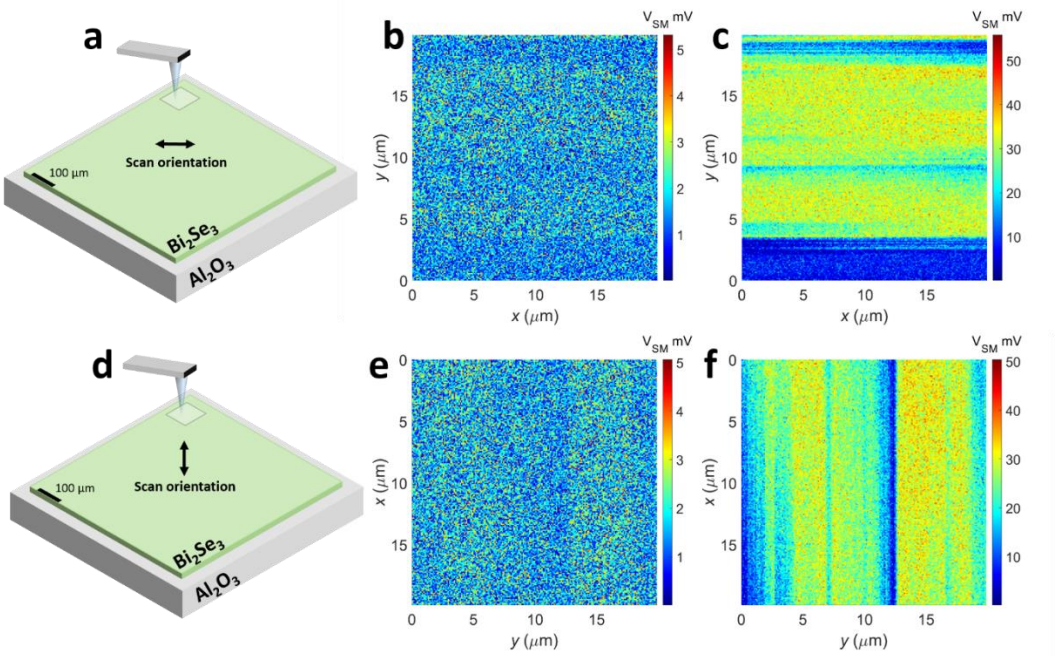

Figure 4.33 - (a,d) Scanning area schematic (not to scale), (b,e) 3Ω THz images and (c,f) 1Ω THz images of two 90 µm x 90 µm THz-s-SNOM measurement of sample MBE210312 in different orientations of the same scanning area. Figures (e) and (f) have been rotated 90⁰ to demonstrate the angle at which the scan was performed.

It can be observed from Figure 4.33 that the orientation of these features correspond to the orientation in which the scan was performed. This suggests that they are independent of the measured material and therefore the result of external changes to the laser operating parameters. The most likely explanation is drift of the QCL temperature, which can vary over time, and is particularly prevalent during scans with a long acquisition times.

To conclude, the images of the unpatterned TI samples did not provide evidence of propagating SPPs. This may be due to several factors, such as inadequate material properties, specifically a small L_{Norm} as predicted by the simulations of Section 4.3.2. Also, the signal variations arising from the substrate (as shown in Figure 4.32) could be masking any signal arising from SPPs. Additionally, degeneration of the sample (as can be seen in the surface features of Figures 4.28b, 4.29c and 4.29f) may prevent a clean reflection of SPPs from the sample edge. Another possibility is that there is insufficient coupling between the excitation beam and SPPs via the tip. Some of these factors will be addressed in the following Sections.

4.5 THz-s-SNOM of Bi_2Se_3 ribbon sample

Similar to the analysis of gold, seen in Chapter 3 and Section 4.2.1.1, for Bi_2Se_3 in the THz range, the dispersion relation is such that a coupling of the incident field to the SPP mode is prevented due to a momentum mismatch. One common technique used to overcome this is a patterning of the sample surface which provides the extra-momentum necessary for coupling. Surface plasmon resonance modes have successfully been excited in graphene nanostructures in the THz and near THz range [17], [185], [230] as well as in nanoribbons and nanorings of Bi_2Se_3 [177], [231].

Here we will consider the ribbons (or grating) of Bi_2Se_3 previously described. For a patterned sample with a ribbon width W, the momentum mismatch is provided by the grating wave vector $k_G = \frac{\pi}{W}$ [177]. From the dispersion relation for this sample, seen in Section 4.3.2 (Figure 4.25), the extra wave vector required to bridge the momentum mismatch at $\omega = 3.45$ THz is $k_G \sim 2.5 \times 10^4$ cm^{-1}. Therefore, the most suitable ribbon width would be $W \sim 1.2$ μm. Furthermore, from Figure 4.25, it can be seen that the wafer from which this sample was patterned should support a plasmon with wavelength $\lambda \sim 2.5$ μm. As such, a ribbon width ~ 2.5 μm would be expected to support a strong surface plasmon resonance for this wafer. This localised surface plasmon resonance mode should then be observed as a bright fringe across the ribbon width. Alternatively, the larger ribbon structures may effectively act as an unpatterned sample, in which SPPs launched from the microscope tip could propagate and be seen as fringes at the ribbon edge due to reflections. It is expected that any fringe pattern measured may be a superposition of these two types of fringe, as described in [17]. Based on the above considerations, single frequency THz images of ribbons with $W = 4.25$ μm and $W = 30$ μm were therefore measured. Each image comprised a 2D area spanning across the vertically aligned ribbon with areas of the substrate either side for contrast.

For SPP launching from the s-SNOM tip, this requires a coupling of the incident field to the tip, which is exclusively provided by p-polarised radiation (in which the incident field has a component out-of-plane with respect to the sample, along the axis of the tip). However, to excite SP resonances via the ribbon/grating structure, an incident field component in-plane is required. This polarisation also removes the dipole-interaction contribution to the V_{SM} signal. Considering this, the $W = 30$ μm ribbon was measured with p-polarised radiation. However, the $W = 4.25$ μm ribbon was measured with both p-polarised and s-polarised radiation with the use of a half-wave plate [15] , in an attempt to capture this resonance.

Figures 4.34 – 4.36 show the scanning area, topology, THz and averaged THz images for the $W = 30$ µm ribbon and both p-polarised and s-polarised images of the $W = 4.25$ µm ribbon.

The images of Figure 4.34 were captured using a tip tapping amplitude of $A \sim 100$ nm and pixel scanning time of $T_{scan} = 100$ ms. The area scanned was 50 µ x 5 µm with a pixel resolution of 200 nm in both the x- and y-directions.

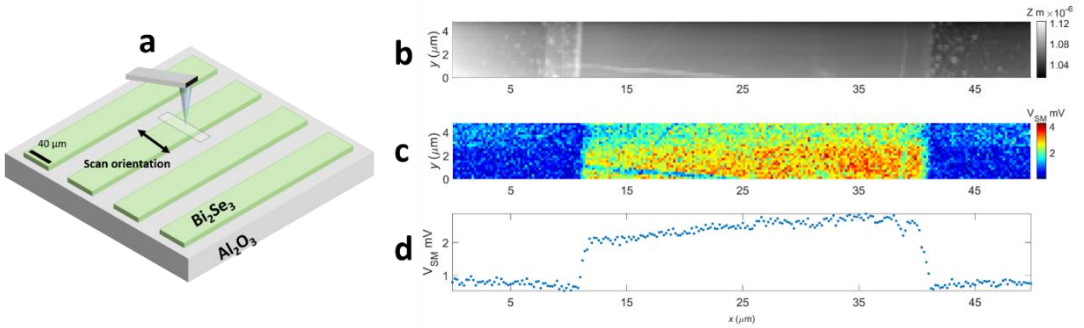

Figure 4.34 – (a) Scanning area schematic, (b) AFM image, (c) 3Ω THz image and (d) averaged THz image in the y-direction, of 30 µm wide ribbon on sample MBE20220536.

The images of Figure 4.35 were captured using a tip tapping amplitude of $A \sim 100$ nm and pixel scanning time of $T_{scan} = 250$ ms. The area scanned was 10 µ x 2.5 µm with a pixel resolution of 100 nm in both the x- and y-directions.

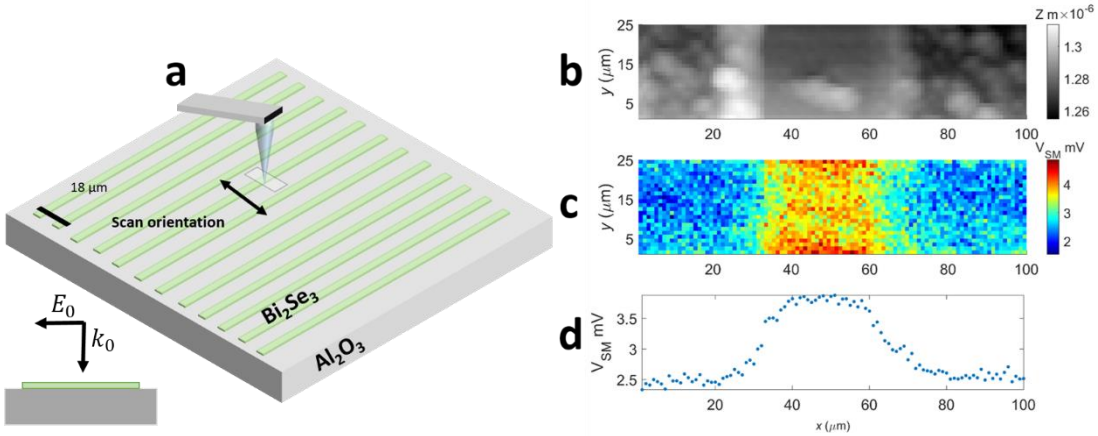

Figure 4.35 – (a) Scanning area schematic, (b) AFM image, (c) 3Ω THz image and (d) averaged THz image in the y-direction, of 4.25 µm wide ribbon on sample MBE20220536. The incident beam was p-polarised denoted by the inset showing the beam direction k_0 and field direction E_0.

The images of Figure 4.36 were captured using a tip tapping amplitude of $A \sim 200$ nm and pixel scanning time of $T_{scan} = 500$ ms. The scanning time T_{scan} was longer for this measurement to adjust for the far smaller V_{SM} signal that is common with s-polarised measurements. As such, the pixel resolution was reduced to 200 nm in both the x- and y-directions to compensate for the long scan time.

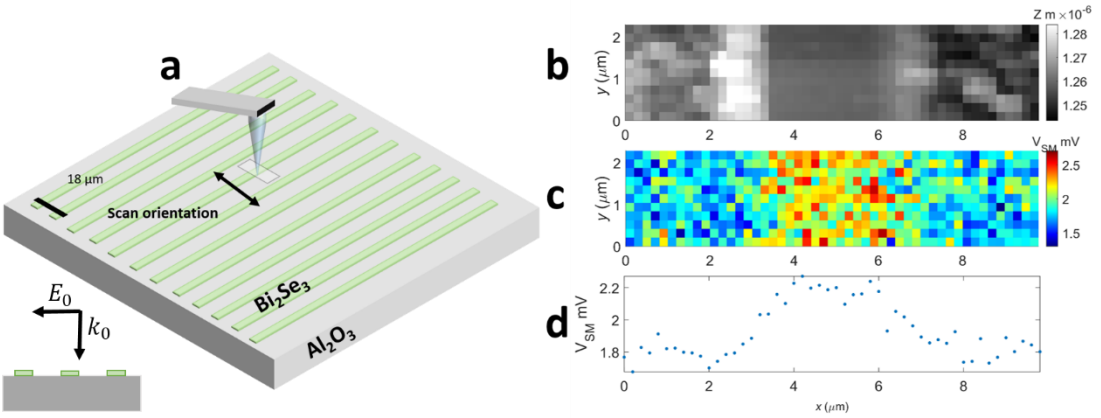

Figure 4.36 – (a) Scanning area schematic, (b) AFM image, (c) 3Ω THz image and (d) averaged THz image in the y-direction, of 4.25 µm wide ribbon on sample MBE20220536. The incident beam was s-polarised denoted by the inset showing the beam direction k_0 and field direction E_0.

To summarise these results, from Figure 4.34, there is a slight field oscillation between $x = 12$ µm and $x = 15$ µm, which may be evidence of SPPs. Performing a fully coherent measurement of this area so that both the magnitude and phase of this signal are recovered may provide a better understanding of this feature (as seen in Section 4.6). However, the inadequate material properties, described in Section 4.3.2, such that $L_{Norm} < 1$, as well as possible degradation of the TI film call into doubt the legitimacy of this result.

Furthermore, from Figures 4.35 and 4.36, it can be seen that the V_{SM} signal across each ribbon is somewhat uniform, suggesting no clear signatures of either SPPs or surface plasmon resonances. The causes of this may be the same as those stated above. Also, the features present at the edge of the ribbon, visible in the AFM image of each of the Figures above, suggests the deposition of material may have occurred during the etching process, which may interfere with the launching and/or observing of SPPs.

4.6 Coherent THz-s-SNOM of gated TI

A further Bi_2Se_3 sample was fabricated with the inclusion of a top gate (Figure 3.37), with the intention of providing the ability of the gate to influence the carrier concentration n_e, and therefore modify the plasmonic characteristics of the sample. Furthermore, to investigate this TI sample in more depth, the coherent system of Chapter 3 was employed, with the aim of mapping both magnitude and phase parameters that may more clearly reveal the presence of SPPs [208].

An initial concern with this sample was the possibility of shielding by the top gate layer which, although thin (~ 5–10 nm), could inhibit the excitation and imaging of SPPs on the TI surface. This is also compounded by the additional 25 nm of dielectric above the TI material, which, whilst may help preserve the TI surface, may also contribute to shielding effects.

It is known that the s-SNOM technique has the ability to probe the field below the surface of a sample, the depth of which is dependent on the tip tapping amplitude [151], [232].

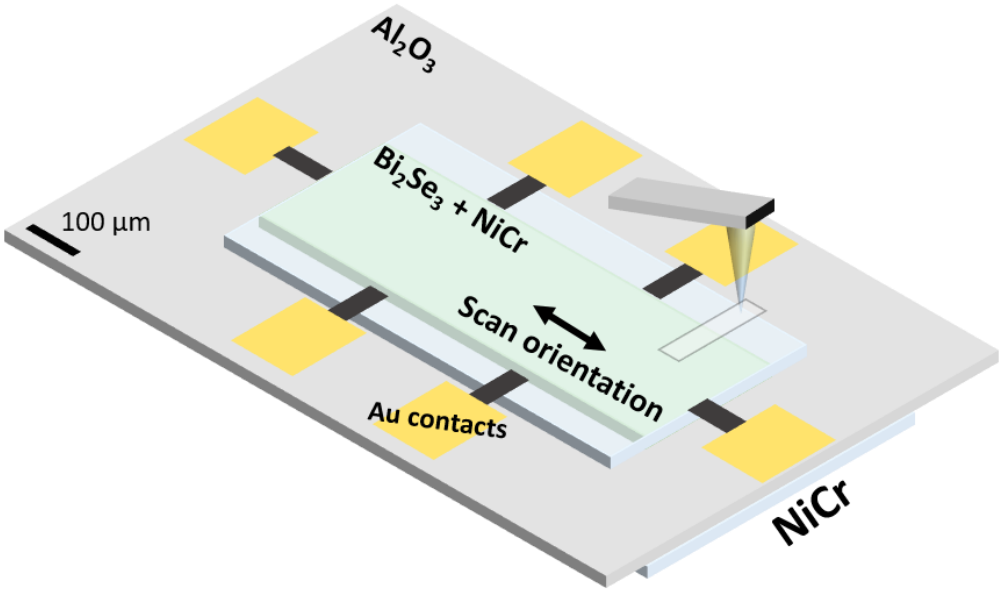

Figure 4.37 – Scanning area schematic of gated Hall bar Bi_2Se_3 sample. Omitted are the Au wires which connect to the Au contacts (yellow) and bottom gate (blue) to provide a bias across the TI.

To determine the extent of this effect, both single frequency ($\nu = 3.45$ THz) and AFM images were taken of a 2D area of the sample. These images comprised a scan area orientated perpendicular to the length of the Hall bar, including: a portion of the substrate, a portion of the gate layer overhanging the TI and a portion of the gated TI bar (as shown in Figure 4.37). This measurement was taken using p-polarised radiation, over an area of 40 µm x 14 µm, with a pixel resolution of 200 nm. A tip tapping amplitude of $A \sim 150$ nm and pixel scanning time of $T_{scan} = 150$ ms was used. An exemplar THz image taken at the $n = 3$ harmonic of the tip tapping frequency and the corresponding topography from AFM are shown in Figures 4.38a and 4.38b, respectively.

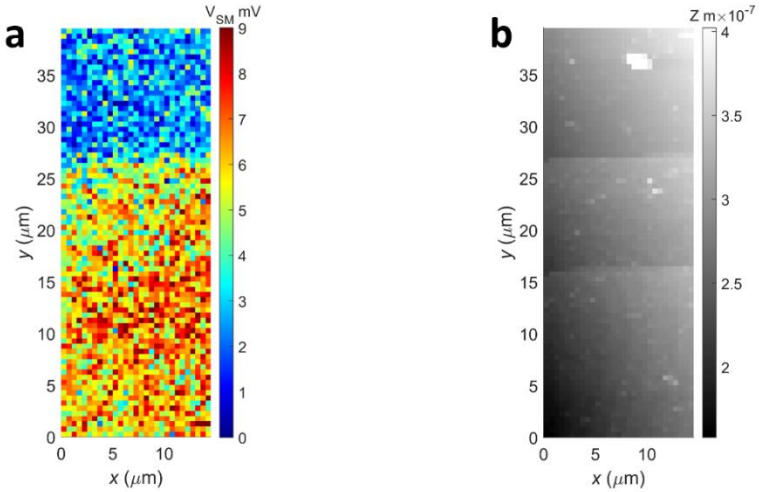

Figure 4.38 – (a) 3Ω THz and (b) topology of the gated Hall bar sample, measured in the scanning area shown in Figure 4.37.

In order to identify the position of the boundaries of the sample layers, the images of Figure 4.38 were averaged in the x-direction to obtain the values displayed in Figures 4.39a and b.

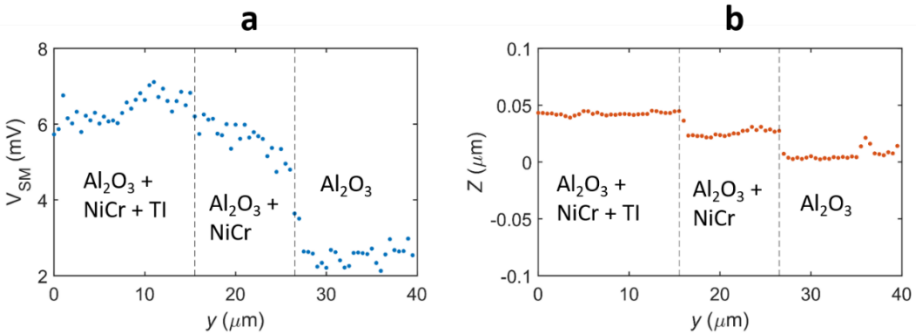

Figure 4.39 – (a) Horizontally averaged values from Figure 4.38a and (b) horizontally averaged values from Figure 4.38b.

The location of the material boundaries can be confirmed from the AFM image (Figure 4.39b) as follows: $y \sim 26.5 - 40$ µm for the substrate region; $y \sim 15.5 - 26.5$ µm for the substrate + NiCr region; and $y \sim 26.5 - 40$ µm for the substrate + Bi_2Se_3 + NiCr region, to which the THz image (Figure 4.39a) can be compared. From this comparison, the contrast between the near-field signals between each of the material areas shows the viability of probing the TI underneath the NiCr gate layer. Therefore, in a similar manner to that seen in Chapter 3 Section 3.5.2, a 22-µm-long 1D coherent measurement of the sample was taken along the long axis of the imaging area shown in Figure 4.37.

To calibrate this measurement, the microscope was aligned with the tip in proximity to the TI and a set of interferometric fringes were generated by stepping the driving current in the range 500 mA to 700 mA. From this measurement the range of currents corresponding to a single fringe were chosen as $I_{start} = 540$ mA to $I_{end} = 582$ mA, as shown in Figure 4.40. Within this current range $N = 8$ current steps were chosen for coherent imaging, according to Equation 3.16.

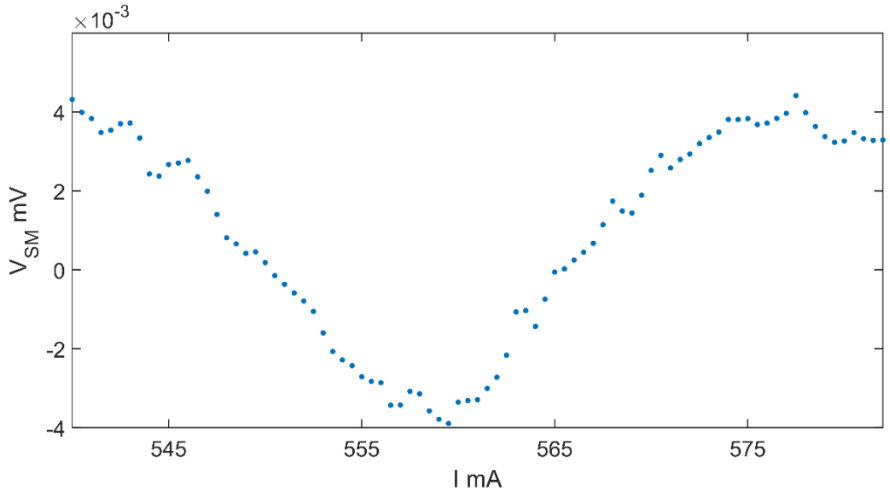

Figure 4.40 – Single interferometric fringe generated by current step between 540 – 582 mA, performed in a similar manner to that shown in Chapter 3.

For coherent imaging, a lock-in time constant of $T_{LI} = 200$ ms, current-step delay of $T_2 = 400$ ms, and s-SNOM scanning time of $T_{scan} = 4$ s was chosen to allow for ample sampling time of the self-mixing signal, which was measured at the $n = 3$ harmonic of the tip tapping frequency ($\sim$ 80 KHz). The scan was 22 µm long with a pixel size 0.2 µm, beginning at the substrate region and measuring perpendicular to the length of the Hall bar, across the material boundaries depicted in Figure 4.39. The total scan time was 7.3 minutes. This process was repeated for a range of gate voltages V_g between +5 and -5 V.

The GPSA of Chapter 3 was then used to extract the amplitude β_m and phase ϕ_m of the self-mixing signal at each pixel, which are determined from Equations 3.9 and 3.10 respectively. An example of the β_m and ϕ_m values for the case $V_g = 0$ V can be seen in Figure 4.41. For the results presented in Figure 4.41 and 4.42, the first data point corresponds to the pixel measured at the start of the TI region of the sample determined from Figure 4.39.

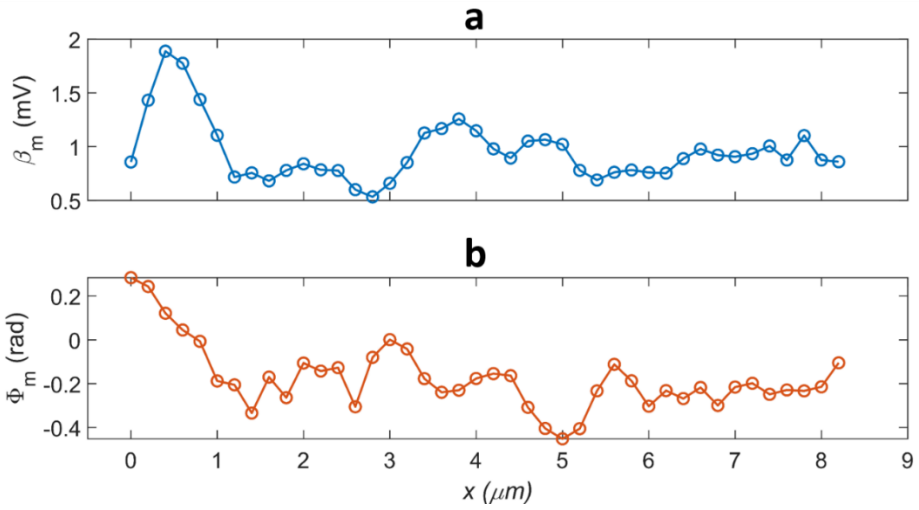

Figure 4.41 – Magnitude (a) and phase (b) extracted using the GPSA of Chapter 3 from a 1D coherent measurement scan of the gated Hall bar TI sample with $V_g = 0$ V.

Furthermore, shown in the red trace of Figure 4.42 is this self-mixing signal plotted in the complex plane, wherein the real part of the field is obtained from $\beta_m \cos \phi_m$ and the imaginary part from $\beta_m \sin \phi_m$. It can be seen that the near-field signal describes a spiral about the complex offset C. This offset accounts for the spatially constant signal due to the tip-dipole interaction and corresponds to the term $\beta_\varepsilon e^{-i\phi_\varepsilon}$ described in Equation 3.18. Very similar signatures have been observed in the literature [208], and are indicative of the presence of a strongly damped SPP propagating on the surface of the TI.

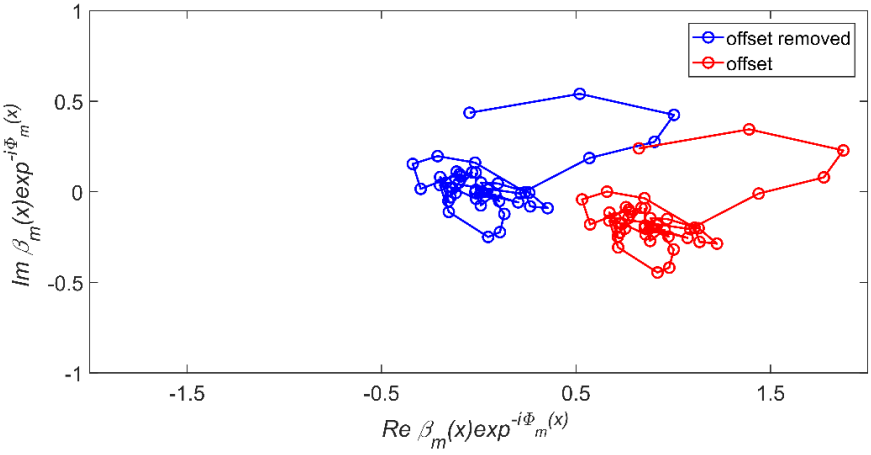

Figure 4.42 – V_{SM} signal of Figure 3.41 plotted in the complex plane with (red) and without (blue) the offset C according to Equation 4.13.

The spiral trends present in the data of Figure 4.42 mimic the form according to Equation 4.13,

$$\beta_m(x)e^{-i\phi_m(x)} = \frac{Ae^{2k_{SPP}ix}}{\sqrt{2x}} + C \qquad 4.13$$

where A is a complex fitting factor.

By removing the offset C and taking the real part of the field, Equation 4.14 can be obtained. This equation is then fitted to the experimental data (shown in the blue trace of Figure 4.42 following subtraction of the complex offset C), from which the SPP propagation length and wavelength can be obtained.

$$Re\left[\beta_m(x)e^{-i\phi_m(x)}\right] = \frac{A}{\sqrt{2x}}\cos(2xk_{SPP})\,e^{-\frac{2x}{L}} \qquad 4.14$$

Analysis of the results presented in Figure 4.43 give very similar plasmon wavelengths for both $V_g = 0$ V and $V_g = 2.5$ V as $\lambda \sim 4$ μm, which is also very close to the plasmon wavelength predicted by the simulations of Figure 4.27. The values obtained for the plasmon propagation length ($L_{V_g=0} = 24.6$ μm and $L_{V_g=2.5} = 15.2$ μm) are somewhat larger than those predicted from the simulations of Figure 4.27. However, it is possible that due to the strong dependence on x arising from the factor $1/\sqrt{2x}$, as described by Equation 4.14, the plasmon propagation length obtained from the fits to these results and each of the other gate biases is unreliable.

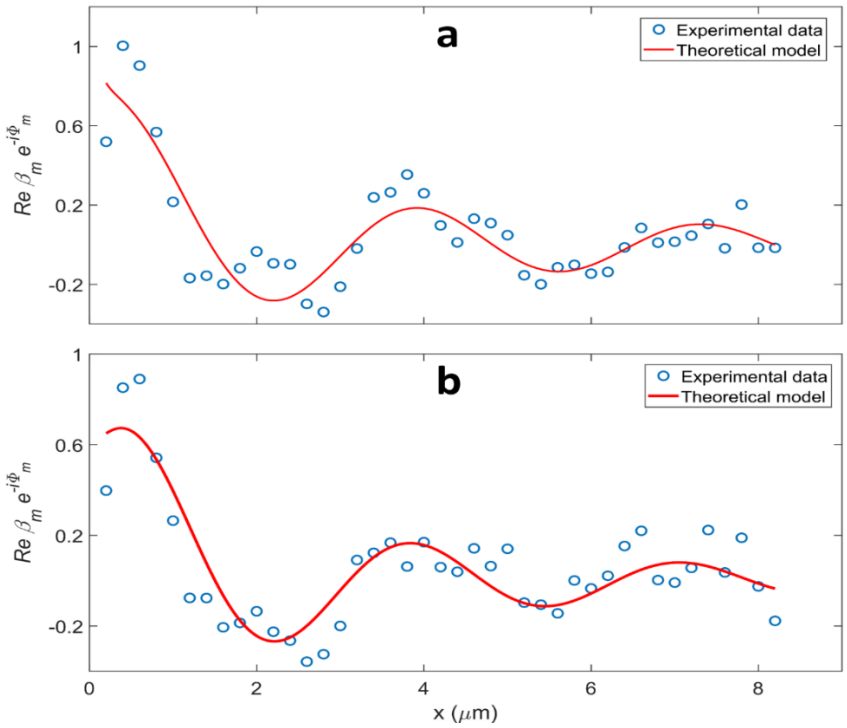

Figure 4.43 – Real part of the SPP field (blue) with Equation 4.14 (red) for coherent measurements of the gated TI using $V_g = 0$ V (a) and $V_g = 2.5$ V (b).

This analysis was performed for each measurement with a different V_g. The SPP wavelength for each of the measurements varying V_g are presented in Figure 4.44.

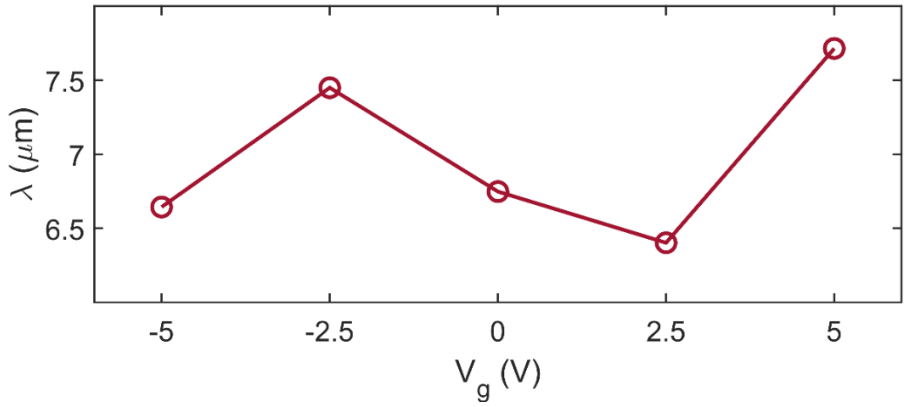

Figure 4.44 – SPP wavelength extracted using Equation 4.13 for coherent measurements of the gated TI sample using a range of gate voltages V_g = -5 – 5 V.

From Figure 4.44, it can be seen that the plasmon wavelength values extracted from each of the measurements are very similar. This suggests that the SPP behaviour in this sample does not tune with gate bias. In fact, this corroborates the findings from an investigation of this sample presented in [21], which shows that the value of V_g does not

appear to affect the carrier concentration, and causes very minimal change to its mobility.

This effect has, however, been accomplished in several other studies [173], [175], [233]. In order to modulate the surface carrier concentration, a dual gate approach is theorised, so that the density of the top and bottom surfaces of the TI can be tuned simultaneously, as explored in [173] and [233]. Additionally, the dimensions of the sample may also be adjusted, to reduce screening effects by the bulk, as seen in [175].

4.7 Summary

This chapter has investigated the examination of topological insulator materials with THz frequency radiation. The mechanisms that give rise to the unique properties of TI materials, such as Bi_2Se_3 have been explored. To understand the light-matter interaction of a thin film TI sample, a Drude-Lorentz model has been used to predict the nature of surface plasmon polaritons at and beyond THz frequencies. By using this model, the dispersion relation and key parameters of SPPs, including wavelength and propagation length, can be predicted. This allowed the variation of these parameters with a number of sample and material parameters, including carrier density, film thickness and Fermi energy to be explored. Furthermore this model was used to predict key parameters of SPPs supported by several experimental samples of bismuth-based TI films, over a range of frequencies, with material parameters acquired via THz-TDS analysis of these materials.

Furthermore, near-field 2D imaging of these samples has been performed using the aforementioned THz-s-SNOM system. From the TI film samples, the influence of the substrate surface has been observed as well as the effects of thermal drift of the laser, which both pose significant challenges when imaging these materials. Additionally, a patterned sample of Bi_2Se_3, comprising a series of ribbons varying in width was imaged in a similar manner, as an alternative means of exciting SPPs, with the optimum width calculated from a theoretical analysis of the structure.

Finally, the coherent THz imaging technique described in Chapter 3 was employed to measure a Bi_2Se_3 film incorporating a top gate. This sample was first imaged using single frequency THz-s-SNOM to determine the viability of measuring the TI through the NiCr gate. Subsequently 1D coherent near-field images of the sample were obtained, for a range of gate voltages. By evaluating the resulting near-field signal in the complex plane,

it was shown that a surface plasmon polariton has been successfully launched and measured using this technique.

The work presented in this Chapter shows, for the first time, the possibility of imaging THz SSPs on TI samples, even with the presence of a top-gate. This opens the way for the investigation and near-field imaging of electrically tunable THz SPPs in TIs.

Chapter 5

THz spoof surface plasmons on waveguide structures

5.1 Spoof plasmons and metamaterials

For most metals, their bulk plasma frequency ω_p lies in the UV regime, and plasmonic effects are therefore theoretically limited to high frequencies. At lower frequencies, the real and imaginary part of the permittivity ε' and ε'' are larger, which allows the permittivity to be dominated by the conductivity $\varepsilon \sim i\sigma/\omega$. This results in a rapid electron response to surface EM excitation, thereby minimising the effects of the EM field [116].

For small enough frequencies, the material acts as a perfect electric conductor (PEC), the limit of which can be described by the skin depth (the depth at which an EM signal attenuates to $1/e$ of its original amplitude) of the material $\delta = 1/k''$. Therefore, ratio between the skin depth and EM wavelength is,

$$\frac{\delta}{\lambda} = \frac{1}{2\pi}\frac{1}{\varepsilon(\omega)''} \tag{5.1}$$

since $k = k_0\sqrt{\varepsilon(\omega)}$.

This relation is directly related to the impedance of the metal $Z(\omega) = 1/\sqrt{\varepsilon(\omega)}$. Therefore, it can be seen that the PEC approximation becomes more accurate for low frequencies as $\varepsilon(\omega) \to \infty$. Crucially, in this regime, there is extremely poor confinement of SPPs such that the electromagnetic field propagates as a weakly confined surface wave.

To overcome this limitation and allow for light-metal confinement at lower frequencies, such as THz, a novel genre of material is required. In 2004, Pendry *et al* [234] proposed a metallic structure comprising an array of holes on the surface of a perfect conductor. Both the size and periodicity of the holes and array were subwavelength, resulting in an

enhanced surface impedance, allowing for confinement of long wavelength radiation to the surface.

Materials such as these, which use artificial structures to augment their EM properties and mimic SPs are called Metamaterials. Consequently, the plasmonic modes that they support are called spoof surface plasmons (SSP), the dispersion relation of which depends on the geometry of the metamaterial rather than its atomic composition [235], [236].

The work presented in [10], on which the remainder of this Chapter takes as a starting point, concerns, amongst other things, the design and characterisation of novel metamaterial geometries that can support SSPs, a summary of which is given in Section 5.2.

5.2 Overview of previous work

5.2.1 PSP waveguide design

It has been seen that light-matter confinement can be facilitated beyond its physical limits using structures such as metamaterials. By engineering specific geometries, waveguides that can support surface modes, henceforth known as spoof surface plasmon polaritons (SSPPs), can be achieved. SSPP propagation on such structures has been demonstrated in helically grooved 'metawires' [237] and periodic rows of 'dominos' [238], [239].

Sub-wavelength confinement of radiation offers great promise of scalable plasmonic circuitry, leading to the development of nanometric optical devices [240], [241]. However, SSPPs are difficult to control when propagating in anything other than straight lines. One answer to this was the proposal of conformal surface plasmons (CSP) which are supported by ultra-thin, flexible waveguides and whose propagation can comply with surface curvature [242]. CSPs have been demonstrated at microwave, THz and mid-infrared frequencies and have been used in many applications such as beam steering [243], [244], frequency manipulation [245], [246] and spoof plasmon propagation/amplification [247], [248].

In previous work [10], a metamaterial waveguide was demonstrated, wherein an ultra-thin CSP-supporting structure is placed on a rigid Si substrate, on which a type of SSPP

called a planar surface plasmon (PSP), owing to the thin nature of the waveguide, can propagate in the THz frequency range.

This structure was analysed using the simulation software ANSYS HFSS, wherein its dispersion relation, out-of-plane electric field E_z, plasmon amplitude and propagation length, S_{21} parameters and cut-off frequency were determined.

Taking inspiration from Shen *et al* [242], the PSP waveguide design (Figure 5.1 inset) is comb-shaped comprising a shaft, protruding perpendicular from which is a series of identical bars with length h and periodicity d (also referred to as the unit length). The distance between each bar is a and the thickness of the whole structure is t. The waveguide material is gold and is placed on a silicon substrate with permittivity, $\varepsilon_s = 11.65$.

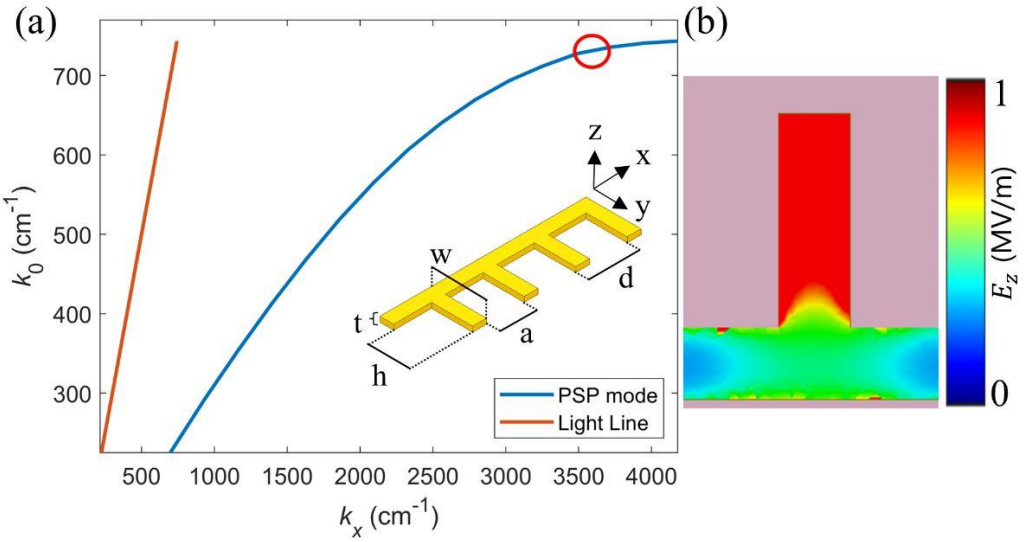

Figure 5.1 – Dispersion relation for fundamental mode of comb-shaped PSP waveguide (a) and normalised amplitude of the out-of-plane electric field of a unit cell obtained using FEM (b). Geometric parameters of the waveguide with $w = 1.07d$, $a = 0.73d$ and $h = 0.8d$ where $d = 7.5$ μm (a inset). Adapted from [10].

The dispersion relation for the fundamental mode of a simulated SSPP propagating along the x-direction of the structure with momentum k_x was calculated using the eigenmode solver of the software ANSYS HFSS (Figure 5.1a). From Figure 5.1a, it can be seen that the dispersion relation for the PSP waveguide deviates from that of a free-space EM wave and therefore suggests that the waveguide supports the propagation of confined modes.

The behaviour of the dispersion relation is determined by h but, as explained in [242], not t, since the magnetic field remains unquantised from very large t to almost zero

thickness. The dimension h dictates the frequency $\omega_c = \frac{\pi c}{2h}$ which determines the asymptote frequency of the PSP mode, whereas a (and therefore d) dictates the waveguide cut-off frequency f_c which increases with a. This cut-off arises due to the waveguide behaving as a low-pass filter, that is, for incident frequencies that lead to the condition $k_x > \pi/d$, the interaction enters the Bragg reflection regime in which no propagation mode is supported [249]. Considering the frequency of radiation with which this waveguide and the following structures comprising thereof would be analysed, as 3.45 THz, the waveguide dimensions were chosen to allow a free-space beam of this frequency to launch SSPPs on the surface with deep sub-wavelength confinement. As a result, the waveguide was designed to have dimensions d = 7.5 µm, $a = 5.5$ µm, $w = 8$ µm, $h = 6$ µm and $t = 0.1$ µm. This produced a waveguide with cut-off frequency $f_c \sim 3.6$ THz.

The SSPP wave-vector k_x was determined from the aforementioned simulations to be $k_x = 3500$ cm^{-1} for an excitation frequency of $f_0 = 3.45$ THz. Given the SSPP wavelength as $\lambda_{SP} = 2\pi/k_x$, this yielded a value of $\lambda_{SP} = 18$ µm, corresponding to $\sim \lambda_0/5$.

5.2.2 Wave port simulations

To capture the nature of SSPPs propagating along the PSP waveguide described above, the out-of-plane electric field E_z and scattering S_{21} parameter were simulated by launching an SSPP from one end to the other of a 208 µm long rendition of the structure, using the wave port simulation environment of ANSYS HFSS (Figure 5.2).

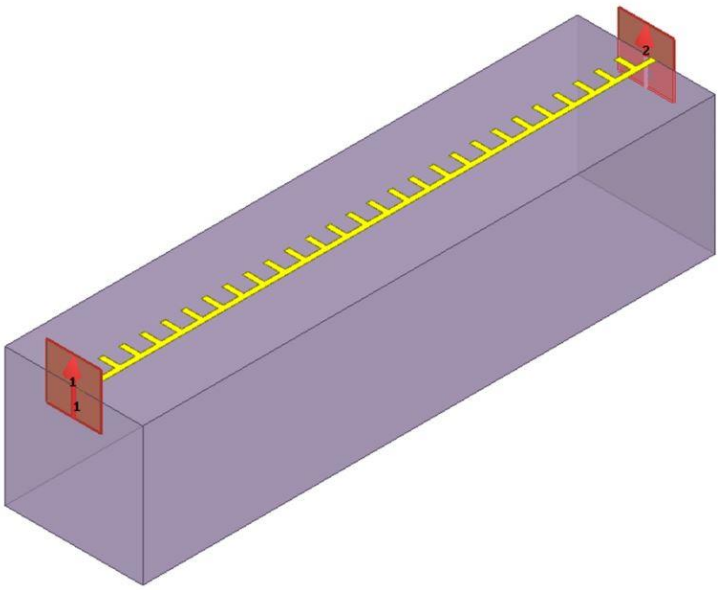

Figure 5.2 – ANSYS HFSS wave port simulation environment for PSP waveguide with SSPP propagating from port 1 and detected at port 2. Adapted from [10].

Figure 5.3 shows the real part of the resulting z-component of the field E_z at the surface of the waveguide for an excitation frequency of 3.45 THz, which clearly depicts a periodic oscillation of the field from $+E_z$ to $-E_z$ along the x-direction. Additionally, the field appears to decay with distance along the x-direction owing to ohmic losses.

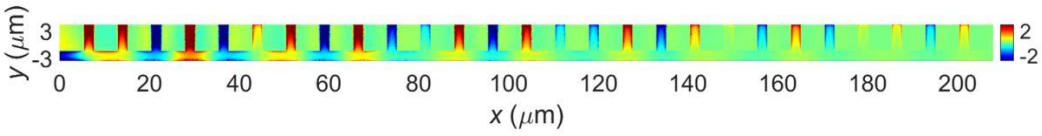

Figure 5.3 – Real part of the out-of-plane electric field E_z (MV/m) on the surface of a 208 μm long PSP waveguide, captured from the simulation environment of Figure 5.2. Adapted from [10].

To extract the SSPP parameters, the field within each bar was spatially averaged and collectively plotted, fitted to which was Equation 5.2 (Figure 5.4). The SSPPs are modelled as bound propagating surface waves with out-of-plane field E_z, wave-vector k_x and propagation length L_p. As such, Equation 5.2 describes a time-independent, single-mode, exponentially decaying sinusoidal function with initial amplitude E_0, phase θ and propagation length L_p.

$$E_z = E_0 \cos(k_x x - \theta) \exp\left(\frac{-x}{L_p}\right) \qquad 5.2$$

From the extracted SSPP wave vector value of $k_x = 3350$ cm^{-1}, the SSPP wavelength was calculated to be $\lambda_{SP} \sim 18.75$ μm, which agrees well with that predicted in Figure 5.1.

In this previous work it was also observed that a significant proportion of the energy of the SSPP that reached the end was reflected back along the waveguide, due to an impedance mismatch experienced by the SSPP at this boundary, producing a standing wave. This has been considered when designing and analysing more complex structures, such as that seen in Section 5.3.

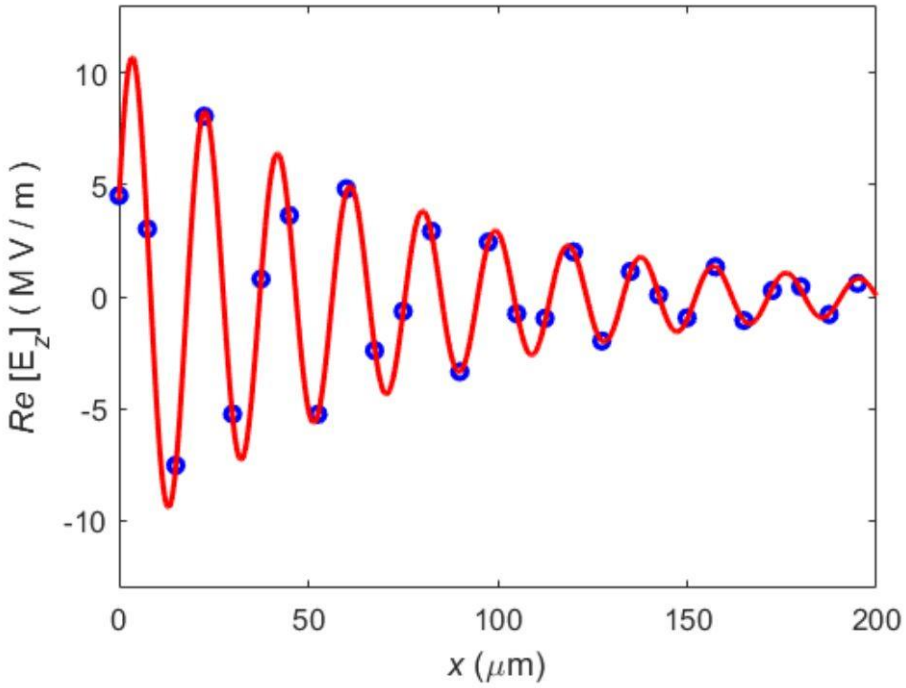

Figure 5.4 – (Blue) Averaged E_z values for each bar of the PSP waveguide extracted from Figure 5.2. (Red) Equation 5.2 with fitting parameters of $E_0 = 11$ MV/m, $k_x = 3350$ cm^{-1}, $\theta = 1.2$ rad and $L_p = 75$ μm. Adapted from [10].

5.2.3 Free-space excitation simulations

In order to improve coupling of an incident beam to the SSPP mode of the PSP waveguide, a grating structure was designed to provide momentum matching [250]. The optimum grating period to achieve this can be found using Equation 5.3,

$$k_z = k_0 \sin\theta_i + q\boldsymbol{k} \tag{5.3}$$

where k_z is the in-plane component of the incident photon momentum after interacting with the grating, k_0 is the free-space wave vector, q is the order of diffraction, θ_i is the angle that the incident beam makes with respect to the in-plane x-direction, and $\boldsymbol{k} = 2\pi/\alpha$, where α is the grating period.

By setting k_z to equal the SSPP wave vector k_{SP} and $q = 1$, then from Equation 5.3 we obtain,

$$\frac{2\pi}{\lambda_{SP}} = \frac{2\pi}{\lambda_0}\sin\theta_i + \frac{2\pi}{\alpha} \tag{5.4}$$

since $\lambda_0 \gg \lambda_{SP}$, it can therefore be seen that optimum coupling occurs for $\alpha \approx \lambda_{SP}$. Nevertheless, the grating structure dimensions have been fully optimised previously through numerical simulations in HFSS, the details of which can be found in [10], [22]. To summarise, it was determined that, for s-polarised excitation under oblique incidence, the presence of the grating improved the coupling strength by over 200 %. The optimised grating (Figure 5.5a) has total length $L_g \sim \lambda_0 = 87$ µm, slit length $L_s = 25$ µm and distance to the waveguide $g_{off} = 10$ µm.

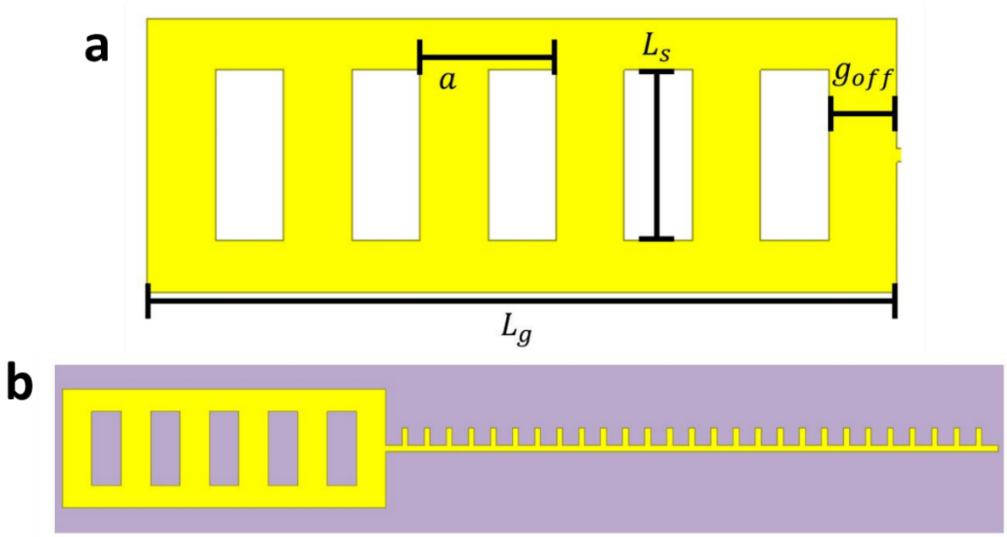

Figure 5.5 – (a) Schematic diagram of grating structure with period $\alpha = 20$ µm, length $L_g \sim 87$ µm, offset $g_{off} = 10$ µ and slit length $L_s = 25$ µm. (b) Schematic diagram of the 208 µm PSP waveguide integrated with the grating of (a). Adapted from [10].

Free-space excitation simulations of the aforementioned 208 µm PSP waveguide, incorporating this grating structure at one end, were then performed using HFSS. The simulation environment comprised the waveguide place on the surface of a silicon substrate with thickness $t = 50$ µm. The environment boundaries were defined with perfectly-matched layers (PML) which were used to absorb reflections and scattered components of the incident field, mimicking an infinite space. The incident plane was placed 174 µm above the substrate emitting a frequency of 3.45 THz. The incident electric field E_0 is in the x-direction when s-polarised and the angle of incidence with the surface normal of the free-space beam k_0 is $\theta_i = 54^0$ under oblique incidence, which was chosen to match the illumination geometry of the THz-s-SNOM. Figure 5.6 shows this beam orientation that was used in the free-space excitation simulations of the waveguide structure.

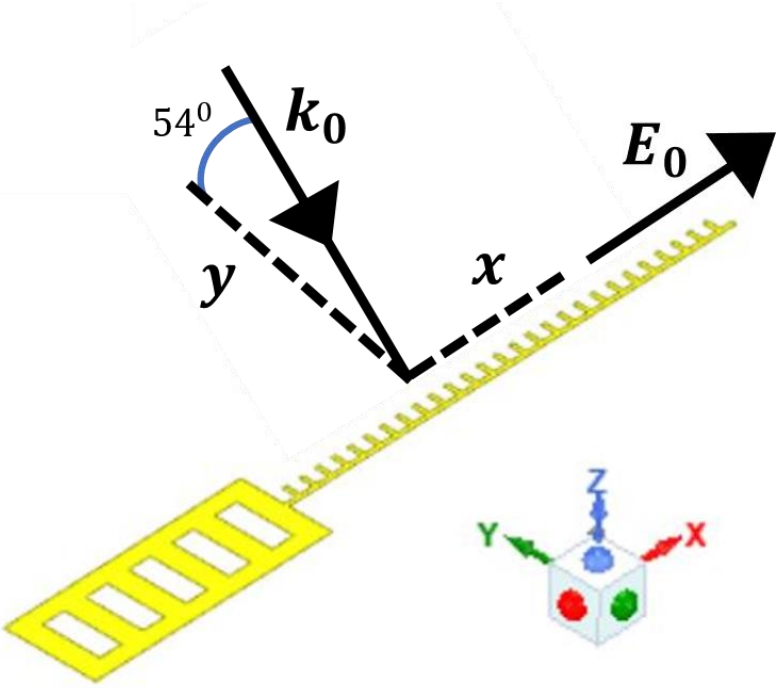

Figure 5.6 – S-polarised simulation orientation showing direction of incident beam wave vector k_0 and electric field E_0 with respect to the waveguide structure. Adapted from [22].

The primary difference with these simulations compared to that of Section 5.2.2 is that the free-space excitation permits the launching of SSPPs at both ends of the waveguide. Therefore, the structure's length (208 μm) was chosen to be sufficiently long so that each SSPP had significantly attenuated before reaching the other, reducing interference and simplifying analyses. Figure 5.7 displays the free-space beam simulation results for an oblique incident angle using s-polarised radiation. With this beam orientation, the beam propagation direction is perpendicular to the length of the waveguide, which leads to the phase of the beam being the same across the whole structure.

Furthermore, the field of the beam has a component in the x-direction which will polarise the bars. The evaluation of this simulation data comprised the real part of the electric field $Re(E_z)$ averaged for each bar plotted and fitted to Equation 5.2 for both the SSPPs launched from both the left and right ends of the waveguide (i.e. with and without grating). Figures 5.7b and c summarise these results, which show a clear oscillating electric field propagating from both sides of the waveguide. The fitted wave-vector agreed well with that determined from the wave-port simulation and yielded a value of $k_x \sim 3600$ cm^{-1}. However, the propagation length appears to be shorter than expected $L_p \sim 60$ μm. Despite the length of the waveguide, this was attributed to interference between the two counter-propagating SSPPs.

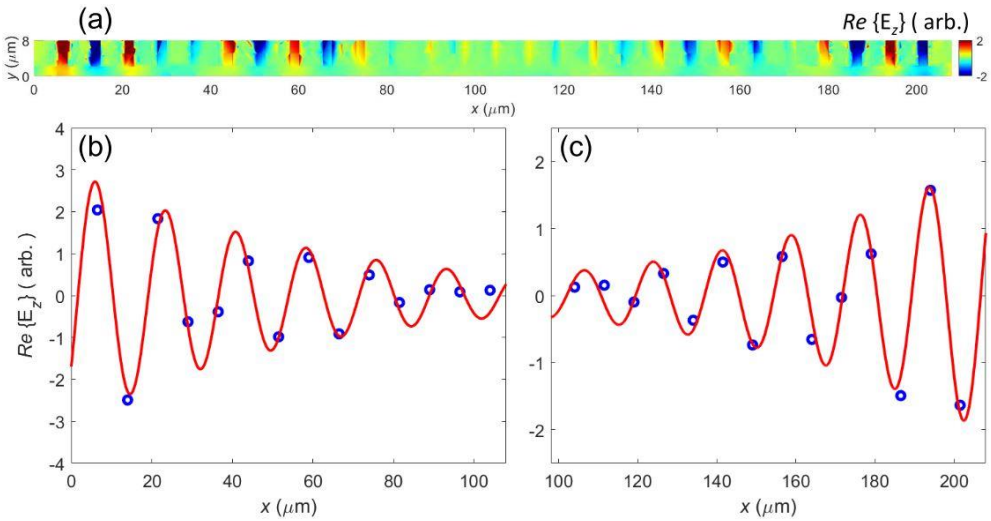

Figure 5.7 – (a) Simulated real part of the out-of-plane field E_z on the surface of a 208 μm-long PSP waveguide excited by an s-polarised 3.45 THz incident beam. Spatially averaged values of E_z per bar for the area $x = 0$ – 104 μm (b) and $x = 104$ – 208 μm (c), fitted to which is Equation 5.2 with fitting parameters $E_0 = 3 \pm 0.18$ (arb), $k_x = 3600$ cm^{-1} and $L_p = 60$ μm. Adapted from [22].

5.2.4 Experimental results

To confirm the excitation of SSPPs in the PSP waveguide and grating design described in the previous Sections, a 208-μm-long PSP waveguide structure with the grating of Figure 5.5a, was fabricated and measured using THz-s-SNOM. Figure 5.8 shows a 3.45-THz image of the sample obtained by s-SNOM, in which the waveguide was excited with s-polarised radiation and the signal is derived from the $n = 2$ harmonic of the self-mixing voltage. Figures 5.8b and c show the spatially-averaged values of field plotted as a function of distance from each end of the waveguide along with the numerical fits to Equation 5.2 (red lines). From this experimental investigation, values of $k_{SP} = 4180$ cm^{-1} and $L_p = 51$ μm were obtained, in reasonable agreement with the simulations of the same structure. This suggested that the electric field associated with SSPPs on the waveguide obtained in Sections 5.2.2 and 5.2.3 have been experimentally confirmed. By proving that this structure can adequately support SSPPs, it was then used in the design of a more complex, dual-waveguide coupling structure described in Section 5.2.5.

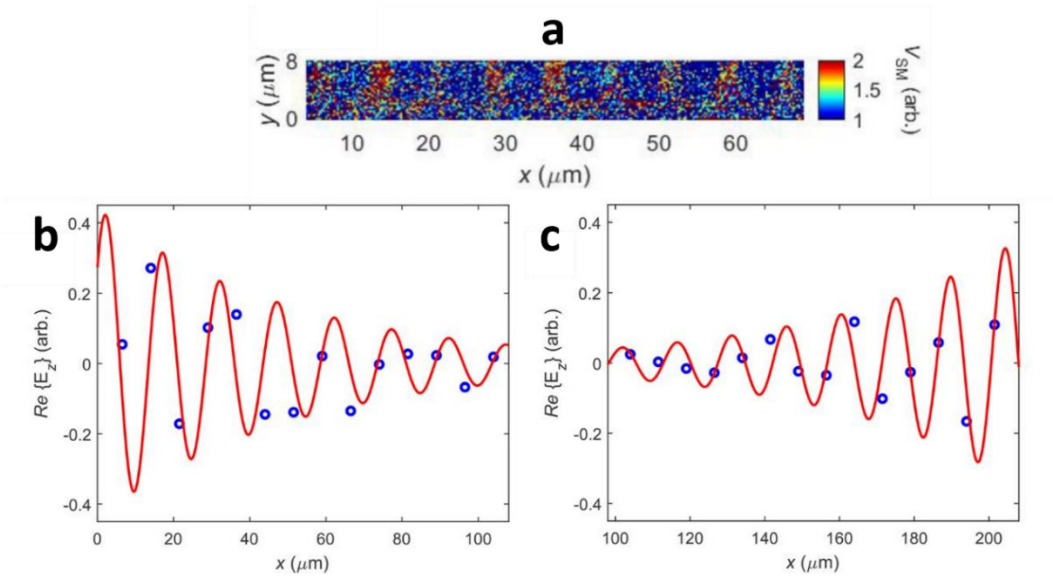

Figure 5.8 – (a) THz image of a portion of the PSP waveguide obtained by THz-s-SNOM, in which the signal is derived from the $n = 2$ harmonic of V_{SM}. Spatially averaged values of E_z per bar for the area $x = 0$ – 104 μm (b) and $x = 104$ – 208 μm (c), fitted to which is Equation 5.2.

5.2.5 Directional coupling waveguides

Advancements in the field of plasmonics have inspired a study of nanophotonic integrated circuits, allowing the compact size of electronic circuits to be combined with the large bandwidth of plasmonics. Such technology requires a variety of basic components, such as wavelength filtering/separation mechanism and plasmonic power/beam splitters. This mechanism can be realised in devices such as direction couplers (DC) [251]–[256]. This device is the subject of Chapter 6 of [10] (an overview of which is given below) and the rest of this Chapter.

The DCs proposed in [10] were designed to operate in the THz range but were inspired by earlier designs that operated in the microwave region [246], [257], [258]. The device comprises three main sections: the excitation region, wherein a SSPP is generated by coupling of light to a waveguide WG1, the interaction region, within which a sharing of the energy between WG1 and second waveguide WG2 occurs, and the S-bend region, consisting of additional waveguides attached at an angle to the end of WG1 and WG2 to enable a physical separation the SSPPs (Figure 5.9). The distance between WG1 and WG2 is g and the length of the interaction region is L. Both of these parameters determine the amount by which the energy is transferred between the two waveguides. The DC devices

displayed here are based on the PSP waveguide design described earlier. For the sake of the work presented later in this Chapter, this review will focus on the excitation and interaction regions.

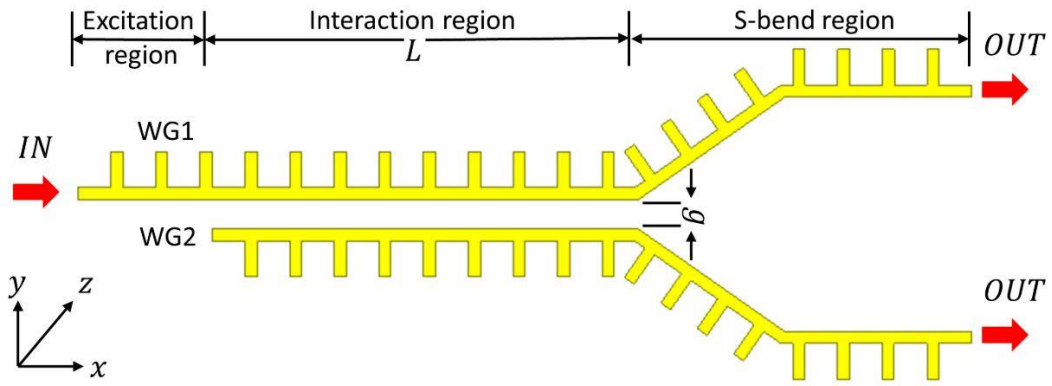

Figure 5.9 – Schematic of the DC structure showing the three regions of interest. The structure is designed so that SSPPs are launched at the beginning of WG1 and couple to WG2 within the interaction region. Adapted from [10].

For sufficiently small g, this type of waveguide structure supports both even and odd SSPP modes. Figure 5.10 shows the dispersion relations of even and odd SSPP modes on the surface of DC structures with a variety of g values. Additionally shown are an example of the simulated field of an even and odd SSPP mode for a unit section of WG1 and WG2.

Figure 5.10a shows that the wave vectors of the even SSPP mode k_{xe} and odd SSPP mode k_{xo} are not equal. This causes even and odd SSPP modes propagating on the DC to interact either constructively or destructively, depending on their relative phases, determining the distribution of the energy associated with the SSPPs into either WG1 or WG2. For certain positions along the x-direction within the interaction zone, the even and odd modes will be in phase, leading to the sum of the fields on WG1 to be a maxima and the sum of those on WG2 to be zero. For other positions along the interaction region, the opposite of this is true. The total energy transfer from WG1 to WG2 is dependent on the coupling length L_c which can be expressed as,

$$L_c = \frac{\pi}{k_{xe} - k_{xo}} \qquad 5.5$$

It can be seen from Figure 5.10a the difference between the wave vectors of the even and odd modes Δk (the denominator of Equation 5.6) decreases with increasing g. Using Equation 5.6, the coupling length L_c for maximum energy transfer from WG1 to WG2,

with $g = 0.5$ µm and with an excitation frequency of 3.45 THz, was found to be $L_c = 73$ µm.

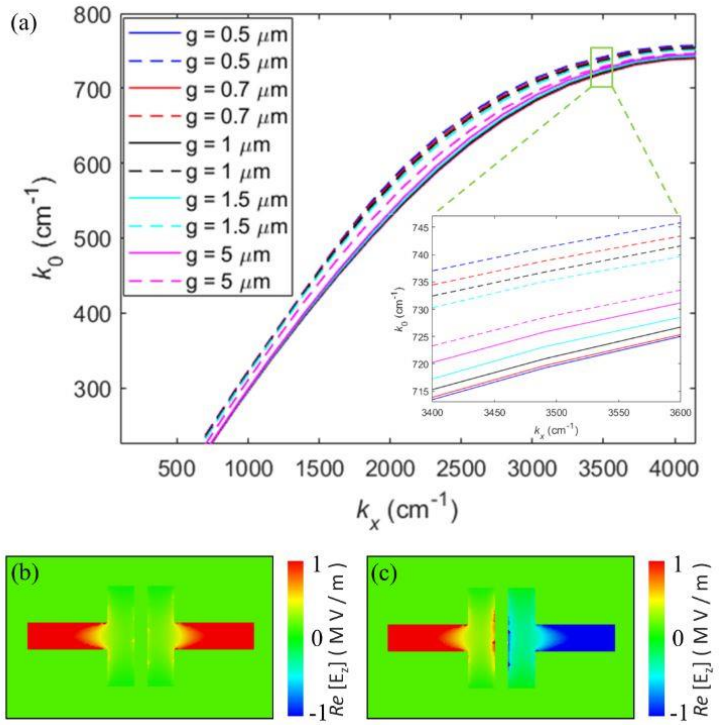

Figure 5.10 – (a) Dispersion relation for even (solid) and odd (dashed) SSPP modes on DC structures with varying g values. (a, inset) Part of the dispersion relations of (a) cropped to the k_x values of interest. Real part of the out-of-plane field E_z of the SSPP even (b) and odd (c) modes obtained via FEM simulations of a DC structure with $g = 0.5$ µm. Adapted from [10].

To further investigate the coupling strength dependence on g, DC structures with 73 µm long interaction regions and various g values between 0.5 – 5 µm were subject to wave-port simulations in ANSYS HFSS, analogous to those seen in Section 5.2.2. The waveguides of the DC structures were designed with period $d = 7.5$ µm, groove width $\alpha = 5.5$ µm, width $w = 8$ µm, height $h = 6$ µm and thickness $t = 0.1$ µm. The excitation region, at the beginning of WG1 was 22.5 µm long, which was chosen to ensure that, in both the simulations and, later, experimental devices, there is no unwanted excitation of SSPPs at the beginning of WG2. Despite these efforts, it will be seen that this problem still occurs and is the subject of rectification in Section 5.3 and onwards.

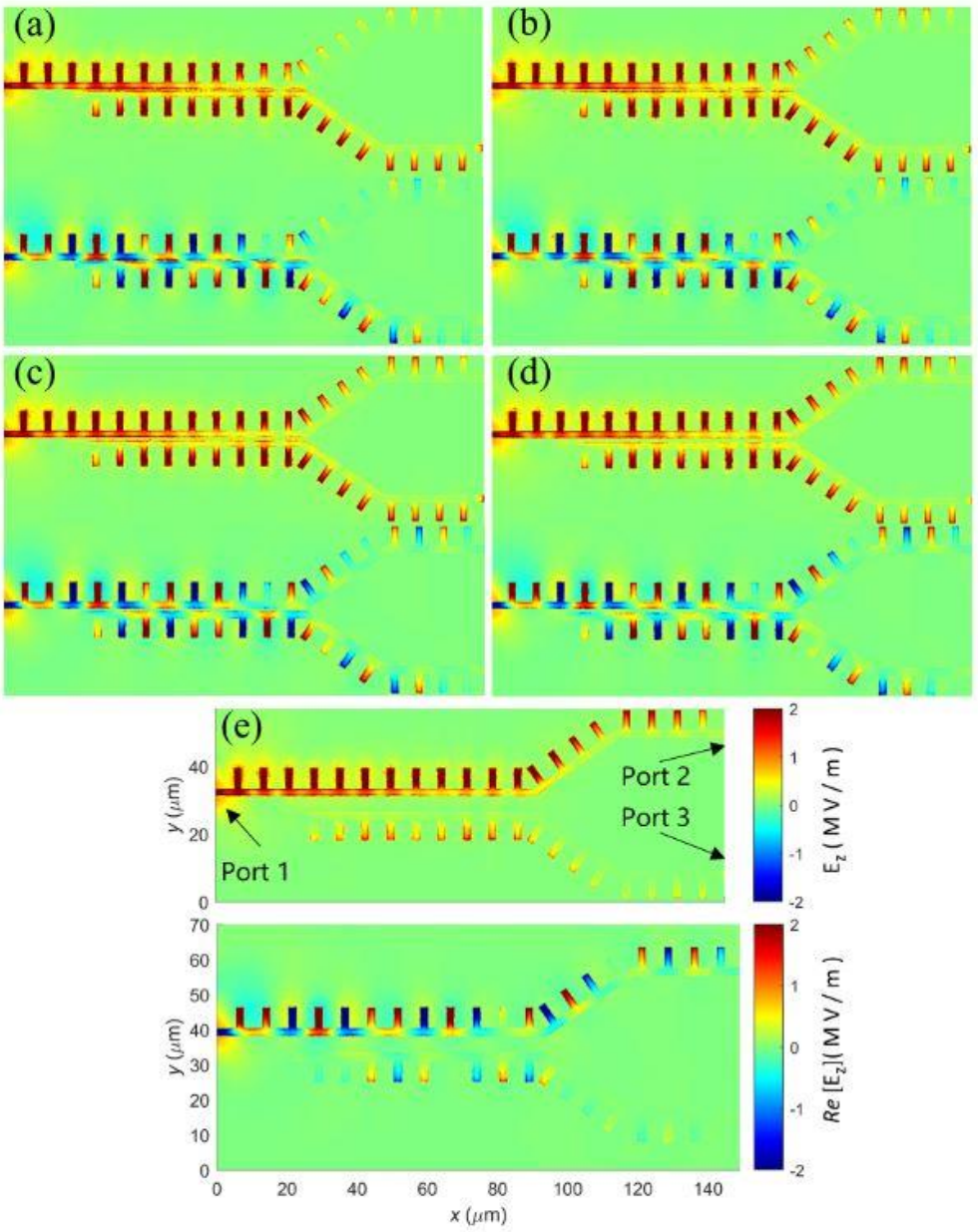

Figure 5.11 – Magnitude (upper) and real part of the out-of-plane electric field (lower) on the surface of the DC structures obtained via wave port simulations. (a) $g = 0.5$ μm, (b) $g = 0.7$ μm, (c) $g = 1$ μm, (d) $g = 1.5$ μm and (e) $g = 5$ μm. Adapted from [10].

From Figure 5.11, it can be seen that for all values of g, SSPPs are expectedly launched at the beginning of WG1. For large values of g, the magnitude of the SSPP field remains and decays in WG1 and very little energy is transferred to WG2 within the IR. However, for small values of g, the SSPP field decays quicker in WG1 as almost all of the power transfers to WG2.

In previous work [10], free-space simulations and experimental measurements of these structures were then carried out. However the results were mostly inconclusive and

difficult to analyse/interpret for various reasons. Firstly, simulations and experiments were only performed for p-polarised excitation. This introduces difficulties whereby the out-of-plane field E_z contains contributions from not only the SSPP mode supported by the waveguide but also the charge distribution induced directly by the obliquely incident THz field, whereby the stubs of the waveguide structure behave as electrically short dipoles. This makes analysis of the SSPP modes more difficult. Also, although p-polarised excitation has been shown to excite SSPPs on similar structures [22], s-polarised excitation is expected to couple more efficiently to SSPPs. In the following Sections, this is addressed by studying these structures both theoretically and experimentally using s-polarised radiation.

Furthermore, it was found that SSPPs were excited directly by the free-space beam at the start of WG2, as well as at the ends of both WG1 and WG2 whereas the intention was only to excite SSPPs directly in WG1. This made it very difficult to interpret how SSPPs behaved in the interaction region of the DC structures. This is addressed in the following Sections with the proposal of waveguide terminations designed to inhibit SSPP excitation, which are investigated theoretically and experimentally.

5.3 Improved DC design

In order to prevent complications arising from unwanted excitation of SSPPs, an improved DC structure was theorised that would supress launching of SSPPs in these regions. This design would incorporate a small device affixed to the beginning of WG2 and/or the end of WG1 and WG2, which are intended to modify the scattering/diffraction of light from the waveguide edge, the interaction between which is responsible for providing the momentum mismatch required to excite SSPP modes. The following Sections detail an investigation of various devices intended to achieve such, referred to hereafter as “waveguide terminations”. For simplicity, this study involves s-polarised free-space excitation simulations of the terminations affixed to one end of the asymmetric PSP waveguide of Section 5.2, to allow for ease of analysis and direct comparison between the performances of each design. Later, a redesigned DC structure encompassing the best performing termination design is evaluated both theoretically and experimentally.

For the initial free-space simulations, the incident plane was placed 174 μm above the substrate and launched an s-polarised plane wave at a frequency of 3.45 THz, which was

obliquely incident on the structure at an angle of $\theta_i = 54^0$ (Figure 5.6). The structure itself comprised a termination affixed to the left-hand side of the PSP waveguide, where $x = 0$ μm. Similarly to that described in Section 5.2.3, the waveguide was 208 μm in length, to ensure significant attenuation of the SSPPs launched from either end, with dimensions d = 7.5 μm, $a = 5.5$ μm, $w = 8$ μm, $h = 6$ μm and $t = 0.1$ μm.

To determine the effectiveness of each termination design, the magnitude of the out-of-plane electric field $|E_z|$ was spatially averaged within each of the 27 bars. The field strength of the first ($n = 1$) and last ($n = 27$) bars of the waveguide were then compared. This method was seen as a good metric by which to measure the success of each design, since the symmetry of the waveguide would suggest that the field due to the SSPP excited at bar 27 of the structure is identical to that which would be excited at bar 1 without the presence of the termination. Therefore, the value of $\varepsilon = \left|E_{z,n=1}\right| / \left|E_{z,n=27}\right|$ should indicate the effectiveness of the design for each simulation, where a value of $\varepsilon = 1$ would be expected for no termination present and a value of $\varepsilon = 0$ would be an idealised termination design.

5.3.1 Ring termination design

These designs comprise a ring with outer diameter $D = 7.5$ μm and inner diameters d varying from 0 – 5.5 μm (where at $d = 0$ μm, the design becomes a solid circle with diameter 7.5 μm). The waveguide end is embedded on the right-hand side of each of the rings where it protrudes a small distance into the annulus, and is positioned so that the vertical centre of the 2 μm wide waveguide shaft is in line with the centre of the ring. The material of the ring is gold and has thickness $t = 0.1$ μm to match the thickness of the waveguide. Both the ring and waveguide are in the same position in the z-plane. Due to technical limitations, the circularity of the design was approximated with a regular icositetragon. Figure 5.12 displays each design.

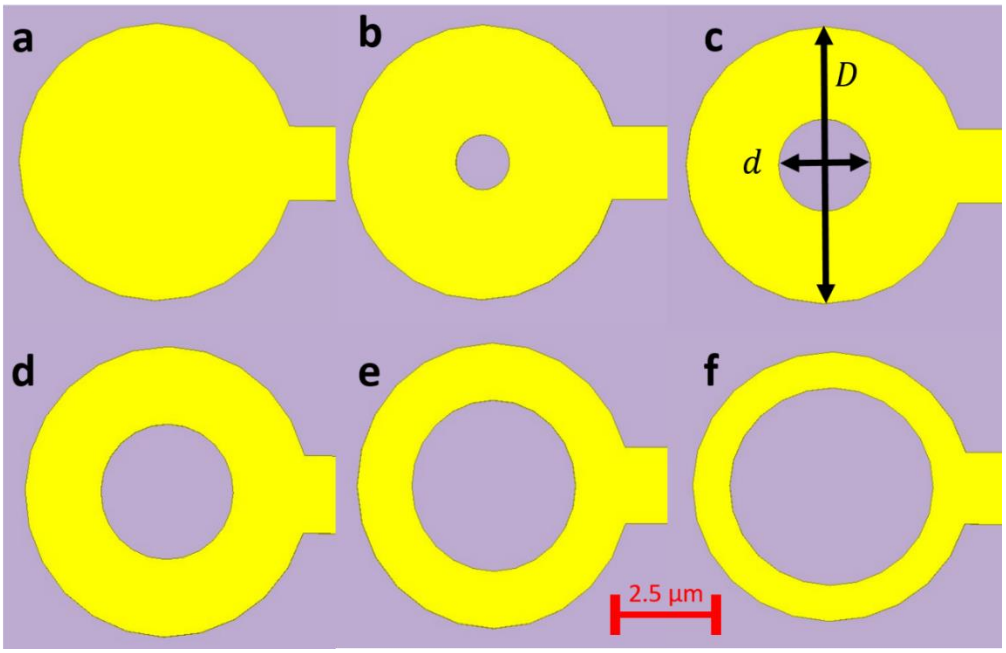

Figure 5.12 – Ring termination designs schematics. (a) $d = 0$ µm, (b) $d = 1.5$ µm, (c) $d = 2.5$ µm, (d) $d = 3.5$ µm, (e) $d = 4.5$ µm and (f) $d = 5.5$ µm.

Figure 5.13 shows the magnitude of the out-of-plane electric field $|E_z|$ for the waveguide simulated under the conditions described above, for each of the designs displayed in Figure 5.12.

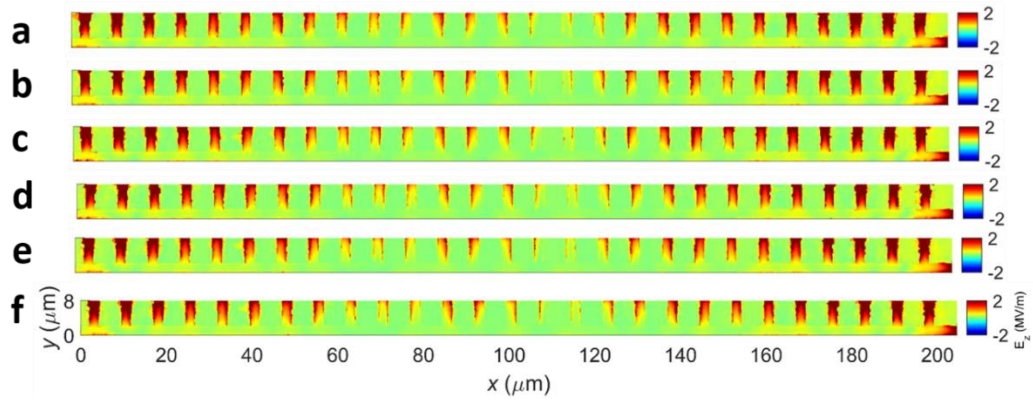

Figure 5.13 – Magnitude of out-of-plane electric field for PSP waveguide with ring terminations acquired via free-space excitation simulations. (a) $d = 0$ µm, (b) $d = 1.5$ µm, (c) $d = 2.5$ µm, (d) $d = 3.5$ µm, (e) $d = 4.5$ µm and (f) $d = 5.5$ µm.

By averaging the field in each bar, the values of $|E_{z,n=1}|$ and $|E_{z,n=27}|$ can be extracted, from which the ε value can be determined for each design. These values are plotted in Figure 5.14, from which it can be seen that every design was somewhat effective at

inhibiting SSPP excitation (i.e. $\varepsilon < 1$), with the designs with $d = 1$ μm and $d = 3$ μm performing the best.

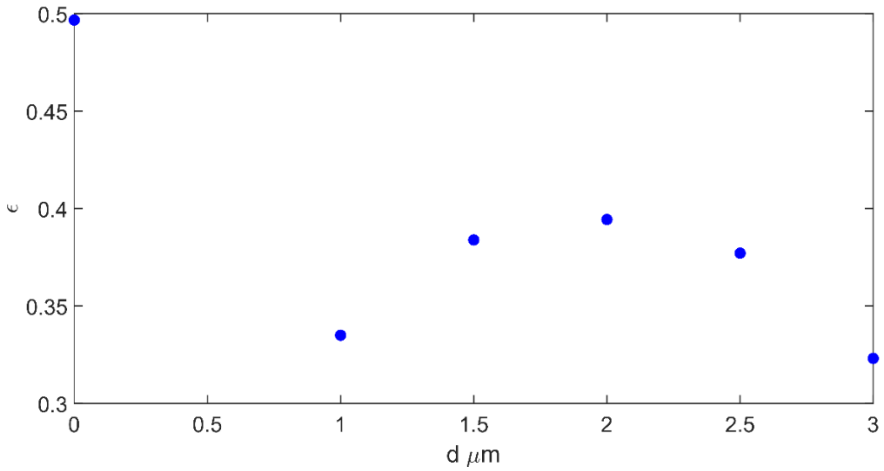

Figure 5.14 – Comparison of the performance of the ring termination designs.

5.3.2 Tapered termination design

These designs have a triangular shape where the waveguide is attached at the base. There are four tapered designs which comprises isoscele triangles with height h and base length b, wherein the base joins the waveguide at the first bar ($n = 1$) and protrudes in the x-direction. The two base lengths are $b = 2$ μm and $b = 8$ μm, and the two heights are $h = 7.5$ μm and $h = 15$ μm, combinations of which make the four designs. Each design has thickness $t = 0.1$ μm. Figure 5.15 displays each of the tapered designs.

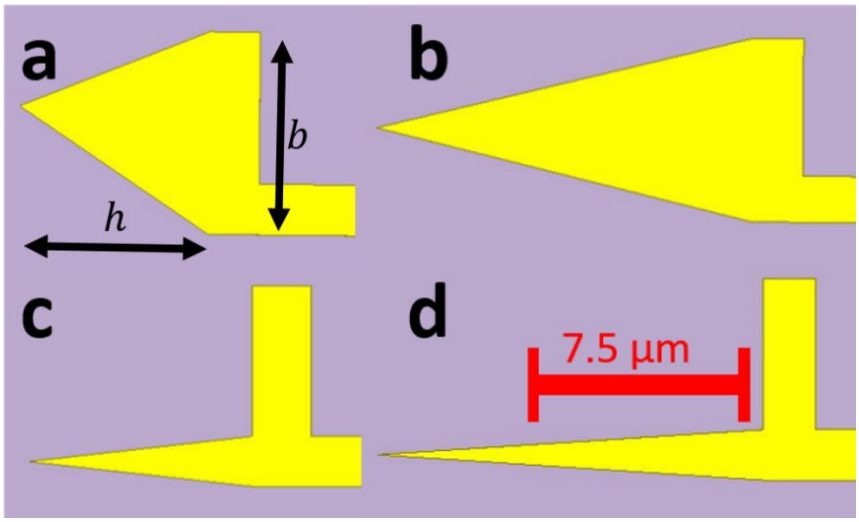

Figure 5.15 – Tapered termination design schematics. (a) $h = 7.5\ \mu m$, $b = 8\ \mu m$, (b) $h = 15\ \mu m$, $b = 8\ \mu m$, (c) $h = 7.5\ \mu m$, $b = 2\ \mu m$ and (d) $h = 15\ \mu m$, $b = 2\ \mu m$.

Figure 5.16 shows the magnitude of the out-of-plane electric field $|E_z|$ for the waveguide simulated under the conditions described above, for each of the designs displayed in Figure 5.15.

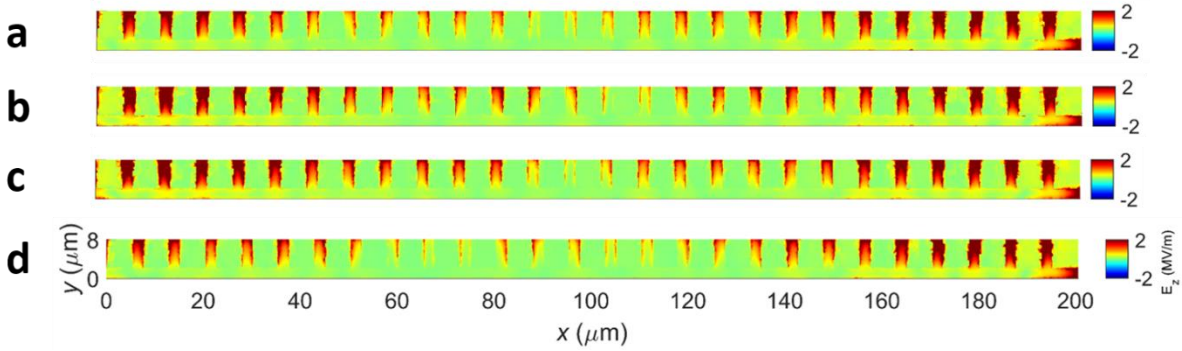

Figure 5.16 – Magnitude of out-of-plane electric field for PSP waveguide with tapered terminations acquired via free-space excitation simulations. (a) $h = 7.5\ \mu m$, $b = 8\ \mu m$, (b) $h = 15\ \mu m$, $b = 8\ \mu m$, (c) $h = 7.5\ \mu m$, $b = 2\ \mu m$ and (d) $h = 15\ \mu m$, $b = 2\ \mu m$.

By averaging the field in each bar, the values of $|E_{z,n=1}|$ and $|E_{z,n=27}|$ can be extracted, from which the ε value can be determined for each design. These values are plotted in Figure 5.17, from which it can be seen that only the design b and d appear to perform as intended, with designs a and c actually improving the coupling efficiency of the incident field to the SSPP modes.

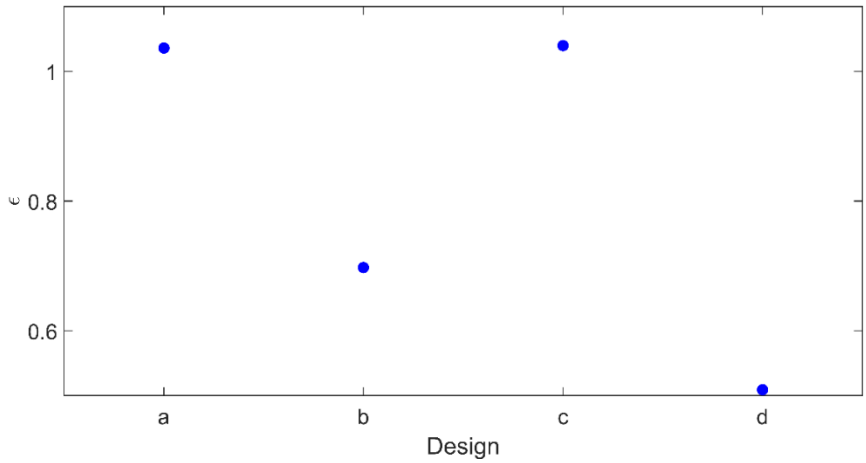

Figure 5.17 – Comparison of the performance of the tapered termination designs.

5.3.3 Extension termination design

The extension design is the simplest of the terminations exhibited in this Chapter. They consist of a bar with width equal to the width of the waveguide shaft, attached to the end of the waveguide shaft, which extends into the x-direction. The designs vary only by bar length L which ranges from 5 – 20 μm. The waveguide shaft, without the addition of a termination, extends a distance of 5.5 μm from the first bar in the x-direction, which defines the start of the waveguide. The termination length L is therefore defined as the distance between the end of the structure and the beginning of the waveguide. The dimensions of these designs can be seen in Figure 5.18.

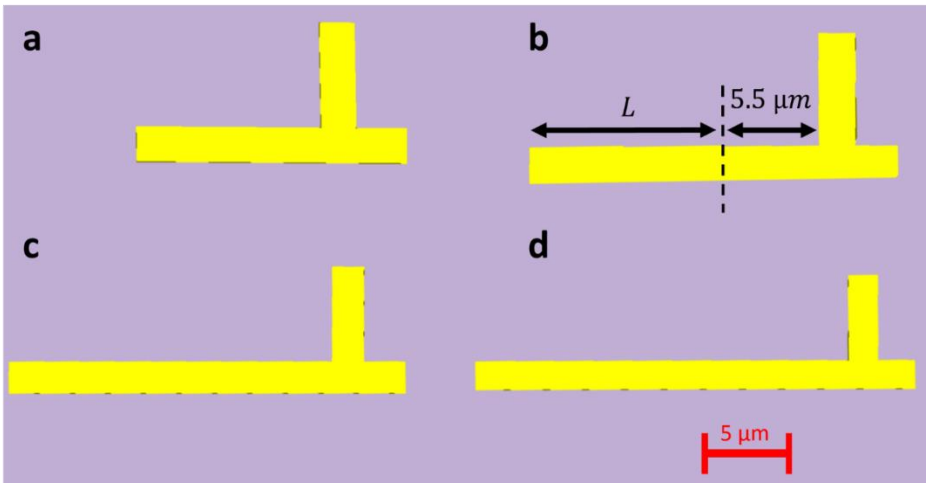

Figure 5.18 – Extension termination design schematics. (a) $L = 5$ μm, (b) $L = 10$ μm, (c) $L = 15$ μm and (d) $L = 20$ μm.

Figure 5.19 shows the magnitude of the out-of-plane electric field $|E_z|$ for the waveguide simulated under the conditions described above, for each of the designs displayed in Figure 5.18.

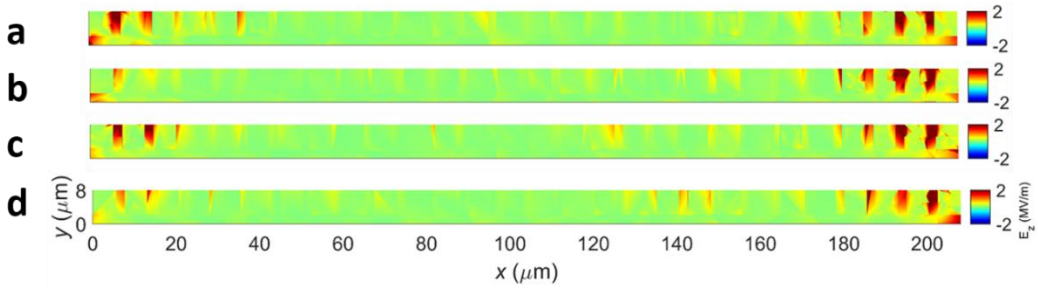

Figure 5.19 – Magnitude of out-of-plane electric field for PSP waveguide with tapered terminations acquired via free-space excitation simulations. (a) $L = 5$ μm, (b) $L = 10$ μm, (c) $L = 15$ μm and (d) $L = 20$ μm.

By averaging the field in each bar, the values of $|E_{z,n=1}|$ and $|E_{z,n=27}|$ can be extracted, from which the ε value can be determined for each design. These values are plotted in Figure 5.20, which show that each design performs as intended, designs b and d far out performing designs a and c.

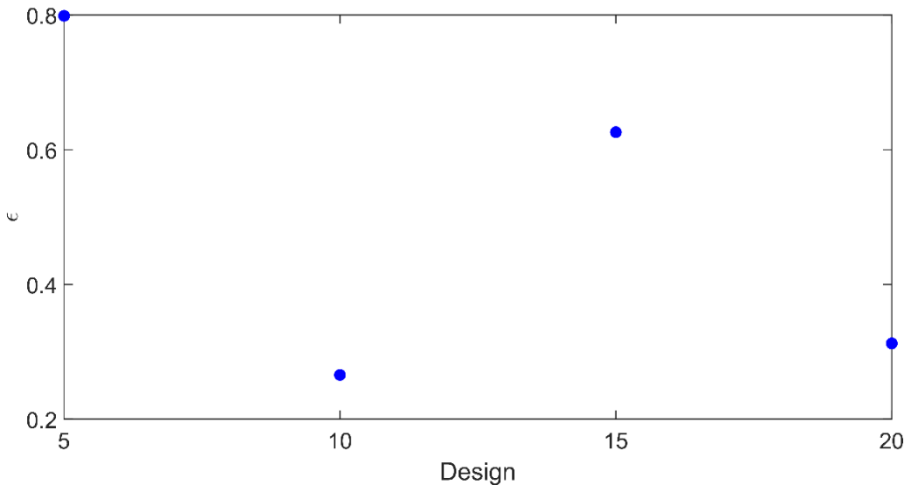

Figure 5.20 – Comparison of the performance of the extension termination designs.

5.3.4. Grating termination design

Section 5.2.4 outlines the use of a grating structure with specific dimensions to enhance the coupling of light to the SSPP mode. It was theorised that using a similar structure with different dimensions or orientation could inhibit this coupling. The gratings

considered here comprise a series of unattached stacked bars, individually measuring 16 µm x 0.5 µm x 0.1 µm. The designs include gratings with bars orientated perpendicular (y-direction) and parallel (x-direction) to the waveguide, with both regular grating periods where $\alpha = 0.5$ µm, and irregular grating periods where α ranges from 0.5 – 2.5 µm. In both orientations, the grating is offset from the centre of the waveguide and the distance from the waveguide to the grating is $g_{off} = 0.5$ µm. In comparison to the gratings of Section 5.2.4, the dimensions of these terminations are well outside of the optimum coupling design and therefore should discourage SSPP excitation. Figure 5.21 shows the grating designs.

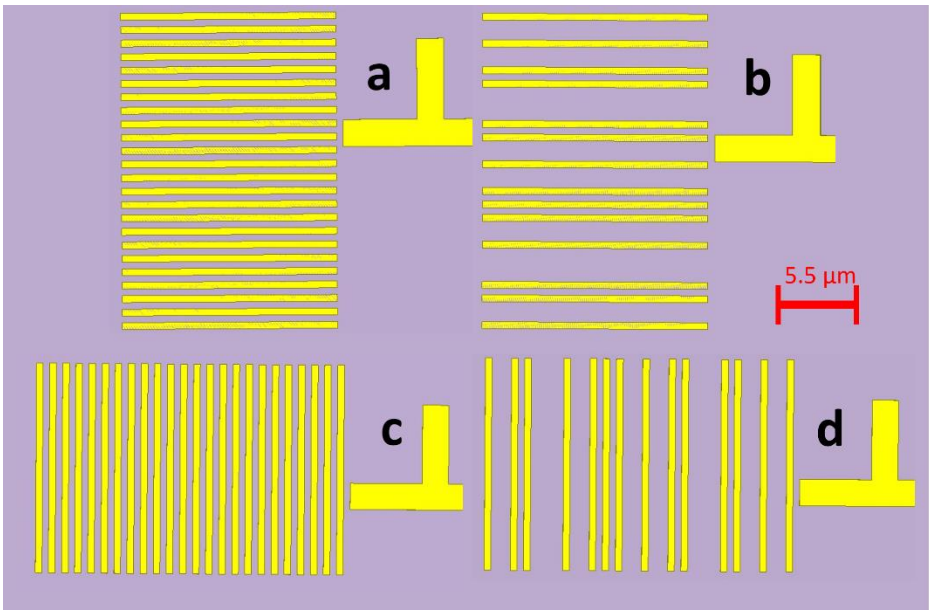

Figure 5.21 – Grating termination design schematics. (a) $a = 0.5$ µm parallel, (b) $a =$ various parallel, (c) $a = 0.5$ µm perpendicular and (d) $a =$ various parallel.

Figure 5.22 shows the magnitude of the out-of-plane electric field $|E_z|$ for the waveguide simulated under the conditions described above, for each of the designs displayed in Figure 5.21.

By averaging the field in each bar, the values of $|E_{z,n=1}|$ and $|E_{z,n=27}|$ can be extracted, from which the ε value can be determined for each design. These values are plotted in Figure 5.23, from which it can be seen that both perpendicular orientated designs were effective at inhibiting the excitation of SSPP modes. Perhaps surprisingly, the parallel orientated gratings greatly improved SSPP coupling. This may be due to the 16 µm length of each bar of the grating providing a momentum mismatch that improves coupling, in a similar manner to the coupling enhancement structure of Figure 5.5, but with a period

of $\alpha = 16$ μm, which is close to $\alpha \sim \lambda_{SP}$. An investigation of this design for different bar lengths may be explored in future work.

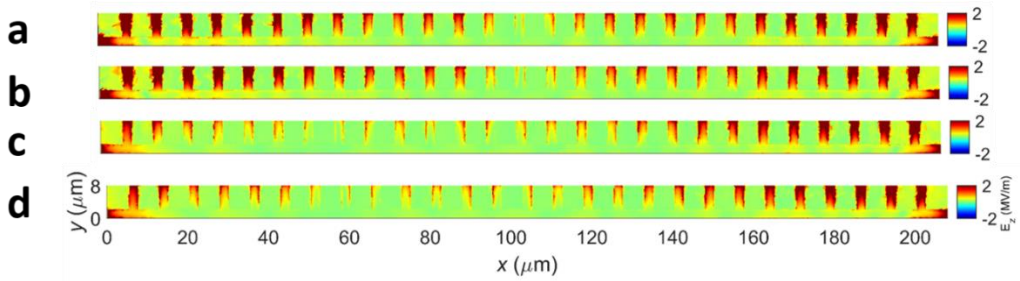

Figure 5.22 – Magnitude of out-of-plane electric field for PSP waveguide with grating terminations acquired via free-space excitation simulations. (a) $a = 0.5$ μm parallel, (b) $a =$ various parallel, (c) $a = 0.5$ μm perpendicular and (d) $a =$ various parallel.

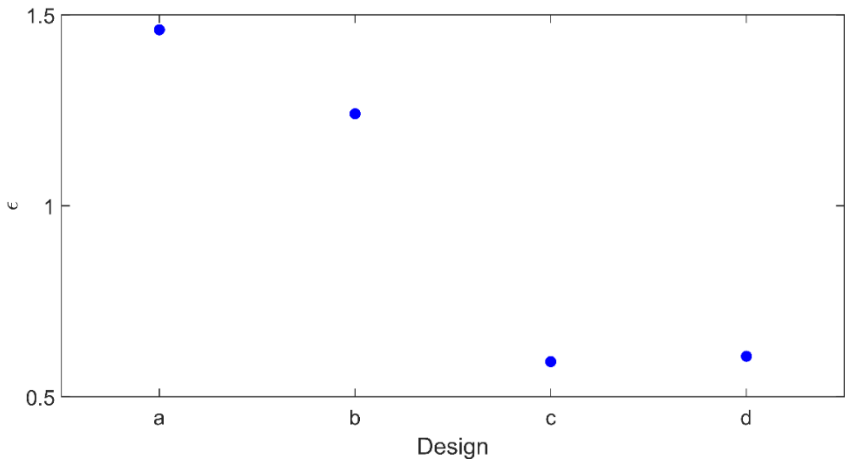

Figure 5.23 – Comparison of the performance of the grating termination designs.

5.4 Nickel waveguide terminations

5.4.1 Wave port comparison

It was theorised that using a material other than gold would improve the performance of the terminations. It is known that in the THz range, nickel is a strong absorber and has previously been used as such [259]–[261]. To quantify this, wave port simulations were performed of 100-nm-thick nickel versions of the PSP waveguide of Section 5.2. The simulations environment was identical to that used to simulate the gold PSP waveguide in Section 5.2.2, with start and end ports located at the beginning and end of a 208 μm waveguide, between which was launched a 3.45 THz SSPP. Figure 5.24 shows a

comparison between the real part of the out-of-plane field of the gold and nickel PSP waveguides.

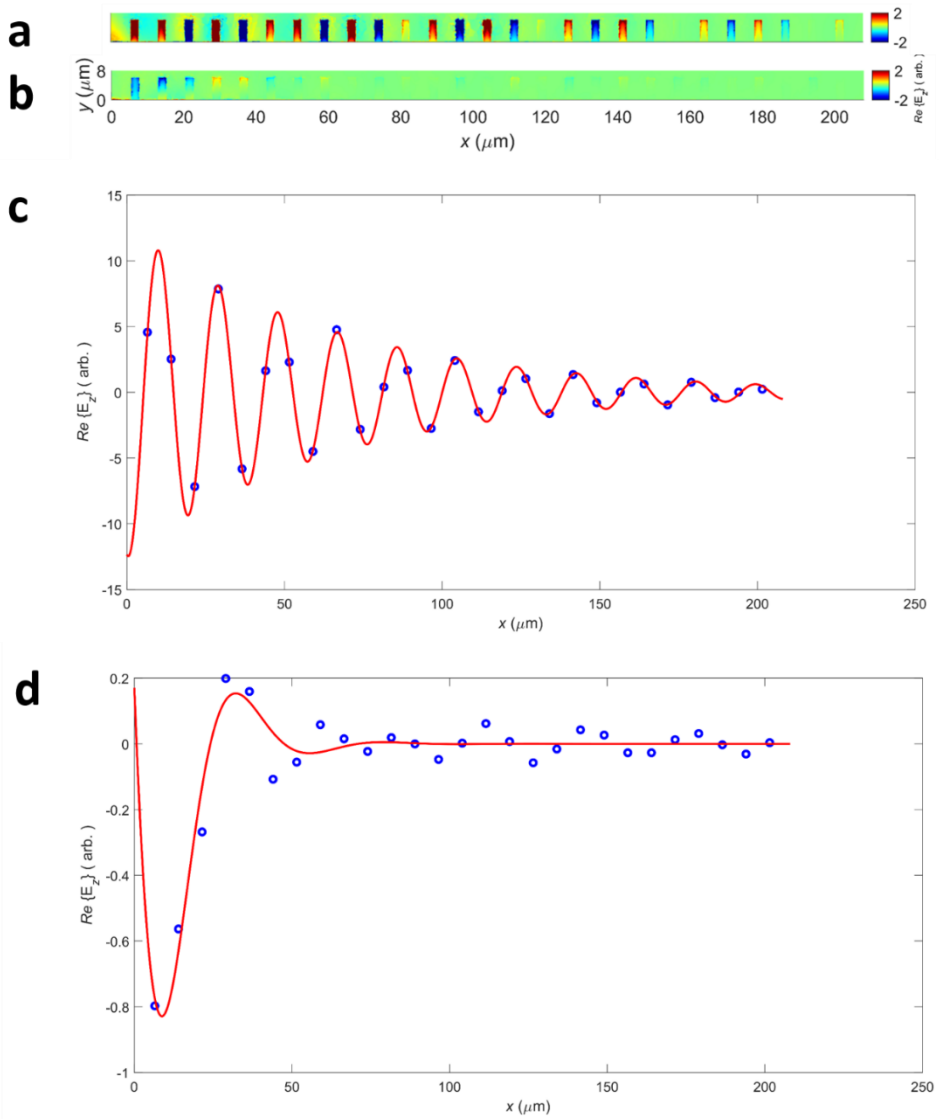

Figure 5.24 – Comparison of wave port simulations of 208 μm gold and nickel PSP waveguides. (a) Real part E_z of gold waveguide, (b) real part E_z of nickel waveguide, (c) Figure 5.4 and (d) (Blue) Averaged E_z values for each bar of nickel PSP waveguide extracted from (b). (Red) Equation 5.2 with fitting parameters of $E_0 = 1.768$ MV/m, $k_x = 0.13$ cm^{-1}, $\theta = 3.05$ rad and $L_p = 14$ μm.

By comparing the results of Figure 5.24c and d, both of which have been fitted to Equation 5.2, it can be seen that the attenuation of the SSPP field in the nickel waveguide is far greater than that in the gold waveguide, with a propagation length of $L_p \sim 14$ μm and also larger SSPP wavelength of $\lambda \sim 30$ μm. These results are both a consequence of the different real and imaginary parts of the permittivity of nickel compared to gold.

Additionally, these simulations allowed for an extraction of the S_{21} Parameter, in order to determine the cut-off frequency of the waveguide. Figure 5.25 shows the transmitted power is heavily attenuated for THz frequencies and that this design has a cut-off frequency of $f_0 \sim 2.3$ THz, which is below the intended operation frequency of the designed DC structures.

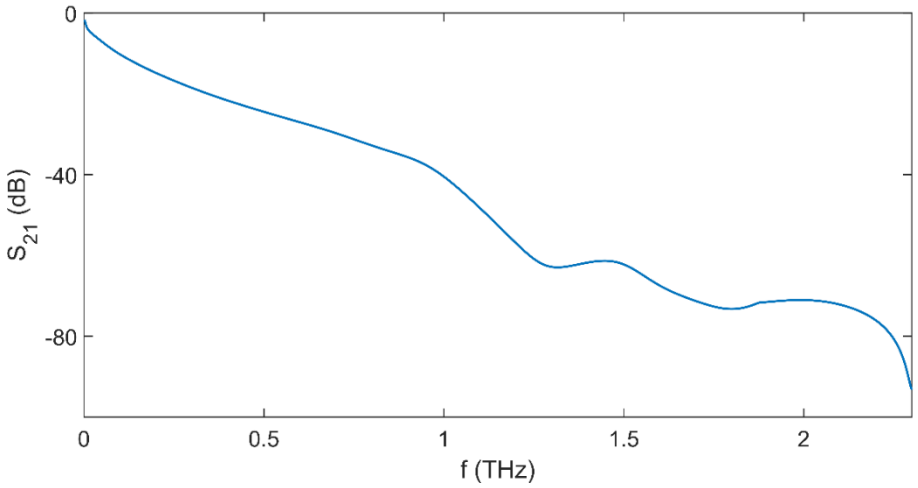

Figure 5.25 – S_{21} Parameters of nickel PSP waveguide with length $L = 208$ µm.

5.4.2 Nickel termination designs

The analysis of Section 5.4.1 suggests that nickel does not support SSPP modes at 3.45 THz and therefore would be a more suitable material for the waveguide termination designs. As such, identical nickel versions of the designs seen in Sections 5.3.2, 5.3.3 and 5.3.4, were created and subject to a similar analysis. The ring termination designs of Section 5.3.1 were omitted since it was realised that their dimensions would be incompatible with the DC structure with which they would be integrated.

The termination designs were all subject to the same free-space excitation simulations as that shown in Section 5.3, from which the average $|E_z|$ values for each bar were extracted. In a similar manner to the analysis present in Section 5.3, the performance of each termination design was evaluated by the $\varepsilon = |E_{z,n=1}|/|E_{z,n=27}|$ criteria. The ε values for each design are shown in Figure 5.26 for each gold design and their nickel counterparts.

It can be seen by the results present in Figure 5.26 that the nickel designs perform better than the gold designs in almost all cases. The best performing termination design is the 10 µm nickel extension with a value of $\varepsilon = 0.1$ and the worst performing is the parallel

grating with period $a = 0.5$ μm, in which the design improved SSPP coupling with a value of $\varepsilon \sim 1.4$.

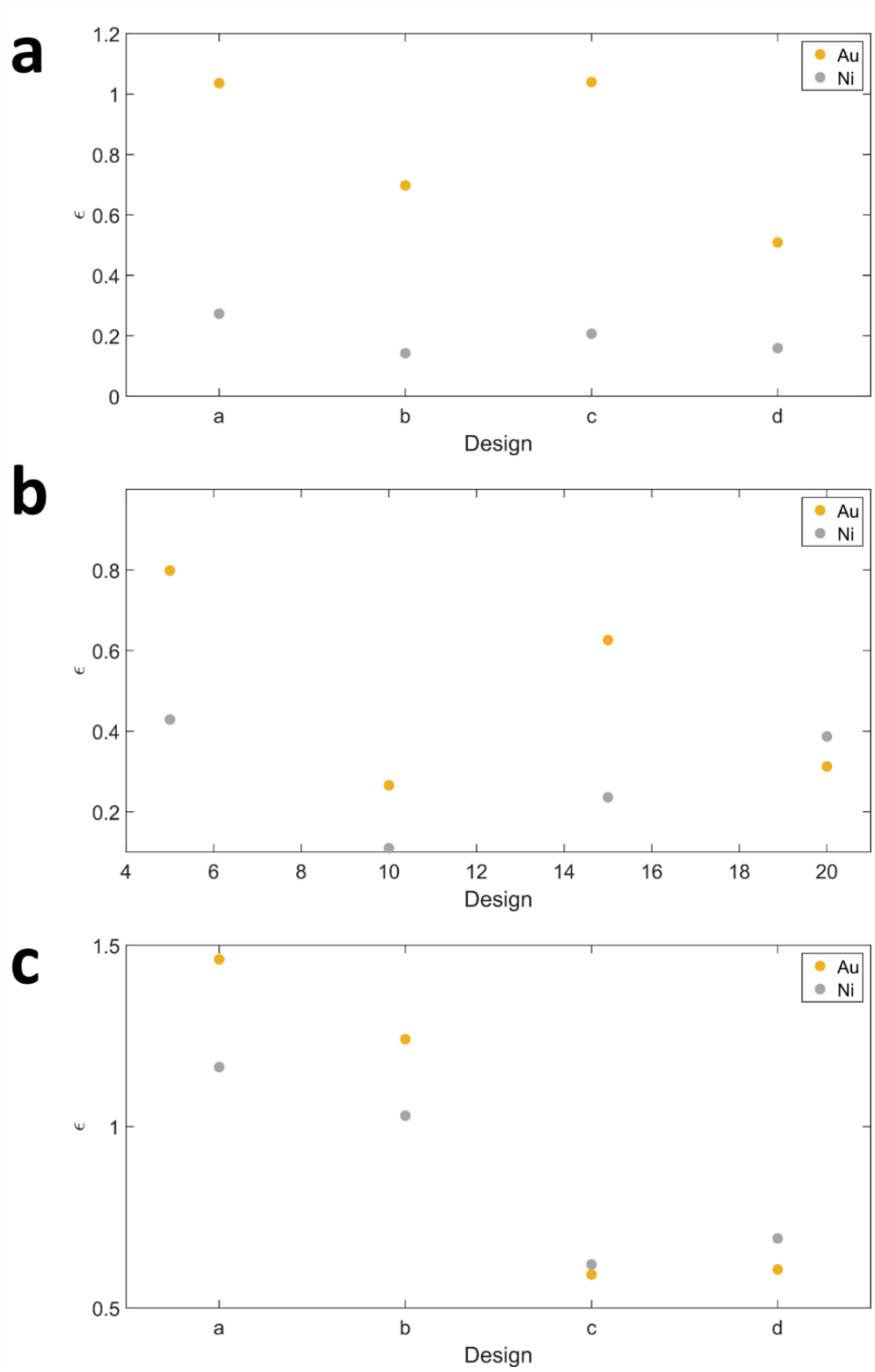

Figure 5.26 – Performance of nickel versions of each termination design with results of corresponding gold designs (a) Figure 5.17, (b) Figure 5.20) and (c) Figure 5.23.

5.4.3 DC structure with nickel extensions

It was determined in Section 5.4.2 that the 10 μm nickel extension termination design performed the best at inhibiting SSPP excitation at the beginning of the PSP waveguide, within the range of designs explored. To incorporate the design into the DC structure, the termination was placed at the beginning of WG2, to deter direct excitation of SSPPs on WG2. For simplicity, the S-bend regions of the DC structure were omitted and the interaction region was made longer, compared to the DC of Section 5.2.5, to mitigate against any SSPPs launched from the waveguide ends (Figure 3.27).

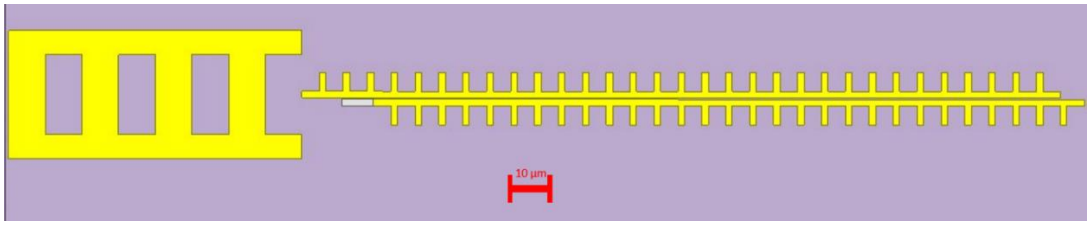

Figure 5.27 – Schematic diagram of DC structure with grating and 10 μm nickel extension on beginning of WG2. The grating has dimensions $a = 20$ μm and $g_{off} = 10$ μm. The IR of the DC is considered to begin at bar $n = 4$ of WG1. The gap between WG1 and WG2 is $g = 0.5$ μm.

The grating and two PSP waveguides constituting WG1 and WG2 of the DC structure had the same dimensions as that described in Section 5.2.6 with a waveguide gap of $g = 0.5$ μm. The structure was subject to simulations in ANSYS HFSS , with a simulation environment practically identical to that described in Section 5.2.3, wherein the structure was excited by an obliquely incident s-polarised free-space plane wave at 3.45 THz.

The out-of-plane electric field E_z of WG1 and WG2 within the active region are presented in Figures 5.28a and b. By spatially averaging E_z within each bar, the SSPP propagation in WG1 and WG2 can be observed, as shown in Figures 5.28c and d. In order to analyse the SSPP behaviour, the following model was used.

The electric fields E_{1e} and E_{2e} associate with the SSPP even mode, expressed as a function of distance x, for WG1 and WG2, can be described by,

$$E_{1e} = E_{0e} \sin(k_e x + \theta_e) e^{-\frac{x}{L_e}} \qquad 5.6$$

and

$$E_{2e} = E_{0e}\sin(k_e x + \theta_e)e^{-\frac{x}{L_e}} \quad 5.7$$

where k_e is the wave vector of the even SSPP mode, θ_e is the phase of the SSPP mode, L_e is the propagation length of the even SSPP mode and the assumption is made that the field amplitude E_{0e} is the same for each waveguide. Here, $x = 0$ is defined as the beginning of the IR. Equations 5.6 and 5.7 describe two in-phase oscillating fields with wavelength $\lambda_e = \frac{2\pi}{k_e}$.

In addition, the electric fields E_{1o} and E_{2o} associate with the SSPP odd mode, expressed as a function of distance x, for WG1 and WG2, can be described by,

$$E_{1o} = E_{0o}\sin(k_o x + \theta_o)e^{-\frac{x}{L_o}} \quad 5.8$$

and

$$E_{2o} = -E_{0o}\sin(k_o x + \theta_o)e^{-\frac{x}{L_o}} \quad 5.9$$

where k_o is the wave vector of the odd SSPP mode, θ_o is the phase of the SSPP mode, L_o is the propagation length of the even SSPP mode and the assumption is again made that the field amplitude E_{0o} is the same for each waveguide. As above, $x = 0$ is defined as the beginning of the IR. Equations 5.8 and 5.9 thereby describe two out-of-phase oscillating fields with wavelength different to the even mode $\lambda_o = \frac{2\pi}{k_o}$.

The total fields E_1 and E_2, expressed as a function of x, for each of WG1 and WG2, is obtained by summing the fields associated with the even and odd modes, which yields,

$$E_1 = E_{0e}\sin(k_e x + \theta_e)e^{-\frac{x}{L_e}} + E_{0o}\sin(k_o x + \theta_o)e^{-\frac{x}{L_o}} \quad 5.10$$

and

$$E_{2o} = E_{0e}\sin(k_e x + \theta_e)e^{-\frac{x}{L_e}} - E_{0o}\sin(k_o x + \theta_o)e^{-\frac{x}{L_o}} \quad 5.11$$

For simplicity, it is now assumed that $L_e = L_o = L$ and $E_{0e} = E_{0o} = E_0$, which gives,

$$E_1 = E_0\sin(k_e x + \theta_e)e^{-\frac{x}{L}} + E_0\sin(k_o x + \theta_o)e^{-\frac{x}{L}} \quad 5.12$$

and

$$E_2 = E_0\sin(k_e x + \theta_e)e^{-\frac{x}{L}} - E_0\sin(k_o x + \theta_o)e^{-\frac{x}{L}} \quad 5.13$$

The averaged fields of WG1 and WG2, presented in Figure 5.28b and c, are fitted to Equations 5.12 and 5.13 respectfully, from which the SSPP parameters are extracted.

Using the trigonometric identity $\sin 2\theta = 2\sin\theta\cos\theta$, Equations 5.12 and 5.13 can be rewritten as

$$E_1 = 2E_0\, sin\left(\frac{(k_e + k_o)x}{2} + \frac{(\theta_e + \theta_o)}{2}\right)\cos\left(\frac{(k_e - k_o)x}{2} + \frac{(\theta_e - \theta_o)}{2}\right)\exp\left(-\frac{x}{L}\right) \quad 5.14$$

$$E_2 = 2E_0\cos\left(\frac{(k_e + k_o)x}{2} + \frac{(\theta_e + \theta_o)}{2}\right)\sin\left(\frac{(k_e - k_o)x}{2} + \frac{(\theta_e - \theta_o)}{2}\right)\exp\left(-\frac{x}{L}\right) \quad 5.15$$

Rewriting $\frac{(k_e+k_o)}{2} = k_{SP}$ and $\frac{(k_e-k_o)}{2} = \Delta k$ then yields,

$$E_1 = 2E_0\, sin\left(k_{SP}x + \frac{(\theta_e + \theta_o)}{2}\right)\cos\left(\Delta kx + \frac{(\theta_e - \theta_o)}{2}\right)\exp\left(-\frac{x}{L}\right) \quad 5.16$$

and

$$E_2 = 2E_0\cos\left(k_{SP}x + \frac{(\theta_e + \theta_o)}{2}\right)\sin\left(\Delta kx + \frac{(\theta_e - \theta_o)}{2}\right)\exp\left(-\frac{x}{L}\right) \quad 5.17$$

In Equation 5.16 and 5.17, the first trigonometric term represents the oscillation of the SSPP field along the x-directionand the second trigonometric term represents an envelope function that describes the energy distribution between WG1 and WG2. This function is shown in the later results of Figure 5.33 and 5.35 to accentuate the coupling behaviour. It can be seen from these relations that when the even and odd modes are perfectly in-phase ($\theta_e - \theta_o = 0$) then, at $x = 0$, all of the energy is in WG1 ($E_2 = 0$). However, when the even and odd modes are perfectly out-of-phase, ($\theta_e - \theta_o = \pi$), then, at $x = 0$, all of the energy is in WG2 ($E_1 = 0$). For intermediate values of $\theta_e - \theta_o$, the energy is distributed between WG1 and WG2.

It can be seen from Figure 5.28 that the simulated SSPP field of WG1 and WG2 fit well to the model and display SSPPs propagation and energy coupling between the two waveguides. The extracted values of k_e and k_o are close to the expected values from the dispersion relation of Figure 3.10 ($k_e = 3600$ cm^{-1} and $k_o = 3150$ cm^{-1}) and are approximately the same for both WG1 and WG2. Additionally, the values of θ_e, θ_o and L extracted are also expectantly similar for both WG1 and WG2. Furthermore, the maxima and minima of WG1 correspond approximately to the minima and maxima of WG2, which is expected for energy coupling between the two. From Equation 5.6, and

using the fitted values of k_e and k_o, an interaction length of $L_c \sim 70$ µm for both waveguides can be obtained.

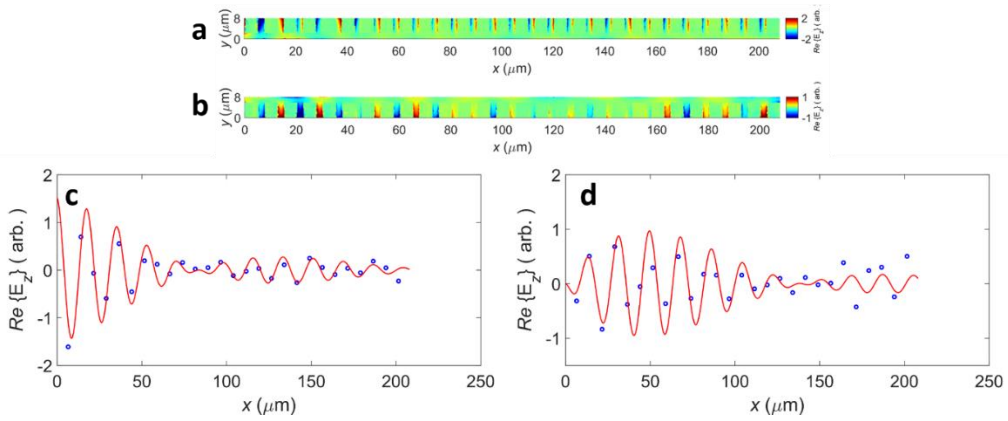

Figure 5.28 – Real part of the out-of-plane electric field of WG1 (a) and WG2 (b) of the DC structure obtained via free-space excitation simulations. (c) Averaged field per bars (dots) of the waveguide of (a) fitted to using Equation 5.10 (line) with fitting parameters $E = 0.8$ mV, $k_{xe} = 3750$ cm^{-1}, $k_{xo} = 3300$ cm^{-1}, $\theta_e = 1.4$ rad, $\theta_o = 2$ rad, $L = 80$ µm. (d) Averaged field per bars (dots) of the waveguide of (b) fitted to using Equation 5.10 (line) with fitting parameters $E_e = 1$ mV, $E_o = 1$ mV, $k_{xe} = 3650$ cm^{-1}, $k_{xo} = 3200$ cm^{-1}, $\theta_e = 1.9$ rad, $\theta_o = 1.9$ rad, $L = 80$ µm.

5.5 Experimental analysis of improved DC structure

The DC structure presented in Section 5.4.3 was fabricated and experimentally analysed using the THz-s-SNOM technique. The length of the active region of the DC was $L_c = 73$ µm and incorporated a grating structure with period $\alpha = 20$ µm, length $L_g = 90$ µm, slit length $L_s = 25$ µm and off-set from the DC waveguides $g_{off} = 10$ µm. The substrate used was high resistance float-zone silicon with resistivity $R > 10000$ Ωcm. The substrate area was 15 x 15 mm and had a thickness of 500 ± 50 µm. The sample was fabricated using standard ELB and atomic deposition by Dr Mark C. Rosamond. The metal deposition layers had thicknesses of 2 nm titanium (Ti) and 100 nm gold (Au)/nickel (Ni). In addition to the nickel termination design at the beginning of WG2, identical structures were also placed at the ends of WG1 and WG2, to reduce launching of SSPPs at the end of the DC (Figure 5.29).

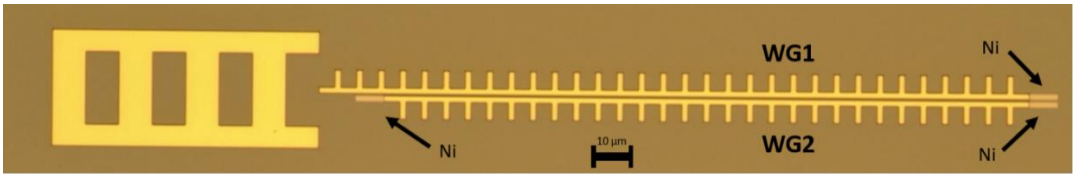

Figure 5.29 – Microscope image of DC structure with nickel terminations.

The THz-s-SNOM system set-up is described in Chapter 2. Individual THz images of the parts of WG1 and WG2 corresponding to the interaction region of the DC were obtained with a pixel size in both the x-direction (parallel to the waveguide) and y-direction (perpendicular to the waveguide) of 250 nm. The time constant used for both measurements was $\tau_s = 100$ ms. The 3.45 THz incident beam was substantially s-polarised through use of a half-wave plate (Figure 2.27) and obliquely incident on the s-SNOM probe tip at an angle of $\sim 54^0$.

The signal component arising from the near-field probe-sample interaction was isolated by operating the microscope in tapping mode, in which the probe tip was dithered with a tapping amplitude of $A_{tip} \sim 200$ nm and frequency $\Omega \sim 34$ KHz, and demodulating the signal at harmonics of Ω. To obtain the images present in Figure 5.30, the V_{SM} signal, arising from the fields scattered from the probe tip and reinjected into the laser cavity, was derived from the $n = 2$ demodulated QCL terminal voltage after amplification using an ac-coupled low-noise voltage amplifier with an amplification factor of 5 x 10^3. By raster-scanning the sample in the x and y directions, images, such as those of Figure 5.30, were obtained with deep sup-wavelength resolution.

5.5.1 WG1

Figure 5.30 shows the THz and AFM images for the part of WG1 corresponding to the interaction region of the DC. To analyse the nature of the out-of-plane electric field E_z present in the image, the V_{SM} values were spatially averaged within each bar and plotted as a function of distance x. To determine the exact position of each bar, the pixels corresponding to the boundaries of the first bar ($n = 1$) were identified using the AFM image. Since the periodicity of the bars is known to be $d = 7.5$ µm, these initial positions could then be used to determine the position of each of the 10 bars in the image.

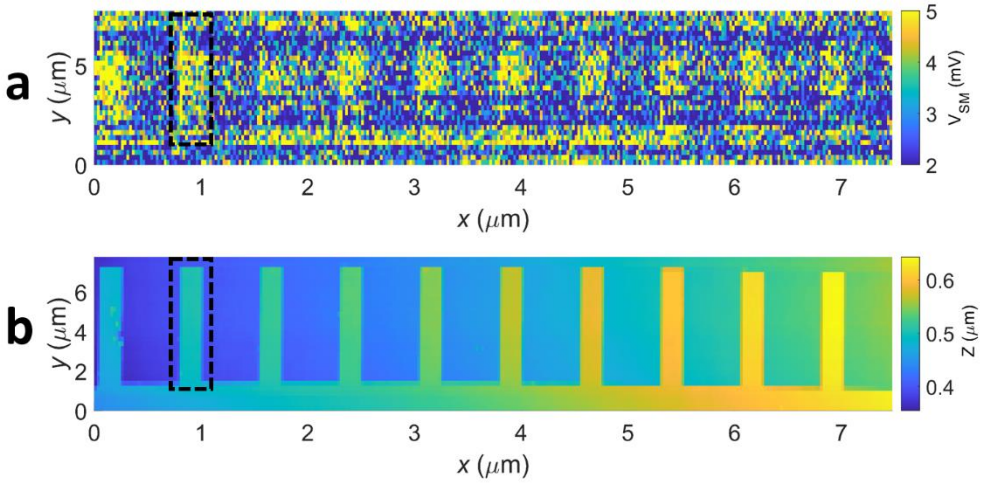

Figure 5.30 – THz s-SNOM (a) and AFM (b) images ($n = 2$) of WG1 IR of the DC structure of Figure 5.29. The dashed line is an example of using the AFM image of (b) to identify the boundary of each bar.

The V_{SM} values for each pixel within the boundaries of each bar, denoted by the dashed line in Figure 5.30, was then averaged to obtain a single V_{SM} value for each bar (Figure 5.31). As well as the component of the V_{SM} signal corresponding to the out-of-plane field of the SSPP mode, there exists an out-of-plane component arising from each bar being slightly polarised in the x-direction by the incident field. This can be well observed in Figure 5.28a, and should average to zero across each bar. Additionally, there exists a signal contribution from the dipole interaction between the tip and sample, corresponding to the term $\beta_\varepsilon e^{-\phi_\varepsilon}$ of Equation 3.18, induced by the non-zero p-polarised component of the beam, which should be constant for all bars. This non-zero offset has, therefore, been removed from the averaged field per bar values of Figure 5.31.

It can be seen that the field oscillates from $+E_z$ to $-E_z$ along the x-direction, which is evidence of SSPPs propagating along the waveguide. It can also be seen that, in addition to an exponential decay of the signal along the x-direction, the field amplitude is greatest at the beginning of the interaction region, decreasing to a minimum at approximately $x \sim 40$ μm, and then increasing again. Crucially, this is consistent with energy coupling between WG1 and WG2.

From the fit according to Equation 5.12, values of $E = 0.6$ mV, $L = 75$ μm, $k_{xe} = 4100$ cm^{-1} and $k_{xo} = 3300$ cm^{-1} were obtained corresponding to a SSPP wave vector of $k_{sp} =$ 3700 cm^{-1}. These parameters are in excellent agreement with the simulated results of Figure 5.38, which predicts a value $k_{sp} = 3525$ cm^{-1}.

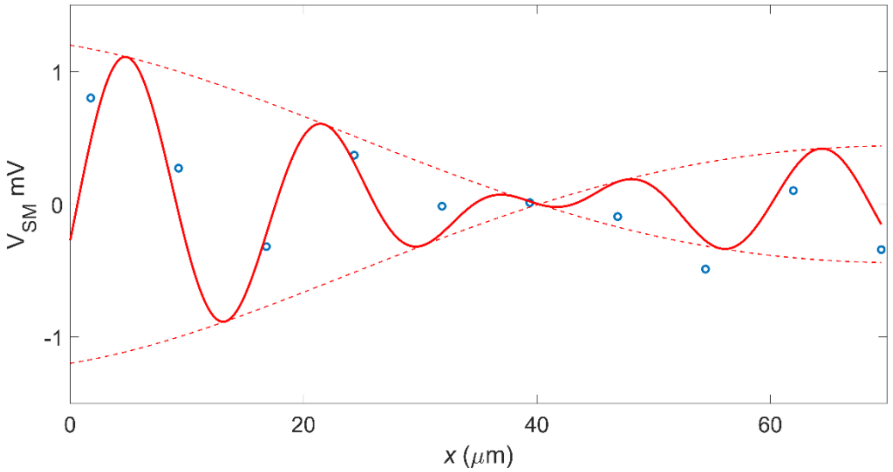

Figure 5.31 – Averaged data per bar (dots) of 5.30a fitted to using Equation 5.12 (solid line) and Equation 5.16 (dashed line) with fitting parameters $E = 0.6$ mV, $k_{xe} = 4100$ cm^{-1}, $k_{xo} = 3300$ cm^{-1}, $\theta_e = -0.26$ rad, $\theta_o = -0.19$ rad, $L = 75$ μm.

5.5.2 WG2

Figure 5.32 shows the THz and AFM images for the part of WG2 corresponding to the interaction region of the DC.

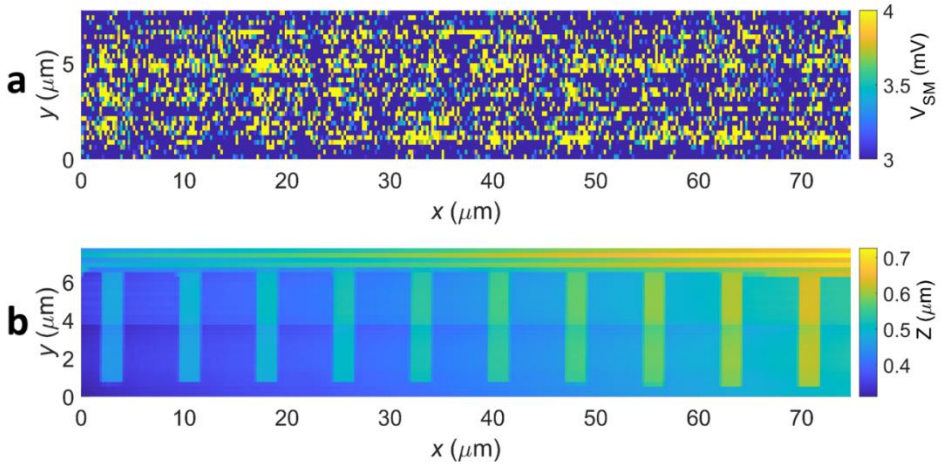

Figure 5.32 – THz s-SNOM (a) and AFM (b) images ($n = 2$) of WG2 IR of the DC structure of Figure 5.29.

In a manner similar to that seen in Section 5.5.1, the out-of-plane electric field E_z for each bar of the waveguide has been averaged and plotted in Figure 5.33. Also shown is the fit to Equation 5.13.

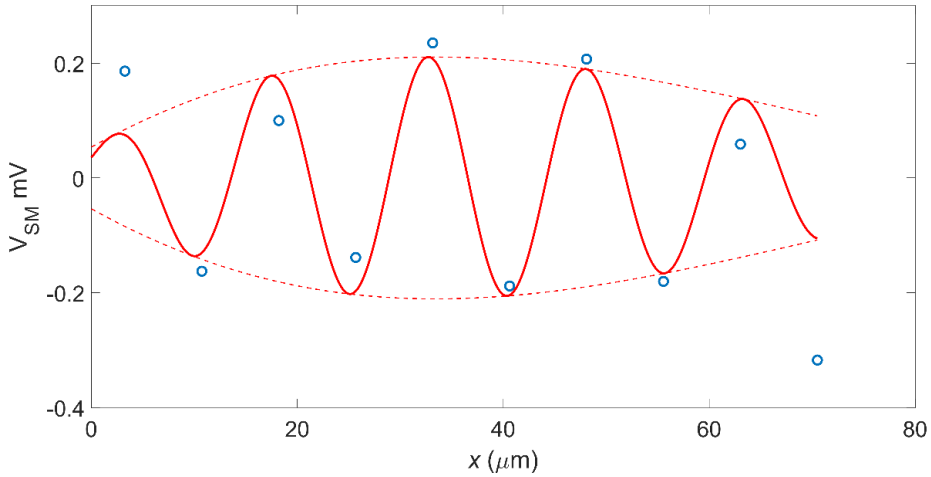

Figure 5.33 – Averaged data per bar (dots) of 5.42a fitted to using Equation 5.13 (solid line) and Equation 5.17 (dashed line) with fitting parameters $E = 0.18$ mV, $k_{xe} = 4400$ cm^{-1}, $k_{xo} = 3800$ cm^{-1}, $\theta_e = -0.7$ rad, $\theta_o = -1$ rad, $L = 75$ μm.

It can be seen, again, that the field oscillates from $+E_z$ to $-E_z$ along the x-direction, indicating SSPP propagation. Furthermore, compared to the results presented in Figure 5.31, the field amplitude of WG2 is much smaller, indicating that the nickel termination design is discouraging coupling between the THz beam and SSPP mode at the beginning of WG2 as intended. As opposed to WG1, it would be expected that the amplitude of the field should be small at the beginning and then increase as energy couples from WG1, as seen in the simulation data of Figure 5.28d. Indeed, the field amplitude in Figure 5.33 does appear to initially increase along the x-direction, until it reaches a maximum at $x \sim 35$μm. This effect is observed despite the expected exponential decay of the field, which indicates that energy coupling between WG1 and WG2 is occurring. Furthermore, after this maximum the field amplitude begins to fall, which may indicate a recoupling of the SSPP energy back to WG1.

From Figure 5.33, values of $E = 0.18$ mV, $L = 75$ μm, $k_{xe} = 4400$ cm^{-1} and $k_{xo} = 3800$ cm^{-1}, corresponding to $k_{sp} = 4100$ cm^{-1} have been obtained. The propagation length agrees excellently with both the simulations of Figure 5.28 and the results of Figure 5.31. The wave vector values are also expectantly similar to those of Figure 5.31 as well as in agreement with the simulations.

5.5.3 Discussion

From the analyses present in Sections 5.5.1 and 5.5.2, there is evidence to suggest that coupling has occurred between the incident THz beam and the SSPP modes of the DC structure. There is also evidence of SSPP coupling between WG1 and WG2 of the

structure. Furthermore, it can be seen that the amplitude of the field at bar $n = 1$ of WG1 is far greater than that of WG2, which indicates that the nickel extension termination has been effective at mitigating against SSPPs being launched at the beginning of WG2.

From the theoretical analysis of the DC structure presented in Section 5.4.3, it would be expected that some of the parameters used to define the functions fitted to both WG1 and WG2 should be the same. The experimental results presented in Figures 5.33 and 5.35 both yield the same value of the propagation length L and similar wave vector values. However, there are slight discrepancies between the values of k_e, k_o, θ_e and θ_o obtained from the fits to both waveguides. These values also deviate slightly from those obtained from the simulations of Section 5.4.3. Consequently, this leads to a coupling length $L \sim 40$ μm calculated from the experimentally obtained values, which is less than that predicted from the free-space simulations ($L = 75$ μm).

There are several reasons that may explain these inconsistencies. Firstly, the incident beam is not purely s-polarised as assumed in the simulations; in fact it is known that the emission from the QCL is slightly elliptically polarised [15]. Secondly, phase retardation effects across the structure may be present in the experimental measurements due to the sample plane not being perfectly perpendicular to the s-SNOM probe (which can be visualised in the AFM images of Figures 5.32b and 5.34b). In addition the small amplitude of the V_{SM} signal measured for both WG1 and WG2, which occurs due to the use of the wave plate for controlling the QCL polarisation, may affect the accuracy of the analysis. Also it is possible that fabrication tolerances may have resulted in slight variation in dimensions between WG1 and WG2. Another consideration is that as sample moves during scanning, the grating structure will be moving relative to the illuminating incident beam spot, which will affect the intensity of the coupling beam and, therefore, the field strength will vary with x and y.

Furthermore, there are several assumptions that have been made in the analytical model used here, such as assuming that the values of L and E_0 are the same for odd and even modes. Also, the nickel termination present at the start of WG2 and the end of the DC will not be perfectly effective at preventing SSPPs from launching from the ends of the waveguides, which will lead to an interference that has not been accounted for in the model.

With these conditions considered, it can be stated that the out-of-plane electric field associated with spoof plasmons polaritons propagating on the surface of a directional coupling device and energy coupling between adjacent waveguides within the structure,

has been successfully imaged using the THz-s-SNOM technique. Furthermore, a comparison between the field amplitude at the parts of WG1 and WG2 corresponding to the beginning of the active region show that the DC design has been improved upon with the addition of a 10 μm nickel waveguide termination.

5.6 Summary

This chapter has presented an investigation into metamaterial waveguides designed to support the propagation of spoof surface plasmon polaritons. A comprehensive summary of the previous work has been presented, which has included the theoretical and experimental analysis of a comb-shaped planar surface plasmon waveguide. Furthermore, a directional coupler structure, previously designed to couple SSPPs modes between two parallel waveguides, has been described. Previous work has suggested that this structure can support SSPPs, although the direct excitation of SSPPs in undesirable areas of the device led to mostly inconclusive experimental data.

To resolve this problem, a series of waveguide terminations, designed to inhibit coupling between the incident beam and SSPP modes have been designed and examined in this chapter. Both gold and nickel versions of the terminations were subject to free-space excitation simulations, in which the magnitude of the SSPPs field launched from the ends of a PSP waveguide was compared to determine the performance of the designs. It was found that a 10 μm nickel extension termination performed the best and resulted in a ~ 90 % decrease in coupling efficiency compared to the unmodified waveguide.

An improved DC structure, incorporating the termination, was then designed and analysed using free-space excitation simulations. The results showed that the SSPPs supported by the waveguides behaved as intended and coupling between the top and bottom waveguides was observed over an interaction length of $L \sim 60$ μm.

Lastly, the improved DC structure was experimentally examined using THz-s-SNOM. These results produced THz images of a 75 μm portion of the interaction regions of WG1 and WG2, which captured not only SSPP propagation but coupling of the SSPP modes between the waveguides over an interaction length of $L \sim 40$ μm.

Chapter 6

Future work

This chapter discusses possible avenues for future research based on the work presented in this thesis.

6.1 Chapter 2

The THz-s-SNOM system, discussed and demonstrated in Chapter 2, relies on self-mixing in a QCL for sensing the small field scattered from the s-SNOM tip. It can be seen from the investigation into the self-mixing effect and THz-s-SNOM approach that the resulting SM signal V_{SM} is generally very small (< 1 mV). Therefore, it would be beneficial to develop new QCLs that give larger V_{SM} signals, afforded by innovations such as the design of new QCL heterostructures.

Furthermore, a recent study [262] has shown how s-SNOM probe tip geometry affects the size and noise figure of the s-SNOM signal, which could be optimised for the system presented in Chapter 2. Similarly, resonant antennae tips have been show to increase the scattering efficiency and field enhancement compared to commercial AFM tips in the MIR range [94]. Development of tips designed to support resonances at THz frequencies may improve both the sensitivity and spatial resolution of our THz-s-SNOM system.

The frequency tuning of QCLs has been demonstrated in this Chapter with a tuning range of ~ 300 MHz. However, using a QCL that can be continuously tuned over a wider frequency range (of a few GHz) [137] would allow for more interferometric fringes to be generated through LFI and, therefore, more accurate amplitude and phase measurements. Additionally, QCLs that give a broad tuning, over a range of several THz [263], may be used to perform spectroscopic near-field measurements of samples. This would enable measurements such as those performed on Bi_2Se_3 in [209], from which the dispersion relation of SPPs was mapped, but without using multiple single mode lasers in consecutive measurements.

6.2 Chapter 3

The coherent imaging system of Chapter 3 required the application of a generalised phase-stepping algorithm in order to extract amplitude and phase data from the acquired V_{SM} signal during post-processing. It has been theorised that by modulating the QCL driving current with a stepped-current waveform, wherein each waveform comprises the N current steps corresponding to the I_i current values with which the QCL is stepped during image acquisition, then by using the frequency of the current modulation as the lock-in frequency for a secondary lock-in amplifier, one could automatically acquire the amplitude and phase values of the V_{SM} fringes during signal acquisition.

This concept has been successfully tested using a THz QCL and moveable reflective target, with a far-field optical set-up similar to that shown in Figure 2.9. By referencing to the frequency of a stepped-current modulation applied to the QCL, the magnitude and phase of the SM fringes could be acquired in real-time, which showed the change in phase as the reflective target was moved over a distance of 80 μm parallel to the beam path (Figure 6.1). By refining this concept, real-time coherent near-field image acquisition may be performed using the stepped frequency system of Chapter 3.

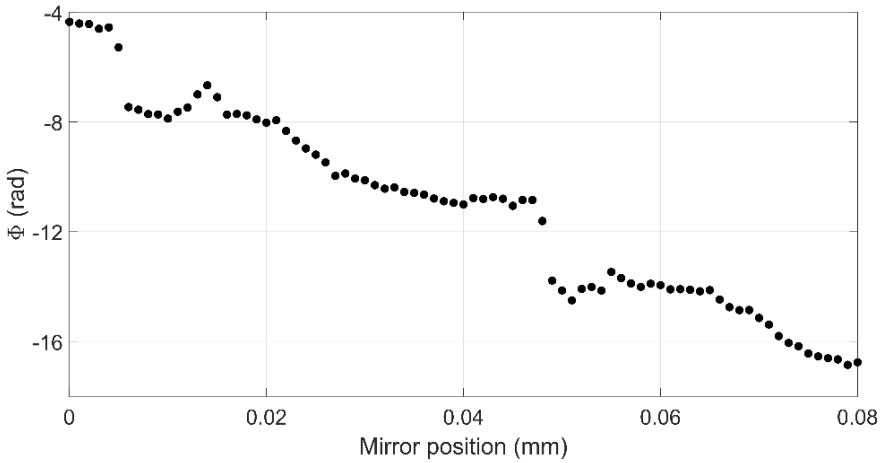

Figure 6.1 – Phase acquired from modulated stepped-frequency measurement.

Furthermore, using broad tuning QCLs, as discussed in Section 6.1, would allow for coherent spectroscopic near-field measurements of samples to be performed using the stepped-frequency system presented in Chapter 3.

One additional avenue for future work addresses a limitation of the GPSA presented in Chapter 3, in that the interferometric fringes to which it fits are assumed to be perfectly sinusoidal. Development of a GPSA in conjunction with the SM signals predicted using the Lang-Kobayashi model for a laser under optical feedback [140], would allow the GPSA to be applied to stronger feedback SM signals ($C > 0.5$).

6.3 Chapter 4

There are several adaptations to the theoretical and experimental investigation of TI samples presented in Chapter 4 that would facilitate future measurement of SPPs within these materials. Firstly, the model described by Equation 4.6 used to predict the SPP nature of the TI materials presented in Chapter 4 fails to account for interactions between phonon polaritons and surface plasmon polaritons. To consider this effect, a more sophisticated model, such as that described in [173], could be used. This would allow more accurate prediction of SPP properties based on results obtained from transport and THz-TDS measurements, as well as allowing more meaningful comparisons with experimental results obtained from TI film samples.

Furthermore, it would be beneficial to investigate the TI ribbon samples (wafer MBE20220536) presented in Section 4.5 using the coherent stepped-frequency system of Chapter 3. By capturing both the magnitude and phase response on the SM signal this may facilitate the investigation of localised surface plasmon resonances and SPPs in a similar manner as that presented in [17]. Additionally, it would be interesting to investigate these phenomenon in different resonant TI structures, such as disks or ring geometries [17].

It was concluded in Chapter 4 that the carrier concentration of the Hall bar sample tuned very little, if at all, with gate voltage V_g. The development of TIs with better electrical tuning of their carrier concentration would allow these effects to be studied. This could also be delivered by ultrafast optical laser illumination of the sample, similar to that presented in [264].

Additionally, near-field imaging of TIs using low-temperature/cryogenic s-SNOM [265], [266] may give higher material mobility and weaker phonon contributions, allowing the capture of SPP activity to be more easily realised [267].

The TI materials experimentally investigated in Chapter 4 were exclusively Bi, Se and Te based. Further study of TI materials using this method may include compounds such as

Bi-Sb-Te, as well as superlattices comprising alternating thin films of TI and dielectric material, such as Bi_2Se_3/ZnSe, the engineering of which has been shown to tune the dispersion curve [268].

Also, in addition to SPPs, the methods presented in Chapter 4 may be used to investigate phonon polaritons in TIs. These are of significant interest and have been observed, for example, in hBN at infrared wavelengths. It is feasible that applications of phonon polaritons, which include include hyperlensing, waveguiding and focusing, could be translated to the THz range using topological insulators such as Bi_2Se_3 [23].

6.4 Chapter 5

A factor that was not considered in the simulations of the DC structures presented in Chapter 5 was the elliptical polarisation of the QCL beam that was used to experimentally investigate them, which consequentially included both s- and p-polarised components. Inclusion of this effect in the simulation environment would allow more accurate comparison between experimental and theoretical results.

In addition to the improved DC structure experimentally investigated in Chapter 5, versions of this DC with different waveguide separations g may also be investigated. This would provide further confirmation of the operation of these structures, and also allow a more detailed analysis of coupling of SSPP modes in these waveguides. Additionally, using a QCL optimised to provide a greater SM signal, as described in Section 7.1, would also help mediate the small signal amplitudes associated with s-polarised excitation of these structures.

Further augmentations to the DC design may also be developed, such as structures with a bar spacing smaller than the SSPP wavelength which would allow for easier mapping of the SSPP field. Another possibility is the integration of a doped semiconductor and gate, allowing tuning/electrical control of the dispersion relation and coupling between WG1 and WG2. The possibility also exists for the development of more complex devices based on these structures, leading to plasmonic integrated circuit technologies and components operating in the THz frequency band, for example, beam-splitters, frequency selective devices, multiplexers, and filters [22].

Reference List

[1] G. Davies and E. Linfield, “Bridging the terahertz gap,” *Phys. World*, vol. 17, no. 4, pp. 37–41, 2004, doi: 10.1088/2058-7058/17/4/34.

[2] J. T. Keeley, “Self-Mixing in Terahertz Quantum Cascade Lasers,” 2016.

[3] R. Paiella, *Intersubband Transitions In Quantum Structures.* McGraw-Hill Education, 2010.

[4] B. S. Williams, “Terahertz quantum-cascade lasers,” *Nat. Photonics*, vol. 1, no. 9, pp. 517–525, 2007, doi: 10.1038/nphoton.2007.166.

[5] B. B. Hu and M. C. Nuss, “Imaging with terahertz waves,” *Opt. Lett.*, vol. 20, no. 16, p. 1716, 1995, doi: 10.1364/ol.20.001716.

[6] S. M. Kim *et al.*, “Biomedical terahertz imaging with a quantum cascade laser,” *Appl. Phys. Lett.*, vol. 88, no. 15, pp. 1–4, 2006, doi: 10.1063/1.2194229.

[7] M. Ravaro *et al.*, “Continuous-wave coherent imaging with terahertz quantum cascade lasers using electro-optic harmonic sampling,” *Appl. Phys. Lett.*, vol. 102, no. 9, 2013, doi: 10.1063/1.4793424.

[8] P. Dean *et al.*, “Terahertz imaging using quantum cascade lasers - A review of systems and applications,” *J. Phys. D. Appl. Phys.*, vol. 47, no. 37, 2014, doi: 10.1088/0022-3727/47/37/374008.

[9] L. L. Hale *et al.*, “Noninvasive Near-Field Spectroscopy of Single Subwavelength Complementary Resonators,” *Laser \& Photonics Rev.*, vol. 14, no. 4, p. 1900254, 2020, doi: https://doi.org/10.1002/lpor.201900254.

[10] N. Sulollari, “Terahertz Near-Field Imaging of Plasmonic Mode Resonances in Metamaterials,” 2022.

[11] W. L. Barnes, A. Dereux, and T. W. Ebbesen, “Surface plasmon subwavelength optics,” *Nature*, vol. 424, no. 6950, pp. 824–830, 2003, doi: 10.1038/nature01937.

[12] T. Taimre, M. Nikolić, K. Bertling, Y. L. Lim, T. Bosch, and A. D. Rakić, “Laser feedback interferometry: a tutorial on the self-mixing effect for coherent sensing,” *Adv. Opt. Photonics*, vol. 7, no. 3, p. 570, 2015, doi: 10.1364/aop.7.000570.

[13] B. Knoll and F. Keilmann, “Enhanced dielectric contrast in scattering-type scanning near-field optical microscopy,” no. August, pp. 321–328, 2000.

[14] V. E. Babicheva, “Multipole resonances and directional scattering by hyperbolic-media antennas,” vol. 25, no. 20, pp. 23935–23944, 2017, [Online]. Available: http://arxiv.org/abs/1706.07259.

[15] N. Sulollari *et al.*, “Coherent terahertz microscopy of modal field distributions in micro-resonators,” *AIP Adv.*, vol. 6, no. 6, 2021, doi: 10.1063/5.0046186.

[16] M. Z. Hasan and C. L. Kane, “Colloquium: Topological insulators,” *Rev. Mod. Phys.*, vol. 82, no. 4, pp. 3045–3067, 2010, doi: 10.1103/RevModPhys.82.3045.

[17] F. Hu *et al.*, “Imaging the Localized Plasmon Resonance Modes in Graphene Nanoribbons,” *Nano Lett.*, vol. 17, no. 9, pp. 5423–5428, 2017, doi: 10.1021/acs.nanolett.7b02029.

[18] S. Chege, P. Ning’i, J. Sifuna, and G. O. Amolo, “Origin of band inversion in topological Bi2Se3,” *AIP Adv.*, vol. 10, no. 9, 2020, doi: 10.1063/5.0022525.

[19] B. T. Wang and P. Zhang, “Phonon spectrum and bonding properties of Bi 2Se 3: Role of strong spin-orbit interaction,” *Appl. Phys. Lett.*, vol. 100, no. 8, 2012, doi: 10.1063/1.3689759.

[20] Y. Deshko, L. Krusin-Elbaum, V. Menon, A. Khanikaev, and J. Trevino, “Surface plasmon polaritons in topological insulator nano-films and superlattices,” *Opt. Express*, vol. 24, no. 7, p. 7398, 2016, doi: 10.1364/oe.24.007398.

[21] C. S. Knox *et al.*, “Optical conductivity of a Bi2Se3 topological insulator with a THz transparent top gate,” *Nanophotonics*, vol. 13, no. 10, pp. 1843–1850, 2024, doi: 10.1515/nanoph-2023-0690.

[22] N. Sulollari *et al.*, “Microscopy of terahertz spoof surface plasmons propagating on planar metamaterial waveguides,” *APL Photonics*, vol. 9, no. 3, 2024, doi: 10.1063/5.0190488.

[23] E. A. A. Pogna, L. Viti, A. Politano, M. Brambilla, G. Scamarcio, and M. S. Vitiello, “Mapping propagation of collective modes in Bi2Se3 and Bi2Te2.2Se0.8 topological insulators by near-field terahertz nanoscopy,” *Nat. Commun.*, vol. 12, no. 1, pp. 1–11, 2021, doi: 10.1038/s41467-021-26831-6.

[24] C. Sirtori, “Bridge for the terahertz gap,” *Nature*, vol. 417, no. 6885, pp. 132–133,

2002, doi: 10.1038/417132b.

[25] E. F. Nichols and J. D. Tear, “Joining the Infra-red and Electric Wave Spectra,” *Proc. Natl. Acad. Sci.*, vol. 9, no. 6, pp. 211–214, 1923, doi: 10.1073/pnas.9.6.211.

[26] T. S. Hartwick, D. T. Hodges, D. H. Barker, and F. B. Foote, “Far infrared imagery,” *Appl. Opt.*, vol. 15, no. 8, p. 1919, 1976, doi: 10.1364/ao.15.001919.

[27] V. P. Wallace, E. MacPherson, J. A. Zeitler, and C. Reid, “Three-dimensional imaging of optically opaque materials using nonionizing terahertz radiation,” *J. Opt. Soc. Am. A*, vol. 25, no. 12, pp. 3120–3133, Dec. 2008, doi: 10.1364/JOSAA.25.003120.

[28] M. Tonouchi, “Cutting-edge terahertz technology,” *Nat. Photonics*, vol. 1, no. 2, pp. 97–105, 2007, doi: 10.1038/nphoton.2007.3.

[29] A. Burnett *et al.*, “Complementary spectroscopic studies of materials of security interest,” in *Optics and Photonics for Counterterrorism and Crime Fighting II*, 2006, vol. 6402, p. 64020B, doi: 10.1117/12.689389.

[30] J. Chen, Y. Chen, H. Zhao, G. J. Bastiaans, and X.-C. Zhang, “Absorption coefficients of selected explosives and related compounds in the range of 0.1-2.8 THz,” *Opt. Express*, vol. 15, no. 19, p. 12060, 2007, doi: 10.1364/oe.15.012060.

[31] W. S. Holland *et al.*, “Submillimetre images of dusty debris around nearby stars,” *Nature*, vol. 392, no. April, pp. 788–791, 1998.

[32] P. Dean *et al.*, “Dual-frequency imaging using an electrically tunable terahertz quantum cascade laser,” *34th Int. Conf. Infrared, Millimeter, Terahertz Waves, IRMMW-THz 2009*, vol. 17, no. 23, pp. 156–159, 2009, doi: 10.1109/ICIMW.2009.5325590.

[33] F. Mohamed, R. A. Zaghlool, and W. El Hotaby, “Terahertz spectroscopic analysis of non-radiated and radiated synthetic and natural polymer / GO nanocomposites,” *J. Mol. Struct.*, vol. 1250, p. 131659, 2022, doi: https://doi.org/10.1016/j.molstruc.2021.131659.

[34] G. Mourou, C. V Stancampiano, A. Antonetti, and A. Orszag, “Picosecond microwave pulses generated with a subpicosecond laser-driven semiconductor switch,” *Appl. Phys. Lett.*, vol. 39, no. 4, pp. 295–296, 1981, doi: 10.1063/1.92719.

[35] A. Bonvalet, M. Joffre, J. L. Martin, and A. Migus, “Generation of ultrabroadband femtosecond pulses in the mid-infrared by optical rectification of 15 fs light pulses at 100 MHz repetition rate,” *Appl. Phys. Lett.*, vol. 67, no. 20, pp. 2907–2909, 1995, doi: 10.1063/1.114838.

[36] P. H. Siegel, “Terahertz technology,” *IEEE Trans. Microw. Theory Tech.*, vol. 50, no. 3, pp. 910–928, 2002, doi: 10.1109/22.989974.

[37] N. Karpowicz, H. Zhong, J. Xu, K.-I. Lin, J.-S. Hwang, and X.-C. Zhang, “Comparison between pulsed terahertz time-domain imaging and continuous wave terahertz imaging,” *Semicond. Sci. Technol.*, vol. 20, no. 7, p. S293, Jun. 2005, doi: 10.1088/0268-1242/20/7/021.

[38] K. J. Siebert *et al.*, “All-optoelectronic continuous wave THz imaging for biomedical applications,” *Phys. Med. Biol.*, vol. 47, no. 21, pp. 3743–3748, Nov. 2002, doi: 10.1088/0031-9155/47/21/310.

[39] I. S. Gregory *et al.*, “Continuous-wave terahertz system with a 60 dB dynamic range,” *Appl. Phys. Lett.*, vol. 86, no. 20, p. 204104, May 2005, doi: 10.1063/1.1935032.

[40] T. Loffler, T. May, A. Alcin, B. Hils, C. am Weg, and H. G. Roskos, “Continuous-wave terahertz imaging with a hybrid system,” in *2007 Conference on Lasers and Electro-Optics (CLEO)*, 2007, pp. 1–2, doi: 10.1109/CLEO.2007.4452875.

[41] Kazarinov R F and Suris R A, “Possibility of the amplification of electromagnetic waves in a semiconductor with a superlattice,” *Sov. Phys. - Semicond.*, vol. 5, no. 4, pp. 707–709, 1971.

[42] J. Faist, F. Capasso, D. L. Sivco, C. Sirtori, A. L. Hutchinson, and A. Y. Cho, “Quantum cascade laser,” *Science (80-.).*, vol. 264, no. 5158, pp. 553–556, 1994, doi: 10.1126/science.264.5158.553.

[43] R. Köhler *et al.*, “Terahertz semiconductor-heterostructure laser,” *Nature*, vol. 417, no. 6885, pp. 156–159, 2002, doi: 10.1038/417156a.

[44] M. S. Vitiello, G. Scalari, B. Williams, and P. De Natale, “Quantum cascade lasers: 20 years of challenges,” *Opt. Express*, vol. 23, no. 4, p. 5167, 2015, doi: 10.1364/oe.23.005167.

[45] C. Gmachl, F. Capasso, D. L. Sivco, and A. Y. Cho, “Recent progress in quantum cascade lasers and applications,” *Reports Prog. Phys.*, vol. 64, no. 11, pp. 1533–

1601, 2001, doi: 10.1088/0034-4885/64/11/204.

[46] L. H. Li *et al.*, “Multi-Watt high-power THz frequency quantum cascade lasers,” *Electron. Lett.*, vol. 53, no. 12, pp. 799–800, 2017, doi: https://doi.org/10.1049/el.2017.0662.

[47] P. Harrison and A. Valavanis, *Quantum Wells, Wires and Dots: Theoretical and Computational Physics of Semiconductor Nanostructures*. John Wiley & Sons, Inc, 2016.

[48] J. Zory P S, *Quantum well lasers*. United States: San Diego, CA (United States); Academic Press, 1993.

[49] B. E. A. Saleh and M. C. Teich, *Fundamentals of photonics*, Third., vol. 50, no. 615. Hoboken: John Wiley & Sons, Inc, 2019.

[50] G. Scalari *et al.*, “Far-infrared ($\lambda \simeq 87$ μm) bound-to-continuum quantum-cascade lasers operating up to 90 K,” *Appl. Phys. Lett.*, vol. 82, no. 19, pp. 3165–3167, 2003, doi: 10.1063/1.1571653.

[51] J. Alton *et al.*, “Optimum resonant tunnelling injection and influence of doping density on the performance of THz bound-to-continuum cascade lasers,” *Terahertz Gigahertz Electron. Photonics IV, R. J. Hwu K. J. Linden, Eds., Int. Soc. Opt. Photonics*, vol. 5727, pp. 65–73, 2005.

[52] J. Faist, F. Capasso, D. L. Sivco, and A. L. Hutchinson, *Intersubband Transitions in Quantum Wells: Physics and Devices*, 1st ed. Springer New York, 1998.

[53] B. S. Williams, H. Callebaut, S. Kumar, Q. Hu, and J. L. Reno, “3.4-THz quantum cascade laser based on longitudinal-optical-phonon scattering for depopulation,” *Appl. Phys. Lett.*, vol. 82, no. 7, pp. 1015–1017, 2003, doi: 10.1063/1.1554479.

[54] M. I. Amanti *et al.*, “Bound-to-continuum terahertz quantum cascade laser with a single-quantum-well phonon extraction/injection stage,” *New J. Phys.*, vol. 11, pp. 0–19, 2009, doi: 10.1088/1367-2630/11/12/125022.

[55] M. Wienold, L. Schrottke, M. Giehler, R. Hey, W. Anders, and H. T. Grahn, “Low-voltage terahertz quantum-cascade lasers based on LO-phonon-assisted interminiband transitions,” *Electron. Lett.*, vol. 45, no. 20, p. 1030, 2009, doi: 10.1049/el.2009.1371.

[56] Q. Hu, B. S. Williams, S. Kumar, H. Callebaut, S. Kohen, and J. L. Reno, "Resonant-phonon-assisted THz quantum-cascade lasers with metal-metal waveguides," *Semicond. Sci. Technol.*, vol. 20, no. 7, 2005, doi: 10.1088/0268-1242/20/7/013.

[57] B. S. Williams, S. Kumar, Q. Hu, and J. L. Reno, "Distributed-feedback terahertz quantum-cascade lasers with laterally corrugated metal waveguides," *Opt. Lett.*, vol. 30, no. 21, p. 2909, 2005, doi: 10.1364/ol.30.002909.

[58] P. R. Smith, D. H. Auston, and M. C. Nuss, "Subpicosecond photoconducting dipole antennas," *IEEE J. Quantum Electron.*, vol. 24, no. 2, pp. 255–260, 1988, doi: 10.1109/3.121.

[59] D. R. Chamberlin *et al.*, "Imaging at 3.4 THz with a quantum-cascade laser," *Appl. Opt.*, vol. 44, no. 1, pp. 121–125, 2005, doi: 10.1364/AO.44.000121.

[60] J. Darmo *et al.*, "Imaging with a Terahertz quantum cascade laser," *Opt. Express*, vol. 12, no. 9, pp. 1879–1884, May 2004, doi: 10.1364/OPEX.12.001879.

[61] U. S. de Cumis *et al.*, "Terahertz confocal microscopy with a quantum cascade laser source," *Opt. Express*, vol. 20, no. 20, pp. 21924–21931, Sep. 2012, doi: 10.1364/OE.20.021924.

[62] P. Dean *et al.*, "Absorption-sensitive diffuse reflection imaging of concealed powders using a terahertz quantum cascade laser," *Opt. Express*, vol. 16, no. 9, pp. 5997–6007, Apr. 2008, doi: 10.1364/OE.16.005997.

[63] M. Ravaro *et al.*, "Detection of a 2.8 THz quantum cascade laser with a semiconductor nanowire field-effect transistor coupled to a bow-tie antenna," *Appl. Phys. Lett.*, vol. 104, no. 8, p. 83116, Feb. 2014, doi: 10.1063/1.4867074.

[64] P. Dean *et al.*, "Terahertz imaging through self-mixing in a quantum cascade laser," *Opt. Lett.*, vol. 36, no. 13, pp. 2587–2589, 2011, doi: 10.1364/OL.36.002587.

[65] A. A. Danylov *et al.*, "Transformation of the multimode terahertz quantum cascade laser beam into a Gaussian, using a hollow dielectric waveguide," *Appl. Opt.*, vol. 46, no. 22, pp. 5051–5055, 2007, doi: 10.1364/AO.46.005051.

[66] A. J. L. Adam *et al.*, "Beam patterns of terahertz quantum cascade lasers with subwavelength cavity dimensions," *Appl. Phys. Lett.*, vol. 88, no. 15, pp. 1–3, 2006, doi: 10.1063/1.2194889.

[67] E. Bründermann *et al.*, “Turn-key compact high temperature terahertz quantum cascade lasers:,” *Opt. Express*, vol. 14, no. 5, pp. 1829–1841, Mar. 2006, doi: 10.1364/OE.14.001829.

[68] H. Richter *et al.*, “A compact, continuous-wave terahertz source based on a quantum-cascade laser and a miniature cryocooler,” *Opt. Express*, vol. 18, no. 10, pp. 10177–10187, May 2010, doi: 10.1364/OE.18.010177.

[69] H.-W. Hübers *et al.*, “Terahertz quantum cascade laser as local oscillator in a heterodyne receiver,” *Opt. Express*, vol. 13, no. 15, pp. 5890–5896, Jul. 2005, doi: 10.1364/OPEX.13.005890.

[70] M. Hajenius *et al.*, “Surface plasmon quantum cascade lasers as terahertz local oscillators,” *Opt. Lett.*, vol. 33, no. 4, pp. 312–314, Feb. 2008, doi: 10.1364/OL.33.000312.

[71] M. Salih *et al.*, “Terahertz quantum cascade lasers with thin resonant-phonon depopulation active regions and surface-plasmon waveguides,” *J. Appl. Phys.*, vol. 113, no. 11, p. 113110, Mar. 2013, doi: 10.1063/1.4795606.

[72] A. A. Danylov *et al.*, “Terahertz inverse synthetic aperture radar (ISAR) imaging with a quantum cascade laser transmitter,” *Opt. Express*, vol. 18, no. 15, p. 16264, 2010, doi: 10.1364/oe.18.016264.

[73] A. D. Rakić *et al.*, “Swept-frequency feedback interferometry using terahertz frequency QCLs: a method for imaging and materials analysis,” *Opt. Express*, vol. 21, no. 19, p. 22194, 2013, doi: 10.1364/oe.21.022194.

[74] S. Barbieri *et al.*, “Phase-locking of a 2.7-THz quantum cascade laser to a mode-locked erbium-doped fibre laser,” *Nat. Photonics*, vol. 4, no. 9, pp. 636–640, 2010, doi: 10.1038/nphoton.2010.125.

[75] P. Dean *et al.*, “Coherent three-dimensional terahertz imaging through self-mixing in a quantum cascade laser,” *Appl. Phys. Lett.*, vol. 103, no. 18, 2013, doi: 10.1063/1.4827886.

[76] A. A. Danylov *et al.*, “Frequency stabilization of a single mode terahertz quantum cascade laser to the kilohertz level,” *Opt. Express*, vol. 17, no. 9, pp. 7525–7532, Apr. 2009, doi: 10.1364/OE.17.007525.

[77] A. L. Betz, R. T. Boreiko, B. S. Williams, S. Kumar, Q. Hu, and J. L. Reno, “Frequency and phase-lock control of a 3 THz quantum cascade laser,” *Opt. Lett.*,

vol. 30, no. 14, pp. 1837–1839, Jul. 2005, doi: 10.1364/OL.30.001837.

[78] G. Giuliani, M. Norgia, S. Donati, and T. Bosch, "Laser diode self-mixing technique for sensing applications," *J. Opt. A Pure Appl. Opt.*, vol. 4, no. 6, 2002, doi: 10.1088/1464-4258/4/6/371.

[79] Y. Leng Lim *et al.*, "Demonstration of a self-mixing displacement sensor based on terahertz quantum cascade lasers," *Appl. Phys. Lett.*, vol. 99, no. 8, p. 81108, Aug. 2011, doi: 10.1063/1.3629991.

[80] S. S. Dhillon *et al.*, "The 2017 terahertz science and technology roadmap," *J. Phys. D. Appl. Phys.*, vol. 50, no. 4, 2017, doi: 10.1088/1361-6463/50/4/043001.

[81] F. P. Mezzapesa, L. L. Columbo, M. Brambilla, M. Dabbicco, M. S. Vitiello, and G. Scamarcio, "Imaging of free carriers in semiconductors via optical feedback in terahertz quantum cascade lasers," *Appl. Phys. Lett.*, vol. 104, no. 4, 2014, doi: 10.1063/1.4863671.

[82] P. Dean *et al.*, "Active phase-nulling of the self-mixing phase in a terahertz frequency quantum cascade laser," *Opt. Lett.*, vol. 40, no. 6, p. 950, Mar. 2015, doi: 10.1364/ol.40.000950.

[83] T. Hagelschuer *et al.*, "Terahertz gas spectroscopy through self-mixing in a quantum-cascade laser," *Appl. Phys. Lett.*, vol. 109, no. 19, p. 191101, Nov. 2016, doi: 10.1063/1.4967435.

[84] E. McLeod and A. Ozcan, "Nano-imaging enabled via self-assembly," *Nano Today*, vol. 9, no. 5, pp. 560–573, 2014, doi: https://doi.org/10.1016/j.nantod.2014.08.005.

[85] J. Beuthan, O. Minet, and G. Muller, "The spatial resolution of near-field optical microscope on chromosomes and cell traces," *IEEE J. Sel. Top. Quantum Electron.*, vol. 7, no. 6, pp. 894–898, Nov. 2001, doi: 10.1109/2944.983290.

[86] A. Cricenti *et al.*, "Optical nanospectroscopy study of ion-implanted silicon and biological growth medium," *J. Alloys Compd.*, vol. 362, no. 1, pp. 21–25, 2004, doi: https://doi.org/10.1016/S0925-8388(03)00557-7.

[87] A. D. Yoffe, "Semiconductor quantum dots and related systems: Electronic, optical, luminescence and related properties of low dimensional systems," *Adv. Phys.*, vol. 50, no. 1, pp. 1–208, 2001, doi: 10.1080/00018730010006608.

[88] M. Brun, S. Huant, J. C. Woehl, J. F. Motte, L. Marsal, and H. Mariette, “Low-temperature near-field spectroscopy of CdTe quantum dots,” *J. Microsc.*, vol. 202, no. Pt 1, pp. 202–208, Apr. 2001, doi: 10.1046/j.1365-2818.2001.00798.x.

[89] P. Tomanek, M. Benesova, D. Kostalova, and P. Letal, “Local optical characteristics of semiconductor surfaces,” in *Selected Papers from Fifth International Conference on Correlation Optics*, Feb. 2002, vol. 4607, pp. 168–177, doi: 10.1117/12.455186.

[90] L. Grmela, J. Kala, and P. Tománek, “Local photoluminescence in InAs/GaAs heterostructures with quantum dots and artificial molecules,” in *Photonics, Devices, and Systems III*, 2006, vol. 6180, p. 61802D, doi: 10.1117/12.675867.

[91] Z. Yang *et al.*, “Near-Field Nanoscopic Terahertz Imaging of Single Proteins,” *Small*, vol. 17, no. 3, p. 2005814, 2021, doi: https://doi.org/10.1002/smll.202005814.

[92] A. J. L. Adam, “Review of near-field Terahertz measurement methods and their applications,” *J. Infrared, Millimeter, Terahertz Waves*, vol. 32, no. 8–9, pp. 976–1019, 2011, doi: 10.1007/s10762-011-9809-2.

[93] S. Mair, B. Gompf, and M. Dressel, “Spatial and spectral behavior of the optical near field studied by a terahertz near-field spectrometer,” *Appl. Phys. Lett.*, vol. 84, no. 7, pp. 1219–1221, Feb. 2004, doi: 10.1063/1.1647707.

[94] A. Leitenstorfer *et al.*, “The 2023 terahertz science and technology roadmap,” *J. Phys. D. Appl. Phys.*, vol. 56, no. 22, p. 223001, Apr. 2023, doi: 10.1088/1361-6463/acbe4c.

[95] M. C. Giordano, L. Viti, O. Mitrofanov, and M. S. Vitiello, “Phase-sensitive terahertz imaging using room-temperature near-field nanodetectors,” *Optica*, vol. 5, no. 5, pp. 651–657, May 2018, doi: 10.1364/OPTICA.5.000651.

[96] E. Yoxall, “Applications of scattering-type scanning near-field optical microscopy in the infrared,” 2013.

[97] L. Aigouy *et al.*, “Near-field optical spectroscopy using an incoherent light source,” *Appl. Phys. Lett.*, vol. 76, no. 4, pp. 397–399, 2000.

[98] H. Wang, L. Wang, and X. G. Xu, “Scattering-type scanning near-field optical microscopy with low-repetition-rate pulsed light source through phase-domain sampling,” *Nat. Commun.*, vol. 7, no. May, pp. 1–8, 2016, doi:

10.1038/ncomms13212.

[99] R. Hillenbrand and F. Keilmann, “Complex Optical Constants on a Subwavelength Scale,” *Phys. Rev. Lett.*, vol. 85, no. 14, pp. 3029–3032, Oct. 2000, doi: 10.1103/PhysRevLett.85.3029.

[100] A. Dereux, C. Girard, and J.-C. Weeber, “Theoretical principles of near-field optical microscopies and spectroscopies,” *J. Chem. Phys.*, vol. 112, no. 18, pp. 7775–7789, May 2000, doi: 10.1063/1.481383.

[101] M. B. Raschke and C. Lienau, “Apertureless near-field optical microscopy: Tip-sample coupling in elastic light scattering,” *Appl. Phys. Lett.*, vol. 83, no. 24, pp. 5089–5091, 2003, doi: 10.1063/1.1632023.

[102] P. Dean *et al.*, “Apertureless near-field terahertz imaging using the self-mixing effect in a quantum cascade laser,” *Appl. Phys. Lett.*, vol. 108, no. 9, 2016, doi: 10.1063/1.4943088.

[103] B. Knoll and F. Keilmann, “Near-field probing of vibrational absorption for chemical microscopy,” *Lett. to Nat.*, vol. 399, no. May, pp. 7–10, 1999.

[104] H. T. Chen, R. Kersting, and G. C. Cho, “Terahertz imaging with nanometer resolution,” *Appl. Phys. Lett.*, vol. 83, no. 15, pp. 3009–3011, 2003, doi: 10.1063/1.1616668.

[105] M. Eisele *et al.*, “Ultrafast multi-terahertz nano-spectroscopy with sub-cycle temporal resolution,” *Nat. Photonics*, vol. 8, no. 11, pp. 841–845, 2014, doi: 10.1038/nphoton.2014.225.

[106] C. Liewald, S. Mastel, J. Hesler, A. J. Huber, R. Hillenbrand, and F. Keilmann, “All-electronic terahertz nanoscopy,” *Optica*, vol. 5, no. 2, p. 159, 2018, doi: 10.1364/optica.5.000159.

[107] a J. Huber, F. Keilmann, J. Wittborn, J. Aizpurua, and R. Hillenbrand, “Terahertz Near-Field Nanoscopy of Nanodevices,” *Nano Lett.*, vol. 8, no. 11, pp. 3766–3770, 2008.

[108] J. Shi *et al.*, “THz photonics in two dimensional materials and metamaterials: Properties, devices and prospects,” *J. Mater. Chem. C*, vol. 6, no. 6, pp. 1291–1306, 2018, doi: 10.1039/c7tc05460b.

[109] P. Alonso-González *et al.*, “Acoustic terahertz graphene plasmons revealed by

photocurrent nanoscopy," *Nat. Nanotechnol.*, vol. 12, no. 1, pp. 31–35, 2017, doi: 10.1038/nnano.2016.185.

[110] G. Acuna, S. F. Heucke, F. Kuchler, H. T. Chen, A. J. Taylor, and R. Kersting, "Surface plasmons in terahertz metamaterials," *Opt. Express*, vol. 16, no. 23, p. 18745, 2008, doi: 10.1364/oe.16.018745.

[111] R. Degl'Innocenti *et al.*, "Terahertz Nanoscopy of Plasmonic Resonances with a Quantum Cascade Laser," *ACS Photonics*, vol. 4, no. 9, pp. 2150–2157, 2017, doi: 10.1021/acsphotonics.7b00687.

[112] A. Zayats and I. Smolyaninov, "Near-field photonics: Surface plasmon polaritons and localized surface plasmons," *J. Opt. A Pure Appl. Opt.*, vol. 5, p. S16, 2003, doi: 10.1088/1464-4258/5/4/353.

[113] X. Zhang and Z. Liu, "Superlenses to overcome the diffraction limit," *Nat. Mater.*, vol. 7, no. 6, pp. 435–441, 2008, doi: 10.1038/nmat2141.

[114] C. Genet and T. W. Ebbesen, "Light in tiny holes," *Nature*, vol. 445, no. 7123, pp. 39–46, 2007, doi: 10.1038/nature05350.

[115] S. Nie and S. R. Emory, "Probing Single Molecules and Single Nanoparticles by Surface-Enhanced Raman Scattering," *Science (80-.).*, vol. 275, no. 5303, pp. 1102–1106, 1997, doi: 10.1126/science.275.5303.1102.

[116] P. A. Huidobro, A. I. Fernández-Domínguez, J. B. Pendry, L. Martín-Moreno, and F. J. Garcia-Vidal, *Spoof Surface Plasmon Metamaterials*. Cambridge University Press, 2018.

[117] J. R. Sambles, G. W. Bradbery, and F. Yang, "Optical excitation of surface plasmons: an introduction," *Contemp. Phys.*, pp. 173–183, 1991.

[118] E. Kretschmann and H. Raether, "Radiative Decay of Non Radiative Surface Plasmons Excited by Light," *Zeitschrift für Naturforsch. A*, vol. 23, no. 12, pp. 2135–2136, 1968, doi: doi:10.1515/zna-1968-1247.

[119] A. Otto, "Excitation of nonradiative surface plasma waves in silver by the method of frustrated total reflection," *Zeitschrift für Phys. A Hadron. Nucl.*, vol. 216, no. 4, pp. 398–410, 1968, doi: 10.1007/BF01391532.

[120] B. Hecht, H. Bielefeldt, L. Novotny, Y. Inouye, and D. W. Pohl, "Local Excitation, Scattering, and Interference of Surface Plasmons," *Phys. Rev. Lett.*, vol. 77, no. 9,

pp. 1889–1892, Aug. 1996, doi: 10.1103/PhysRevLett.77.1889.

[121] H. Ditlbacher *et al.*, “Fluorescence imaging of surface plasmon fields,” *Appl. Phys. Lett.*, vol. 80, no. 3, pp. 404–406, Jan. 2002, doi: 10.1063/1.1435410.

[122] R. H. Ritchie, E. T. Arakawa, J. J. Cowan, and R. N. Hamm, “Surface-Plasmon Resonance Effect in Grating Diffraction,” *Phys. Rev. Lett.*, vol. 21, no. 22, pp. 1530–1533, Nov. 1968, doi: 10.1103/PhysRevLett.21.1530.

[123] H. Raether, *Surface Plasmons on Smooth and Rough Surfaces and on Gratings*, vol. 111. 1988.

[124] I. Kundu *et al.*, “Frequency Tunability and Spectral Control in Terahertz Quantum Cascade Lasers with Phase-Adjusted Finite-Defect-Site Photonic Lattices,” *IEEE Trans. Terahertz Sci. Technol.*, vol. 7, no. 4, pp. 360–367, 2017, doi: 10.1109/TTHZ.2017.2707800.

[125] P. Rubino, “Near-field Imaging Using Self Mixing in Terahertz frequency Quantum Cascade Lasers,” 2019.

[126] J. Keeley *et al.*, “Three-dimensional terahertz imaging using swept-frequency feedback interferometry with a quantum cascade laser,” *Opt. Lett.*, vol. 40, no. 6, p. 994, 2015, doi: 10.1364/ol.40.000994.

[127] A. D. Rakić *et al.*, “Optical feedback effects on terahertz quantum cascade lasers: modelling and applications,” *Infrared, Millimeter-Wave, Terahertz Technol. IV*, vol. 10030, no. 10030, p. 1003016, 2016, doi: 10.1117/12.2250621.

[128] K. Gürel *et al.*, “Frequency tuning and modulation of a quantum cascade laser with an integrated resistive heater,” *Photonics*, vol. 3, no. 3, pp. 1–12, 2016, doi: 10.3390/photonics3030047.

[129] M. Hempel, B. Röben, M. Niehle, L. Schrottke, A. Trampert, and H. T. Grahn, “Continuous tuning of two-section, single-mode terahertz quantum-cascade lasers by fiber-coupled, near-infrared illumination,” *AIP Adv.*, vol. 7, no. 5, 2017, doi: 10.1063/1.4983030.

[130] J. M. Supplee, E. A. Whittaker, and W. Lenth, “Theoretical description of frequency modulation and wavelength modulation spectroscopy,” *Appl. Opt.*, vol. 33, no. 27, p. 6294, 1994, doi: 10.1364/ao.33.006294.

[131] G. C. Bjorklund, “Frequency-modulation spectroscopy: a new method for

measuring weak absorptions and dispersions," *Opt. Lett.*, vol. 5, no. 1, pp. 15–17, 1980.

[132] G. Agnew *et al.*, "Model for a pulsed terahertz quantum cascade laser under optical feedback," *Opt. Express*, vol. 24, no. 18, p. 20554, 2016, doi: 10.1364/oe.24.020554.

[133] D. B. Kolker *et al.*, "Tunable mid-infrared laser sources for trace-gas analysis," *J. Phys. Conf. Ser.*, vol. 2067, no. 1, 2021, doi: 10.1088/1742-6596/2067/1/012013.

[134] D. Fröhlich, R. Wille, W. Schlapp, and G. Weimann, "Optical quantum-confined Stark effect in GaAs quantum wells," *Phys. Rev. Lett.*, vol. 59, no. 15, pp. 1748–1751, 1987, doi: 10.1103/PhysRevLett.59.1748.

[135] L. Gao, L. Zhao, J. L. Reno, and S. Kumar, "Electrical tuning of a terahertz quantum cascade laser based on detuned intersubband absorption," *Appl. Phys. Lett.*, vol. 115, no. 14, 2019, doi: 10.1063/1.5118770.

[136] B. Röben, X. Lü, M. Hempel, K. Biermann, L. Schrottke, and H. T. Grahn, "Terahertz quantum-cascade lasers as high-power and wideband, gapless sources for spectroscopy," *Opt. Express*, vol. 25, no. 14, p. 16282, 2017, doi: 10.1364/oe.25.016282.

[137] I. Kundu *et al.*, "Continuous Frequency Tuning with near Constant Output Power in Coupled Y-Branched Terahertz Quantum Cascade Lasers with Photonic Lattice," *ACS Photonics*, vol. 5, no. 7, pp. 2912–2920, 2018, doi: 10.1021/acsphotonics.8b00251.

[138] W. Guan *et al.*, "Frequency tuning behaviour of terahertz quantum cascade lasers revealed by a laser beating scheme," *Int. Conf. Infrared, Millimeter, Terahertz Waves, IRMMW-THz*, vol. 2021-Augus, no. 14, pp. 21269–21279, 2021, doi: 10.1109/IRMMW-THz50926.2021.9566863.

[139] M. S. Vitiello and A. Tredicucci, "Tunable emission in THz quantum cascade lasers," *IEEE Trans. Terahertz Sci. Technol.*, vol. 1, no. 1, pp. 76–84, 2011, doi: 10.1109/TTHZ.2011.2159543.

[140] R. Lang and K. Kobayashi, "External Optical Feedback Effects on Semiconductor Injection Laser Properties," *IEEE J. Quantum Electron.*, vol. 16, no. 3, pp. 347–355, 1980, doi: 10.1109/JQE.1980.1070479.

[141] P. Dean *et al.*, *Self-Mixing in Quantum Cascade Lasers: Theory and Applications*. Cambridge University Press, 2023.

[142] Y. Yu, G. Giuliani, and S. Donati, "Measurement of the linewidth enhancement factor of semiconductor lasers based on the optical feedback self-mixing effect," *IEEE Photonics Technol. Lett.*, vol. 16, no. 4, pp. 990–992, 2004, doi: 10.1109/LPT.2004.824631.

[143] R. Kliese *et al.*, "Solving self-mixing equations for arbitrary feedback levels: a concise algorithm," *Appl. Opt.*, vol. 53, no. 17, p. 3723, 2014, doi: 10.1364/ao.53.003723.

[144] C. H. Henry, "Theory of the Linewidth of Semiconductor Lasers," *IEEE J. Quantum Electron.*, vol. 18, no. 2, pp. 259–264, 1982, doi: 10.1109/JQE.1982.1071522.

[145] R. P. Green *et al.*, "Linewidth enhancement factor of terahertz quantum cascade lasers," *Appl. Phys. Lett.*, vol. 92, no. 7, pp. 1–4, 2008, doi: 10.1063/1.2883950.

[146] J. Keeley *et al.*, "Detection sensitivity of laser feedback interferometry using a terahertz quantum cascade laser," *Opt. Lett.*, vol. 44, no. 13, p. 3314, 2019, doi: 10.1364/ol.44.003314.

[147] T. Taubner, F. Keilmann, and R. Hillenbrand, "Effect of tip modulation on image contrast in scattering-type near-field optical microscopy," *J. Korean Phys. Soc.*, vol. 47, no. SUPPL. 1, pp. 213–216, 2005.

[148] G. Lu, R. Zhao, H. Yin, Z. Xiao, and J. Zhang, "Improved Point Dipole Model for Subwavelength Resolution Scattering Near-Field Optical Microscopy (SNOM)," *Int. J. Antennas Propag.*, vol. 2020, 2020, doi: 10.1155/2020/9293018.

[149] T. Taubner, R. Hillenbrand, and F. Keilmann, "Performance of visible and mid-infrared scattering-type near-field optical microscopes," *J. Microsc.*, vol. 210, no. 3, pp. 311–314, 2003, doi: 10.1046/j.1365-2818.2003.01164.x.

[150] S. Mastel, A. A. Govyadinov, C. Maissen, A. Chuvilin, A. Berger, and R. Hillenbrand, "Understanding the Image Contrast of Material Boundaries in IR Nanoscopy Reaching 5 nm Spatial Resolution," *ACS Photonics*, vol. 5, no. 8, pp. 3372–3378, 2018, doi: 10.1021/acsphotonics.8b00636.

[151] R. Krutokhvostov *et al.*, "Enhanced resolution in subsurface near-field optical microscopy," *Opt. Express*, vol. 20, no. 1, p. 593, 2012, doi: 10.1364/oe.20.000593.

[152] D. Roy and A. E. Knight, “Scanning Near-Field Optical Microscopy and Related Techniques,” in *Encyclopedia of Spectroscopy and Spectrometry*, Academic Press, 2017, pp. 1–6.

[153] M. C. Giordano *et al.*, “Phase-resolved terahertz self-detection nearfield microscopy,” *Opt. Express*, vol. 26, no. 14, pp. 3430–3438, 2018.

[154] Y. L. Lim *et al.*, “Coherent imaging using laser feedback interferometry with pulsed-mode terahertz quantum cascade lasers,” *Opt. Express*, vol. 27, no. 7, 2019.

[155] G. Lai and T. Yatagai, “Generalized phase-shifting interferometry,” vol. 8, no. 5, pp. 822–827, 1991.

[156] N. Yoshikawa and K. Kajihara, “Statistical generalized phase-shifting digital holography with a continuous fringe-scanning scheme,” *Opt. Lett.*, vol. 40, no. 13, p. 3149, 2015, doi: 10.1364/ol.40.003149.

[157] T. Nomura and K. Shinomura, “Generalized sequential four-step phase-shifting color digital holography,” *Appl. Opt.*, vol. 56, no. 24, p. 6851, 2017, doi: 10.1364/ao.56.006851.

[158] L. Vabre, A. Dubois, and A. C. Boccara, “Thermal-light full-field optical coherence tomography,” vol. 27, no. 7, pp. 530–532, 2002.

[159] A. Dubois, L. Vabre, A. C. Boccara, and E. Beaurepaire, “High-resolution full-field optical coherence tomography with a Linnik microscope,” *Appl. Opt.*, vol. 41, no. 4, pp. 805–812, 2002, doi: 10.1364/AO.41.000805.

[160] M. Wienold *et al.*, “Real-time terahertz imaging through self-mixing in a quantum-cascade laser,” *Appl. Phys. Lett.*, vol. 109, no. 1, 2016, doi: 10.1063/1.4955405.

[161] P. Rubino *et al.*, “All-Electronic Phase-Resolved THz Microscopy Using the Self-Mixing Effect in a Semiconductor Laser,” *ACS Photonics*, vol. 8, no. 4, pp. 1001–1006, 2021, doi: 10.1021/acsphotonics.0c01908.

[162] E. A. A. Pogna, C. Silvestri, L. L. Columbo, M. Brambilla, G. Scamarcio, and M. S. Vitiello, “Terahertz near-field nanoscopy based on detectorless laser feedback interferometry under different feedback regimes,” *APL Photonics*, vol. 6, no. 6, p. 1ENG, 2021, doi: 10.1063/5.0048099.

[163] Y. Ando, “Topological insulator materials,” *J. Phys. Soc. Japan*, vol. 82, no. 10, Oct. 2013, doi: 10.7566/JPSJ.82.102001.

[164] J. Sinova, D. Culcer, Q. Niu, N. A. Sinitsyn, T. Jungwirth, and A. H. MacDonald, “Universal intrinsic spin Hall effect,” *Phys. Rev. Lett.*, vol. 92, no. 12, pp. 1–4, 2004, doi: 10.1103/PhysRevLett.92.126603.

[165] D. Backes *et al.*, “Disentangling surface and bulk transport in topological-insulator p-n junctions,” *Phys. Rev. B*, vol. 96, no. 12, 2017, doi: 10.1103/PhysRevB.96.125125.

[166] T. Topological *et al.*, “Experimental Realization of a Three-Dimensional Topological Insulator, Bi2Te3,” vol. 178, no. July, pp. 1–4, 2009, doi: 10.1126/science.1173034.

[167] D. Kong *et al.*, “Ambipolar field effect in the ternary topological insulator (Bi xSb1-x)2 Te3 by composition tuning,” *Nat. Nanotechnol.*, vol. 6, no. 11, pp. 705–709, 2011, doi: 10.1038/nnano.2011.172.

[168] J. Zhang *et al.*, “Band structure engineering in (Bi1-xSbx) 2Te3 ternary topological insulators,” *Nat. Commun.*, vol. 2, no. 1, 2011, doi: 10.1038/ncomms1588.

[169] C. Weyrich *et al.*, “Growth, characterization, and transport properties of ternary (Bi1-xSbx)2Te3 topological insulator layers,” *J. Phys. Condens. Matter*, vol. 28, no. 49, 2016, doi: 10.1088/0953-8984/28/49/495501.

[170] Z. Zhang *et al.*, “Transport properties of Sb2Te3/Bi2Te3 topological insulator heterostructures,” *Phys. Status Solidi - Rapid Res. Lett.*, vol. 7, no. 1–2, pp. 142–144, 2013, doi: 10.1002/pssr.201206391.

[171] M. Eschbach *et al.*, “Realization of a vertical topological p-n junction in epitaxial Sb2Te3/Bi2Te3 heterostructures,” *Nat. Commun.*, vol. 6, no. May, 2015, doi: 10.1038/ncomms9816.

[172] J. Chen *et al.*, “Gate-voltage control of chemical potential and weak antilocalization in Bi2Se3,” *Phys. Rev. Lett.*, vol. 105, no. 17, pp. 1–4, 2010, doi: 10.1103/PhysRevLett.105.176602.

[173] J. Chen *et al.*, “Tunable surface conductivity in Bi2Se3 revealed in diffusive electron transport,” *Phys. Rev. B - Condens. Matter Mater. Phys.*, vol. 83, no. 24, pp. 1–4, 2011, doi: 10.1103/PhysRevB.83.241304.

[174] J. G. Checkelsky, Y. S. Hor, R. J. Cava, and N. P. Ong, “Bulk band gap and surface state conduction observed in voltage-tuned crystals of the topological insulator Bi2Se3,” *Phys. Rev. Lett.*, vol. 106, no. 19, pp. 4–7, 2011, doi: 10.1103/PhysRevLett.106.196801.

[175] H. Steinberg, J. B. Laloë, V. Fatemi, J. S. Moodera, and P. Jarillo-Herrero, “Electrically tunable surface-to-bulk coherent coupling in topological insulator thin films,” *Phys. Rev. B - Condens. Matter Mater. Phys.*, vol. 84, no. 23, pp. 5–8, 2011, doi: 10.1103/PhysRevB.84.233101.

[176] N. Nagaosa, “A New State of Quantum Matter,” in *Science*, vol. 318, no. 5851, American Association for the Advancement of Science, 2007, pp. 758–759.

[177] P. Di Pietro *et al.*, “Terahertz plasmonic excitations in Bi2Se3 topological insulator,” *J. Phys. Condens. Matter*, vol. 29, p. 183002, 2017.

[178] S. Dai, Z. Fei, M. Wagner, A. S. McLeod, and M. K. Liu, “Tunable Phonon Polaritonsin Atomically Thin van der WaalsCrystals of Boron Nitride,” *Science (80-.).*, vol. 343, no. March, pp. 1125–1129, 2014.

[179] C. L. Kane and E. J. Mele, “Quantum Spin hall effect in graphene,” *Phys. Rev. Lett.*, vol. 95, no. 22, pp. 1–4, 2005, doi: 10.1103/PhysRevLett.95.226801.

[180] S. Murakami, N. Nagaosa, and S. C. Zhang, “Spin-Hall insulator,” *Phys. Rev. Lett.*, vol. 93, no. 15, pp. 6–9, 2004, doi: 10.1103/PhysRevLett.93.156804.

[181] J. Hu, J. Alicea, R. Wu, and M. Franz, “Giant topological insulator gap in graphene with 5d adatoms,” *Phys. Rev. Lett.*, vol. 109, no. 26, pp. 1–5, 2012, doi: 10.1103/PhysRevLett.109.266801.

[182] K. S. Novoselov et al, “Electric Field Effect in Atomically Thin Carbon Films,” in *Science*, vol. 306, no. 5696, American Association for the Advancement of Science, 2004, pp. 666–669.

[183] R. E. V. Profumo, R. Asgari, M. Polini, and A. H. MacDonald, “Double-layer graphene and topological insulator thin-film plasmons,” *Phys. Rev. B - Condens. Matter Mater. Phys.*, vol. 85, no. 8, pp. 1–8, 2012, doi: 10.1103/PhysRevB.85.085443.

[184] S. Das Sarma and E. H. Hwang, “Collective modes of the massless dirac plasma,” *Phys. Rev. Lett.*, vol. 102, no. 20, pp. 1–4, 2009, doi: 10.1103/PhysRevLett.102.206412.

[185] L. Ju *et al.*, “Graphene plasmonics for tunable terahertz metamaterials,” *Nat. Nanotechnol.*, vol. 6, no. 10, pp. 630–634, 2011, doi: 10.1038/nnano.2011.146.

[186] P. Y. Chen, H. Huang, D. Akinwande, and A. Alù, “Graphene-Based Plasmonic Platform for Reconfigurable Terahertz Nanodevices,” *ACS Photonics*, vol. 1, no. 8, pp. 647–654, 2014, doi: 10.1021/ph500046r.

[187] M. Tamagnone *et al.*, “Near optimal graphene terahertz non-reciprocal isolator,” *Nat. Commun.*, vol. 7, pp. 1–6, 2016, doi: 10.1038/ncomms11216.

[188] Z. Sun, A. Martinez, and F. Wang, “Optical modulators with 2D layered materials,” *Nat. Photonics*, vol. 10, no. 4, pp. 227–238, 2016, doi: 10.1038/nphoton.2016.15.

[189] T. Otsuji, V. Popov, and V. Ryzhii, “Active graphene plasmonics for terahertz device applications,” *J. Phys. D. Appl. Phys.*, vol. 47, no. 9, 2014, doi: 10.1088/0022-3727/47/9/094006.

[190] Z. Fei *et al.*, “Infrared nanoscopy of dirac plasmons at the graphene-SiO2 interface,” *Nano Lett.*, vol. 11, no. 11, pp. 4701–4705, 2011, doi: 10.1021/nl202362d.

[191] X. Gu, I. T. Lin, and J. M. Liu, “Extremely confined terahertz surface plasmon-polaritons in graphene-metal structures,” *Appl. Phys. Lett.*, vol. 103, no. 7, 2013, doi: 10.1063/1.4818660.

[192] O. Mitrofanov *et al.*, “Terahertz near-field imaging of surface plasmon waves in graphene structures,” *Solid State Commun.*, vol. 224, pp. 47–52, 2015, doi: 10.1016/j.ssc.2015.08.013.

[193] V. W. Brar *et al.*, “Hybrid Surface-Phonon-Plasmon Polariton Modes in Graphene/ Monolayer h - BN Heterostructures,” 2014.

[194] I. Crassee *et al.*, “Intrinsic terahertz plasmons and magnetoplasmons in large scale monolayer graphene,” *Nano Lett.*, vol. 12, no. 5, pp. 2470–2474, 2012, doi: 10.1021/nl300572y.

[195] T. Low and P. Avouris, “Graphene Plasmonics for Terahertz to Mid-Infrared Applications,” *ACS Nano*, vol. 8, no. 2, pp. 1086–1101, Feb. 2014, doi: 10.1021/nn406627u.

[196] Y. Li, K. Tantiwanichapan, A. K. Swan, and R. Paiella, “Graphene plasmonic

devices for terahertz optoelectronics," vol. 9, no. 7, pp. 1901–1920, 2020, doi: doi:10.1515/nanoph-2020-0211.

[197] Z. Fei, G. X. Ni, B. Y. Jiang, M. M. Fogler, and D. N. Basov, "Nanoplasmonic Phenomena at Electronic Boundaries in Graphene," *ACS Photonics*, vol. 4, no. 12, pp. 2971–2977, 2017, doi: 10.1021/acsphotonics.7b00477.

[198] J. Chen *et al.*, "Optical nano-imaging of gate-tunable graphene plasmons," *Nature*, vol. 487, no. 7405, pp. 77–81, 2012, doi: 10.1038/nature11254.

[199] Z. Fei *et al.*, "Gate-tuning of graphene plasmons revealed by infrared nano-imaging," *Nature*, vol. 487, no. 7405, pp. 82–85, 2012, doi: 10.1038/nature11253.

[200] D. Hsieh *et al.*, "A topological Dirac insulator in a quantum spin Hall phase (experimental realization of a 3D Topological Insulator)," *Nature*, no. 452, pp. 970–974, 2008, [Online]. Available: http://arxiv.org/abs/0910.2420.

[201] H. Zhang, C. X. Liu, X. L. Qi, X. Dai, Z. Fang, and S. C. Zhang, "Topological insulators in Bi 2 Se 3, Bi 2 Te 3 and Sb 2 Te 3 with a single Dirac cone on the surface," *Nat. Phys.*, vol. 5, no. 6, pp. 438–442, 2009, doi: 10.1038/nphys1270.

[202] T. Hirahara *et al.*, "Role of spin-orbit coupling and hybridization effects in the electronic structure of ultrathin Bi films," *Phys. Rev. Lett.*, vol. 97, no. 14, pp. 10–13, 2006, doi: 10.1103/PhysRevLett.97.146803.

[203] S. Nakajima, "The crystal structure of Bi2Te3-xSex," *J. Phys. Chem. Solids*, vol. 24, no. 3, pp. 479–485, 1963, doi: 10.1016/0022-3697(63)90207-5.

[204] S. J. Allen, D. C. Tsui, and R. A. Logan, "Observation of the two-dimensional plasmon in silicon inversion layers," *Phys. Rev. Lett.*, vol. 38, no. 17, pp. 980–983, 1977, doi: 10.1103/PhysRevLett.38.980.

[205] P. Di Pietro *et al.*, "Observation of Dirac plasmons in a topological insulator," *Nat. Nanotechnol.*, vol. 8, no. 8, pp. 556–560, 2013, doi: 10.1038/nnano.2013.134.

[206] J. S. Wu, D. N. Basov, and M. M. Fogler, "Topological insulators are tunable waveguides for hyperbolic polaritons," *Phys. Rev. B - Condens. Matter Mater. Phys.*, vol. 92, no. 20, pp. 1–12, 2015, doi: 10.1103/PhysRevB.92.205430.

[207] A. Bhattacharya, G. Georgiou, S. Sawallich, C. Matheisen, M. Nagel, and J. Gómez Rivas, "Large near-to-far field spectral shifts for terahertz resonances," *Phys. Rev.*

B, vol. 93, no. 3, p. 35438, Jan. 2016, doi: 10.1103/PhysRevB.93.035438.

[208] S. Chen *et al.*, "Real-space nanoimaging of THz polaritons in the topological insulator Bi2Se3," *Nat. Commun.*, vol. 13, no. 1, pp. 1–9, 2022, doi: 10.1038/s41467-022-28791-x.

[209] V. Pistore *et al.*, "Terahertz Plasmon Polaritons in Large Area Bi2Se3 Topological Insulators," *Adv. Opt. Mater.*, vol. 12, no. 4, p. 2301673, 2024, doi: https://doi.org/10.1002/adom.202301673.

[210] V. Pistore *et al.*, "Holographic Nano-Imaging of Terahertz Dirac Plasmon Polaritons in Topological Insulator Antenna Resonators," *Small*, vol. 20, no. 22, p. 2308116, 2024, doi: https://doi.org/10.1002/smll.202308116.

[211] Stefan A. Maier, *Plasmonics: Fundamentals and Applications*. New York: Springer US, 2007.

[212] T. Stauber, G. Gómez-Santos, and L. Brey, "Spin-charge separation of plasmonic excitations in thin topological insulators," *Phys. Rev. B - Condens. Matter Mater. Phys.*, vol. 88, no. 20, pp. 1–6, 2013, doi: 10.1103/PhysRevB.88.205427.

[213] T. Fan *et al.*, "Crystal growth and characterization of topological insulator BiSb thin films by sputtering deposition on sapphire substrates," *Jpn. J. Appl. Phys.*, vol. 59, no. 6, 2020, doi: 10.35848/1347-4065/ab91d0.

[214] Y. Wang, T. P. Ginley, and S. Law, "Growth of high-quality Bi2Se3 topological insulators using (Bi1-xInx) 2Se3 buffer layers Growth of high-quality Bi 2 Se 3 topological insulators using (Bi 1-x In x) 2 Se 3 buffer layers," *J. Vaccum Sci. Technol. B*, vol. 36, no. 2, p. 02D101, 2018.

[215] M. Wiesner *et al.*, "The effect of substrate and surface plasmons on symmetry breaking at the substrate interface of the topological insulator Bi 2 Te 3," *Sci. Rep.*, vol. 9, no. 1, pp. 1–8, 2019, doi: 10.1038/s41598-019-42598-9.

[216] S. Roberts and D. D. Coon, "Far-Infrared Properties of Quartz and Sapphire," *J. Opt. Soc. Am.*, vol. 52, no. 9, p. 1023, 1962, doi: 10.1364/josa.52.001023.

[217] B. S. Mendoza and W. L. Mochán, "Ab initio theory of the Drude plasma frequency," *J. Opt. Soc. Am. B*, vol. 38, no. 6, p. 1918, 2021, doi: 10.1364/josab.416741.

[218] T. Stauber and G. Gómez-Santos, "Plasmons in layered structures including

graphene," *New J. Phys.*, vol. 14, no. 10, p. 105018, Oct. 2012, doi: 10.1088/1367-2630/14/10/105018.

[219] S. Just, F. Lüpke, V. Cherepanov, F. S. Tautz, and B. Voigtländer, "Parasitic conduction channels in topological insulator thin films," *Phys. Rev. B*, vol. 101, no. 24, p. 245413, 2020, doi: 10.1103/PhysRevB.101.245413.

[220] Y. Xia *et al.*, "Observation of a large-gap topological-insulator class with a single Dirac cone on the surface," *Nat. Phys.*, vol. 5, no. 6, pp. 398–402, 2009, doi: 10.1038/nphys1274.

[221] J. G. Analytis *et al.*, "Bulk Fermi surface coexistence with Dirac surface state in Bi2 Se3: A comparison of photoemission and Shubnikov-de Haas measurements," *Phys. Rev. B - Condens. Matter Mater. Phys.*, vol. 81, no. 20, pp. 1–5, 2010, doi: 10.1103/PhysRevB.81.205407.

[222] E. Uesugi *et al.*, "Fermi level tuning of Ag-doped Bi 2 Se 3 topological insulator," *Sci. Rep.*, vol. 9, no. 1, pp. 3–10, 2019, doi: 10.1038/s41598-019-41906-7.

[223] J. Black, E. M. Conwell, L. Seigle, and C. W. Spencer, "Electrical and optical properties of some M2v–bN3vi–b semiconductors," *J. Phys. Chem. Solids*, vol. 2, no. 3, pp. 240–251, 1957, doi: https://doi.org/10.1016/0022-3697(57)90090-2.

[224] D. L. Greenaway and G. Harbeke, "Band structure of bismuth telluride, bismuth selenide and their respective alloys," *J. Phys. Chem. Solids*, vol. 26, no. 10, pp. 1585–1604, 1965, doi: https://doi.org/10.1016/0022-3697(65)90092-2.

[225] M. Bianchi *et al.*, "Coexistence of the topological state and a two-dimensional electron gas on the surface of Bi2Se3," *Nat. Commun.*, vol. 1, no. 1, p. 128, 2010, doi: 10.1038/ncomms1131.

[226] D. R. Bacon *et al.*, "Free-space terahertz radiation from a LT-GaAs-on-quartz large-area photoconductive emitter," *Opt. Express*, vol. 24, no. 23, pp. 26986–26997, Nov. 2016, doi: 10.1364/OE.24.026986.

[227] J. Yuan *et al.*, "Infrared Nanoimaging Reveals the Surface Metallic Plasmons in Topological Insulator," *ACS Photonics*, vol. 4, no. 12, pp. 3055–3062, 2017, doi: 10.1021/acsphotonics.7b00568.

[228] M. Zhao *et al.*, "Visible Surface Plasmon Modes in Single Bi2Te3 Nanoplate," *Nano Lett.*, vol. 15, no. 12, pp. 8331–8335, 2015, doi: 10.1021/acs.nanolett.5b03966.

[229] J. Y. Ou, J. K. So, G. Adamo, A. Sulaev, L. Wang, and N. I. Zheludev, “Ultraviolet and visible range plasmonics in the topological insulator Bi1.5Sb0.5Te1.8Se1.2,” *Nat. Commun.*, vol. 5, pp. 1–7, 2014, doi: 10.1038/ncomms6139.

[230] H. Yan *et al.*, “Tunable infrared plasmonic devices using graphene/insulator stacks,” *Nat. Nanotechnol.*, vol. 7, no. 5, pp. 330–334, 2012, doi: 10.1038/nnano.2012.59.

[231] H. Schlömer, Z. Jiang, and S. Haas, “Plasmons in two-dimensional topological insulators,” *Phys. Rev. B*, vol. 103, no. 11, pp. 1–9, 2021, doi: 10.1103/PhysRevB.103.115116.

[232] T. Taubner, F. eilmann, and R. Hillenbrand, “Nanoscale-resolved subsurface imaging by scattering-type near-field optical microscopy,” *Opt. Express*, vol. 13, no. 22, pp. 8893–8899, Oct. 2005, doi: 10.1364/OPEX.13.008893.

[233] F. Yang *et al.*, “Dual-Gated Topological Insulator Thin-Film Device for Efficient Fermi-Level Tuning,” *ACS Nano*, vol. 9, no. 4, pp. 4050–4055, Apr. 2015, doi: 10.1021/acsnano.5b00102.

[234] J. B. Pendry, L. Martín-Moreno, and F. J. Garcia-Vidal, “Mimicking surface plasmons with structured surfaces,” *Science (80-.).*, vol. 305, no. 5685, pp. 847–848, 2004, doi: 10.1126/science.1098999.

[235] D. R. Smith, J. B. Pendry, and M. C. K. Wiltshire, “Metamaterials and Negative Refractive Index,” *Science (80-.).*, vol. 305, no. 5685, pp. 788–792, 2004, doi: 10.1126/science.1096796.

[236] J. B. Pendry, “Negative Refraction Makes a Perfect Lens,” *Phys. Rev. Lett.*, vol. 85, no. 18, pp. 3966–3969, Oct. 2000, doi: 10.1103/PhysRevLett.85.3966.

[237] A. I. Fernández-Domínguez, C. R. Williams, F. J. García-Vidal, L. Martín-Moreno, S. R. Andrews, and S. A. Maier, “Terahertz surface plasmon polaritons on a helically grooved wire,” *Appl. Phys. Lett.*, vol. 93, no. 14, pp. 10–13, 2008, doi: 10.1063/1.2988897.

[238] E. Brock, E. Hendry, and A. Hibbins, “Subwavelength lateral confinement of microwave surface waves,” *Appl. Phys. Lett.*, vol. 99, 2011, doi: 10.1063/1.3622646.

[239] Y. Zhang *et al.*, “Terahertz spoof surface-plasmon-polariton subwavelength waveguide,” *Photonics Res.*, vol. 6, no. 1, p. 18, 2018, doi: 10.1364/prj.6.000018.

[240] S. A. Maier, M. L. Brongersma, P. G. Kik, S. Meltzer, A. A. G. Requicha, and H. A. Atwater, “Plasmonics - A route to nanoscale optical devices,” *Adv. Mater.*, vol. 13, no. 19, pp. 1501–1505, 2001, doi: 10.1002/1521-4095(200110)13:19<1501::AID-ADMA1501>3.0.CO;2-Z.

[241] K. Tanaka and M. Tanaka, “Simulations of nanometric optical circuits: Open-type surface plasmon polariton gap waveguide,” *Japanese J. Appl. Physics, Part 2 Lett.*, vol. 42, no. 6 A, pp. 256–266, 2003, doi: 10.1143/jjap.42.l585.

[242] X. Shen, T. J. Cui, D. Martin-Cano, and F. J. Garcia-Vidal, “Conformal surface plasmons propagating on ultrathin and flexible films,” *Proc. Natl. Acad. Sci. U. S. A.*, vol. 110, no. 1, pp. 40–45, 2013, doi: 10.1073/pnas.1210417110.

[243] Y. Yang, H. Chen, S. Xiao, N. A. Mortensen, and J. Zhang, “Ultrathin 90-degree sharp bends for spoof surface plasmon polaritons,” *Opt. Express*, vol. 23, no. 15, pp. 19074–19081, Jul. 2015, doi: 10.1364/OE.23.019074.

[244] Y. Li *et al.*, “k-dispersion engineering of spoof surface plasmon polaritons for beam steering,” *Opt. Express*, vol. 24, no. 2, pp. 842–852, Jan. 2016, doi: 10.1364/OE.24.000842.

[245] H. F. Ma, X. Shen, Q. Cheng, W. X. Jiang, and T. J. Cui, “Broadband and high-efficiency conversion from guided waves to spoof surface plasmon polaritons,” *Laser \& Photonics Rev.*, vol. 8, no. 1, pp. 146–151, 2014, doi: https://doi.org/10.1002/lpor.201300118.

[246] J. Y. Yin, J. Ren, H. C. Zhang, B. C. Pan, and T. J. Cui, “Broadband Frequency-Selective Spoof Surface Plasmon Polaritons on Ultrathin Metallic Structure,” *Sci. Rep.*, vol. 5, no. 1, p. 8165, 2015, doi: 10.1038/srep08165.

[247] Y. Yang, X. Shen, P. Zhao, H. C. Zhang, and T. J. Cui, “Trapping surface plasmon polaritons on ultrathin corrugated metallic strips in microwave frequencies,” *Opt. Express*, vol. 23, no. 6, pp. 7031–7037, Mar. 2015, doi: 10.1364/OE.23.007031.

[248] H. C. Zhang, S. Liu, X. Shen, L. H. Chen, L. Li, and T. J. Cui, “Broadband amplification of spoof surface plasmon polaritons at microwave frequencies,” *Laser \& Photonics Rev.*, vol. 9, no. 1, pp. 83–90, 2015, doi: https://doi.org/10.1002/lpor.201400131.

[249] P. Cheben, R. Halir, J. H. Schmid, H. A. Atwater, and D. R. Smith, “Subwavelength

integrated photonics," *Nature*, vol. 560, no. 7720, pp. 565–572, 2018, doi: 10.1038/s41586-018-0421-7.

[250] X. Zhang *et al.*, "Terahertz surface plasmonic waves: a review," *Adv. Photonics*, vol. 2, p. 1, 2020, doi: 10.1117/1.AP.2.1.014001.

[251] T. Holmgaard, Z. Chen, S. Bozhevolnyi, L. Markey, and A. Dereux, "Design and Characterization of Dielectric-Loaded Plasmonic Directional Couplers," *Light. Technol. J.*, vol. 27, pp. 5521–5528, 2010, doi: 10.1109/JLT.2009.2031654.

[252] L. Liu, Z. Han, and S. He, "Novel surface plasmon waveguide for high integration," *Opt. Express*, vol. 13, no. 17, pp. 6645–6650, Aug. 2005, doi: 10.1364/OPEX.13.006645.

[253] A. Boltasseva, T. Nikolajsen, K. Leosson, K. Kjaer, M. S. Larsen, and S. I. Bozhevolnyi, "Integrated optical components utilizing long-range surface plasmon polaritons," *J. Light. Technol.*, vol. 23, no. 1, pp. 413–422, Jan. 2005, doi: 10.1109/JLT.2004.835749.

[254] F. Liu, Y. Rao, Y. Huang, W. Zhang, and J. Peng, "Coupling between long range surface plasmon polariton mode and dielectric waveguide mode," *Appl. Phys. Lett.*, vol. 90, no. 14, p. 141101, Apr. 2007, doi: 10.1063/1.2719169.

[255] D. K. Gramotnev, K. C. Vernon, and D. F. P. Pile, "Directional coupler using gap plasmon waveguides," *Appl. Phys. B*, vol. 93, no. 1, pp. 99–106, 2008, doi: 10.1007/s00340-008-3206-0.

[256] A. Degiron, S.-Y. Cho, T. Tyler, N. M. Jokerst, and D. R. Smith, "Directional coupling between dielectric and long-range plasmon waveguides," *New J. Phys.*, vol. 11, no. 1, p. 15002, Jan. 2009, doi: 10.1088/1367-2630/11/1/015002.

[257] X. Gao *et al.*, "Ultrathin dual-band surface plasmonic polariton waveguide and frequency splitter in microwave frequencies," *Appl. Phys. Lett.*, vol. 102, no. 15, p. 151912, Apr. 2013, doi: 10.1063/1.4802739.

[258] X. Gao *et al.*, "Ultra-wideband surface plasmonic Y-splitter," *Opt. Express*, vol. 23, no. 18, pp. 23270–23277, Sep. 2015, doi: 10.1364/OE.23.023270.

[259] P. Yang *et al.*, "3D Nickel Skeletons as Ultrabroadband Terahertz Absorbers," *Adv. Electron. Mater.*, vol. 7, no. 10, p. 2100626, 2021, doi: https://doi.org/10.1002/aelm.202100626.

[260] D. Chen, B. Xu, Z. Qiu, X. Wang, J. Wu, and kaikai Huang, “Ultra-broadband terahertz metamaterial absorber based on flexible wave-absorbing material,” *Results Phys.*, vol. 52, p. 106880, 2023, doi: https://doi.org/10.1016/j.rinp.2023.106880.

[261] J. Gou, J. Wang, W. Li, H. Tai, D. Gu, and Y. Jiang, “Terahertz Absorption Characteristics of NiCr Film and Enhanced Absorption by Reactive Ion Etching in a Microbolometer Focal Plane Array,” *J. Infrared, Millimeter, Terahertz Waves*, vol. 34, no. 7–8, pp. 431–436, Aug. 2013, doi: 10.1007/s10762-013-9992-4.

[262] V. Pistore *et al.*, “Near-field probes for sensitive detectorless near-field nanoscopy in the 2.0–4.6 THz range,” *Appl. Phys. Lett.*, vol. 124, no. 22, p. 221105, May 2024, doi: 10.1063/5.0179714.

[263] S. P. Khanna, M. Salih, P. Dean, A. G. Davies, and E. H. Linfield, “Electrically tunable terahertz quantum-cascade laser with a heterogeneous active region,” *Appl. Phys. Lett.*, vol. 95, no. 18, p. 181101, Nov. 2009, doi: 10.1063/1.3253714.

[264] P. Liu, C. Eckberg, L. Pan, P. Zhang, K. L. Wang, and G. Lüpke, “Ultrafast optical control of surface and bulk magnetism in magnetic topological insulator/antiferromagnet heterostructure,” *Sci. Rep.*, vol. 12, no. 1, p. 12117, 2022, doi: 10.1038/s41598-022-16205-3.

[265] H. Yang, E. Hebestreit, E. Josberger, and M. Raschke, “A cryogenic scattering-type scanning near-field optical microscope,” *Rev. Sci. Instrum.*, vol. 84, p. 23701, 2013, doi: 10.1063/1.4789428.

[266] D. Lang *et al.*, “Infrared nanoscopy down to liquid helium temperatures,” *Rev. Sci. Instrum.*, vol. 89, no. 3, p. 33702, Mar. 2018, doi: 10.1063/1.5016281.

[267] W. Luo *et al.*, “High sensitivity variable-temperature infrared nanoscopy of conducting oxide interfaces,” *Nat. Commun.*, vol. 10, no. 1, p. 2774, 2019, doi: 10.1038/s41467-019-10672-5.

[268] Z. Chen, L. Zhao, K. Park, T. A. Garcia, M. C. Tamargo, and L. Krusin-Elbaum, “Robust Topological Interfaces and Charge Transfer in Epitaxial Bi2Se3/II–VI Semiconductor Superlattices,” *Nano Lett.*, vol. 15, no. 10, pp. 6365–6370, Oct. 2015, doi: 10.1021/acs.nanolett.5b01358.